INFORMATION TO USERS

This manuscript has been reproduced from the microfilm master. UMI films the text directly from the original or copy submitted. Thus, some thesis and dissertation copies are in typewriter face, while others may be from any type of computer printer.

The quality of this reproduction is dependent upon the quality of the copy submitted. Broken or indistinct print, colored or poor quality illustrations and photographs, print bleedthrough, substandard margins, and improper alignment can adversely affect reproduction.

In the unlikely event that the author did not send UMI a complete manuscript and there are missing pages, these will be noted. Also, if unauthorized copyright material had to be removed, a note will indicate the deletion.

Oversize materials (e.g., maps, drawings, charts) are reproduced by sectioning the original, beginning at the upper left-hand corner and continuing from left to right in equal sections with small overlaps.

ProQuest Information and Learning
300 North Zeeb Road, Ann Arbor, MI 48106-1346 USA
800-521-0600

Experimental Investigation of Compressible Turbulent Jets

by

Zhexuan Wang

A Dissertation Submitted to the Graduate Faculty in Engineering in partial fulfillment of the requirements for the degree of Doctor of Philosophy, The City University of New York.

2003

This manuscript has been read and accepted for the Graduate Faculty in Engineering in satisfaction of the dissertation requirement for the degree of Doctor of Philosophy.

1/23/03
Date

Professor Yiannis Andreopoulos
Chair of Examining Committee

1-23-2003
Date

Dean Mumtaz Kassir
Executive Officer

Professor Yiannis Andreopoulos
Dept. of Mech. Eng., CCNY

Professor Latif M. Jiji
Dept. of Mech. Eng., CCNY

Professor Jimmy Feng
Dept. of Mech. Eng., CCNY

Professor Damian Rouson
Dept. of Mech. Eng., CCNY

Professor Nadine Aubry
Dept. of Mech. Eng., NJIT

Supervisory Committee

THE CITY UNIVERSITY OF NEW YORK

Abstract

Experimental Investigation of Compressible Turbulent Jets

by

Zhexuan Wang

Adviser: Professor Yiannis Andreopoulos

The motivation of this study is the important role of jets in subsonic and supersonic combustion. To understand the details of a jet mixing with the ambient air, an experimental study was conducted on subsonic compressible jet flows of different gases issued into the air. How quickly and how well a jet flow can be mixed with ambient flow will have a major influence on combustion efficiency, heat release rate, pollutant formation, jet noise suppression and size reduction of such functions.

The jet exit used in this work is circular in cross section with a diameter of 7mm. Three different gases were used, nitrogen, helium and krypton respectively at three distinct Mach numbers 0.3, 0.6, and 0.9, which lead to conclusions based on density and velocity variation. Total pressure, total temperature, and velocity measurements, were carried out with the aid of pressure transducers, thermocouples, and the well-known Particle Image Velocimetry (PIV) technique respectively. Compressibility effects combined with density effects were thus obtained.

Compressibility (based on Mach number) and density effects were found to be the key factors in this present work. The PIV scheme with the Cross-Correlation and Auto-

Correlation methods was carried out with two pulsed-lasers, which provided the light source for visualization and quantitative measurements, and talcum powders, which seeded the jet flows for light scattering. The velocity distribution along the centerline obtained from experimental data indicated that the velocity decay of helium is the fastest, while the velocity decay of krypton is the slowest of the three used gases. Total pressure distribution along the centerline also showed the same results. Correspondingly, the level of turbulent fluctuations is also higher in the case of helium jets indicating better mixing with the ambient air. The centerline velocity decays in proportion to the inverse of location away from the jet exit, as well as velocity decay constants were obtained for different jet flows and compared with the existing information. The present results were found to be in good agreement with previous work. Total temperature results revealed that at a low subsonic Mach number range, the total temperature could be treated as a constant, which is equivalent to the ambient temperature.

By using helium, a lighter than air gas and krypton a heavier than air gas, density effects were studied in combination with compressibility effects. Distributions of mean concentration and mean density in the mixing zones were computed from the measurements of total pressure, total temperature and velocity with satisfactory accuracy.

Acknowledgments

I would like to offer my most grateful acknowledgment to my mentor, Dr. Yiannis Andreopoulos, whose direction of the experimental program has been the key guidance for this treatise. I would also like to thank Mr. Minwei Gong, Mr. Savvas Xanthos, and Mr. Alexis Pierides, whose comments helped me find a solution to many difficulties during the experiments; Mr. Klaus Hermening, who contributed to some of the initial setup in performing the experiments; Mr. Jinrui Chen and Mr. Luis Hernandez, who designed and installed several parts of the setup; Mr. Kaixin He and Miss Paula Washington, who helped in the typing and collecting the contents of the present work. I would like to express my special thanks to Ms. Adriana Romo, who contributed tremendously with the wording and syntax of the present work. Without the generous support of the aforementioned individuals, this treatise would not have been possible.

I am grateful to my parents for their trust and understanding, and to my brother and sister for their moral support and confidence on me.

Table of Contents

Nomenclature

a	sonic speed
a^*	critical sonic speed
a_o	total sonic speed
A	cross-section area or surface area of thermocouple
C_p	constant pressure heat capacity
C_{pa}	constant pressure heat capacity of air
C_{pH}	constant pressure heat capacity of Helium
C_{pK}	constant pressure heat capacity of Krypton
C_v	constant volume heat capacity
c	concentration
$\bar{c}$	mean concentration
$\tilde{c}$	mean concentration obtained by mean total temperature, velocity, and total pressure
C_{ij}	correlation coefficient
dX	displacement of frames in X direction
dY	displacement of frames in Y direction
dZ	displacement of frames in Z direction
d_{ij}	deviatoric stress tensor
d_p	tracer particle diameter
D	jet diameter

DC	direct current
D_H	hydraulic diameter
D_r	decay rate
f	friction coefficient
$\bar{f}$	average friction coefficient
g	gravity acceleration
h_o	total enthalpy
h	enthalpy or heat transfer coefficient
h^*	critical enthalpy
L	length of loss
L_a	horizontal length of loss
L_b	vertical length of loss
L_e	elbow equivalent length of loss
L_{max}	maximum duct length to obtain M 1
m	mass of thermocouple sensor
$\dot{m}$	mass exchange rate between jet and ambient
M	Mach number
$\bar{M}$	mean Mach number
$\bar{\bar{M}}$	mean Mach number obtained through mean pressure
M_c	convective Mach number
M_{CL}	centerline Mach number
M_j	jet exit Mach number

M^*	critical Mach number
P	static pressure
P^*	critical pressure
P_0	total pressure
P_0'	total pressure fluctuation
$\overline{P_0}$	mean total pressure
$\dot{q}$	heat transfer rate to the sensor by convection
r.m.s.	root mean square
R	specific gas constant
$\overline{R}$	universal gas constant
Re	Reynolds number
S	entropy
s^*	critical entropy
S^2	variance
T	static temperature
T_0	total temperature
T_m	media temperature
T^*	critical temperature
$\overline{T_0}$	mean total temperature
U	velocity
U_c	convective velocity
U_j	jet exit velocity

$\bar{U}$	mean velocity in x direction
U_g	velocity induced by gravity
U_p	tracer particle velocity
U_s	Stokes velocity
U_{CL}	centerline velocity
U	velocity or voltage
$\bar{U}$	mean velocity
U^*	critical velocity
U_{max}	maximum velocity with full expansion
x	distance from jet exit
Xspot	length of interrogation zone
Yspot	width of interrogation zone
y	distance off the centerline
α	thermal diffusivity
ε	roughness of surface
γ	gas constant
γ_a	gas constant of air
γ_H	gas constant of Helium
γ_K	gas constant of Krypton
λ	ratio of velocity and critical sonic speed
μ	dynamic viscosity
ρ	density

$\bar{\rho}$ mean density

ρ_t total density

ρ_p particle density

ρ_a air density

ρ_c centerline density

ρ_j jet flow density

ρ^* critical density

τ time constant

τ_s tracer particle settle down time

τ_w shear stress at wall

ν kinematic viscosity

$\bar{\Omega}$ mean voriticity

List of Tables

List of Figures

Chapter I Introduction to Jet Flows and Previous Work

Anyone who has experienced air traveling has heard of the term jet planes. Some people have had the rare experience of maneuvering such jet planes. It is, —some people say—, the jet technology that advanced our society. What is then a jet? What's involved in the jet flows? These interesting questions are the motivation for the introduction of this topic.

1.1 Motivation

Jets in general are not only confined to jet planes. As we all know, jets are used in many different applications and configurations, such as water jets, air jets, planar jets, wall jets, and so on, and they can be classified by their function. We dwell with jets in our everyday life: for example, the Windex cleaner contains a small jet that injects a uniform spray on a dirty surface that needs to be cleaned. Inkjet printers are another example, essential peripherals in every day computer based life, which use micro jets that bring to life fonts and pictures by spraying ink onto paper.

Jets have also been observed in many other practical applications, such as aeroacoustics, combustion and jet flames. One example of jets used in the field can be found in the car, where fuel injector, as a prototype of jet is being used. Fuel injectors are nozzles that inject a spray of fuel into an intake of air, as shown in Figure 1.1. A metered amount of fuel is trapped in the nozzle end of the injector and at some proper time the nozzle is opened and the fuel sprays into the surrounding air, very similar to a jet. High liquid spray velocity is necessary to assure evaporation and mixing with the air which is considered quasi-stationary just before the intake valve opens. Injectors that spray into a combustion chamber directly, a technique that assures a very constant fuel input cycle to cycle and cylinder to cylinder, must operate with much higher pressures than injectors that spray into the intake system (some as high as 10MPa) since the air into which the fuel must be injected, is at a much higher pressure within the combustion chamber than the air in the intake system which is at about one atmosphere.

After vaporization where small droplets of liquid fuel evaporate to vapor, the fuel vapor must mix with the air to form a mixture within the AF (air to fuel ratio) range which is combustible. This mixing comes about because of the high fuel injection velocity added to the swirl and turbulence of the air in the cylinder. The non-homogenous distribution of air-fuel ratio that develops around the injected fuel jet is shown in Figure 1.1. The jet and the air-fuel vapor zones around the inner liquid core are identified. The later is surrounded by successive zones of vapor, which are:

[A] = too rich to burn

[B] = rich combustible

[C] = stoichiometric

[D] = lean combustible

The point of interest here is the process of mixing and combustion. which will be further elaborated upon. It can be seen that to control mixing is very important in combustion. which will lead to safety and efficiency issues. Another choice of fuel is in gas phase.

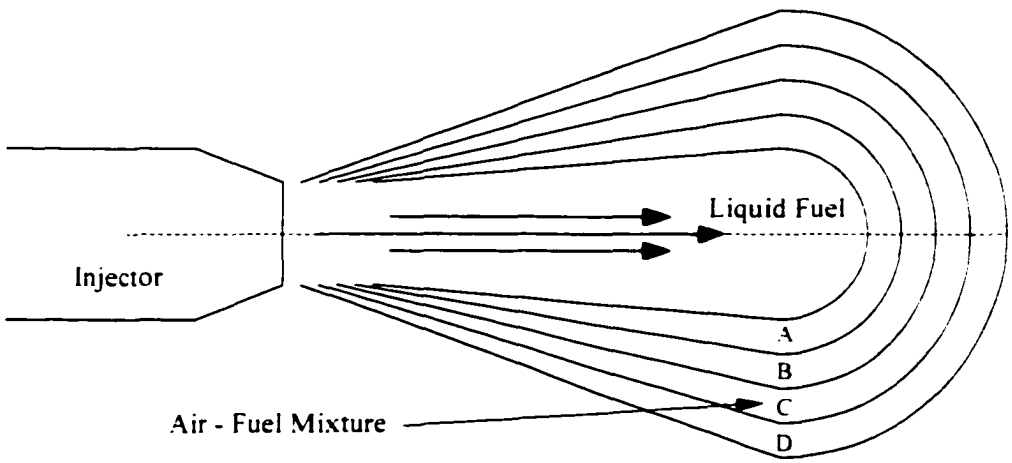

Figure 1.1: Fuel Injector

Great differences exist between the design of a jet engine and a car engine. As for the design of aircraft engines, there is the need to predict and control low subsonic to high subsonic speed flows for optimization. At a wide Mach number range from 0.3 to 0.9, the flow becomes compressible, thus large variations in pressure, density and/or temperature may take place that will have an impact on the dynamics of the occurring turbulent flow. Improving prediction capabilities and providing effective control of compressible flows require an accurate description of the large and small scales dynamics as well as the time-averaged statistical properties of the flow [8]. Although a substantial amount of work has been devoted in the past to study the behavior of turbulent flows, some remain as unsolved problems for the science and engineering community. Thus a better fundamental understanding of the turbulent flow structure is essential.

My specific motivation to research jet flows derives from the safety and efficiency issues, two extremely important factors in the design of aircraft engines. The physics of the mixing process between jet flow and ambient fluid is of considerable interest from both fundamental and practical points of view. It has been widely suggested that the mixing process is intimately connected with the turbulence. In the wide range of engineering flows, the mixing process that governs the mixing rate in combustion chambers, such as the jet noise level of airplanes and vehicles, and the spread of pollutants at industrial sites is a critical technical problem to be dealt with. In many of these applications, the solution is the mixing enhancement of a jet flow with ambient

flows. How quickly and how well a jet flow can be mixed with ambient flows will have a major influence on combustion efficiency, heat release rate, pollutant formation, jet noise suppression and size reduction of such functions. Considering these important factors on efficiency and its relation to safety, the need for more investigation of jet flows is a must.

Jets are considered as one of the typical free shear flows and the studies on such flow geometry will contribute to further understanding of free shear flows. The following part gives a brief introduction on jet flows with both physical description and mathematical models used in this research.

1.2 Introduction to Turbulent Jets and the Governing Equations

1.2.1 Jet Model

To simulate the jets in combustion chambers, where several jets may be present, investigators have done extensive research on two jet mixing [41][61]. But it is necessary to learn the case with one single jet before going into more complicated flow fields. The basic understanding of the physics of such flows has been obtained through investigations in conveniently selected and reasonably simplified flow configurations. Figure 1.2 shows a typical flow schematic, where a free circular jet issuing in ambient air, a case that has been investigated experimentally.

Some quantities are of great interest to our research. Figure 1.2 displays a few of them. ρ_a and ρ_j are the ambient and jet flow density respectively. U_j is the velocity at the jet exit. $\bar{U}$ and $\bar{\rho}$ are the mean velocity and mean density profiles respectively. $\dot{m}$ is the mass exchange rate with the ambient entrainment. $\bar{\Omega}$ is the mean vorticity, which can be derived from the velocity distribution. $\bar{T}$ is the mean static temperature.

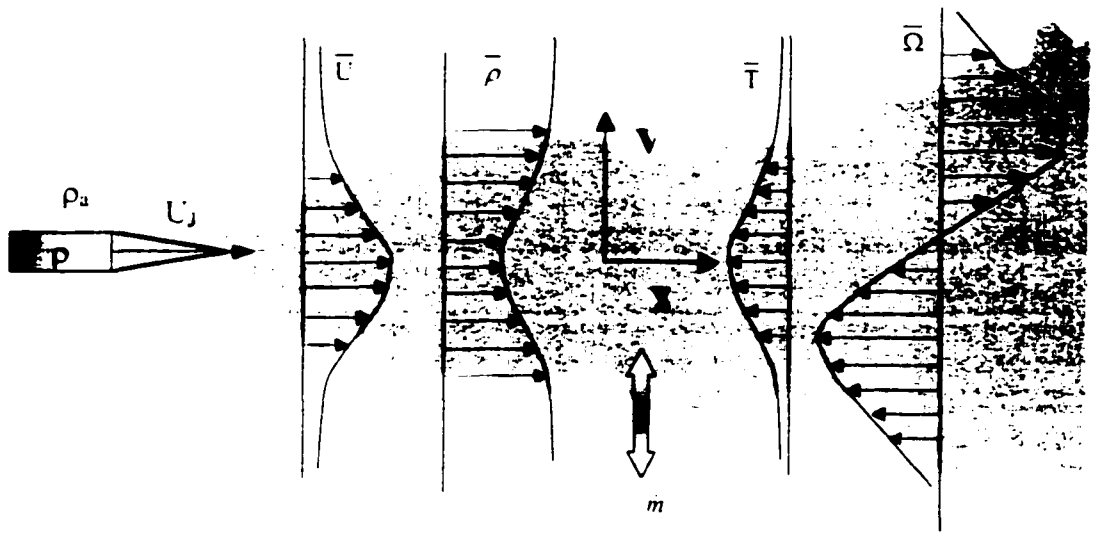

Figure 1.2: Conceptional Jet

As it is known so far, the jet flow, without the presence of shock waves, contains several regions, which are shown in Figure 1.3.

It is interesting to note that generally, jet flows become turbulent within a distance along the jet axis at about 10 exit diameters (this distance may vary with different exit conditions). The region between the exit plane and the onset of the turbulent region is the potential core, as shown in the Figure 1.3. In the potential core, the velocity is constant in the radial direction and gradually describes a bell-curve shape as the flow develops downstream. This region after the potential core is named transition zone, followed by a fully turbulent region, which in incompressible flows is self-similar. The interesting phenomenon for this region is that the velocity decays inversely linearly

against the location, no matter what kind of gas is used in the jet [66][67][71][105]. Close to the edge shown in the same figure, the jet flow is mixing with ambient air in this region. Because of the velocity difference on both sides of the range, there is shear stress created, which gives the name to this region, shear layer [11][74][91]. Usually, the shear layer is associated with turbulence, noise, so it affects the instability of jet flows. Many researchers have also investigated this region [15][20][60].

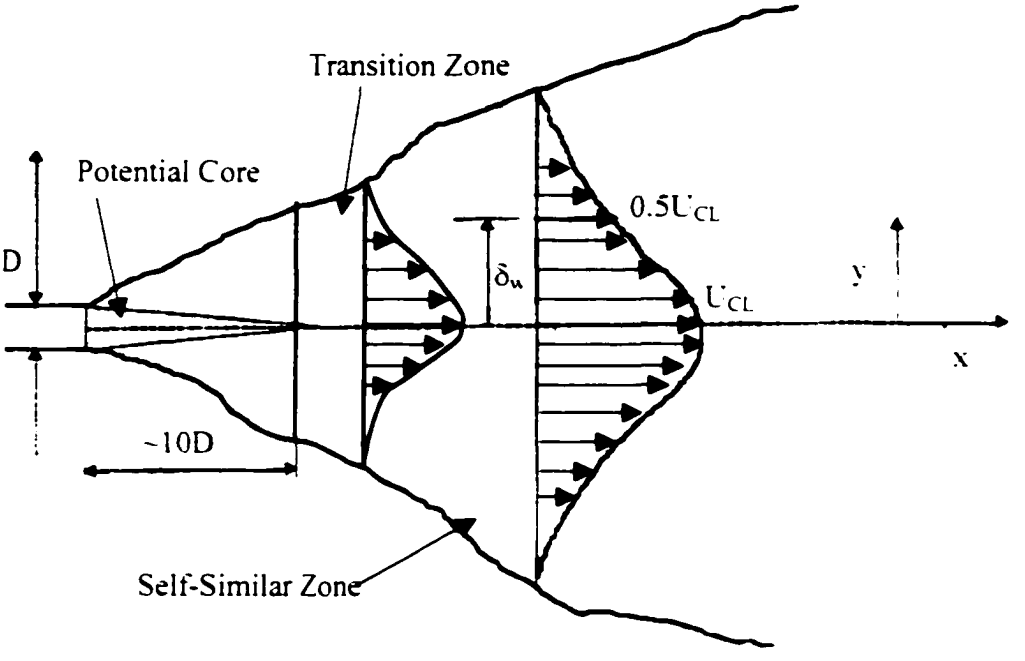

Figure 1.3: Regions in Jet Flow

The jet flow is characterized by two length scales in the self-preserving region. U_{CL}, which is the centerline velocity and δ_w, which is the transverse location off the centerline when the velocity reaches half of the centerline velocity [94].

1.2.2 Governing Equations

Jet flow is assumed to be perfect gas with constant specific heats. The governing equations of motion for a compressible, viscous, heat conducting fluid in the form of tensors are,

$$\frac{\partial \rho}{\partial t} + \frac{\partial \rho u_i}{\partial x_i} = 0 \qquad (1.2.1)$$

$$\rho \frac{\partial u_i}{\partial t} + \rho u_j \frac{\partial u_i}{\partial x_j} = -\frac{\partial p}{\partial x_i} + \frac{\partial d_{ij}}{\partial x_j} \qquad (1.2.2)$$

$$\rho \frac{\partial h_0}{\partial t} + \rho u_j \frac{\partial h_0}{\partial x_j} = \frac{Dp}{Dt} - \frac{\partial}{\partial x_j}\left(k \frac{\partial T}{\partial x_j}\right) + d_{ij} \frac{\partial u_i}{\partial x_j} \qquad (1.2.3)$$

respectively the continuity, momentum and energy equations, where ρ is density, u_i is the velocity component, p is static pressure, T is static temperature, k is thermal conductivity, and h is the enthalpy defined by constant pressure heat capacity C_p as $h_0 = C_p T_0$. The deviatoric stress tensor d_{ij} is given by

$$d_{ij} = \mu\left(\frac{\partial u_i}{\partial x_j} + \frac{\partial u_j}{\partial x_i} - \frac{2}{3}\frac{\partial u_k}{\partial x_k}\delta_{ij}\right)$$

Energy equation can be rewritten as,

$$\rho C_p \frac{DT}{Dt} = \frac{Dp}{Dt} - \frac{\partial}{\partial x_j}\left(k \frac{\partial T}{\partial x_j}\right) + d_{ij} \frac{\partial u_i}{\partial x_j} \qquad (1.2.4)$$

The above equations can be integrated for one-dimensional isentropic flow to yield the well-known relations developed from thermodynamics equations under the condition that no dissipation, no work associate with pressure presenting [82]. Starting with energy equation.

$$h_1 + \frac{V_1^2}{2} = h_2 + \frac{V_2^2}{2} = h + \frac{V^2}{2} = const \qquad (1.2.5)$$

where, h is enthalpy and V is velocity.

Equation (1.2.5) applies to several of flow including shock waves, friction and other adiabatic flows. For isentropic gas, enthalpy can be expressed as.

$$h = C_p T = \frac{a^2}{\gamma - 1} = \frac{\gamma}{\gamma - 1}\frac{p}{\rho} = \frac{\gamma}{\gamma - 1} RT \qquad (1.2.6)$$

where T is static temperature, a is the sonic speed, p is the static pressure, ρ is the density, γ is a gas constant, which has the following definition.

$$\gamma = \frac{c_p}{c_v}$$

where C_p and C_v are the constant-pressure specific heat and constant-volume specific heat respectively. C_p is given by $C_p = \frac{\gamma R}{\gamma - 1}$. The well-known gas constant for air is 1.4.

R is another gas constant called specific gas constant of a particular gas. R has the following definition.

$$R = \frac{\bar{R}}{\bar{M}}$$

where $\bar{R}$ is the universal gas constant, equal to 8.314 KJ/Kmol K, while $\bar{M}$ is the molecular weight. For air, $\bar{M}$ =28.97 Kg (Kmol). So the gas constant for air is given by,

$$R = \frac{\bar{R}}{\bar{M}} = \frac{8.314}{28.97} = 0.287\,\text{KJ/Kg K or } 287\,\text{J/Kg K}$$

Sonic speed a is defined as:

$$a = \sqrt{\gamma RT}$$

while γ and R were given above. T is temperature in Kelvin. So when air is at 20°C, the sonic speed is

$$a = \sqrt{\gamma RT} = \sqrt{1.4 \times 287 \times (20 + 273)} = 343 \text{ m/s}$$

ρ is density.

With one more relation $p = \rho RT$, the energy equation (1.2.5) can take any of the following forms.

$$C_p T + \frac{V^2}{2} = const \qquad (1.2.7a)$$

$$\frac{a^2}{\gamma - 1} + \frac{V^2}{2} = const \qquad (1.2.7b)$$

$$\frac{\gamma}{\gamma - 1}\frac{p}{\rho} + \frac{V^2}{2} = const \qquad (1.2.7c)$$

$$\frac{\gamma}{\gamma - 1} RT + \frac{V^2}{2} = const \qquad (1.2.7d)$$

To find fixed constant from the equations above, three different types of parameters are used.

1). Stagnation parameters (subscript 0):

When the flow velocity reaches 0 (not necessary to have such location), other flow parameters are called stagnation parameters as follows.

$$h + \frac{V^2}{2} = h_0 = C_p T_0 = \frac{a_0^2}{\gamma - 1} = \frac{\gamma}{\gamma - 1}\frac{p_0}{\rho_0} = \frac{\gamma}{\gamma - 1} RT_0 \qquad (1.2.8)$$

where h_0, T_0, p_0, and ρ_0 are called stagnation enthalpy, stagnation temperature, stagnation pressure and stagnation density respectively. To differentiate them from static parameters h, T, p, and ρ, they are referred to as total enthalpy, total temperature, total pressure and total density. h_0, T_0, $\frac{p_0}{\rho_0}$, a_0 all reflect the energy amplitude.

2). Maximum velocity (V_{max}):

From energy equation (1.2.5), if the gas expands to vacuum, when h=0, T=0, then the maximum velocity is reached (this state does not exist in reality), and thus can be used to express the constant mentioned above.

$$\frac{\gamma}{\gamma - 1}\frac{p}{\rho} + \frac{V^2}{2} = \frac{V_{max}^2}{2} \qquad (1.2.9)$$

Comparing equations (1.2.9) and (1.2.8),

$$V_{max} = \sqrt{2h_0} = \sqrt{2C_p T_0} = a_0\sqrt{\frac{2}{\gamma - 1}} = \sqrt{\frac{2\gamma}{\gamma - 1}\frac{p_0}{\rho_0}} = \sqrt{\frac{2\gamma}{\gamma - 1} RT_0}$$

3). Critical parameters (superscript *)

When V=a=a*, where a* is called critical velocity, then all the parameters now are called critical parameters, expressed by h^*, T^*, p^*, ρ^*. Thus the energy equation again can be expressed as

$$\frac{a^2}{\gamma-1}+\frac{V^2}{2}=\frac{a^{*2}}{\gamma-1}+\frac{a^{*2}}{2}=\frac{\gamma+1}{\gamma-1}\frac{a^{*2}}{2} \qquad (1.2.10)$$

Since Mach number is defined as $M=\frac{V}{a}$, it is obvious that in this case M=1.

Utilizing the above equations we can derive several useful relations. For example, by combining equation (1.2.7d) and (1.2.8), one can get

$$\frac{\gamma}{\gamma-1}RT+\frac{V^2}{2}=\frac{\gamma}{\gamma-1}RT_0$$

or

$$\frac{T_0}{T}=1+\frac{\gamma-1}{2}\frac{V^2}{\gamma RT}=1+\frac{\gamma-1}{2}M^2 \qquad (1.2.11)$$

Note that T_0 is the same for all points in the flow, provided that the flow is adiabatic.

When a perfect gas flows isentropically, its pressure and density are related to temperature in the following ways.

$$\frac{p_0}{p}=\left[\frac{T_0}{T}\right]^{\frac{\gamma}{\gamma-1}} \text{ and } \frac{\rho_0}{\rho}=\left[\frac{T_0}{T}\right]^{\frac{1}{\gamma-1}} \qquad (1.2.12)$$

By combining these with Eq. (1.2.11), pressure and density can be expressed in terms of Mach number:

$$\frac{p_0}{p} = \left[1 + \frac{\gamma - 1}{2} M^2\right]^{\frac{\gamma}{\gamma - 1}} \qquad (1.2.13)$$

$$\frac{\rho_0}{\rho} = \left[1 + \frac{\gamma - 1}{2} M^2\right]^{\frac{1}{\gamma - 1}} \qquad (1.2.14)$$

$\frac{T_0}{T}$, $\frac{p_0}{p}$, and $\frac{\rho_0}{\rho}$ are tabulated in Figure 1.4 (refer to page 16). Values are based on $\gamma = 1.4$.

To calculate the Reynolds number $\mathrm{Re} = \frac{\rho U L}{\mu}$, the viscosity coefficient μ is needed, which can be obtained in many references for the room temperature. For other temperatures, the viscosity is defined by the well-known Sutherland formula based on a different temperature T.

$$\frac{\mu}{\mu_0} = \frac{T_r + S_1}{T + S_1}\left(\frac{T}{T_r}\right)^{\frac{3}{2}} \qquad (1.2.15)$$

where, μ_0 is the viscosity at the reference temperature T_r.

As it is known, for air, S_1=110.3, $\mu_0 = 1.789 \times 10^{-5} \frac{kg}{m \cdot s}$ and $T_r = 288K$, hence

$$\mu = 1.46 \times 10^{-6} \frac{T^{1.5}}{T + 110.3} \qquad (1.2.16)$$

The same formula with a larger coefficient is listed for helium.

$$\mu = 1.52\times10^{-6}\frac{T^{1.5}}{T+98} \qquad (1.2.17)$$

Combining Eq. (1.2.7a), (1.2.8), and (1.2.12), the following equation is written as.

$$\frac{P_0}{P} = \left(\frac{T_0}{T}\right)^{\frac{\gamma}{\gamma-1}} = \left(\frac{T_0}{T_0 - \frac{V^2}{2C_p}}\right)^{\frac{\gamma}{\gamma-1}} \qquad (1.2.18)$$

In helium jets or krypton jets, due to the mixure with ambient air, the gas constants γ and C_p are unknown, both depend on concentration of the gas from the jet. In the case of a helium jet, they are defined as.

$$\gamma = c\cdot\gamma_H + (1-c)\cdot\gamma_A \qquad (1.2.19a)$$

$$C_p = c\cdot C_{pH} + (1-c)\cdot C_{pA} \qquad (1.2.19b)$$

where c is the local concentration in the jet flow field.

It can then be concluded that to find the concentration c at any location, total pressure P_0, total temperature T_0, and velocity V are needed at the same location of flow. If all the three quantities can be measured experimentally, concentration c can be determined. This is the reason for which three separate experiments were set up in order to measure total pressure, total temperature, and velocity respectively. Chapter VII will provide more details on the calculation algorithm and Chapter VIII will analyze the corresponding error involved.

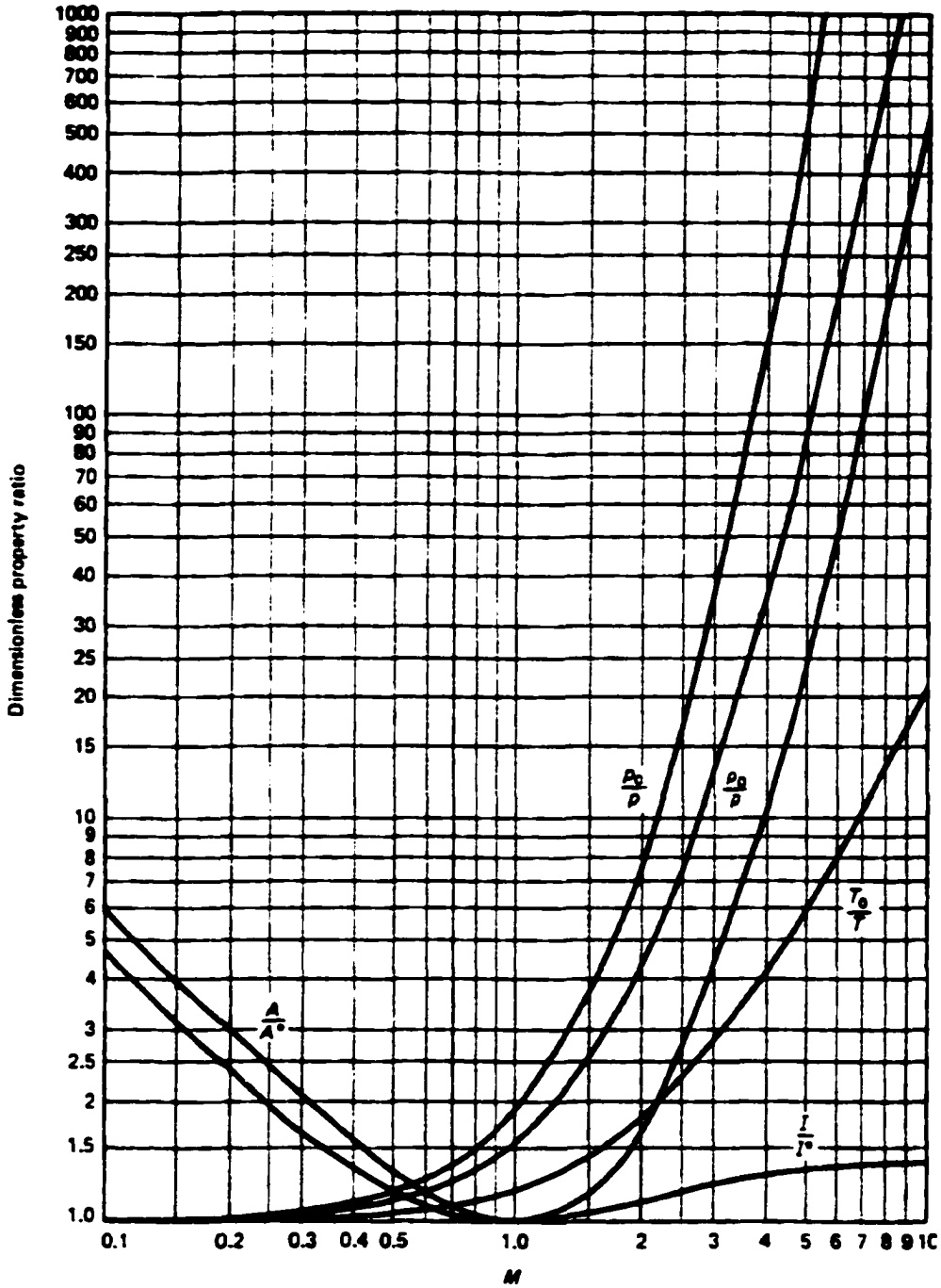

Figure 1.4: Isentropic Relations

(Saad, M.A. Compressible Fluid Flow Second Edition)

1.3 Literature Review

Previous works offered images, data and results on jet flows, on various research issues, which will be discussed below. The research work advances our knowledge on jet flows and provides data for possible comparison with theoretical and computational results. The following part is a survey of the past work.

1.3.1 Research Interests

Different types of jets were designed and put to use for many purposes, as was introduced before. The corresponding research involved in these fields was carried out in various geometries and configurations, such as planar jets [9][36], wall jets [28], pulsed jets [12], and so on. The jet flow researched in this study is circular and continuous, with a jet exit diameter of 7mm, running at subsonic speeds.

Thus far what scientists and engineers have been looking for in jet flows is as follows:

1. Pressure, velocity, density, temperature as well as concentration distribution

It is important to obtain detailed and accurate data for mean and turbulent quantities in order to provide information on turbulence enclosures. Obviously, if all the quantities mentioned above are known, the flow field can be described. For instance, knowing the velocity distribution along the centerline, the self-similar region can be determined [66][67][98][104]. Density is used to discuss the density effects of the jet flow

[38][87][101]. Temperature is a measure of the energy and sonic speed [44][45][69]. The Mach number is associated with pressure information. Therefore to discuss the Mach number effect. or compressibility effect. pressure is necessary [11]. Researchers have been working on different aspects of the jet flow. such as the velocity distribution. the pressure distribution ad so on. However. little work has been done to combine all the information and to give a general view of jet flows. This is because of the shortage of common fields. in which researchers are working on the same issues. Our research work will go into said issues.

2. Spreading Rate

The spreading rate is a characteristic indicative of mixing [40][52]. When the self-similar state is reached. the mixing layer spreads linearly with a constant value of the spreading rate. One typical method for defining the spreading rate is. utilizing the velocity distribution along the transverse direction. When the velocity reaches half of the corresponding centerline velocity. a typical thickness of the mixing layer can be defined. By applying this procedure at various locations downstream. the spreading rate is obtained. It can be observed that the spreading rate shows the mixing layer growth. The other method of defining the spreading rate is a semi-empirical law proposed by Brown and Roshko [13]. as shown in Figure 1.5.

$$(\frac{\partial \delta_\omega}{\partial x})_0 = C_\delta \frac{(1-r)(1+\sqrt{s})}{2(1+r\sqrt{s})} \qquad (1.3.1)$$

where, $r = U_2 / U_1$, velocity ratio between external flows, $s = \rho_2 / \rho_1$ the density ratio, C_δ is a constant ($\cong 0.181$), which represents the spreading rate of the mixing layer at uniform density, δ_w is the vorticity thickness at the wall given by $\delta_w = \dfrac{U_1 - U_2}{\left(\dfrac{\partial U}{\partial y}\right)_{max}}$.

where $U_1 - U_2$ is the velocity difference between external flows, while $\left(\dfrac{\partial U}{\partial y}\right)_{max}$ is the maximum mean velocity gradient of the flow. It can be seen that the spreading rate depends on the velocity distribution, density effects and the degree of compressibility of the gas.

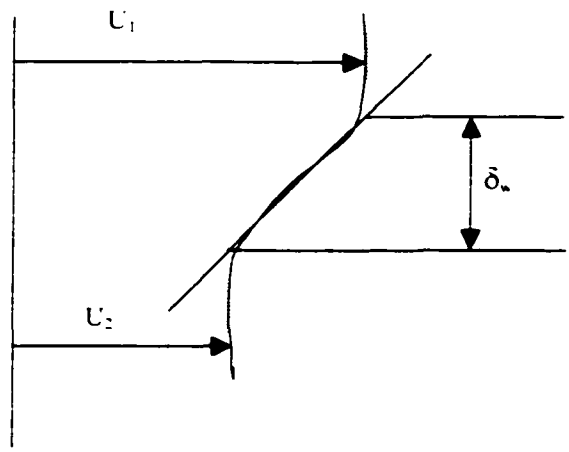

Figure 1.5: Schematic Shape of the Mean Streamwise Velocity Profile of a Mixing Layer

3. Shear Layers

Jet flow is a typical model of shear layers which have led to some papers discussing the shear layers since [11][15][74][75][91] referred articles were published. The problem of hydrodynamic instability has been the main subject in this research field because it controls for the jet mixing with ambient air fluid [20][60][62]. There is a difference in shear layer growth between an incompressible flow and compressible flow [74].

4. Self-Similarity Field

Previous work offered different results for velocity measurement. Using a new method of analyzing hot-wire signals, Rodi (1975a) [81] made measurements of mean velocity and turbulent intensities and showed that the mean velocity decay along the axis of the jet conformed to the x^{-1}, which was expected from similarity analysis, but the measurements of Wygnanski & Fiedler (1969) [102] gave different results as no self-similarity that could be reached in the same cases.

5. Noise Generation

Research interest in compressible jet flows is also motivated by the need to understand and reduce noise, which is associated with density and pressure fluctuations in the large scale of coherent structures and small scale of turbulence presence in the flow [22][32][33][68].

6. Interaction Between Jets

It is meaningful to discuss the interaction between jets, especially for the combustion chambers that consist of several injections. In other cases such as the inkjet printers, several micro jets are working together in the printing operation [21][56][61].

7. Interaction Between a Jet and a Shock Wave

This situation happens very often in supersonic jets [4][8][70]. It is claimed that the shock wave will have a strong effect on the turbulence. Considerable change in the flow structures of the jets was found in all cases after the interaction with shock waves. The shock wave that have interaction with the helium jet appears to promote substantially more mixing than in the other cases, i.e. nitrogen and krypton [4].

8. Compressibility Effects (or Mach number effects)

Compressibility effects on turbulence are significant when the energy associated with dilatational fluctuations are large or when the mean flow is compressed or expanded. Most of the previous work on compressible turbulence has been carried out in shear layers (Gutmark et al., 1995, for the most recent review on compressible free shear flows) [29] or boundary layers (Spina et al., 1994) [92]. Different contributions to the understanding of compressibility effects on turbulence are reviewed in detail by Lele (1994) [46].

Compressibility plays a crucial role in the stability and mixing of supersonic shear layers. Its effects being capable of producing order-of-magnitude changes compared with incompressible flow [74].

9. Density Effect

Many turbulent flows of practical interest involve significant density fluctuations. There are several gases, which have different density than the air, can be used for jet. The density effect thus presents in such flow mixing with the ambient. helium jets are discussed very often as this type of jets [2][3][39][67][96][97].

Large changes of the density ratio across the mixing layer were found to have a relatively small effect on the spreading rate, and it is concluded that in supersonic jets, the spreading rate difference is due to the compressibility effects, but not density effects [13]. Then in subsonic jets, what plays an important role? Our research will try to answer that question.

10. Convective Mach number

Another useful parameter for jet flows has been found to be the convective Mach number originally named by Papamoschou and Roshko (1988) [74] who drew upon linear stability analysis of a vortex sheet for justistification of the particular formulation. Figure 1.6 clearly shows the basis of the convective Mach number concept.

In a frame of reference bed to large scale structures traveling with a constant convective velocity U_c, one can define two Mach numbers of the external streams

$$M_1 = \frac{U_1 - U_c}{a_1} \text{ and } M_2 = \frac{U_c - U_2}{a_2} \qquad (1.3.2)$$

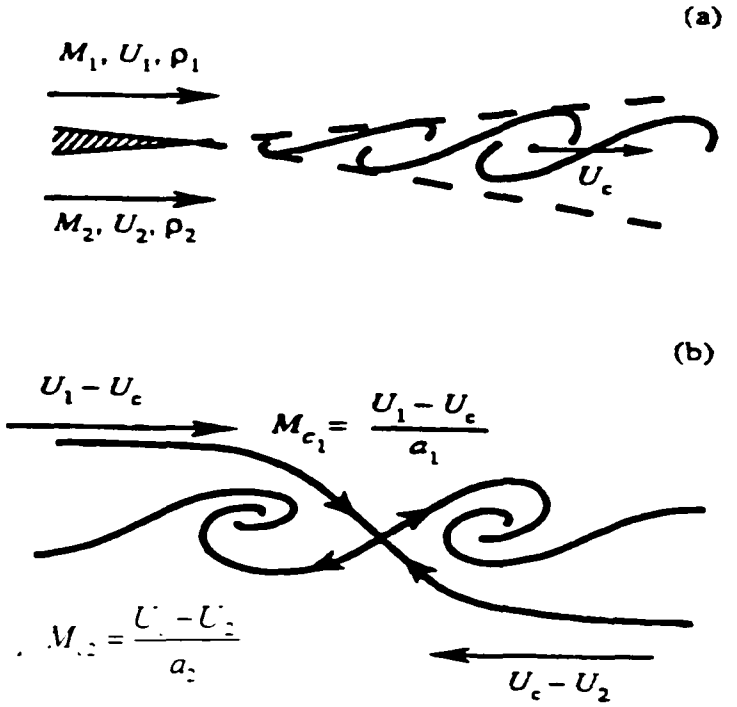

Figure 1.6: Convective Mach Number Concept (Papamoschou and Roshko 1988) [74]
(a) Laboratory Frame of Reference: (b) Convective Frame of Reference.

In the convected frame of reference there exists a saddle point between two adjacent eddies. If it is assumed that the static pressure is constant across the mixing layer and that the compression of fluid along particle paths leading to the saddle points are isentropic. then the mechanical equilibrium of this saddle point leads to the relation

$$\left[1+\frac{\gamma_1-1}{2}M_{c1}^2\right]^{\frac{\gamma_1}{\gamma_1-1}}=\left[1+\frac{\gamma_2-1}{2}M_{c2}^2\right]^{\frac{\gamma_2}{\gamma_2-1}} \qquad (1.3.3)$$

where γ_1 and γ_2 are the ratios of specific heats for the two streams of fluid. Using the definition of the two convective Mach numbers, an expression for U_c can be obtained as follows for the simplified case where $\gamma_1=\gamma_2$

$$U_c=\frac{a_1U_2+a_2U_1}{a_1+a_2} \qquad (1.3.4)$$

This convective Mach number also affects spreading rate. Both experimental and numerical studies have confirmed that the spreading rate decreases when the convective Mach number increases [74].

11. Reynolds Number Effects

It is clear that increasing Reynolds number leads to more and more small scale turbulent structures, but the initial large scale structures persist even at high Reynolds numbers. When the Reynolds number is sufficiently large the flow reaches an asymptotic downstream state where self-similarity of the mean and turbulent fields is observed [8]. How will the Reynolds number affect other properties of the jet flow, such as the spreading rate remains unanswered.

1.3.2 DNS Research

To resolve several of the above mentioned issues that are associated with jet flows, researchers have tried numerous approaches and developed different tools. Considerable research efforts, involving experiments, theoretical analysis or numerical simulations, have been devoted to investigating the characteristics of jet flows. Here we discuss mainly Direct Numerical Simulations (DNS).

Direct Numerical Simulations (DNS) of compressible flows have mainly focused on simple homogeneous flows, with shocks or without shocks. Numerical simulation is increasingly recognized as an attractive method of studying turbulent flows. The DNS method has several advantages compared to experimental approaches, for instance, it is independent of experimental work, easy to control the simulation conditions, and so on. However, on the other hand, numerical simulations bring along some problems. First is to make the correct choice of the different numerical methods available, which is a key point in capturing the nature of turbulence. Therefore, within the few numerical methods for turbulence simulation, turbulence models are seldom used in computing jet flow. Direct numerical simulation (DNS) is the most exact approach, but it requires an extremely fine mesh size on an appropriate grid system to capture the small scales of the turbulence present in the flow. In addition, the time increment to advance the solution must be extremely small to simulate the time dependent nature of the turbulence. Therefore, another approach—large eddy simulation (LES) is chosen, which simulates

the larger scales of motion of the turbulence while approximating the smaller ones through appropriate modeling. The second difficulty is the formulation of the boundaries. The influence of finite computational domain on real jet flow cannot be neglected, since unsuitable outflow boundary conditions will introduce unphysical reflections to the upstream. The lateral boundary condition must ensure that the entrainment of this flow is correctly described.

1.3.3 Experimental Research

The first issue with experiments is to obtain sufficiently high flow quality, for which the repeatability of the experiments is considered a requirement. Different techniques, Pressure Transducer, Thermocouple, Hot-Wire, Laser Doppler Anemometry (LDA), Particle Image Velocimetry (PIV), Global Doppler Velocimetry (GDV), Schlieren, and Planar Laser Induced Fluorescence (PLIF), have all been tested and used in experiments. The choice of technique itself depends on many factors, such as the requirements and objectives of the measurements, the range of velocities expected in the experimental facility, the spatial resolution, the accessibility of the flow field, the temporal resolution, the availability of the necessary equipment and human expertise. It would be more appropriate to list the characteristics of each of the techniques to further discuss its advantages and disadvantages.

Pressure Transducer

Pressure transducer has several advantages for point measurement. It is easy to calibrate, easy to operate, very accurate and it has good sensitivity for turbulence capturing. However, it is intrusive to the flow. Also it has a finite yaw response to the velocity vector, therefore misalignment may result in inaccurate data.

Thermocouple

Thermocouple is an accurate temperature measurement probe, which can be used with a wide temperature range. Its linear response to temperature change makes it easier to calibrate. It is also easy to operate. However, it is also intrusive, and the frequency response is very low. Thus it is not good for turbulence measurement. If only mean quantity is needed, thermocouple measurement is a good choice. Further more, it did not show directional response from our experiments, which helped improve the accuracy on measurements.

Hot-Wire

HWA (Hot-Wire Anemometry), which in most cases is called SHW (Stationary Hot-Wire), that can be either CCA (Constant Current Anemometry) or CTA (Constant Temperature Anemometry), are point measurement techniques. Hot-Wire probe is widely used in velocity measurement because they are appropriate for the measurement of time series in 1D, 2D or 3D flows, where high spatial and temporal resolution is required. It requires no special fluid preparation i.e., seeding and the small dimensions of

probe allow measurement in locations that are not readily accessible. They can be used to provide velocity, temperature, density and molecular concentration information at the point of measurement with high frequency response. On the other hand, Hot-Wire is intrusive, influencing the flow in some respect. It has an ambiguity in measuring the velocity direction in jet flow measurement [96]. The problem exists primarily because of its capability in measuring both mean and fluctuating velocities and also because a Hot-Wire could not be used under the more severe conditions, where flow direction is changing [7]. When transonic Mach numbers and low Reynolds numbers are involved, the calibration is a major difficulty [8]. The other disadvantage is its frequent breakings, especially in the case of high speed flow. Thus to repair the wires requires specialized skills.

LDA

LDA (Laser Doppler Anemometry) or LDV (Laser Doppler Velocimetry) is also a point measurement technique. It is not intrusive and directional sensitive due to the imposed phase shifting and it is good for reversing flows, where physical intrusive sensors, is difficult or impossible to use. It provides high spatial and temporal resolution due to the small measuring volume and no calibration needs to be performed. Even though it provides highly accurate results, without seeding, or addition of tracer particles, no result can be obtained. In highly sheared supersonic compressible flows, such as mixing layers at high M_c, seeding problems may corrupt the experimental results [8].

PIV and GDV

PIV (Particle Image Velocimetry) and GDV (Global Doppler Velocimetry) techniques for obtaining instantaneous whole field velocity data in high speed flows. For low to moderate velocity regions, PIV is a better choice at this time compared to GDV, due to its simplicity and ease of implementation. GDV can simultaneously measure in real time the three components of velocity of an entire particle field illuminated by a laser light sheet. It allows the quantification of complex 3D flow fields at video camera rates. They are both non-intrusive and very accurate. GDV, however, would be recommended for higher flow velocities since the magnitude of the Doppler shift for this scenario increases, which improves the accuracy of GDV compared to PIV. The most difficult or challenging part of GDV, which is actually the heart of this method, is the direct measurement of the frequency change in the laser light due to Doppler shift. PIV, with its rapid development, is now able to handle Mach 4 jets [30].

For evaluation, the digital PIV recording is divided into small subareas called "interrogation areas". The local displacement vector for the images of the tracer particles of the first and second illumination is determined for each interrogation area by means of statistical methods (auto- and cross- correlation). It is assumed that all particles within one interrogation area have moved homogeneously between the two illuminations. The projection of the vector of the local flow velocity into the plane of the light sheet (2-component velocity vector) is calculated taking into account the time delay between the two illuminations and the magnification at imaging.

The process of interrogation is repeated for all interrogation areas of the PIV recording. With modern video cameras (1k X 1k sensor elements) it is possible to capture more than 100 PIV recordings per minute. The evaluation of one video PIV recording with 3600 instantaneous velocity vectors (depending on the size of the recording and of the interrogation area) is of the order of a few seconds with standard computers. If even faster availability of the data is required for online monitoring of the flow, dedicated hardware processors are commercially available which perform evaluations of similar quality within fractions of a second.

Schlieren

Schlieren system is widely used in high speed flows for image capturing. It requires a density gradient to be shown in the image. So it works well when there is a shock wave, or a shear layer, where high density change is expected [3][13]. This system can also be used to find concentration, however, it is difficult to use it in the flows with low density variation. Furthermore, tedious calibration has to be done before the experiments.

PLIF

PLIF (Planar Laser Induced Fluorescence) is a concentration measurement technique, which requires dying of the flow field [27]. It is non-intrusive, however, it works only with certain flows that have low Reynolds number and low speed. Dying of the flow field for concentration measurement is also difficult.

In conclusion. all the above techniques. based on the researcher needs. could be used to measure different quantities. Based on our needs for the total pressure. total temperature and velocity. pressure transducers. thermocouples. and a PIV system were chosen for the individual measurement. It can be seen from the results that these choices did offer satisfactory results.

For jet flows. the mixing with ambient fluid. is always the most interesting aspect. Temporally and spatially. the mixing happens without control. There are no unique empirical formulas for gas constant and other property estimation. This makes it hard to obtain desired quantities. This is a good reason for using averaging techniques.

1.4 Objectives

In reviewing the existing work on the jet flow structure, it became evident that a deficiency existed in terms of experimental work. While the existing numerical work does provide a significant amount of data on the structures of these flows, there are, however, only scarcely available corresponding measured data. Experimental work relies mostly on the available facility, therefore most researchers are working in the same aspect using their available resources. There is also a lack of experimental data with the same experimental conditions that are critical for the results. To bridge this gap, further experimental study needed to be performed for a better understanding of the physics and mechanics involved in this line of research. Also experimental data have to be available to validate the numerical results and other researchers' work.

The present work is an experimental investigation and is concentrated on three objectives: (1) Analyze the data obtained and search for jet flow structures by looking into data of velocity, total pressure and total temperature; (2) Establish and document density effects and Mach number effects on the jet flows; (3) Obtain parameters such as concentration that are not available by measurements directly.

The approach to meet the research objectives requires the development of experimental techniques, some of them being newly applied in this field. For example, the Particle Image Velocimetry for high speed flow measurements. To disclose the Mach number

effect, jet flows were confined to run under certain exit condition, i.e., exit Mach number M_J=0.3, 0.6, and 0.9. To create a distinct comparison in jet flows for density effect, helium, nitrogen and krypton gases were used in the present investigation of compressible jets issuing into still air. Their properties, as introduced in the governing equations, are listed at ambient temperature in Table 1.1.

Table 1.1: Gas Properties at Ambient Temperature

gas	γ	Mol. Weight	R (J Kg.K)	a (m s)	ρ (Kg m^{-3})	μ (10^{-6} Pa.sec)	C_p (J Kg.K)	α (m^2 s)
Nitrogen	1.400	28.013	296.8	346	1.13	17.9	1042	0.000028
Helium	1.667	4.003	2077	1007	0.1615	20.0	5193	0.00018
Krypton	1.240	83.800	99	191	3.4360	25.0	511.5	0.0000053

where α is the thermal diffusivity.

With the gases listed above, the following tasks were carried out:

1. Pressure Measurements

Pressure distributions of nitrogen, helium, and krypton jets issuing into still air at various Mach numbers 0.3, 0.6, and 0.9 were measured by using a pressure probe. This allowed a comparison between different effects, such as Mach number effect to be compared by keeping the jet flow under the same condition, except Mach number while changing

only the Mach number. Applying the same method, the Mach number can be kept constant while the density can be changed by issuing a different gas into the ambient fluid. Chapter II introduced the measurement technique and the results were given in Chapter IV.

2. Velocity Measurements

Similar to pressure distribution measurement, velocity was measured under the same conditions by PIV techniques, which allowed a combination of Mach number effects and density effects to be studied.

PIV technology for velocity measurements is based on correlation of images. Two type of correlation schemes, crosscorrelation and autocorrelation were used together to resolve the velocity. A comparison between the two schemes was obtained by applying them into the same flow condition. PIV method will be introduced in Chapter III and the results from jet flows will be given in Chapter V.

3. Temperature Measurements

Temperature measurements, by using thermocouples, were used to investigate the same effects mentioned above, and in the mean time, the results from temperature measurements were used to calculate the concentration distribution in the cases of helium jets and krypton jets. The measurement technique will be introduced in Chapter II and the results will be shown in Chapter VI.

4. Other Quantities

Different approaches to the same jet flows will definitely help the study on the jet flows. Is it possible for us to estimate other flow parameter, which cannot be measured directly, by using values of measured quantities? The answer is yes. The data obtained from the above experiments were studied and analyzed in Chapter VII. Based on the data, derivation of formulas for concentration and other parameters was attempted and the corresponding error analysis (Chapter VIII) were discussed. It is to our great interest that a substantial amount of work could be eliminated with this method.

Table 1.2 lists the bulk properties for the flows, such as the exit velocity from the jet, Mach number, convective Mach number, density of the gas, Reynolds number and density ratio between the given gas and air.

Table 1.2. Experiments Carried Out

Gas Name	Exit Mach number M_J	Jet Exit Velocity (m s)	Density Ratio $\rho_J \rho_a$	Reynolds Number Re	Convective Mach number Mc
Helium	0.3	297	0.0885	11.000	0.217
	0.6	569	0.0917	25.000	0.429
	0.9	831	0.1018	40.000	0.64
Nitrogen	0.3	103	0.7413	34.000	0.149
	0.6	199	0.7902	74.000	0.293
	0.9	288	0.846	122.000	0.432
Krypton	0.3	57	2.4347	45.000	0.110
	0.6	111	2.5217	91.000	0.217

Chapter II Experimental Setup and Measurement Techniques

2.1 Overview and Sketch of the Jet Facility

A smooth, seamless, stainless steel tube of an outer diameter of 3/8" (9.5mm) with an inside diameter of 0.277" (7.0mm) was chosen to supply the jet flow. This tube was designed to be strong enough to withstand strong loads, and even a shock wave without bending. Its inside diameter of 7mm is within the range of the size of gas injectors of large combustion engines, but it is still small enough for the camera that can cover a jet length of more than 10 diameters. In order to use the jet under different circumstances, such as in the shock tube that needs the jet exit to be flexibly aligned, the tube contains one 90° elbow, as indicated in Figure 2.1. The length L_a should be long enough so the flow at the jet exit will recover symmetrically before issuing it into the ambient air. L_e is the equivalent length of head loss from the elbow, which will be explained in the following part.

A pressure gauge, mounted before the jet exit, was used to monitor the pressure at this point so that the jet exit condition can be controlled. The corresponding explanation as to how the exit condition is controlled will be shown later.

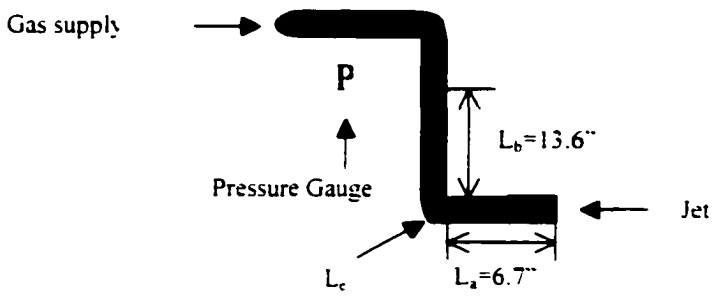

Figure 2.1: Sketch of the Designed Jet

Figure 2.2 shows the actual jet used in the laboratory. As it can be seen, there is a steel holder underneath the jet, which is mounted on an XYZ table and allows for the jet to move with in a large space to various of positions, so that measurements can take place anywhere desired.

Figure 2.2: Outlook of the Jet Used in Experiments

System overview

Based on previous discussion, we designed the jet system as shown below. This system includes a jet, pressure gauge mounted on the jet, one valve, an air tank to supply gas, a pressure regulator that allows constant pressure for the flow to leave this point and several pieces of tubes and fittings.

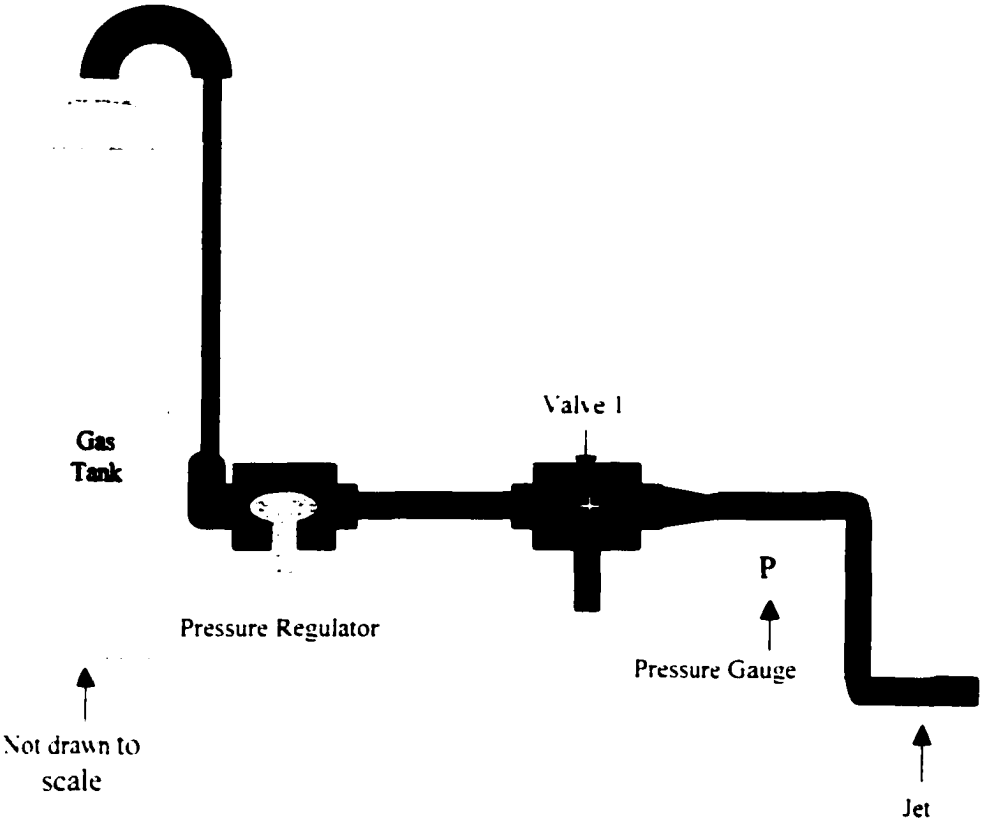

Figure 2.3: Jet Setup for Pressure Measurement

To run the jet under a constant Mach number, constant pressure is needed to supply gas from the gas tank. This was achieved by a pressure regulator, which can be regulated precisely and maintained to a certain pressure value. The questionnaire: What should the pressure be at the pressure regulator? How should the exit Mach number be controlled? How is it linked to the exit Mach number? The following section answers these questions.

2.2 Control of exit Mach number

To control the jet running under a steady Mach number, a constant pressure is needed to maintain a constant Mach number at the jet exit. This conclusion was obtained by mounting a pressure gauge just upstream of the jet exit (Figure 2.1). It is easy to judge that corresponding to a certain pressure, there must be only one exit Mach number. To find out this pressure, a program was set based on the related equations in Appendix A.

In Appendix A, a set of equations has been derived that relates to the flow variables of the adiabatic frictional compressible flow in a constant area duct. The flow variables are Mach number M, the velocity V, the pressure p and the ratio $\frac{4\bar{f}L}{D_H}$, which will be explained later on.

The flow governing equations are the following:

$$\frac{4\bar{f}L}{D_H} = \frac{1}{\gamma}\left(\frac{1}{M_1^2} - \frac{1}{M_2^2}\right) + \frac{\gamma+1}{2\gamma}\ln\frac{M_1^2}{M_2^2}\left(\frac{1+\frac{\gamma-1}{2}M_2^2}{1+\frac{\gamma-1}{2}M_1^2}\right) \tag{A.31}$$

$$\frac{V}{V^*} = M\sqrt{\frac{\gamma+1}{2+(\gamma-1)M^2}} \tag{A.32}$$

$$\frac{p}{p^*} = \frac{1}{M}\sqrt{\frac{\gamma+1}{2+(\gamma-1)M^2}} \tag{A.33}$$

where, L is the length of the tube and D_H is the hydraulic diameter, which in this case is equal to the actual inside diameter of the tube. γ is the specific heat quotient and M is the Mach number of the flow at one location of the tube. p and V are pressure and velocity, respectively. Average friction coefficient $\bar{f}$ is defined as:

$$\bar{f} = \frac{1}{L}\int_0^L f dx \tag{A.31}$$

The friction coefficient can be obtained by Figure A.2 in Appendix A, Moody Diagram or by using the Karman-Nikuradse formula:

$$\frac{1}{\sqrt{4f}} = -0.8 + 2\log_{10}(\mathrm{Re}\sqrt{4f}) \tag{A.5}$$

The equation A.30 can be achieved from a force balance on an infinite control volume consisting of a cross section of the tube. It takes friction, geometry, continuity, compressibility energy conservation and the definition of the Mach number into account. The derivation can be found in Appendix A.

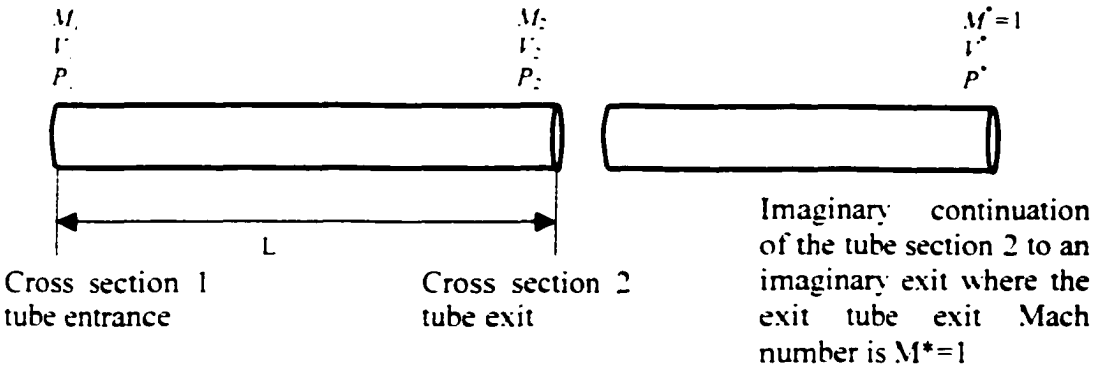

Figure 2.4: Scheme of the Tube With Different Cross Sections

Figure 2.4 illustrates the application of the three equations A.31, A.32 and A.33. The equation A.31 relates the average friction coefficient $\bar{f}$, the tube length L, the tube diameter D_H, the heat capacity quotient γ to the Mach numbers of the flow at the cross sections one and two. If a certain tube is chosen and the length of the tube is fixed and the average friction factor is known or estimated, this equation enables us to calculate the entrance Mach number M_1 from a desired exit Mach number M_2. The pressure P_2 is the static pressure at the exit of the tube. This is the pressure of the surrounding p_{amb}. With the given Exit Mach number M_2 and the known exit pressure P_2 Equation A.33 on previous page, allows the pressure P^* to be calculated. This would be the pressure at the point of the tube where the flow reaches sonic speed, as shown in figure 2.4. If p^* is known, the equation A.33 can be used to calculate the entrance pressure p_1, which is the flow variable that is used to control the Mach number M_2 at the exit of the tube. This number also controls the speed of the exiting jet.

The equation A.31 on page 42 is implicit in M_1 that makes a straightforward solution difficult. Also, we need to calculate M_1 for many cases with different gases and Mach numbers. To generalize everything and use it anytime, a simple program was developed This program uses the Newton-Raphson Method to deal with this set of non-linear equations.

It should be mentioned here that for the tube Length L, as was discussed earlier, one elbow has to be included in the jet design, which allows easy installation in the shock tube. The influence of the elbows on the flow is taken into account by the equivalent length method. The equivalent length for a 90° standard elbow is $L_e=30D_H=8.3"$ The total length L of the tube according to Figure 2.1 is:

$$L=L_a+L_e+L_b = 6.7"+8.3"+13.6"=27.6"$$

Where L_a and L_b are two straight parts of the tube shown in the same figure.

All the necessary variables for program are given as follows.

$$\bar{f}=0.0068,\ D_H=0.2",\ L=6.7+13.6+30*D_H$$

Appendix C has the program used to find out at what Gauge pressure the jet exit reaches to the required condition of a certain Mach number (i.e. 0.3, 0.6). The following table shows all the corresponding results from the program in Appendix A.

Table 2.1 Gauge Pressure from Program

Gas	Exit Mach Number	Gauge Pressure
Helium	0.3	3.18
Helium	0.6	12.66
Helium	0.9	27.08
Nitrogen	0.3	2.67
Nitrogen	0.6	10.67
Nitrogen	0.9	22.84
Krypton	0.3	2.36
Krypton	0.6	9.47
Krypton	0.9	20.29

Three types of measurements were carried out in our experimental setup: pressure measurement, velocity measurement, and temperature measurement. Pressure measurement requires one pressure transducer to read the corresponding total pressure, while velocity measurement requires either a double pulse or a combination of two lasers, and the temperature measurements utilizes a thermocouple to give the corresponding temperature information. In addition, each of the three measurement methods described above, necessities not only different measuring equipment, but also a modification of the jet facility. The differences of these three measurements lies not only

on the measuring equipment used, but also on the jet facility. For velocity measurement, tracer particles needed to be added to the flow field, which involves more controls compared to the pressure and temperature measurement cases. Therefore, additional information for the setups used in velocity measurement was put in a separate chapter following this one.

2.3 Pressure transducer setup for Total Pressure Measurement

Figure 2.5 shows the schematic of the jet flow supplying tube and the corresponding measurement system. As shown in the picture, the length L_a has to be long enough so that the flow at jet exit has recovered from the 90° turn perturbation and renders an axisymmetric profile at the exit and downstream when the flow issues into the ambient air. Flow visualization and measurement of mean Mach number profile have confirmed the symmetry of the flow field with the given $L_a/D=24.2$. The jet was mounted on an XYZ table, which was capable of moving in three-dimensions while the probe was stationary. The pressure gauge mounted on the jet tube was used to monitor the exit pressure. During experiments, the jet tube, mounted on the movable table constrained with Y, Z directions that allowed measurement along the centerline. Such setup is capable of taking measurements of the transverse pressure profile, by confining the moving perpendicularly to the jet centerline.

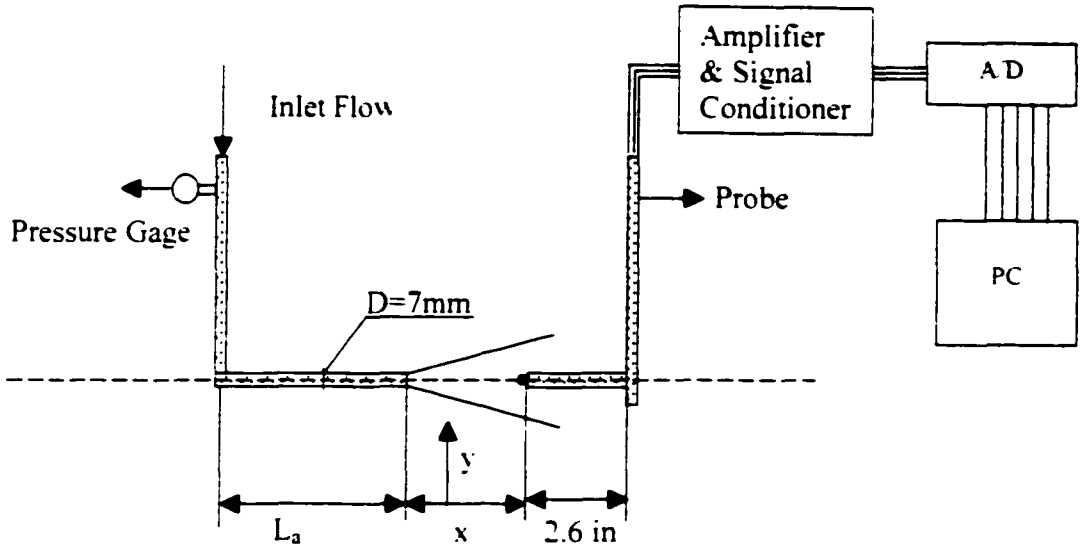

Figure 2.5: Pressure Transducer Setup

A high-frequency response, sub-miniature, pressure transducer fabricated by Kulite Semiconductors was used to measure the total pressure along the centerline of the jet. The signals were acquired with an DATEL data acquisition system. The DATEL 416G board is a 14 bit PCI data acquisition system, capable of sampling simultaneously 8 channels at 500 KHz each channel. Three of those boards are currently available providing 24 simultaneous sampled channels at 333 KHz per channel.

In order to increase productivity of the pressure measurement, another type of pressure probe with three transducers was also used as shown in Figure 2.6. This probe offers more information at the same time compared with the single transducer probe.

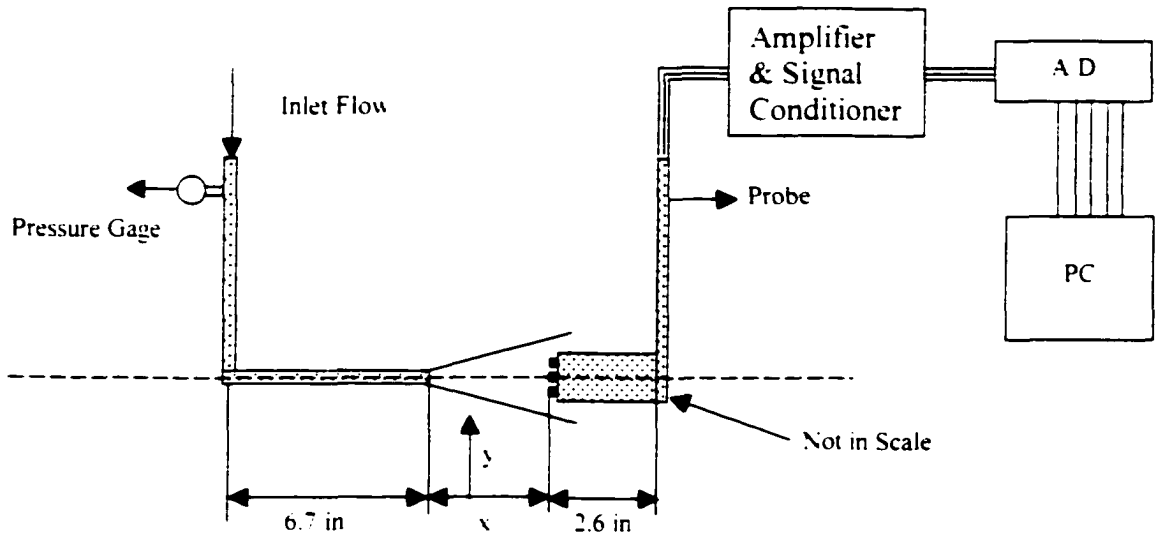

Figure 2.6: 3-Transducer Pressure Probe

Figure 2.7 shows one actual pressure transducer used in the experiments. Pressure transducers need batteries to power up and the signal captured is transferred to a computer. The wires shown in the figure above have two for the power supply and another two for the signal transfer. The output signal of the pressure transducer was amplified with a gain of 100 and recorded by a Personal Computer.

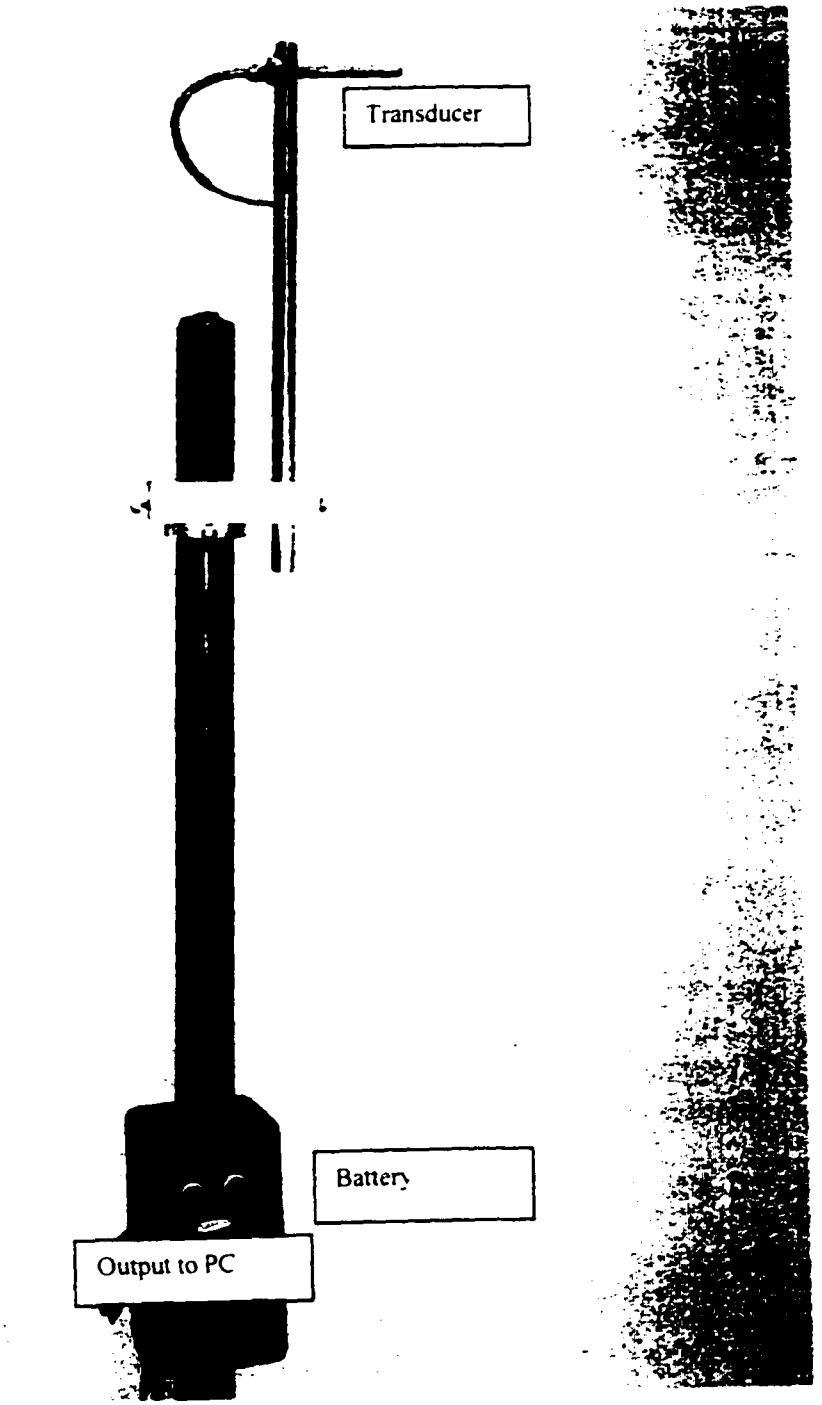

Figure 2.7: Actual Pressure Transducer Setup

2.4 Thermocouple Setup for Total Temperature Measurement

Thermocouple Introduction

The most common electric method of temperature measurements uses thermocouples, which are manufactured using the principle of thermo electricity. Thermocouples are made of two similar metals joined together as shown in Fig. 2.8. Consider the thermocouple circuit shown. The junction labeled 1 and 2 are at temperatures T_1 and T_2, respectively. If T_1 and T_2 are not equal, a finite open-circuit electric potential emf_1, will be measured. Here the term emf stands for *electromotive force* and is equivalent to an electric potential. The magnitude of the emf will depend on the difference in the junction temperatures and the particular materials A and B used for the thermocouple. This phenomenon is called the *Seebeck effect*. This emf can be measured by potentiometer as shown in the figure below.

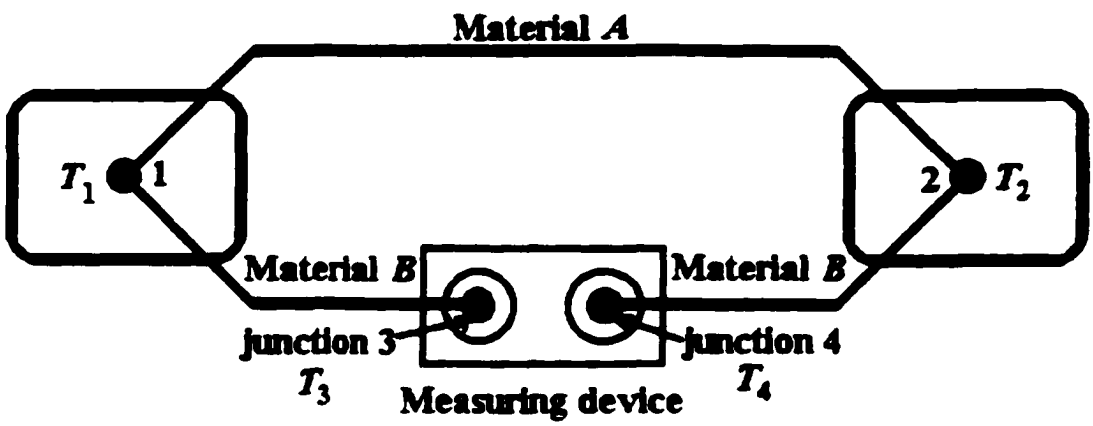

Figure 2.8: A Typical Thermocouple and the Measuring Circuit

If the two materials are connected to an external circuit in such way that a current I is drawn, the emf (called emf_2) may be altered slightly owing to a phenomenon called the *Peltier effect*, which accounts for the extra heat transfer other than the I-R that occurs at the junction to maintain a constant temperature. Hence, if a temperature gradient exists along either or both of the materials, the junction emf may undergo an additional slight alteration. This is called the *Thomson effect* phenomenon. There are, then, three emfs present in a thermoelectric circuit: the Seebeck emf, due to the junction of dissimilar metals; the Peltier emf, caused by a current flow in the circuit; and the Thomson emf, which happens because a temperature gradient is manifested in the materials. For temperature measurement, the Seebeck emf is the most important since it depends on junction temperature. If the emf generated at the junction it may be utilized for temperature measurement. This junction is called a thermocouple.

The sensitivity as a function of temperature for six different types of thermocouples is shown in Fig. 2.9. It should be noted that the sensitivity, i.e., the voltage output per Celsius degree, for a typical thermocouple is quite small and needs a digital thermometer with at least a microvolt resolution for recording and displaying. To calibrate the thermocouple circuit, techniques with reference junction immersed in an ice bath are usually adopted, as shown in Fig. 2.10.

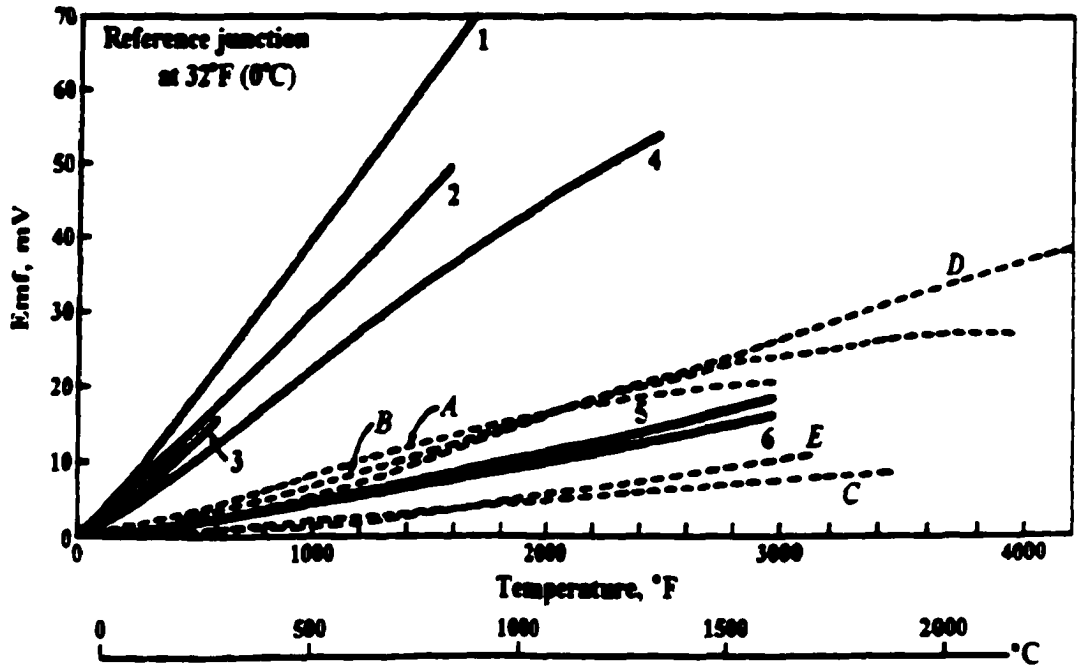

Figure 2.9: Emf-Temperature Curves for Typical Thermocouple Materials

Legend:	Tentative curves:
1. Chromel-constantan (type E)	A Rhenium-molybdenum
2. Iron-constantan (type J)	B Rhenium-tungsten
3. Copper-constantan (type T)	C Iridium-iridium rhodium
4. Chromel-Alumel (type K)	D Tungsten-tungsten rhenium
5. Platinum-platinum rhodium (type R)	E Platinum rhodium-platinum 10% rhodium
6. Platinum-platinum rhodium (type S)	

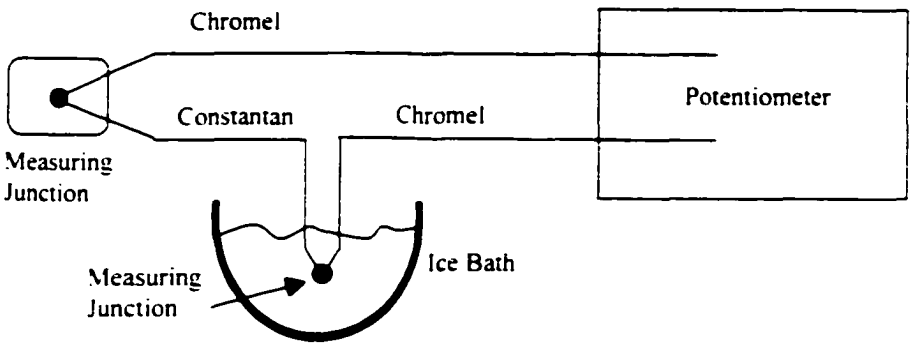

Figure 2.10: Calibration of Thermocouple

In sum, the three *fundamental laws of thermocouples* are listed as follows:

1) *Law of Homogeneous Materials.* A thermo electric current cannot be sustained in a circuit of a single homogeneous material by the application of heat alone, regardless of how it might vary in cross section.
2) *Law of Intermediate Materials.* The algebraic sum of the thermoelectric forces in a circuit composed of any number of dissimilar materials is zero if all of the circuit is at a uniform temperature.
3) *Law of Successive or Intermediate Temperatures.* If two dissimilar homogeneous materials produce thermal emf_1 when the junctions are at T_1 and at T_2 produce thermal emf_2 when the junctions are at T_2 and T_3, then the emf generated when the junctions are at T_1 and T_3 will be emf_1 and emf_2

Step Response of a Temperature Sensor

A typical example of the first-order instruments is the step response of a temperature sensor. The rate of heat transfer between a temperature sensor and its surrounding medium can be described by the following first-order differential equation:

$$\frac{mc}{hA}\frac{dT}{dt} + T = T_m \qquad (2.5.1)$$

where

$\dot{q}$ = the rate of heat transfer to the sensor by convection.

h = the convective heat-transfer coefficient.

A = the surface area of the sensor through which heat poses.

T_m = the temperature of the surrounding medium at time t.

T = the temperature of the sensor at time t.

m = the mass of the sensor.

c = the species heat capacity of the sensor.

Assume that at time t = 0, the sensor temperature T is T_0. If the sensor is suddenly immersed in a medium which is maintained at a constant temperature T_m, i.e., a step-function input, the temperature response of the sensor can then be expressed as:

$$\frac{T - T_m}{T_0 - T_m} = e^{-t/\tau} \qquad (2.5.2)$$

Here $\frac{mc}{hA}$ is the time constant of this first-order measurement. Figure 2.11 below shows the results for cases when $T_m < To$ (i.e., cooling, the step is T_0-T_m) and $T_m > To$ (i.e., cooling, the step is T_m-T_0). It is clear that the time constant τ of an ideal temperature sensor should be small. That is to say, the sensor would have a miniature mass *m*, a small specific heat capacity c, a sufficient surface area A for heat transfer, and a large convective heat-transfer coefficient h.

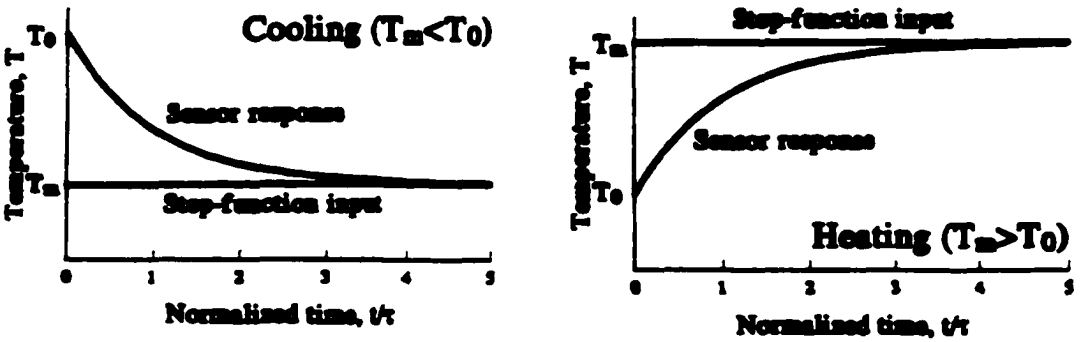

Figure 2.11: Responses of a Temperature Sensor to a Step Input..

Present Thermocouple Setup

Considering the availability and step response of different thermocouples, J type thermocouple with diameter 0.25mm was used in the experiments. The response time was compared with other thermocouples from other laboratories and was found to be

fast enough to take measurements in subsonic turbulent flows. Figure 2.12 shows the mounting of our thermocouple on the holder. The thin thermocouple was mounted on the tip of the probe. (the white tip on the right side) and the two leads were covered by ceramic. which was done intentionally by means of no heat transfer between the wires.

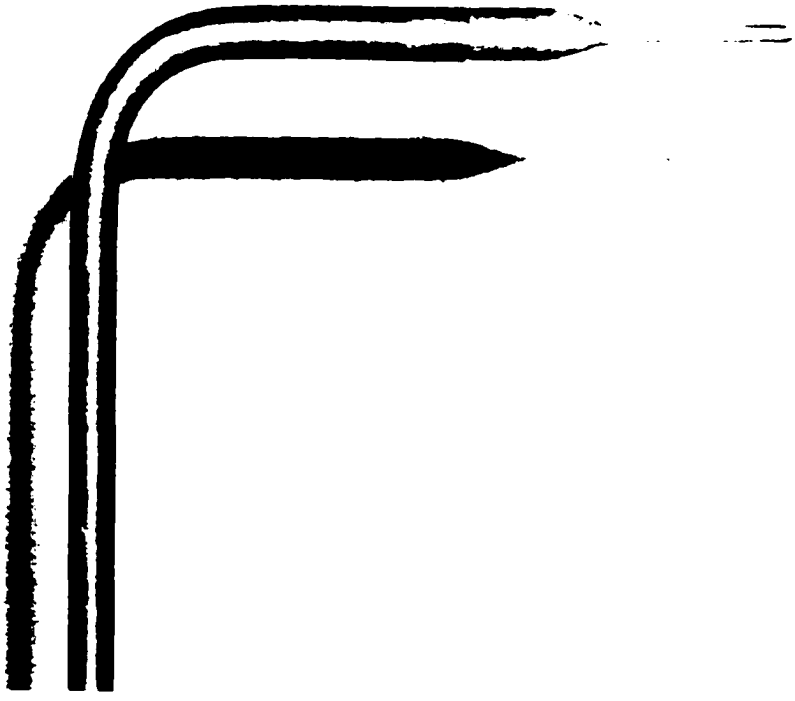

Figure 2.12: Mounting of Thermocouple

Figure 2.13 is the overall setup of both jet supply and the thermocouple. The signals were amplified by AT&T amplifier and acquired with an DATEL data acquisition system as they were mentioned for pressure measurements. Sampling frequency was set to 50K. and the gain was 1000.

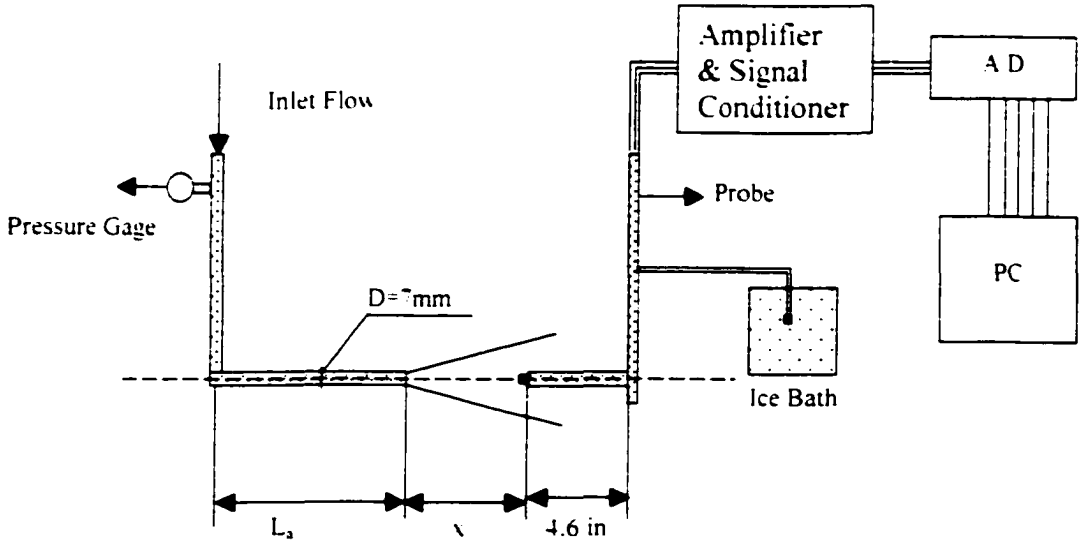

Figure 2.13: Setup of Jet and Thermocouple for Temperature Measurement

The actual setup was photographed in Figure 2.14. The gas tank and control panel are missing because of the picture size.

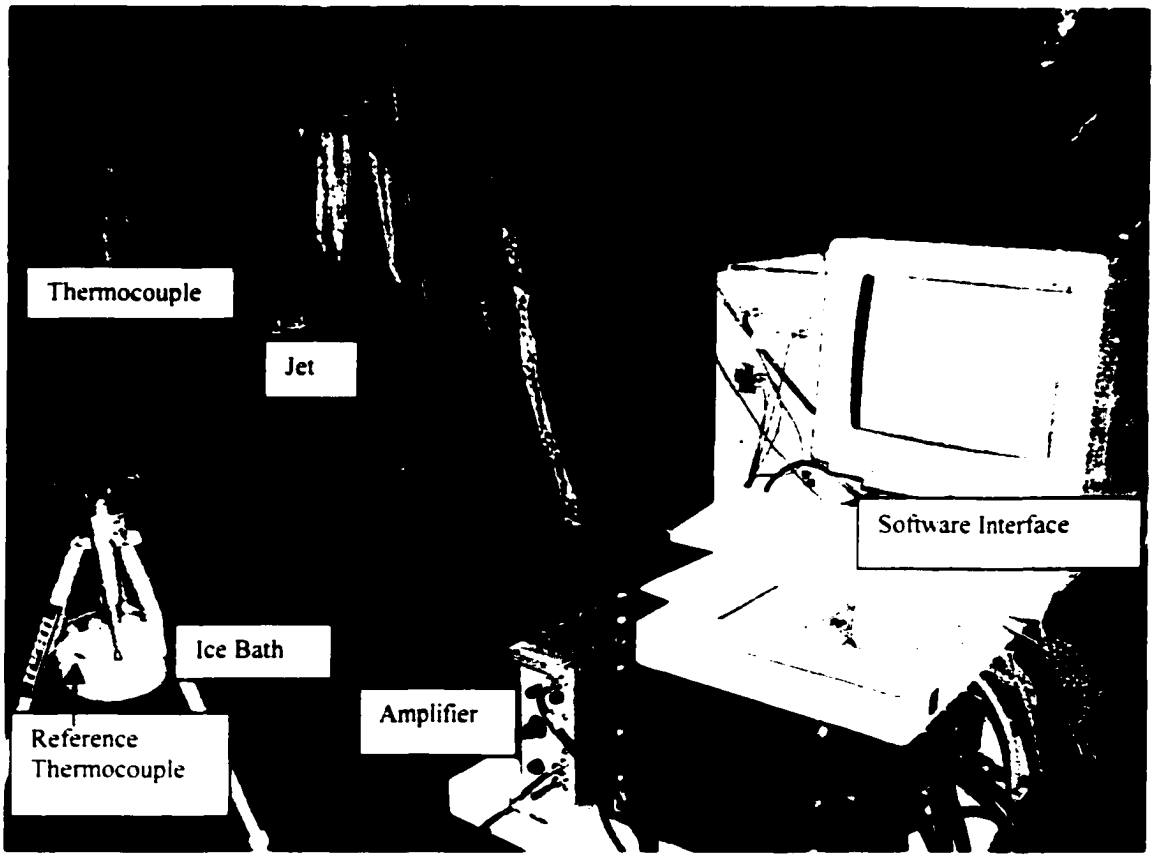

Figure 2.14: Actual Setup of Jet and Thermocouple for Temperature Measurement

Directional Response

Several experiments with different alignment were performed to find the directional response of the thermocouple. The thermocouple was first aligned at the centerline of the jet, then it was rotated against the centerline so the angle between the jet was increased from 0^{o} to 90^{o}. Temperature was found to be constant in the case of the same jet flow for these different alignments. This helped to reduce the alignment error.

Chapter III: PIV System and Velocity Measurement

The picture on the left was taken one century ago by Ludwig Prandtl, which depicts a manually rotated blade in a moving flow. The flow is visualized by distributing a suspension of mica particles on the surface of the water. Prandtl studied the structures of the flow in steady as well as in unsteady flow in the arrangement of this experiment.

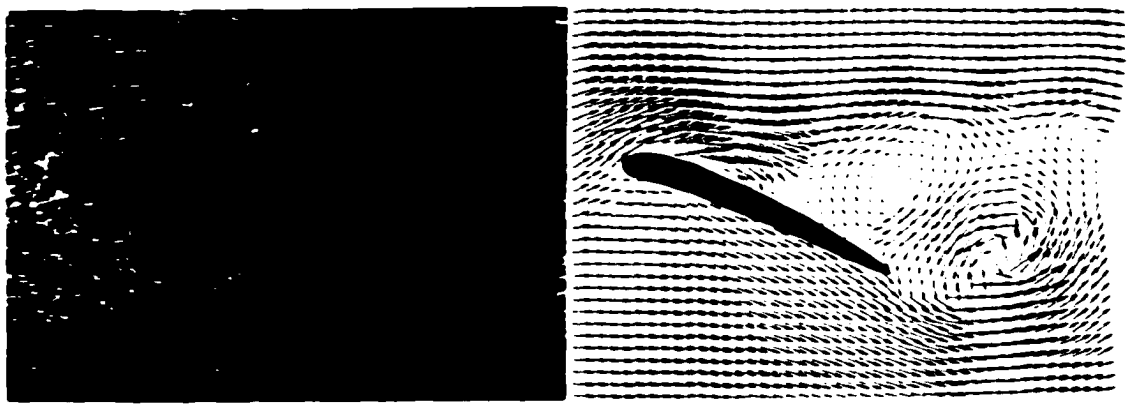

Figure 3.1: Separated Flow Behind Wing in a Ludwig Prandtl's Tunnel

(Raffel, M., Willert, C., Kompenhans, J. Particle Image Velocimetry *Springer*)

Being able to change a number of parameters of the experiment, such as model, angle of incidence, flow velocity, steady-unsteady flow. Prandtl gained insight into many basic features of unsteady flow phenomena. However, only a qualitative description of the

flow field was possible at that time. No quantitative data about flow velocity could be achieved then.

After a century, it is now possible to also extract quantitative information about the instantaneous flow velocity field exactly from the same kind of images as those available to Prandtl. The right side of Figure 3.1 gives out the map of instantaneous velocity field corresponding to the Prandtl's tunnel. One of the techniques to extract velocity vectors is called Particle Image Velocimetry or PIV.

3.1 Principle of Particle Image Velocimetry in Jet Flow Measurement

The PIV system used in our experiment is from TSI, which was the first company to commercialize PIV systems worldwide. In the following introduction to PIV techniques, we will mention TSI because some theories are based on TSI system.

The experimental set-up of a PIV system typically consists of several sub-systems. In most applications tracer particles have to be added to the flow. These Particles have to be illuminated in a plane of the flow at least twice within a short time interval. The light scattered by the particles has to be recorded either on a single frame or on a sequence of frames. The displacement of the particle images between the light pulses has to be determined through evaluation of the PIV recordings. In order to be able to handle the great amount of data that can be collected employing the PIV technique, a sophisticated post-processing system is required.

Figure 3.2 briefly explains a typical set-up for TSI PIV recording in a jet flow measurement. Small tracer particles (talcum) are added to the flow. A plane (light sheet), about 1mm thick within the flow is illuminated by means of a dual laser system(the time delay between pulses depending on the mean flow velocity and the magnification at imaging). It is assumed that the tracer particles move with local flow velocity between the two illuminations. The light scattered by the tracer particles is recorded via a high quality lens either on a single photographical negative or on two separate frames on a special cross correlation CCD sensor. After development the photographical PIV recording is digitized by means of a scanner. The output of the CCD sensor is stored in real time in the memory of a computer, directly.

For evaluation the digital PIV recording is divided in small subareas called "interrogation areas". The local displacement vector for the images of the tracer particles of the first and second illumination is determined for each interrogation area by means of statistical methods (auto- and cross- correlation). It is assumed that all particles within one interrogation area have moved homogeneously between the two illuminations. The projection of the vector of the local flow velocity into the plane of the light sheet (2-component velocity vector) is calculated taking into account the time delay between the two illuminations and the magnification at imaging.

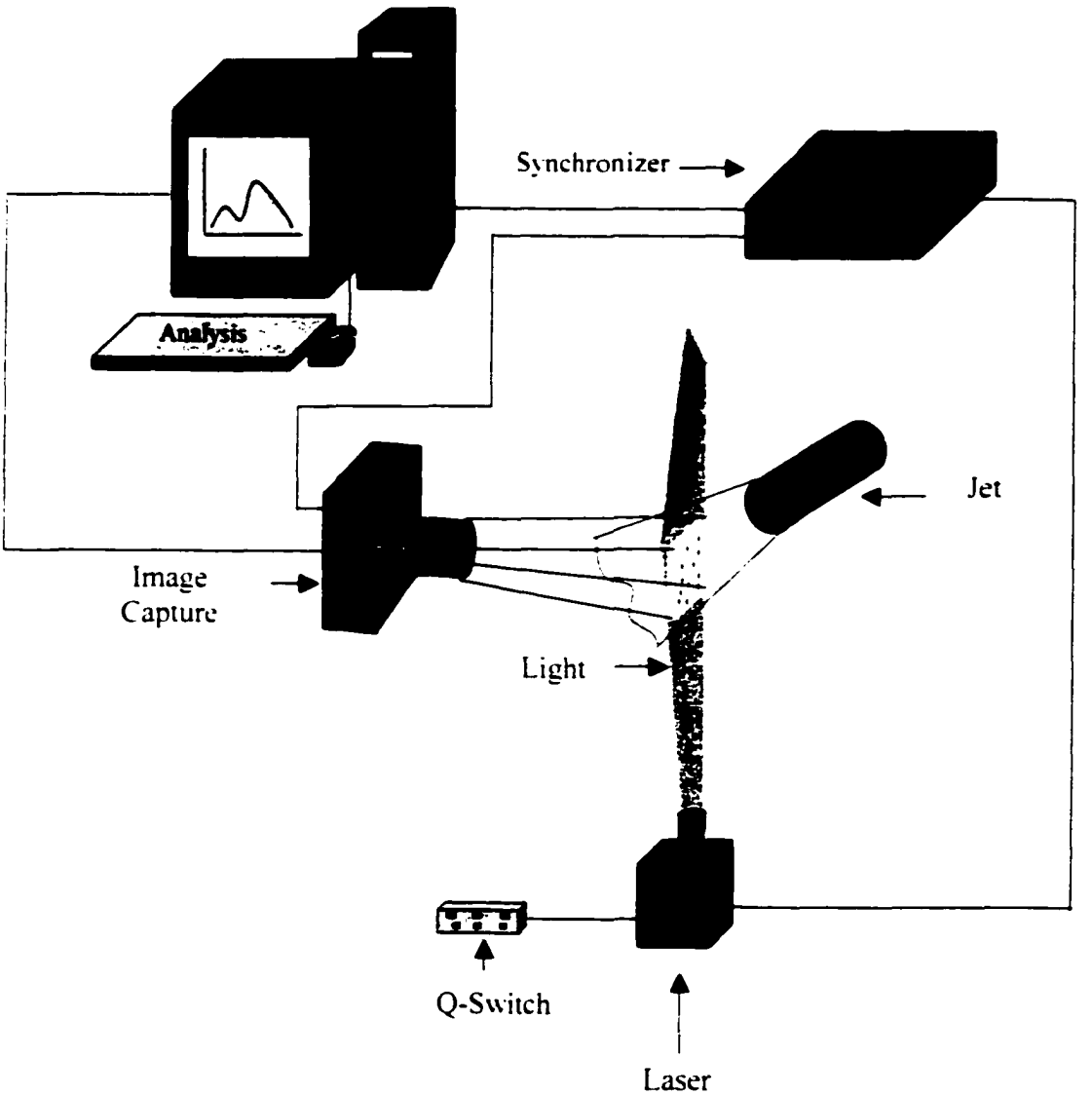

Figure 3.2: Experimental Arrangement for Particle Image Velocimetry in the Jet Flow Facility

For evaluation the digital PIV recording is divided in small subareas called "interrogation areas" as mentioned earlier. The local displacement vector for the images of the tracer particles of the first and second illumination is determined for each interrogation area by means of statistical methods (auto- and cross- correlation). It is assumed that all particles within one interrogation area have moved homogeneously between the two illuminations. The projection of the vector of the local flow velocity into the plane of the light sheet (2-component velocity vector) is calculated taking into account the time delay between the two illuminations and the magnification at imaging.

The process of interrogation is repeated for all interrogation areas of the PIV recording. With modern video cameras PIVCAM 10-30 (1K x 1K sensor elements) it is possible to capture more than 100 PIV recordings per minute. The evaluation of one video PIV recording with 3600 instantaneous velocity vectors (depending on the size of the recording and of the interrogation area) is of the order of a few seconds with standard computers. If an even faster availability of the data is required for on line monitoring of the flow, a dedicated hardware processors are commercially available which perform evaluations of similar quality within fractions of a second.

3.2 Present PIV Setup

To measure velocity in different jet flows, the jet was adjusted to work under different conditions, including the powder supply and so on. A panel with all the controls was designed for this purpose, which was shown in Figure 3.3. Where gas tank supplies all types of gases, including nitrogen, krypton and helium. Valve 1 controls the flow from tank; valve 2 controls the flow rate in the main branch; valve 3 controls the pressure to the powder container; valve 4 allowed the powder injection into the powder container are shown. As mentioned before, pressure gauge was used to monitor the jet exit condition. The funnel is used to inject powder into the powder container anytime that the powders are not enough. To supply the gas uniformly to the jet, the gas tank was equipped with a pressure regulator that adjusts the pressure leaving that point to be a constant.

The powder container mixes the powders with incoming gas from the branch flow and make sure the mixture goes out in a proper proportion to the main flow. There is no unique way to control the powder supply, therefore, we had to design our own container that pumps up powders. This task was a challenging and time-consuming part of this research. The design selected was the most successful one so far, and it was proved to be very easy to control.

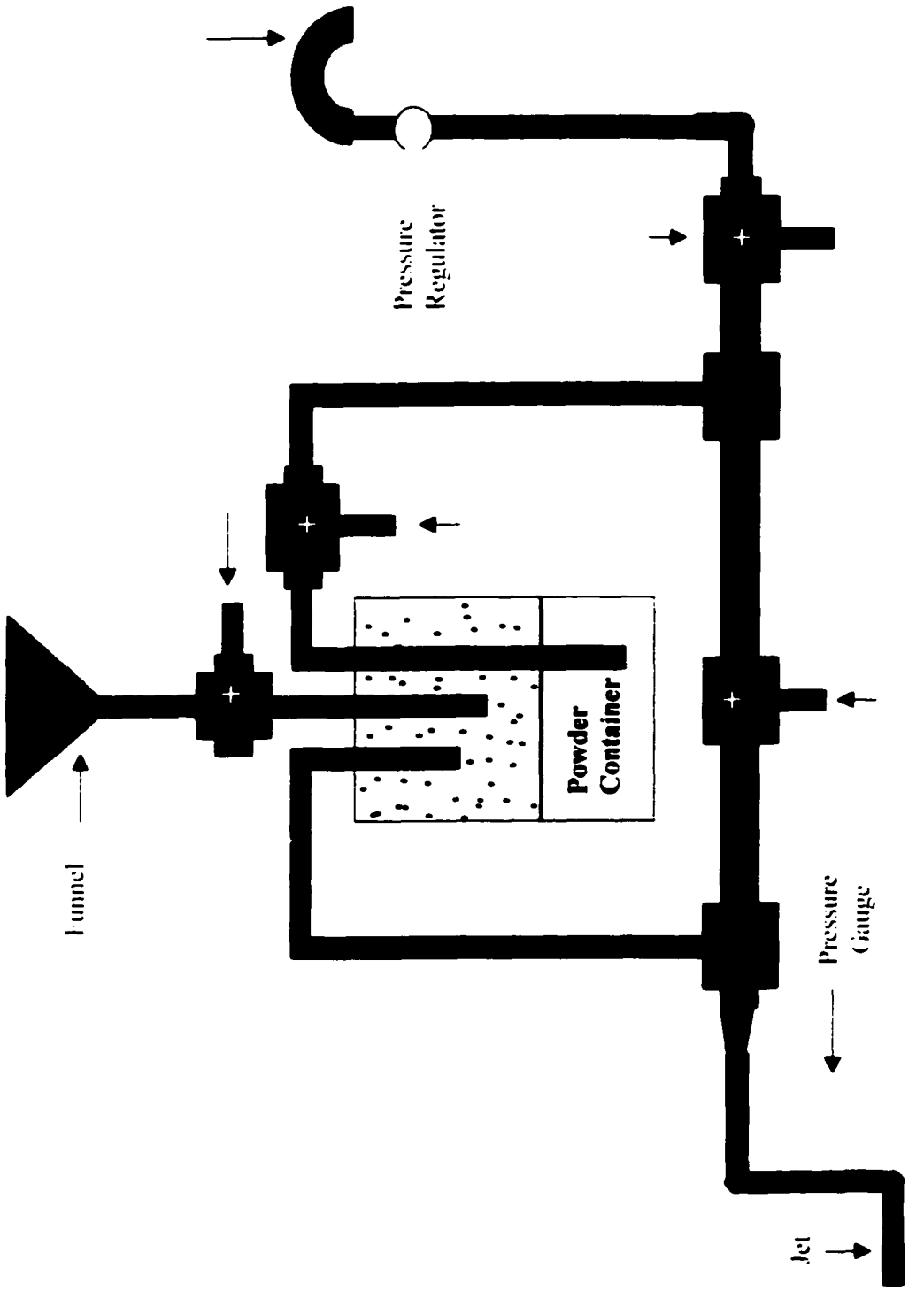

Figure 3.3 Jet System Overview

3.3 Tracer Particles:

It is clear from the principle of PIV as described earlier that PIV, in contrast to techniques using hot-wire or pressure probes, is based on the direct determination of the two fundamental dimensions of the velocity: length and time. On the other hand, the technique measures indirectly, because it is the particle velocity, which is determined instead of fluid velocity. Therefore, fluid mechanical properties of the particles have to be checked in order to avoid significant discrepancies between measurements of fluid and particle motion.

A primary source of error is the influence of gravitational forces if the densities of the fluid ρ and the tracer particles ρ_p do not match. Even if it can be neglected for practical purposes, we will derive the gravitationally induced velocity U_g from STOKES drag law in order to introduce the particle's behavior under acceleration. Therefore, we assume spherical particles in a viscous fluid at a very low Reynolds number. This yields:

$$D = 3\pi\mu U d_p \qquad (3.1)$$

and

$$U_g = d_p^2 \frac{\rho_p - \rho}{18\mu} g \qquad (3.2)$$

where D is the drag exerted on the spherical particle by the viscous flow, g is the acceleration due to gravity, μ is the dynamic viscosity of the fluid, and d_p is the diameter of the particle.

In analogy to equation (3.2), we can derive an estimate for the velocity lag of a particle in a continuously accelerating fluid:

$$U_s = U_p - U = d_p^2 \frac{\rho_p - \rho}{18\mu} a \qquad (3.3)$$

where U_p is the particle velocity and a is the flow acceleration. The step response of U_p typically follows an exponential law if the density of the particle is much greater than that of the fluid density

$$U_p(t) = U[1 - \exp(-\frac{t}{\tau_s})] \qquad (3.4)$$

with the relaxation time τ_s given by

$$\tau_s = d_p^2 \frac{\rho_p}{18\mu} \qquad (3.5)$$

If the fluid acceleration is not constant or STOKES drag does not apply (e.g. at higher flow velocities) the equations of the particle motion become more difficult to solve, and the solution is no longer a simple exponential decay of the velocity. Nevertheless, τ_s remains a convenient measure for the tendency of particles to attain velocity equilibrium with the fluid. The result of equation (3.4) is illustrated in figure 3.4 where the time response of particles with different diameters is shown for a strong deceleration in airflow.

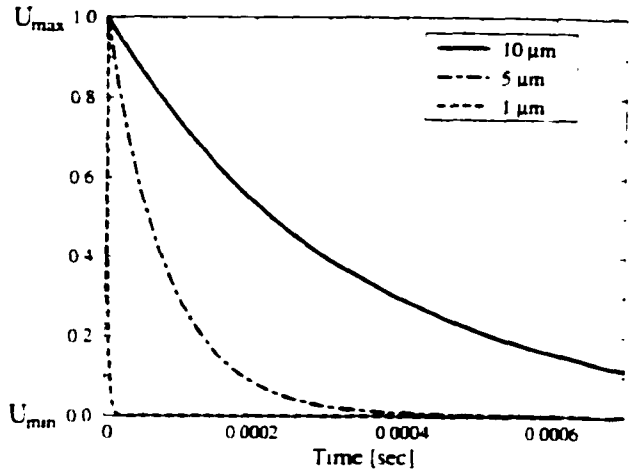

Figure 3.4: Time Response of Oil Particles with Different Diameters in a Decelerating Air Flow

When applying PIV to liquid flows the problems of finding particles with matching densities are usually not severe, and solid particles with adequate fluid mechanical properties can often be found. Usually their size can easily be determined before suspension into the liquid and will not change afterwards. Some of the most often used tracers are listed in the section below. However, early applications of PIV have already shown that difficulties arise when providing high quality seeding in gas flows compared to applications in liquid flows. The problems are similar to those, which are faced when applying laser Doppler velocimetry. From equation (3.2) on page 66, it can be seen that due to the difference in density between the fluid and the tracer particles, the diameter of the particles should be very small in order to ensure good tracking of the fluid motion.

On the other hand, the particle diameter should not be too small as light scattering properties have also to be taken into account as it will be shown in the following section. Therefore, it is clear that a compromise has to be found.

Table 3.1 Different Powders, Used for the Flow Visualization.

Name	Formula	Size[μm]	Density[kg l]
Titanium Dioxide		0.3-1.9	4.26
Zinc Oxide	Al	1-5 x	5.606
Aluminium, spherical	Al	1-3	2.699
Aluminium, flakes, highly reflective powder	Al	1-2	2.699
Silicium Dioxide, Powder, fused	Si_2	1-5	2.32
Silicon Dioxide, fumed, technical grade		submicron	2.32
Talcum Powder			
Polystyrene Micro Spheres		0.99	1.05
Flourescent Polystyrene Micro Spheres		0.99	1.05

Considering the specification of the intended experiments, many of the previously listed particles or substances had been excluded from the beginning. The high speed of the flow $V=440m\,s$ and the diameter of the jet generating tube system of $7mm$ result in a volumetric flow of more than $20\ l\,s$. This flow cannot be seeded intensively and responsibly with cigarette smoke. The experience with a smog or fog generator that uses mineral oil to produce tracer particles for previous experiments in a wind tunnel did not give satisfactory results. The fog smells bad and the oil condenses everywhere. The use of other oil droplets or similar fluids like glycerin or DOP was dismissed because of the bad experience with the mineral oil. They would create a layer of viscous liquid in the tube and on other systems which could not be removed easily. A promising alternative would have been the use of fast evaporating fluids like alcohol or acetone. These ideas had been dismissed because it did not seem certain that alcohol or acetone droplets would not evaporate due to the environment temperature. Additionally both of the fluids are flammable. To mix them with air and expose this mixture to high temperature is dangerous. Additionally, the air in the laboratory would have been enriched with the vapor of the alcohol or the acetone. This would have changed the properties of the gas in the experiments.

However, considering the above, one of the first design decisions was to use solid tracer particles. Their main objective is to make every motion that may be present in the fluid, visible. Therefore the particles should follow the flow exactly and be sufficiently reflective to make it visible. To make sure that the particles follow the flow, their size has to be of the order of 1 μm and their specific weight should be moderate. Table 3.1

lists a set of powders of the desired size range, which are white or metallic, nontoxic, easily available and not excessively expensive.

Titanium dioxide and zink dioxide are two white powders with nearly similar properties. Titanium dioxide is used as white pigment in commercial paints. It is slightly lighter and brighter thin zink dioxide. Both substances are hard and stick a little together. Spherical Aluminum is a grey, dusty powder. It lumps less than Titanium and Zink Dioxide and has less than the half specific weight. The disadvantage was the grey, not very bright color.

The highly reflective Aluminum flakes with a size of 1-2 μm and a low specific weight unites both advantages, the brightness and the low weight. In its container it behaves nearly like fluid. Unfortunately this powder was labeled as a dangerous material. Nevertheless, it remains an interesting material for further flow visualization in the future.

Fused silicium dioxide is a white powder, similar to titanium tioxide and zinc oxide. Its size is 1-5 μm, a little above the target of 1μm. Additionally, it lumps.

The fumed silicon Dioxide is submicron and very light. It comes in a very airy state, in which it has more than ten times the volume of the other powders. It is reminiscent of very fine dust of mineral wool.

Talcum powder is a white, soft powder with a size of about one micron. It doesn't lump as much as the other white powders. Here baby powder that contains more than 90 % talcum powder was used instead of the pure talcum.

Polystyrene Spheres have the advantage that their low weight and the defined size. They were also available in a flourescent version. Their disadvantage was the extremely high price of $389 g for the plain but not flourescent particles.

Apart from the aluminium flakes and the polystyrene spheres, all the above-mentioned powders were tested after a working particle seeding system had been set up. These tests were performed with pressurized air. The jet generating tube system was installed in the shock tube to protect the environment from being polluted. This was also the case for the camera and the laser that receives the images and illuminates the jet respectively. Good pictures were taken with the spherical aluminium powder, the fumed silicon dioxide and the talcum powder. They mixed well with the air, gave a more or less constant particle concentration and revealed nicely the shape and the structure of the jet. The Titanium dioxide, the zink oxide and the silicium dioxide did not deliver such good results. They stuck together, built lumps in the tubes and in the mixing unit and delivered a very unsteady particle concentration in the jet. Using low pressure to create a not too fast jet, the best images were taken with fumed silica. But turning to higher pressure in order to create a high speed jet, the high initial volume of the fumed silica made it impossible to load the mixing unit with a quantity that would be sufficient to seed a high volumetric flow over about a minutes.

Johnson Baby powder mainly was used in this experiment although the experience with cheaper brands was not worse, and easily attained with the talcum powder. The results were satisfying in such a manner that the further use of the much more expensive aluminum powder was dismissed. The talcum powder was the choice at the moment. The photographs, which are the results of these comparative experiments, are shown in details in later sections.

3.4 Insight NT Software

Insight NT is the software package from TSI, used as the interface of PIV. The software package contains all the laser operation, setup, image control, synchronization and postprocessing. Without the package, it is impossible to go into the details of the jet flow. The manual can be obtained from TSI with all the information.

3.5 Images

This section shows some pictures taken during the experiments, including the overview, the autocorrelation images crosscorrelation images, and the resultant velocity vectors.

3.5.1 Jet Structure

Prior to the detailed velocity measurement for jet flow, the overall structure of the flow was captured by our the high resolution PIVCAM 10-30 camera. Figure 3.5 shows a nitrogen jet issuing into air at Mach 0.6. The structure captured by PIVCAM camera gives us an qualitative insight for the jet.

Figure 3.5: Nitrogen Jet at Mach 0.6

3.5.2 Autocorrelation Images

The following picture was taken for nitrogen jet at Mach 0.6. The double pulse was set as 5μs, and the picture size is 4cm X 4cm (Figure 3.6 removed some parts in the vertical direction to show more details.

It can be seen that the particles in this picture are shown in pairs, because the same particle or particle structure was illuminated twice at different locations. This is how Insight NT software uses autocorrelation scheme to extract velocity in different interrogation zones.

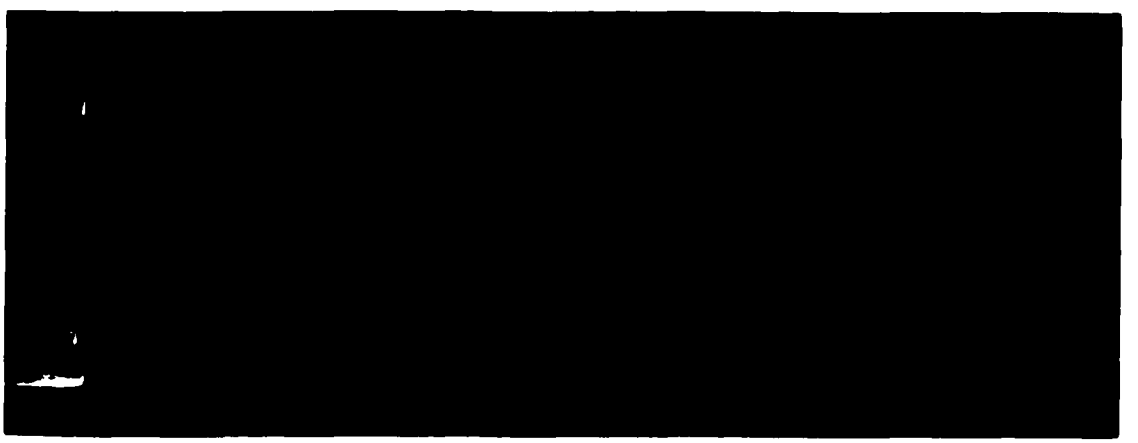

Figure 3.6. Autocorrelation Image of Nitrogen Jet at Mach Number 0.6

Velocity can be extracted from these images with double exposure. The same technique can be used for helium and krypton. The following two images show not only the image, but the resultant velocity field.

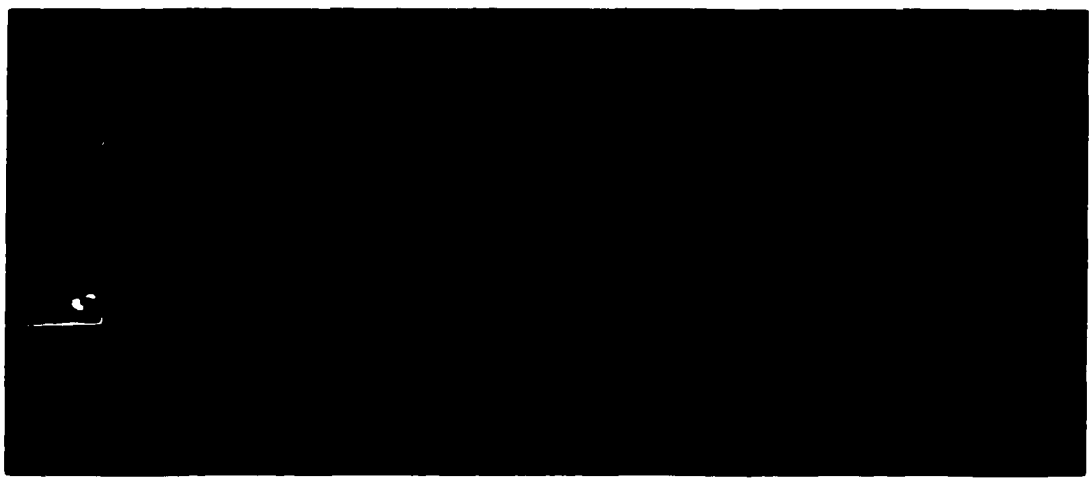

Figure 3.7: Autocorrelation Image of Helium Jet at Mach Number 0.3

Figure 3.7 shows the autocorrelation image similar to Figure 3.6 which is for nitrogen. Because of the small particles, the image is not as clear as that from the nitrogen jet, but the computer algorithm can recognize these particles by light intensity.

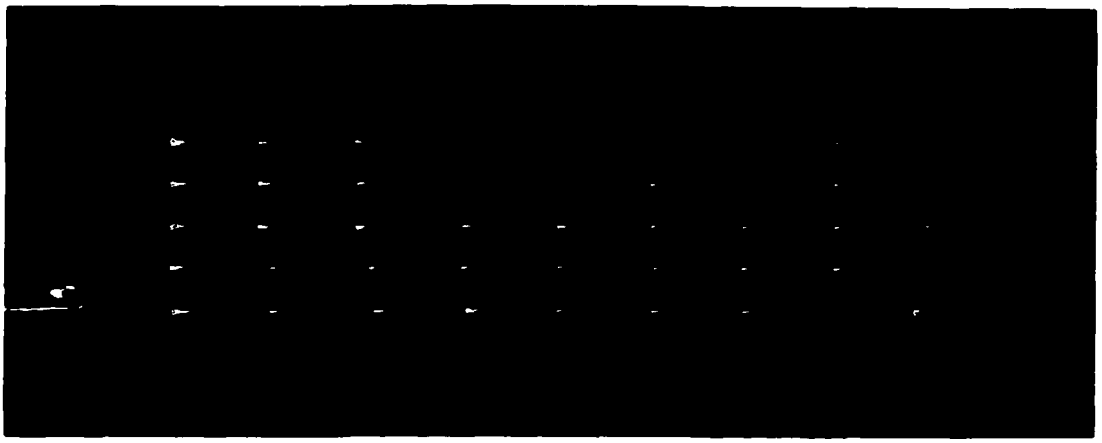

Figure 3.8: Resultant Velocity Vectors from Helium Jet at Mach Number 0.3

Figure 3.8 indicates the resultant velocity extracted from Figure 3.7 by Insight NT software. The vectors show both the direction and magnitude of the velocity locally. The existing sparse is because of insufficient seeding at the corresponding location.

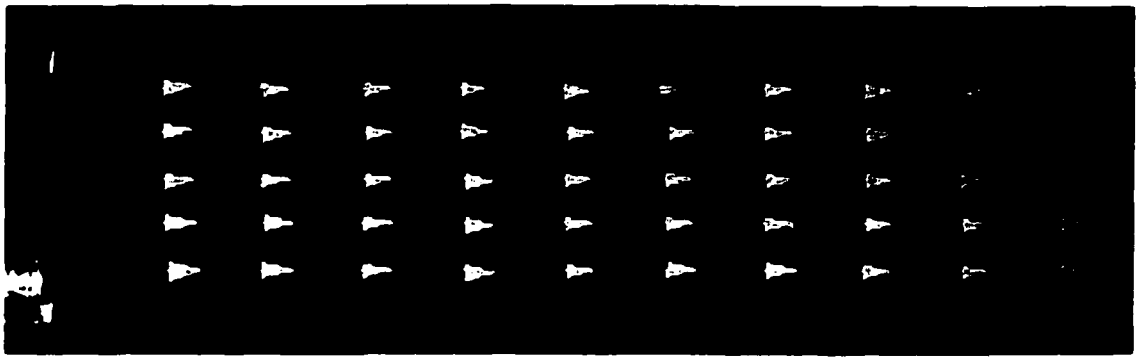

Figure 3.9: Autocorrelation for Krypton Jet at Mach Number 0.3

Figure 3.9 shows the resultant velocity vectors from the corresponding experiment, for which the particles are shown in the picture.

Comparing all three types of jets, krypton jet has the best properties for seeding. Because the density is high enough to carry big structure of particles. While it is different for helium, which explains why with helium jet, the particles were not shown clearly.

3.5.3 Crosscorrelation Images

The following two images were taken for nitrogen jet issuing into air at a Mach number of 0.3. If we overlap these two images, we could see the same particle shows up in different locations, which will make the same images as that from autocorrelation. The movement of particles from one image to the other will allow us to extract the velocity in that interrogation zone.

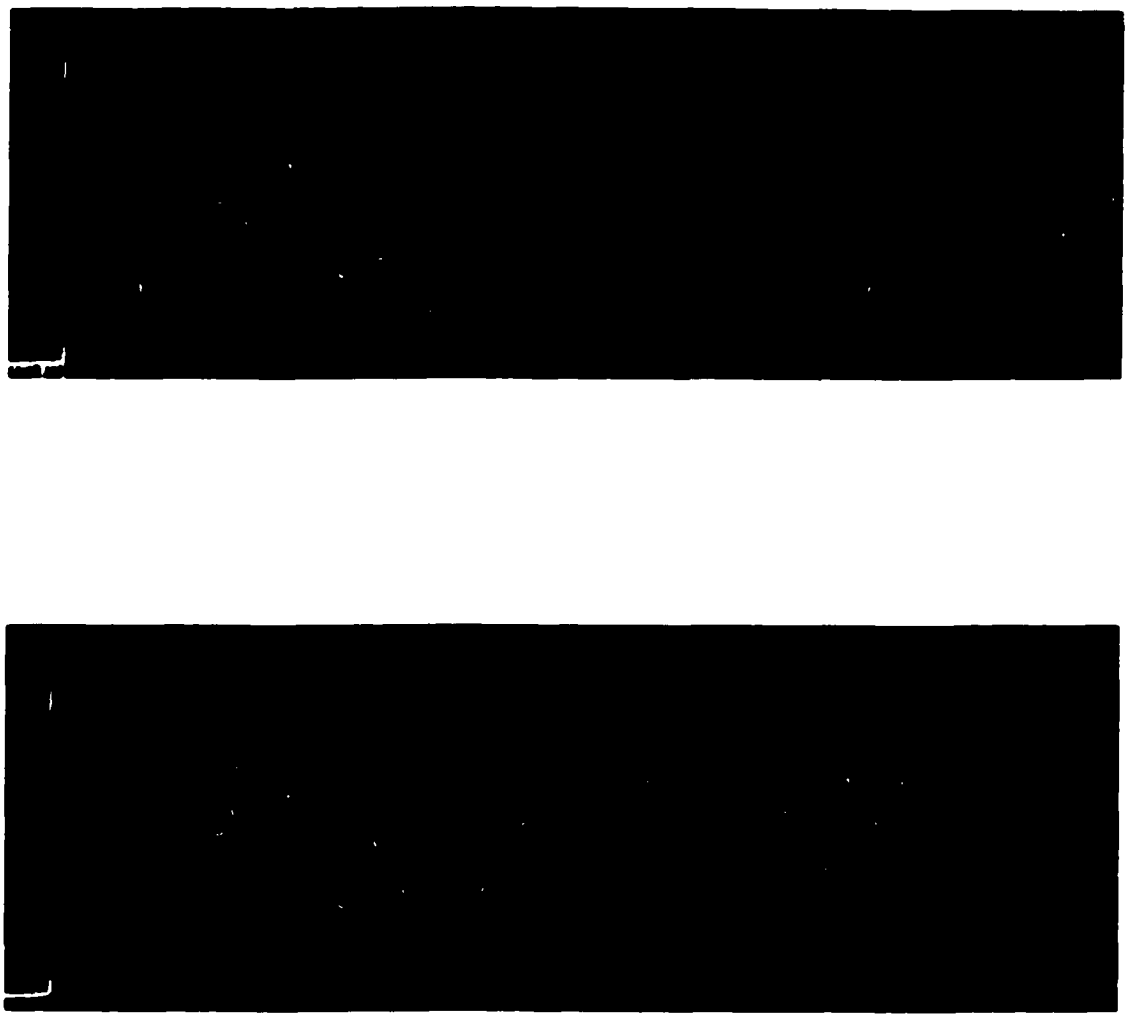

Figure 3.10: Crosscorrelation Images for Nitrogen Jet at Mach Number 0.3

The resultant velocity vector field is shown below in Figure 3.11.

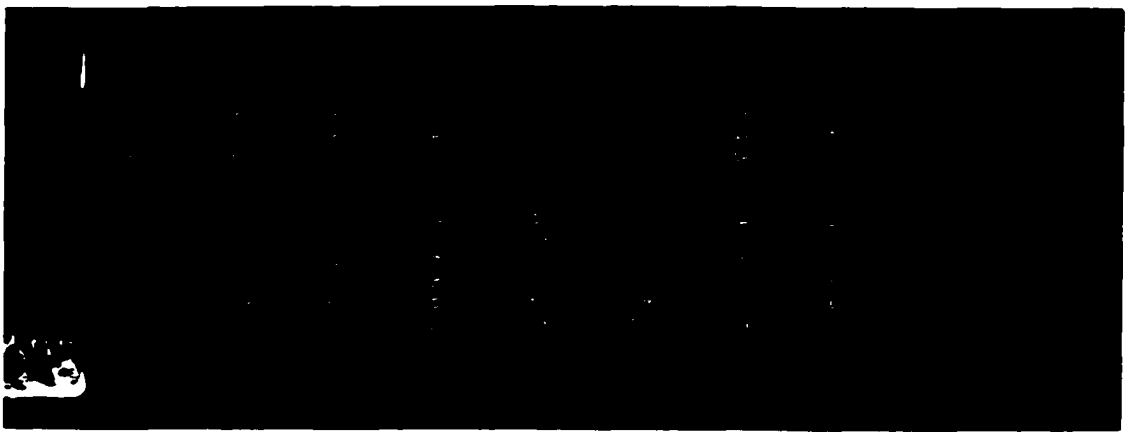

Figure 3.11: Resultant Velocity for Nitrogen Jet at Mach Number 0.3

There are more available vectors extracted from the two images in Figure 3.10, which proves that the crosscorrelation has a better signal-to-noise ratio. Therefore, for low speed measurement, we prefer to use crosscorrelation instead of autocorrelation.

Advantages of PIV (Particle Image Velocimetry) Technology

This technique develops rapidly and it is used in jet flows research widely. For years, Pitot tube pressure measurement, Laser Images, Laser Doppler Anemometer, and Hotwire were used. Introduction to PIV was placed in Appendix B.

There are several advantages for using a PIV measurement.

Nonintrusive velocity measurement. In contrast to techniques for the measurement of flow velocities employing probes as pressure tubes or hot wires, the PIV technique being an optical technique works nonintrusively. This allows the application of PIV even in high speed flows with shocks or in boundary layers close to the wall, where the flow may be disturbed by the presence of probes. The Hot-Wire needs to be placed in the flow, therefore, it will intrude in the flow.

Whole field technique. PIV is a technique, which allows us to record images of large parts of flow fields in a variety of applications in gaseous and liquid media and to extract the velocity information out of these images. This feature is unique to the PIV technique. Except Doppler global velocimetry (DGV), which is a new technique particularly appropriate for high speed air flows, all other techniques for velocity measurements allow only the measurement of the velocity of the flow at a single point, however in most cases this happens with a high temporal resolution. Instantaneous image capture and high spatial resolution at PIV allow the detection of spatial structures even in

unsteady flow fields. Whole field technique allows us to detect not only the interior of the jet flow, but also the edges.

Time delay between illumination pulses. The time delay between the illumination pulses must be long enough to be able to determine the displacement between the images of the tracer particles with sufficient resolution and short enough to avoid particles with an out-of-plane velocity component leaving the light sheet between subsequent illuminations. PIV has conquered the difficulty for particles to move off the desired plane because of its extremely short time between two frames.

Number of components of the velocity vector. Due to the planar illumination of the flow field only two (in plane) components of the velocity vector can be determined in standard PIV (2C-PIV). In our experiment, we need 2 velocity components.

Chapter IV. Total Pressure Measurement

Having introduced the pressure transducer (refer to Chapter II), measurement of total pressure was performed both along the centerline direction and the transverse direction, normal to the centerline, from which the Mach number could be obtained locally. The next section gives the details.

4.1 Introduction to Mach Number Measurement

To obtain the Mach number from pressure information, the following relation from Chapter I was used.

$$\frac{p_0}{p} = (1 + \frac{\gamma - 1}{2} M^2)^{\frac{\gamma}{\gamma - 1}} \qquad (1.2.9)$$

from which the Mach number can be calculated as,

$$M = \sqrt{\frac{2}{\gamma - 1}[(\frac{p_0}{p})^{\frac{\gamma - 1}{\gamma}} - 1]} \qquad (4.1)$$

where ambient pressure is used for p, while p_0 is measured by a pressure transducer. Thus the only unknown parameter is the gas constant γ to solve for the Mach number.

The above relation provides the instantaneous values of the Mach number if the values of γ were known at the same time. In the case of a nitrogen jet, γ is known to be 1.4.

However instantaneous values of γ depend on the concentration of the mixture between the gas and the entrained ambient air in the cases of helium jets and krypton jets. If it is assumed that the concentration is 1. the Mach number can be calculated. Although this assumption seems to be reasonable. at locations closed to the jet exit and in the vicinity of centerline where exit gas time-averaged. concentrations are expected to be high. At downstream. where mixing between the gas and the ambient air has increased. the gas concentration in the mixture is expected to decrease. Therefore. the estimation error may go up.

In order to obtain an estimate of the sensitivity of the results on γ. values of the Mach number have been computed from the corresponding pressure ratios p_o/p for the values of γ that correspond to the three different gases used in the present experiments. The results are shown in Figure 4.1. The curves in these figures are indicative of 100% gas concentrations. The data in this figure show that. at low Mach numbers. for a given pressure ratio the difference between the computed Mach numbers is a little over 3%. At higher Mach numbers this difference is of the order of 6.6% more than double.

The curves shown can be used only for estimation. To find out the accurate Mach number. we have to resort to the equations introduced in Chapter I for a mixture concentration calculation. This method will also be introduced in Chapter VII.

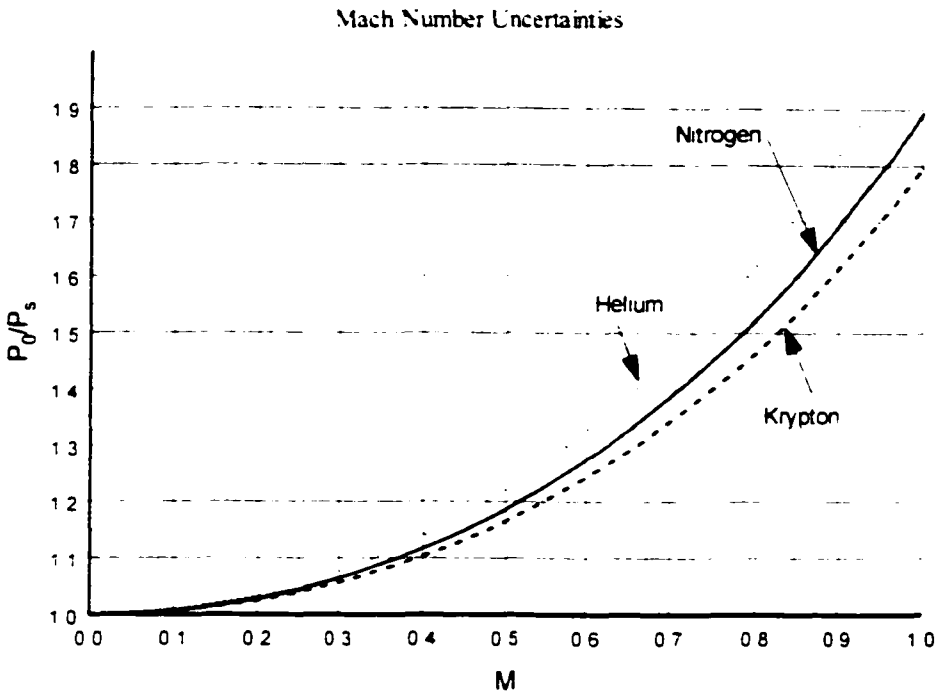

Figure 4.1: Mach Number Uncertainties Due to Different Gas Constant

4.2 Pressure Transducer Calibration

In order to relate the voltage output to the pressure on the surface of the pressure transducer, the measuring system had to be calibrated. Accordingly, the pressure probe was mounted in a pressurized tank, inside which, the tank pressure was regulated with a pressure regulator and displayed on a test pressure gauge mounted on the tank. Table 4.1 lists the corresponding pressure and voltage values. Recall from Chapter II that one 3-transducer probe was introduced.

Table 4.1 Calibration Data of the Pressure Probe

Pressure (psi)	Bottom transducer (Volt)	Middle transducer (Volt)	Top transducer (Volt)
0	0.094	0.020	0.457
6	0.263	0.143	0.612
10	0.436	0.281	0.753
14	0.642	0.464	0.946
20	0.960	0.728	1.194
25	1.176	0.950	1.393
30	1.432	1.137	1.596
35	1.654	1.360	1.790

The linear relation between input pressure and output voltage leads to the following formula:

$$P=e_1V-e_o \qquad (4.2)$$

Where P is the pressure input while V is the voltage output. e_1 is the sensitivity, and e_o is the DC offset from the amplifier, which has to be balanced prior to each experiment.

Given a series of P and V, e_1 and e_o can be found by least square fitting. With the data

given in Table 4.1 for the three transducer probe. the relation for all three pressure transducers is given.

Bottom Transducer P=21.454V-0.3521

Middle Transducer P=24.833V+0.1722

Top Transducer P=25.255V-10.094

The calibration for all three transducers is plotted in Figure 4.2. The linearity property can be seen from all of the three transducers. Each transducer has a different slope. meaning that they have individual sensitivity. as they will give different output voltage even with the same pressure input.

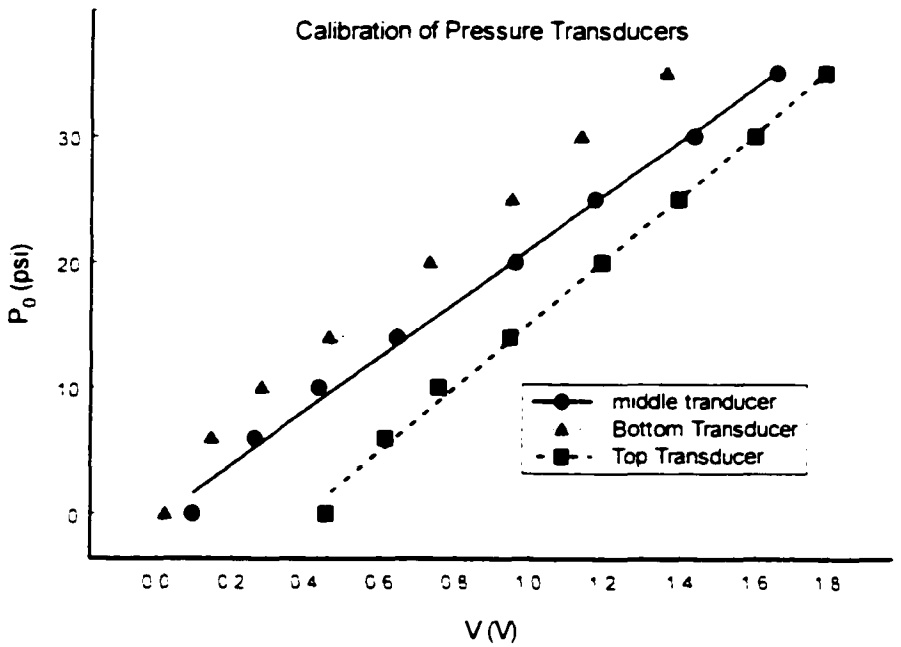

Figure 4.2: Calibration of 3 Transducers by Least Square Fitting

Typical Pressure Signal and the Power Spectrum

A typical reduced signal from the pressure probe is shown in Figure 4.3. The signal was taken for nitrogen jet at x/D=17 along the centerline with jet exit Mach number M_J=0.6.

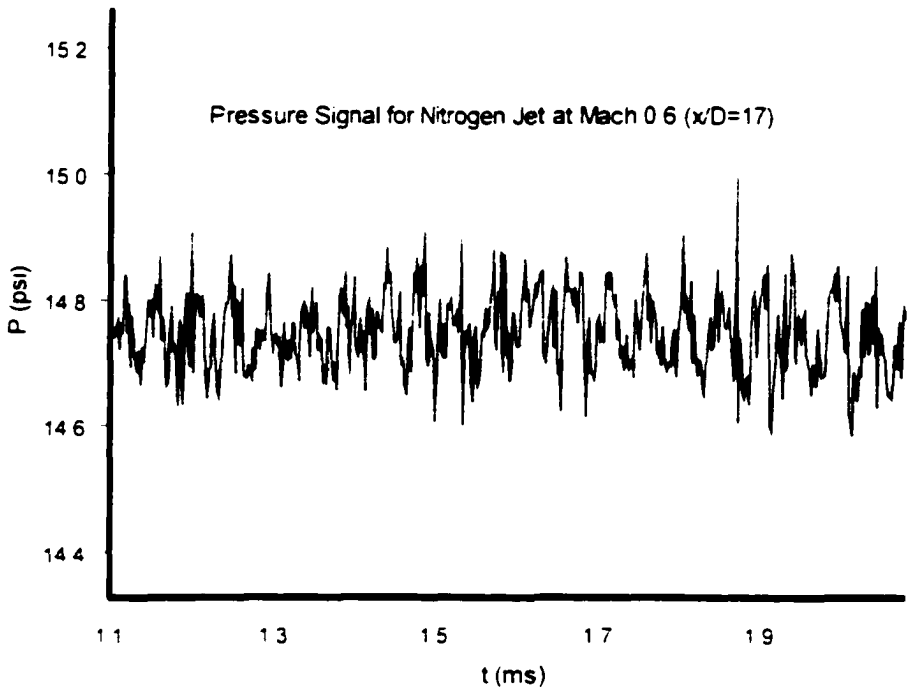

Figure 4.3: Pressure Signal from Kulite Transducer for Nitrogen Jet at Exit Mach Number M_J=0.6

An FFT was performed based on the previous signal and the corresponding power spectrum is shown in Figure 4.4. The dominant frequency of the jet flow is at 20.000 Hz. where the peak power is found.

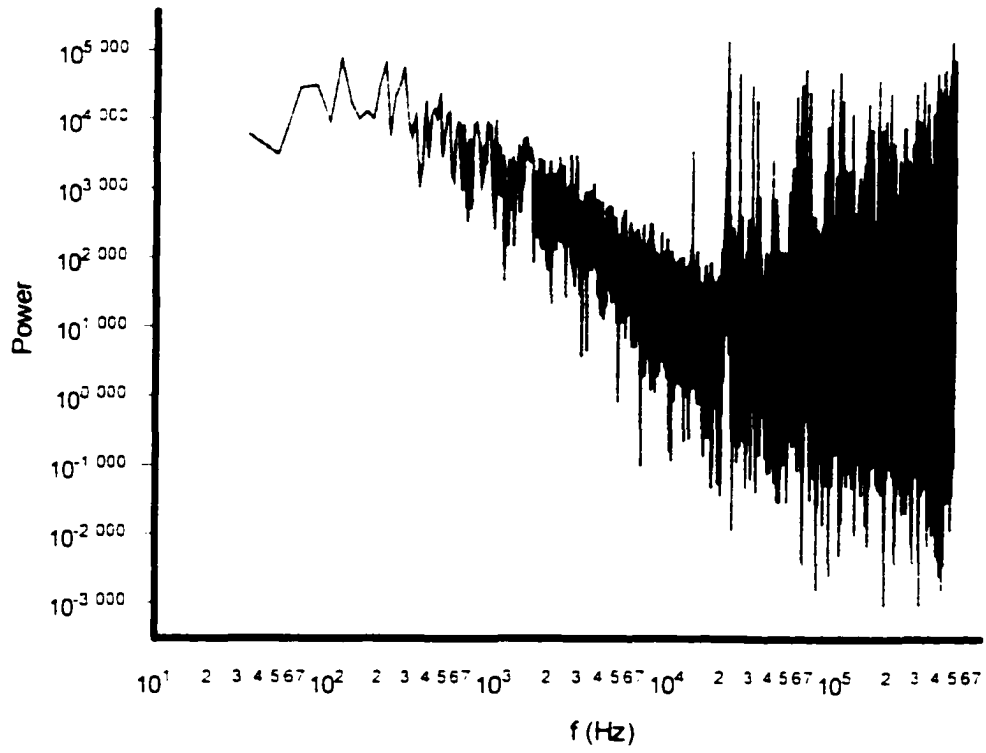

Figure 4.4: Power Spectrum for Nitrogen Jet Flow at Exit Mach Mumber M_j=0.6, x D=17

4.3 Centerline Pressure Measurement

With the pre-calibrated pressure transducer, the centerline pressure for three types of jets at various Mach numbers was measured. The following section lists some fundamental results from the measurements with both mean properties and fluctuations.

Figure 4.5(a) on page 92 indicates how pressure changes along the centerline of a nitrogen jet at different Mach numbers 0.3, 0.6, and 0.9. It can be seen that the pressure for Mach number 0.9 jet increases first then starts decreasing. The starting point of decay changes for different Mach numbers. For M_j=0.9 jets, the starting point is the latest, meaning that when the exit Mach number increases, the decay starts further downstream.

To discuss further differences between these three curves, a new term decay rate (symbolized by D_r) has to be defined.

From the observation of numerous such graphs obtained by the pressure measurements, referring to Figure 4.5(b), it was found that if the range for any curve is splitted into 4 zones, then different phenomena could be found in these individual zones. The zone close the maximum data range, for example the zone between line a and b, which divides the Mach number 0.9 curve, has an increase of pressure, then a decrease, but overall, the pressure does not vary too much against location. The zone close to the minimum data range, for example the zone between d and e, has usually a decrease

through the end. However, this change is limited, because the pressure in this zone is approaching ambient, therefore, overall it's close to ambient, which means the change in this zone against location is not much either. Great changes can be found in the two zones located in the middle of the four, i.e. one zone between b and c, the other zone between c and d. The change against location in these two zones, compared to the other two, is obvious. So this is where the actual decay happens, which is the reason that this zone is called transition zone. Thus a term D_r is defined as the maximum rate of total pressure change in these two zones.

$$D_r = \overline{\frac{dp_t}{dx}} \qquad (4.3)$$

Instead of using each individual local slope, that varies with location, equation (4.3) uses a mean value which can be approximated. As shown in Figure 4.5(b), 5 lines, a, b, c, d, and intersect with the pressure curve from M_J=0.9. Line b and d which constrains the decay rate definition zone, have two intersections with this curve, so the line labeled 1 that passes the two intersections defines one rate that can be used to approximate the decay rate D_r.

The same procedure was repeated for the other two curves for M_J=0.6 and M_J=0.3 respectively, then another two lines 2 and 3 were obtained that approximated the decay rate of M_J=0.6 and M_J=0.3 jets. Thus a comparison of decay rate between the three curves is possible. In the following part, decay rate D_r has been considered without these auxiliary lines shown on the curves.

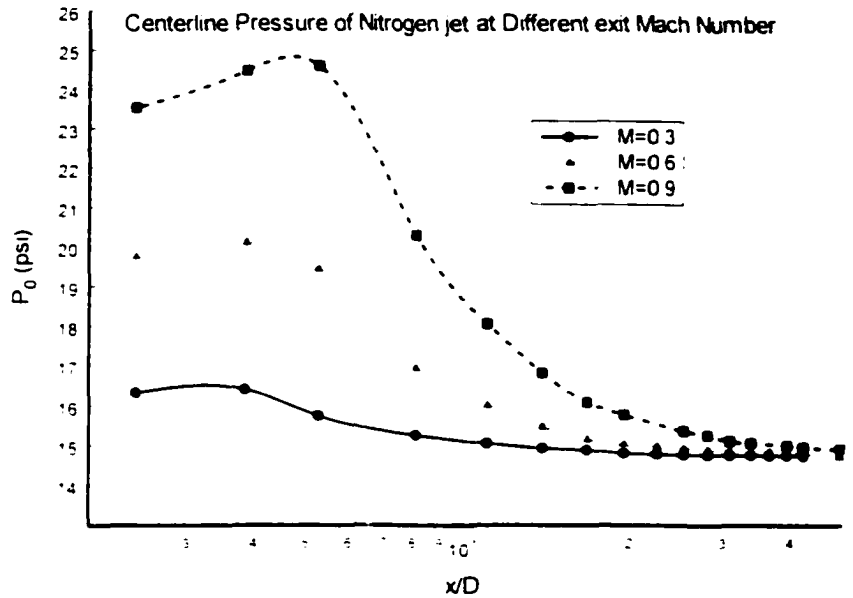

Figure 4.5(a): Decay of Pressure for Nitrogen Jets at 3 Mach Numbers

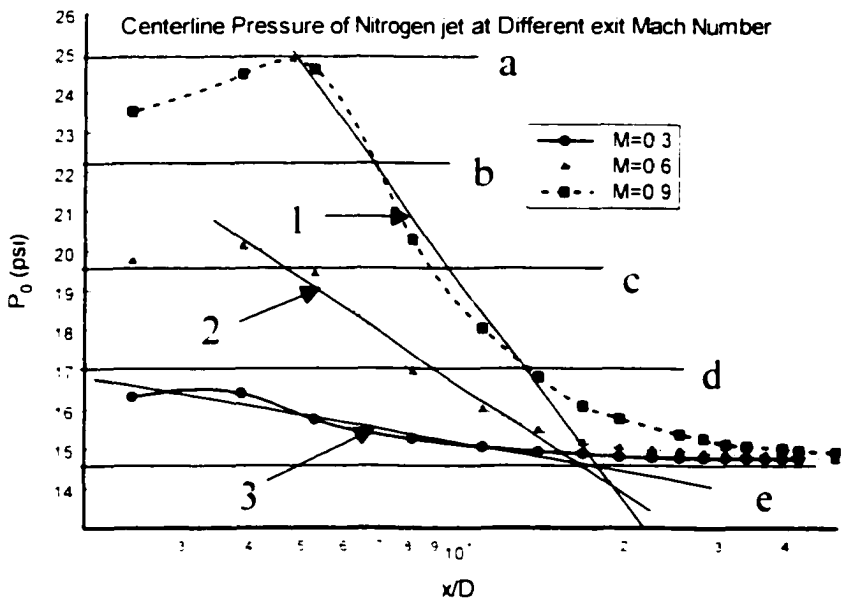

Figure 4.5(b): Concept of Decay Rate

It can be seen from Figure 4.5(b) that the decay rate for M_j=0.9 jet is the highest, meaning that Mach 0.9 jet slows down the fastest along the centerline against the distance from the jet exit. Mach 0.3 jet slows down at the slowest rate along the jet centerline.

It might be interesting to compare the Mach number distribution along the centerline. Figure 4.5 (c) indicates the decay of Mach number for nitrogen jets at 3 different Mach numbers. Note M_{CL} indicates the centerline Mach number of the jet flow.

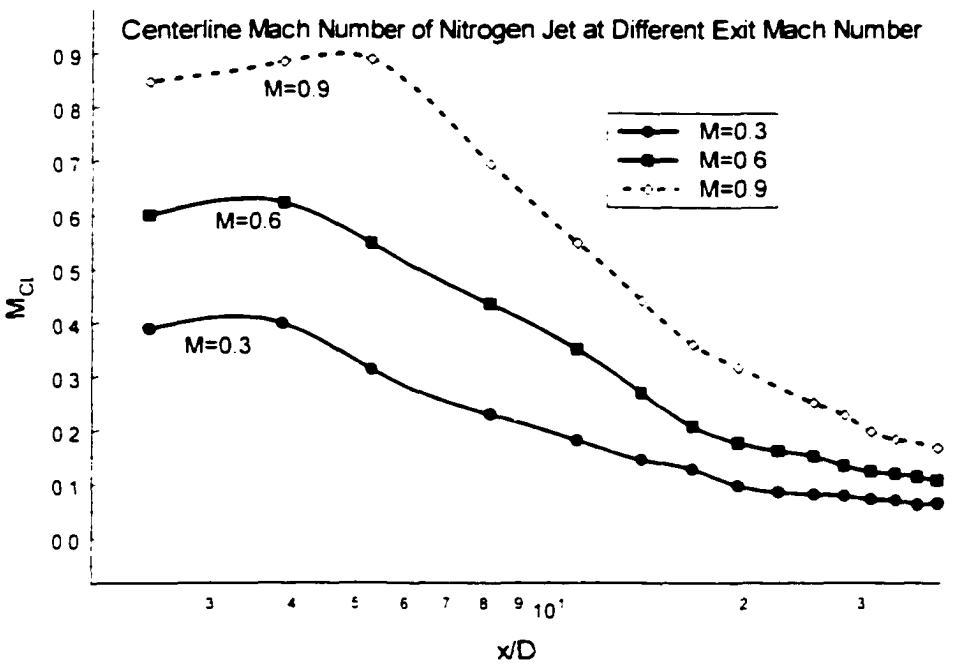

Figure 4.5(c): Decay of Mach Number for Nitrogen Jets at 3 Mach Numbers

The change can be interpreted as the compressibility effect. When nitrogen jet is at a low Mach number less than 0.3, it is usually considered as an incompressible flow. This type of flow does not mix well with the ambient air, so the decay is very slow. When Mach number changes from 0.3 to 0.9, the compressibility increases, and the Reynolds number as well. Correspondingly the flow mixes well with ambient air, so the decay is faster.

Figure 4.6 and Figure 4.7 indicate how pressure changes along the centerline of a helium jet and a krypton jet at different Mach numbers 0.3, 0.6, and 0.9 (for krypton jet, M_J=0.9 was not presented). It can be seen again that the starting point for decay at M_J=0.9 is the latest. This means that when the exit Mach number increases, the decay starts further downstream. Also we notice that the decay rate for M_J=0.9 is also the highest as compared to nitrogen jets. This means that Mach 0.9 jet slows down the fastest.

The interesting fact on krypton jet is that the pressure is not changing significantly. Therefore, the pressure decay rate is slow. This will be clearer if the comparison was made to nitrogen jets and helium jets.

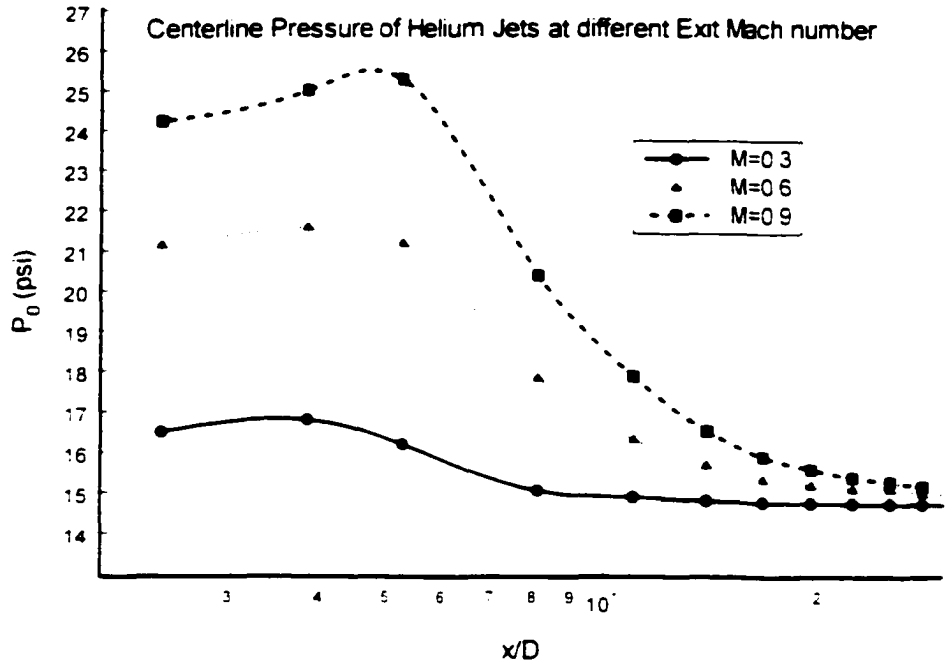

Figure 4.6: Decay of Pressure for Helium Jets

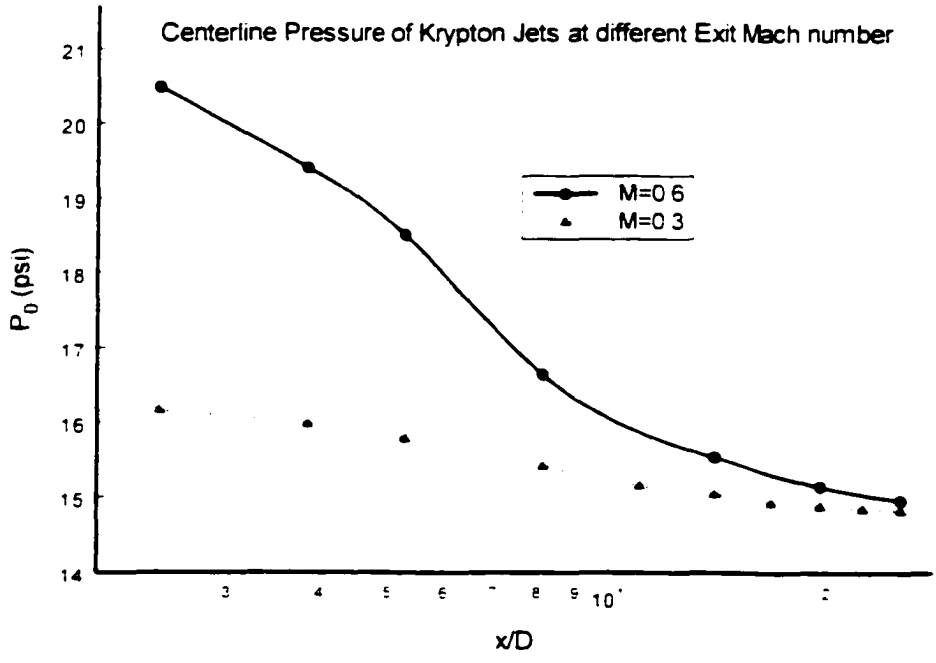

Figure 4.7: Decay of Pressure for Krypton Jets

Now that the data for all types of is are obtained. those jets with the same Mach number are compared. Figure 4.8 and Figure 4.9 indicate at the same exit Mach number M_J=0.3 and 0.6 respectively. how the decay rate differs from each other.

The comparison for three types of jets. despite of the exit Mach number M_J. indicated that the decay rate for krypton is the slowest. while it is the fastest in the case of helium. As the condition was kept the same. the effect from the compressibility effect has been removed. The difference between these three jets is now the density or density ratio to ambient air of the jet. When density ratio increases. the mixing with ambient air is not obvious.

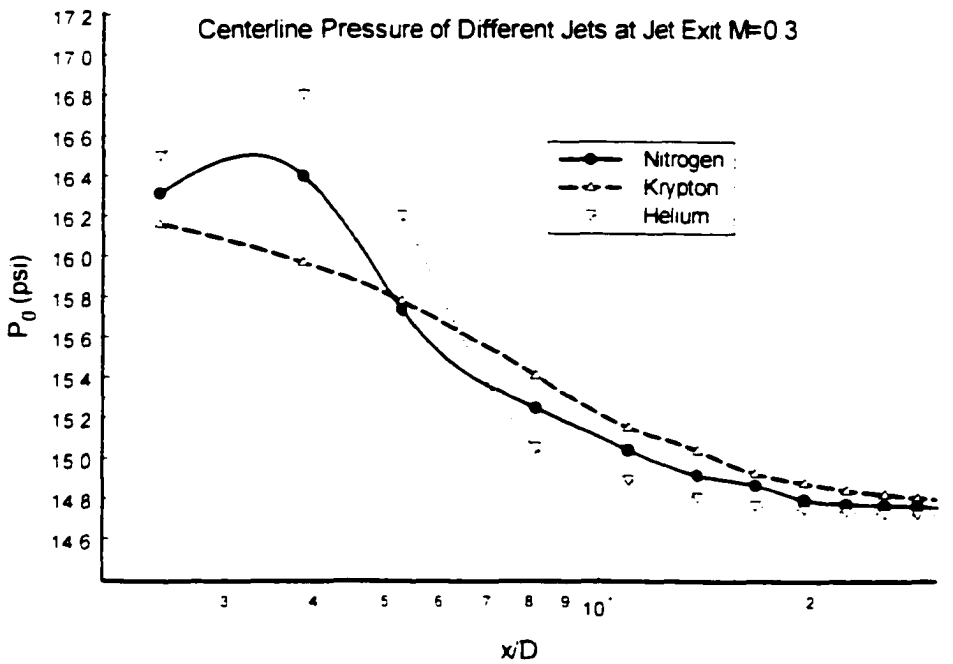

Figure 4.8: Pressure Comparison of Different Jets at M_J=0.3

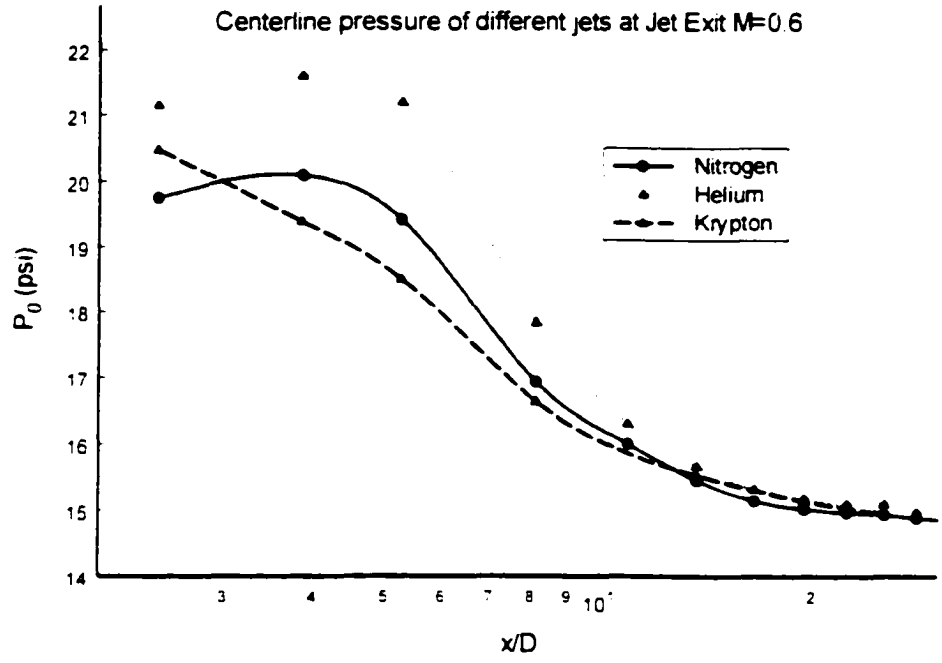

Figure 4.9: Different Jets Comparison at M_J=0.6

It seemed that the mean pressure information showed the compressibility effect and density effect. Will the same effect exist in the fluctuation data? The following part will analyze the data for fluctuation.

Figure 4.10 indicates the standard deviation of the pressure fluctuations measured in helium jets at three different Mach numbers, normalized by $\gamma p M^2$ (or ρU^2). It can be seen that except for the exit Mach number 0.9 jet, all jets had their fluctuations going up then down from the jet exit except for krypton, that goes down from the start. This can

be explained by considering some of the physics. At the exit of the jet, there is no mixing with the air yet, which leads to very low fluctuation. When the distance from the exit increases, more and more mixing is in process, therefore, the fluctuation becomes higher than the one compared at the exit of the jet. Further downstream, the jet dies out, so there is only a small fluctuation. The peak of pressure fluctuation for different Mach numbers occurs at a different location depending on the Mach number.

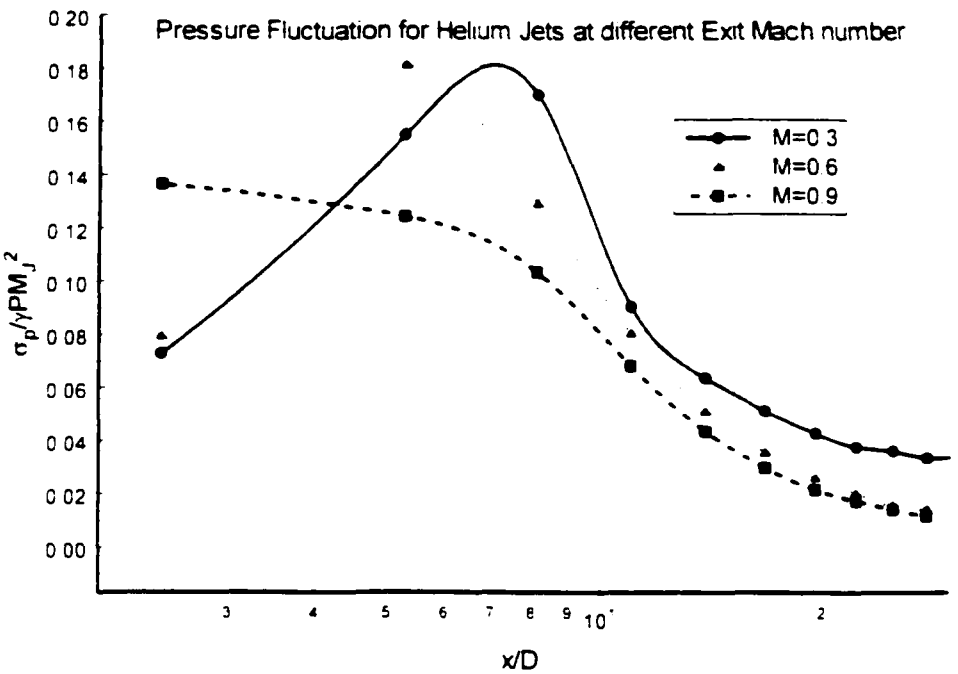

Figure 4.10: Pressure Fluctuation of Helium Jets at Different Mach Numbers

Figure 4.11 and 4.12 indicate the pressure fluctuations of nitrogen jets and krypton jet respectively at three different Mach numbers, normalized by γpM_J^2 (or $\rho_J U_J^2$). As the helium jets, the fluctuation goes up then down from the jet exit.

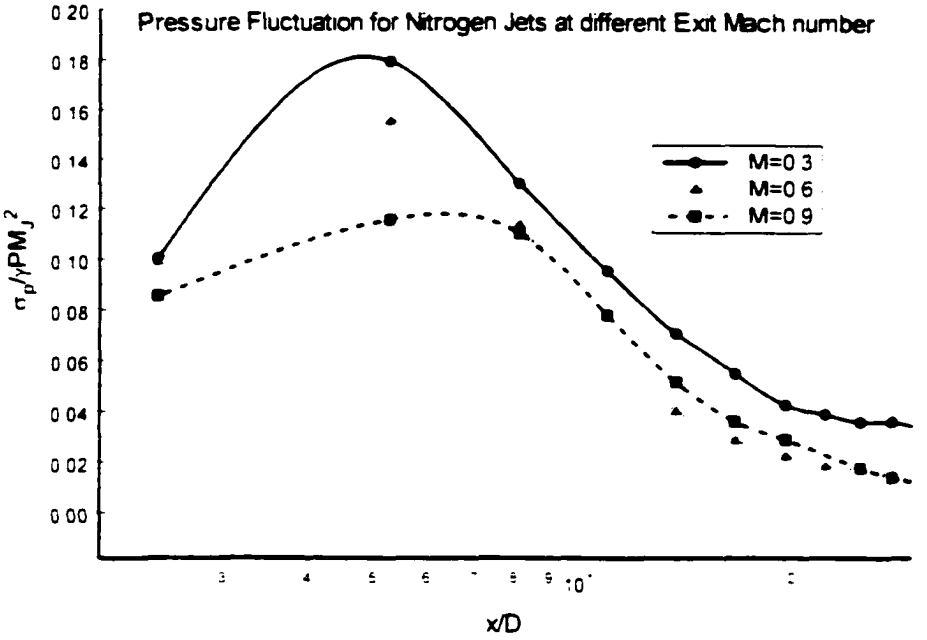

Figure 4.11: Centerline Pressure Fluctuations of Nitrogen Jets

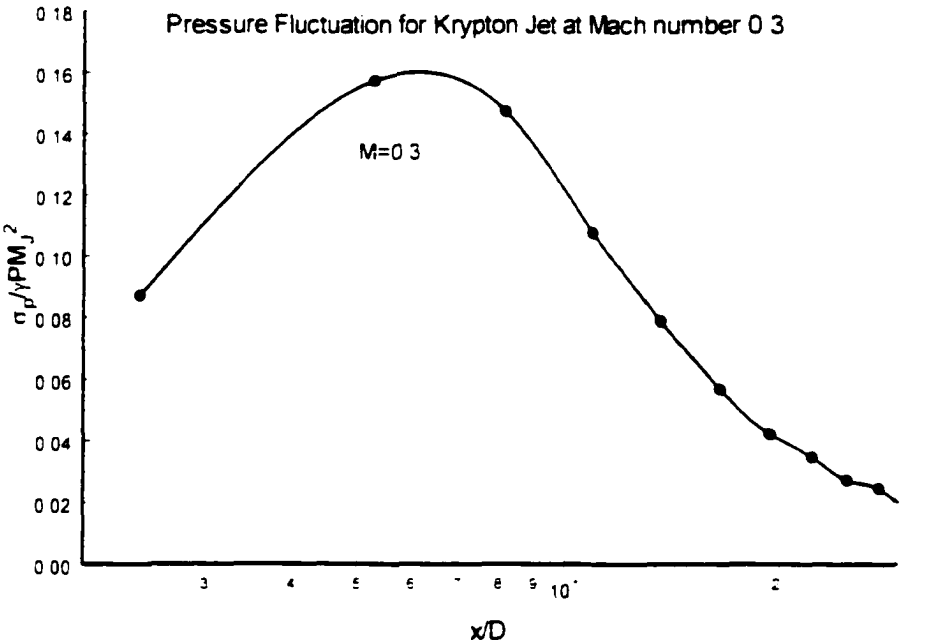

Figure 4.12: Centerline Pressure Fluctuations of Krypton Jets

Figure 4.13 and 4.14 indicate the pressure fluctuations of different jets at the same Mach number 0.3 and 0.6 respectively, normalized by $\gamma p M_j^2$ (or $\rho . V_j^2$). The peak fluctuation is detected at different locations for the three different jets depending on the jet flow density. At higher density, the peak is reached closer to the jet exit and vice versa.

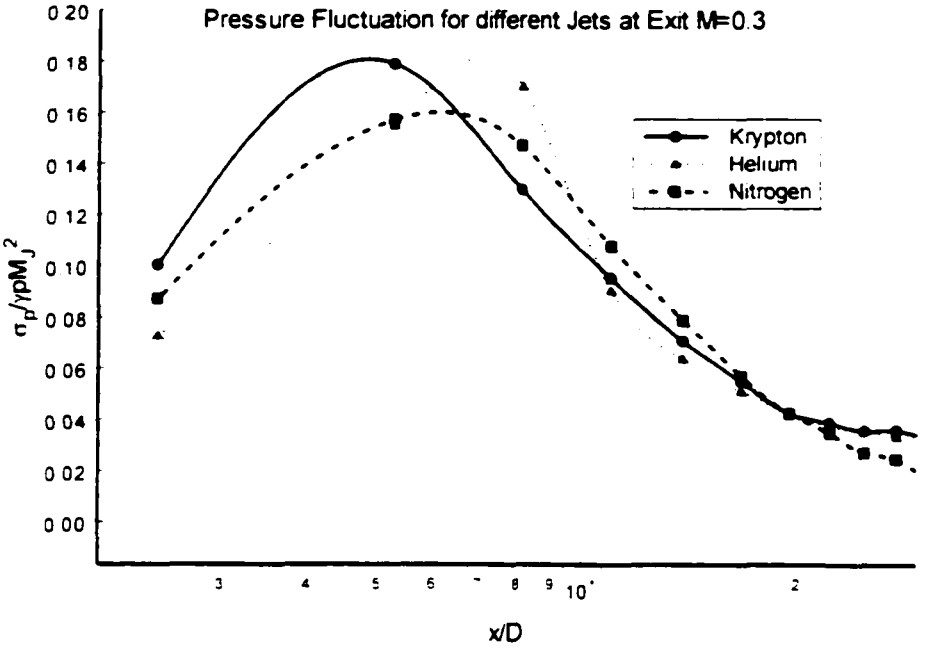

Figure 4.13: Comparison of Pressure Fluctuation for M_J=0.3 Jets

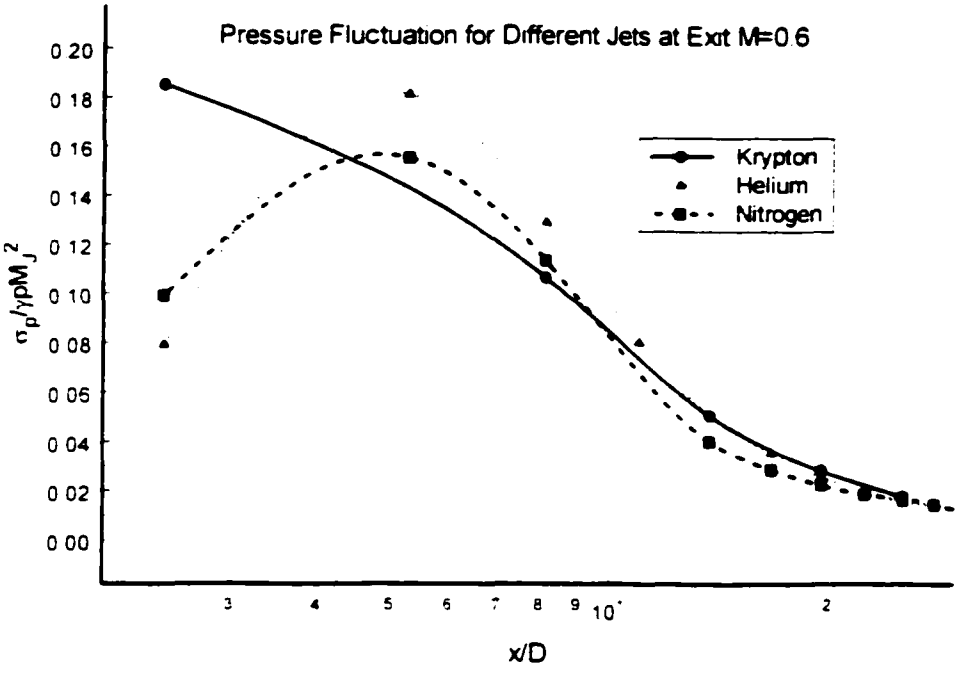

Figure 4.14: Comparison of Pressure Fluctuation for M_J=0.6 Jets

From the above results, one conclusion that can be made here is that the compressibility or Mach number plays a key role in the development of turbulent jets.

From the comparison for different jets, we come to the conclusion that density ratio is also affecting the development of turbulent jets.

4.4 Transverse Pressure Measurement

Besides pressure profile along the centerline, transverse profiles were also obtained through the experiments. Due to the low availability of krypton gas, the experiments for krypton were not carried out. So the transverse pressure results include only helium and krypton pressure profiles.

Three locations along the centerline were chosen for transverse pressure measurements, x/D=8.14, x/D=13.86, x/D=19.57 respectively. Here x is the distance from the jet exit, while D is the diameter of the jet, which is 7mm. For each location, the probe is moving perpendicular to the jet centerline at 2mm step away from the jet centerline. Therefore, for three Mach 0.3, 0.6, and 0.9, nine sets of experiments were carried out.

The following part lists all the profiles including pressure, Mach number and fluctuations. The distance is labeled y in these graphs because it is along the direction that is perpendicular to the centerline direction, which was labeled x.

Figure 4. 15 indicates the transverse profiles of helium jet at M_J=0.3. It can be seen that the pressure is going down when the measurement is taken further off the centerline. There is large gradient for pressure when the profile is taken closer to the jet (i.e. x D=8.14 in this case). At locations where y D larger than 1.0, there is only small pressure change, meaning that the measurement was taken out of the jet flow.

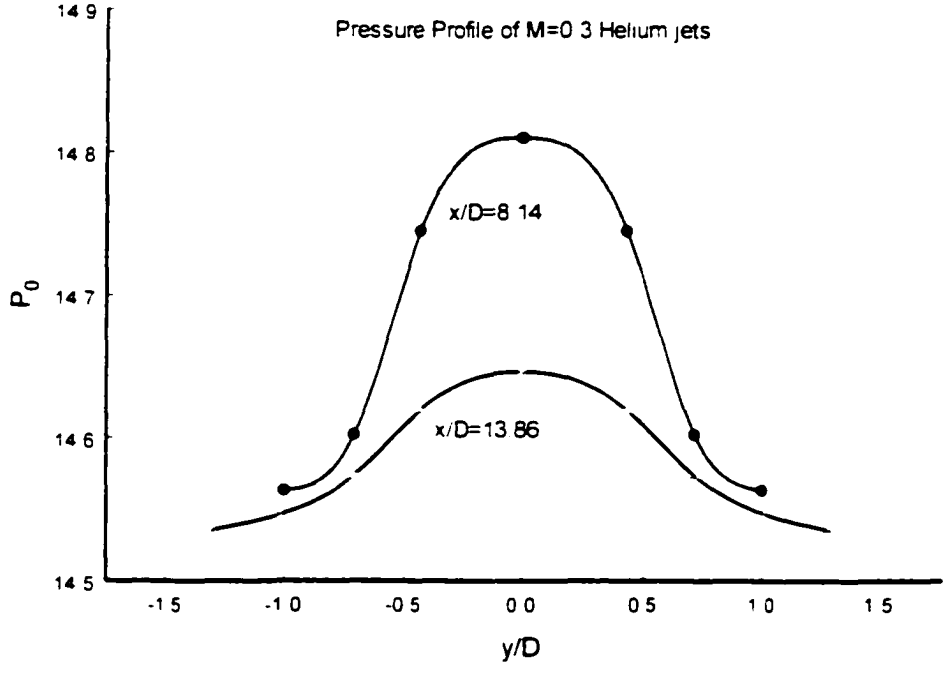

Figure 4. 15: Transverse Pressure Profiles of Helium Jet at M_J=0.3

Another interesting phenomenon was also found from the above figure. When the profile is taken further down stream, i.e. x D=13.86, the profile looks more flat. This shows that the jet flow is spreading and expanding from close to the jet exit to downstream.

Figure 4.16 indicates the transverse profiles of helium jets at M_J=0.6. The pressure changes pretty much the same way as the M_J=0.3 jets. Again, large pressure gradient occurs when the profile is taken closer to the jet exit. Pressure stops going down for the transverse profile taken at x D=8.14, after y D is larger than 1.5, meaning the jet edge has been reached. The other two profiles taken further downstream keep going down and level after 2.0, showing the measurement were taken within the jet flow.

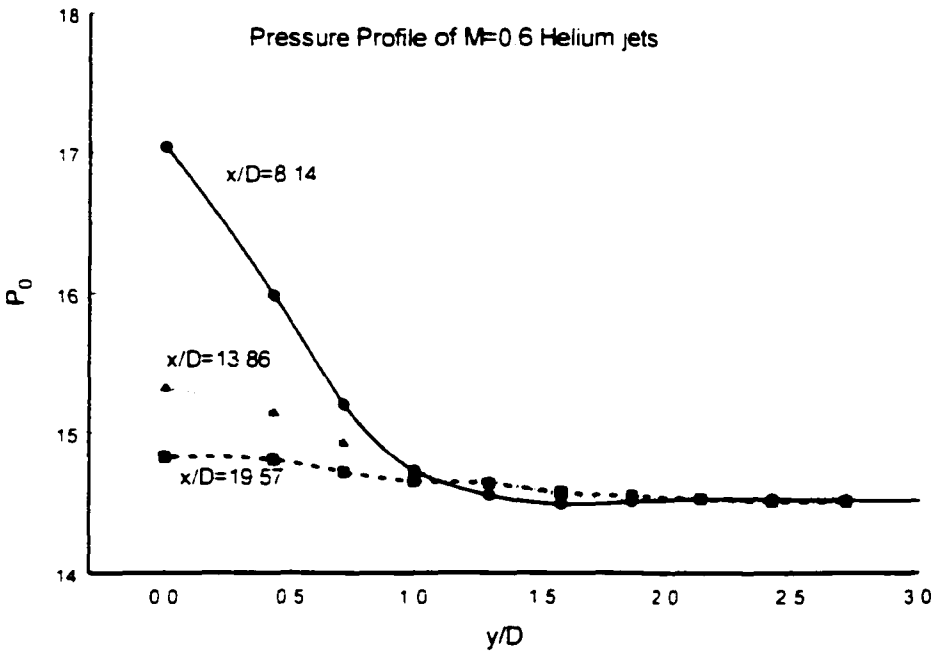

Figure 4. 16: Transverse Pressure Profiles of Helium Jet at M_J=0.6.

It can be seen from the pressure profiles that the decrease is different in the y direction, perpendicular to the centerline, than in the x direction. The decrease is higher when the x location is chosen to be closes to the exit. The pressure is this case reaches the ambient pressure in a shorter range, which means that the jet does not spread out widely yet. Similar behavior can be seen from the fluctuation distribution along the y direction in the following graphs.

Figure 4.17 indicates the fluctuation profiles of a helium jet at M_J=0.3. Figure 4. 18 indicates the fluctuation profiles of a helium jet at M_J=0.6.

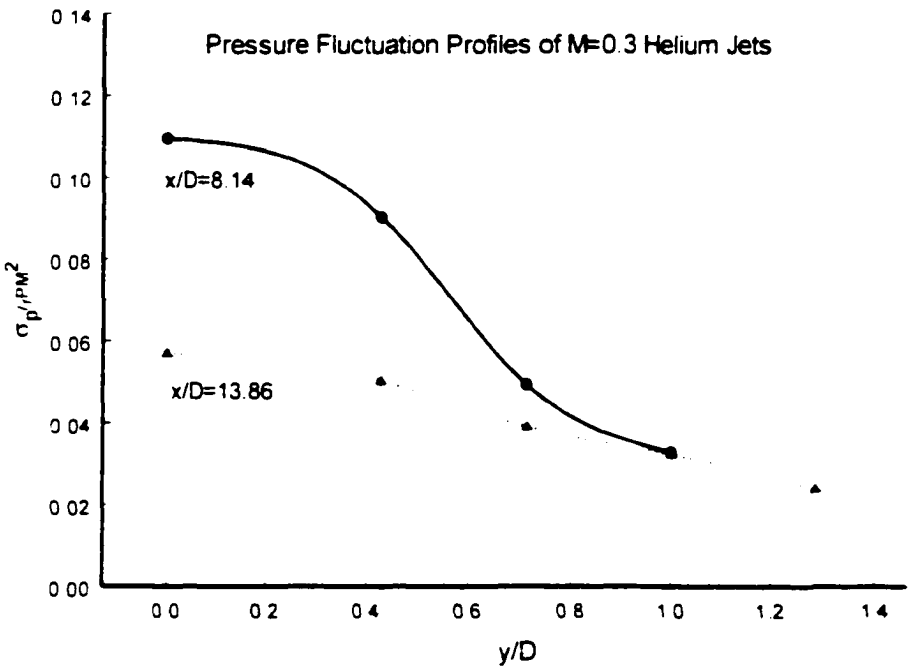

Figure 4. 17: Transverse Pressure Fluctuation Profiles of Helium Jet at M_J=0.3.

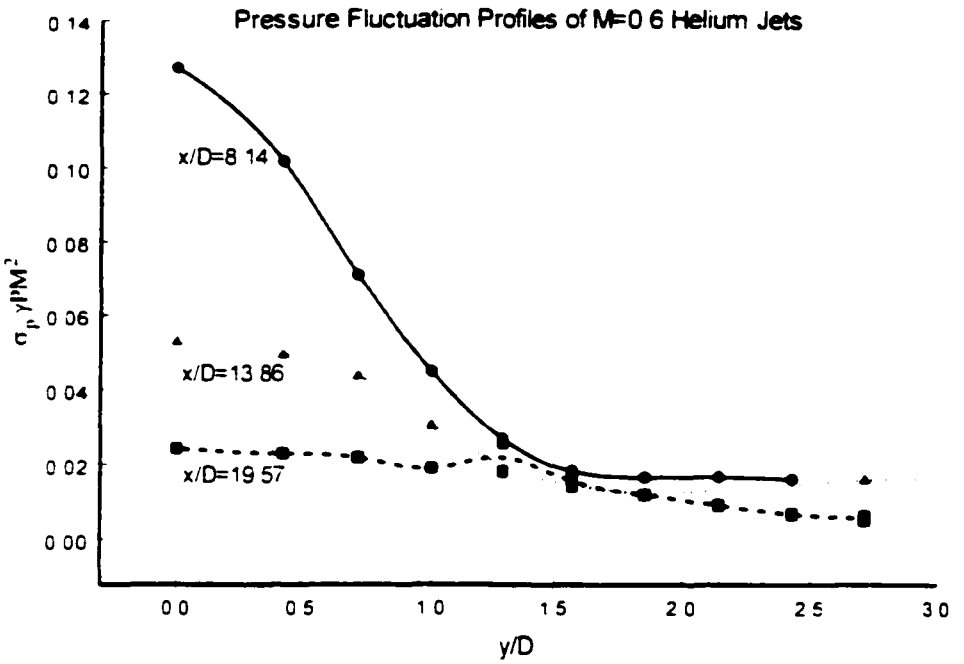

Figure 4. 18: Transverse Pressure Fluctuation Profiles of Helium Jet at M_J=0.6.

Figure 4. 19 and Figure 4.20 indicate the transverse pressure and Mach number profiles of nitrogen jets at M_J=0.3. Figure 4.21 and 4.22 indicate the transverse pressure and Mach number profiles of nitrogen jets at M_J=0.9 respectively.

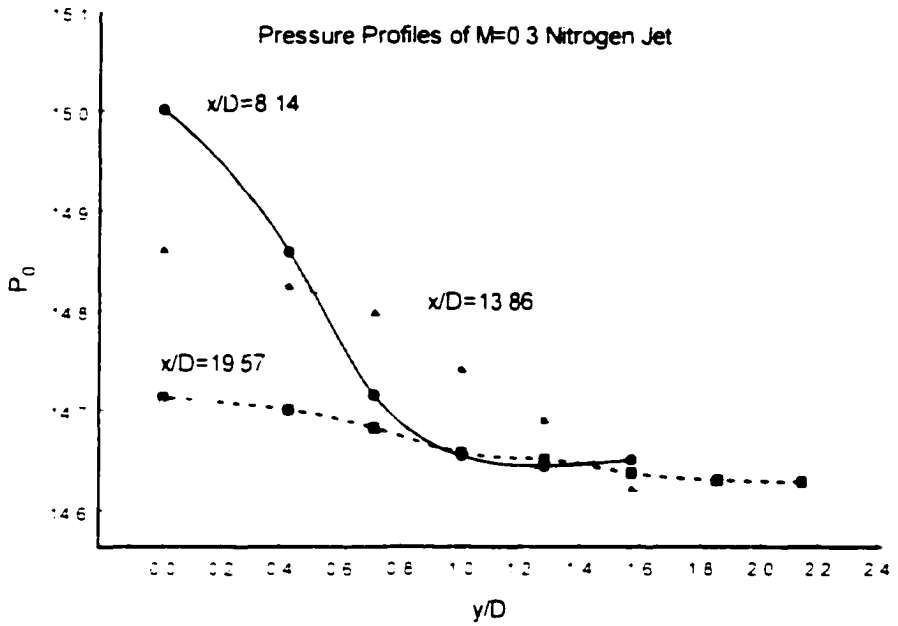

Figure 4. 19: Transverse Pressure Profiles of Nitrogen Jets at M_J=0.3

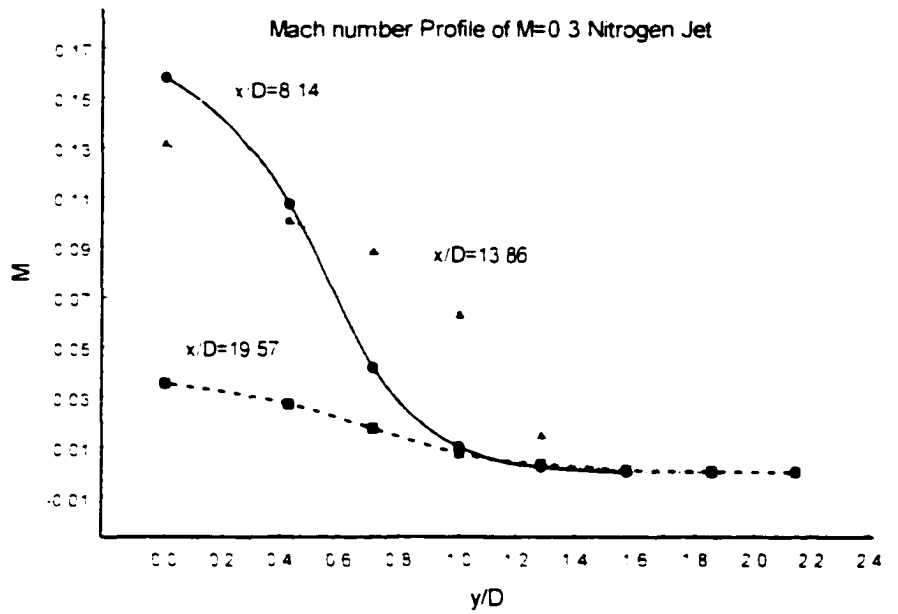

Figure 4.20: Transverse Mach Number Profiles of Nitrogen Jets at M_J=0.3

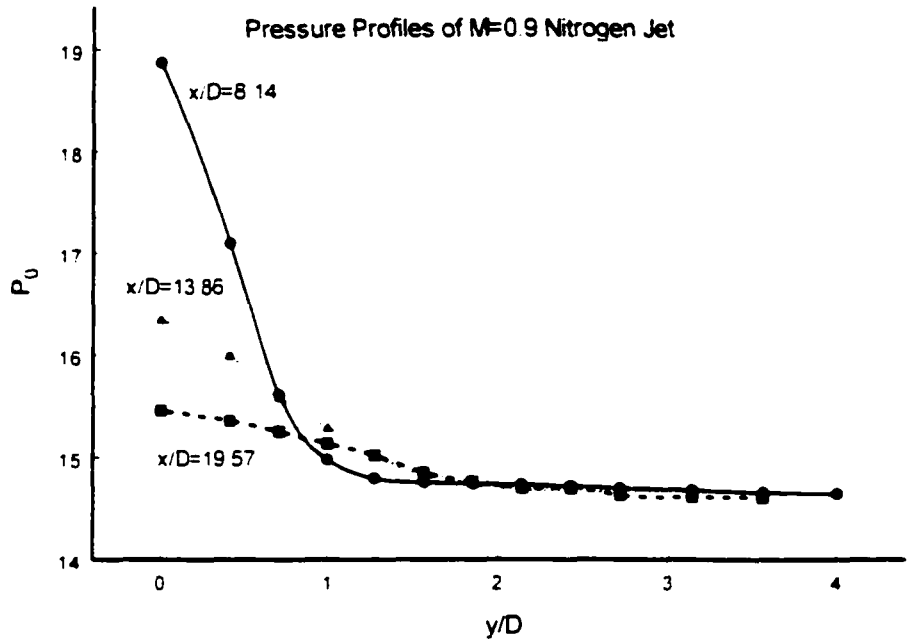

Figure 4.21: Transverse Pressure Profiles of Nitrogen Jets at M_J=0.9

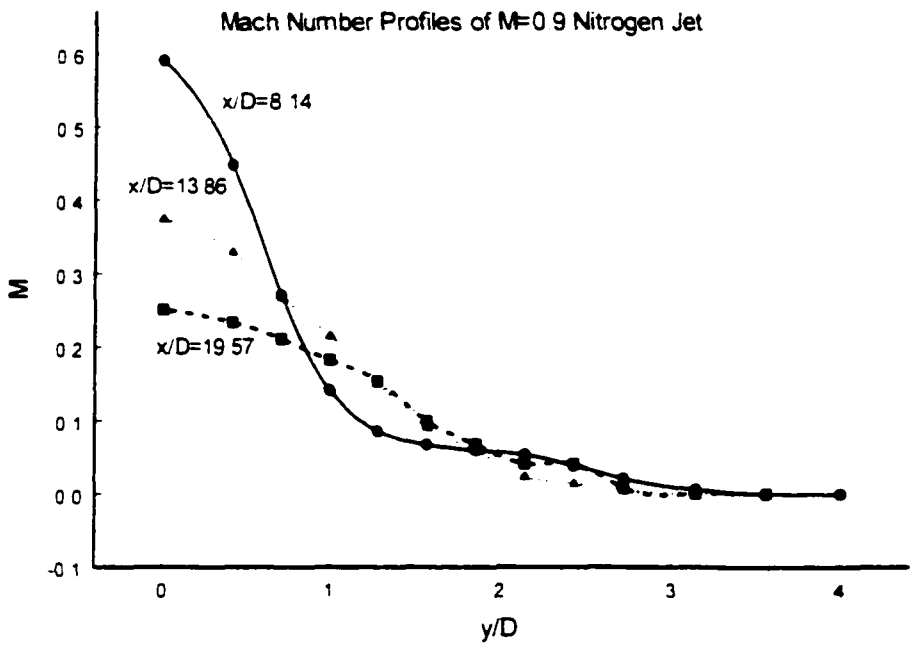

Figure 4.22: Transverse Mach Number Profiles of Nitrogen Jets at M_J=0.9

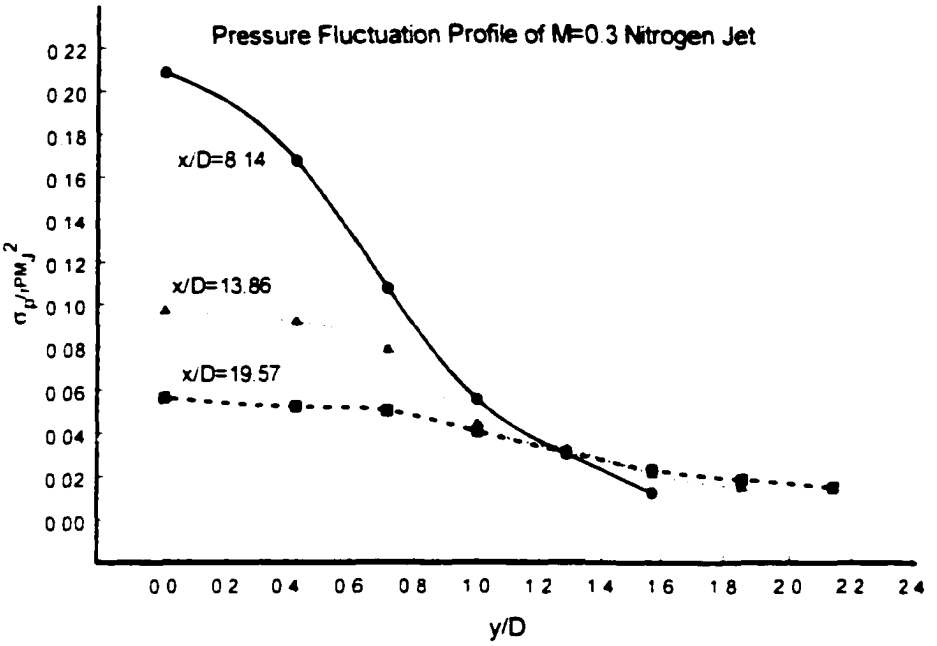

Figure 4. 23: Pressure Fluctuation Profiles of Nitrogen Jets at M_J=0.3

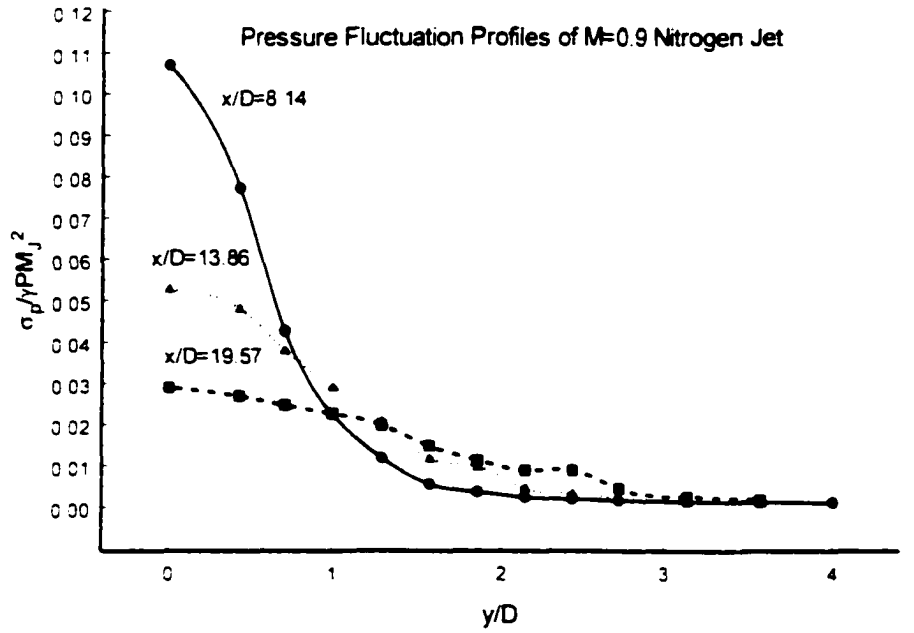

Figure 4. 24: Pressure Fluctuation Profiles of Nitrogen Jets at M_J=0.9

Now that the transverse pressure profile is obtained, the comparison between the same jet at different Mach numbers can be used to look for Mach number effect.

Figure 4.25 compares the pressure profiles of nitrogen jets at 2 Different Mach Numbers, the data was taken at x/D=8.14. It can be seen that the decrease in the transverse direction is higher in the case of a higher Mach number.

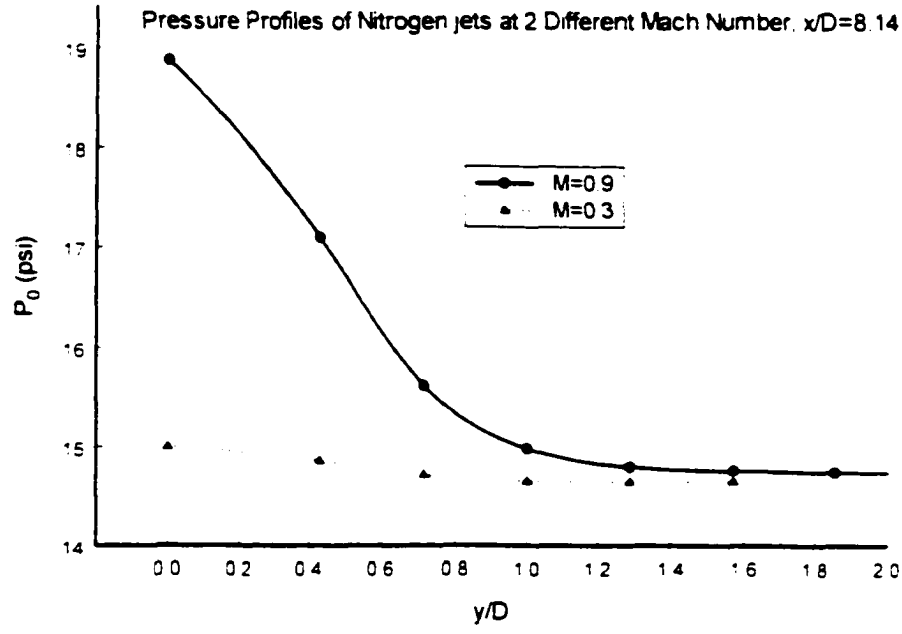

Figure 4.25: Pressure Profiles of Nitrogen Jets at two Different Mach Numbers, X/D=8.14

Figure 4.26 compares the pressure profiles of nitrogen jets at 3 Different Mach Numbers. the data was taken at x D=19.57. It can be seen that the decrease is higher in the case of higher Mach number again.

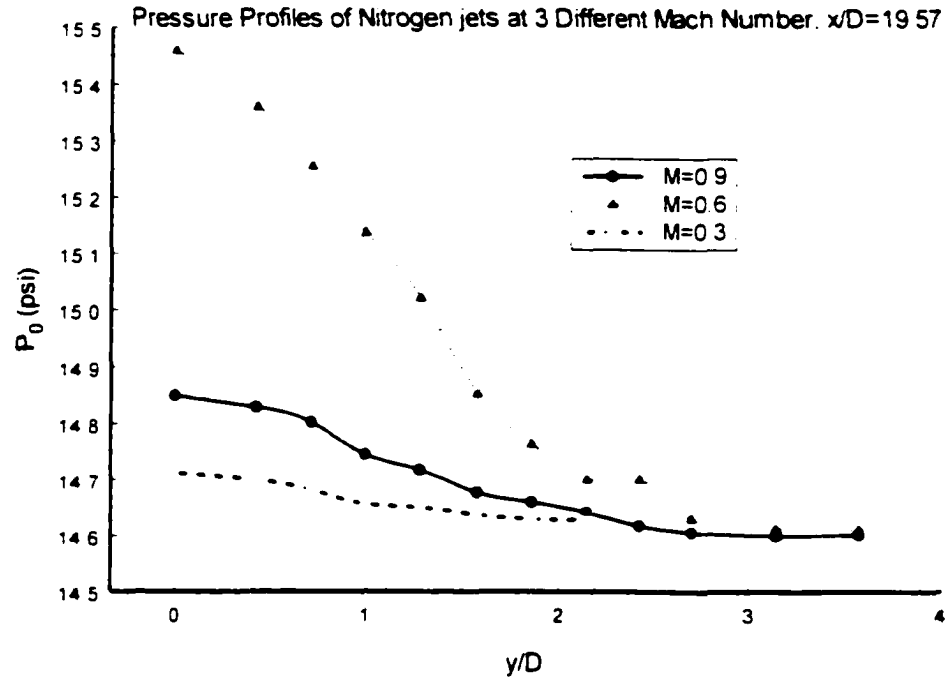

Figure 4.26: Pressure Profiles of Nitrogen Jets at Three Different Mach Numbers. X/D=19.57

It can be concluded once again that the Mach number effect does exist in turbulent jets. When the compressibility is higher. or the Mach number is higher. the flow decays faster.

To find out if the Reynolds number is the key factor on turbulent jets, two pressure signals are compared. From Table 1.2, two jets at about the same Reynolds number were chosen, helium at M_J=0.9 and krypton at M_J=0.3. The figure below shows the comparison of the pressure along the centerline. Similar behavior hasn't been found out between these two jets, therefore, Reynolds number could not be considered as a key factor for the flow in this Mach number range. Further evidence for Reynolds number effect will be discussed in the velocity measurement.

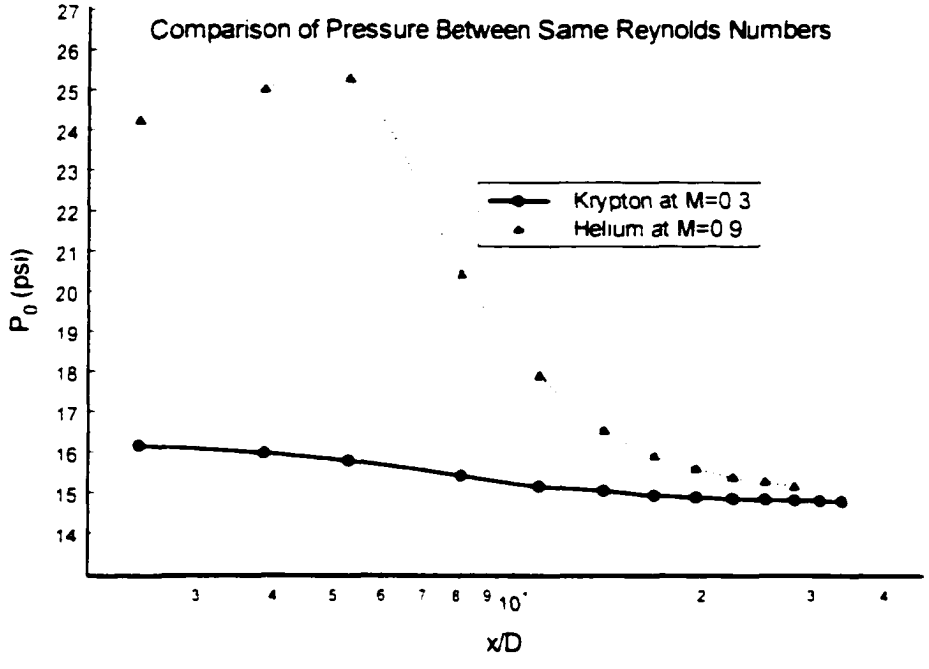

Figure 4.27: Comparison of Pressure Between the Same Reynolds Number Jets

The r.m.s. (root mean square) of pressure fluctuations was compared with DNS results as shown in Figure 4.28. The two curves from DNS were plotted at the exit surface with x/D=0 and y/D>0.5, where measurement of fluctuations happened outside of the jet potential core. Four curves from the experiments were plotted at x/D=8.14. All signals were normalized by $\gamma p M_j^2$.

It can be seen that the r.m.s. fluctuations decrease as the distance off the centerline increases. They also decrease as the exit Mach number increasing. This difference between these curves happens mainly because the measurements were taken at different x locations. The difference between helium jets and nitrogen jets is due to the density effect.

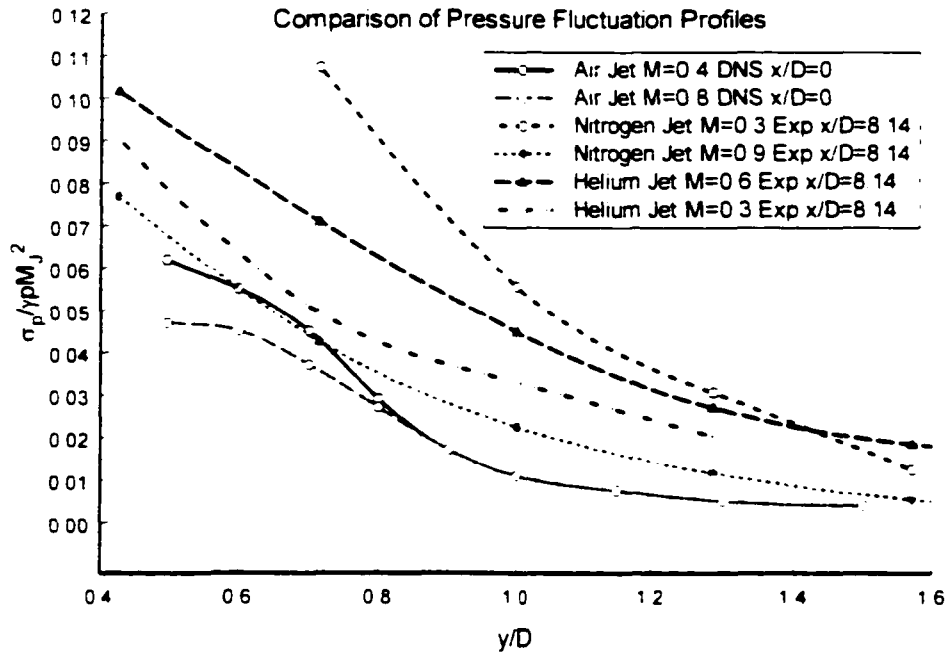

Figure 4.28: Comparison of Pressure Fluctuation with DNS Results

4.5 Spreading Rate

Spreading rate is an important parameter characterizing the mixing in jet flows. If spreading rate is large, then the jet flow entrains ambient fluid which is indicative of strong mixing. As been introduced in Chapter I, the spreading rate was defined by the spreading of the half points where velocity is half of that at the centerline.

As the jet flow is going downstream, the fluid is spreading in the lateral direction. This is evident not only in the velocity profiles, but in other parameters as well, such as the pressure, which was observed from the transverse total pressure measurements. So it is also possible to define the spreading rate based on the total pressure change. To be consistent with the velocity-defined spreading rate, the relation between the total pressure and the velocity has to be analyzed, so that the pressure-defined spreading rate could be compared with the one from the velocity.

Recall equation (1.2.9) from Chapter I,

$$\frac{p_t}{p} = \left(1 + \frac{\gamma - 1}{2} M^2\right)^{\cdots}$$

When the jet flow is subsonic, the above equation may be approximated by Taylor's expansion as follows,

$$\frac{p_0}{p} \sim 1 + \frac{\gamma}{2} M^2$$

or

$$\frac{p_0 - p}{p} \sim \frac{\gamma}{2} \frac{V^2}{a^2} \qquad (4.4)$$

where $p_0 - p$ is the gauge pressure because p is the ambient or static pressure. Sonic speed a can be treated as a constant, which depends only on temperature, and the variations of temperature were measured in a very small range. (Will be shown in Chapter VI)

It can be seen from equation (4.4) that if velocity becomes half, then $p_0 - p$ changes to one quarter of itself. Therefore, if the total pressure signal on the transverse direction is reduced by the ambient pressure, then starting from the centerline on the transverse direction towards the edge of the jet flow, the point that is one quarter of the corresponding pressure could be read as the jet flow edge. With several points read, the jet edge is determined from the total pressure signals, and so is the spreading rate.

Such procedure was performed on the nitrogen jet at the exit Mach number 0.9. The result of the spreading rate, as shown in Figure 4.29, is 0.082. Helium jets were also analyzed and the results for both types of jets were compared with existing data from the velocity-defined spreading rate as shown in Figure 4.30.

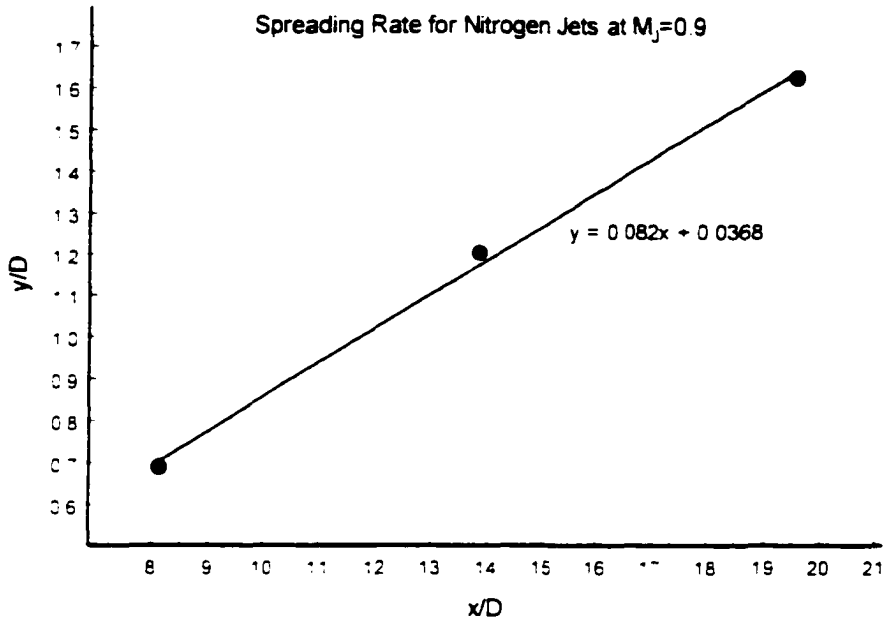

Figure 4.29: Spreading Rate of Nitrogen Jets at M_J=0.9

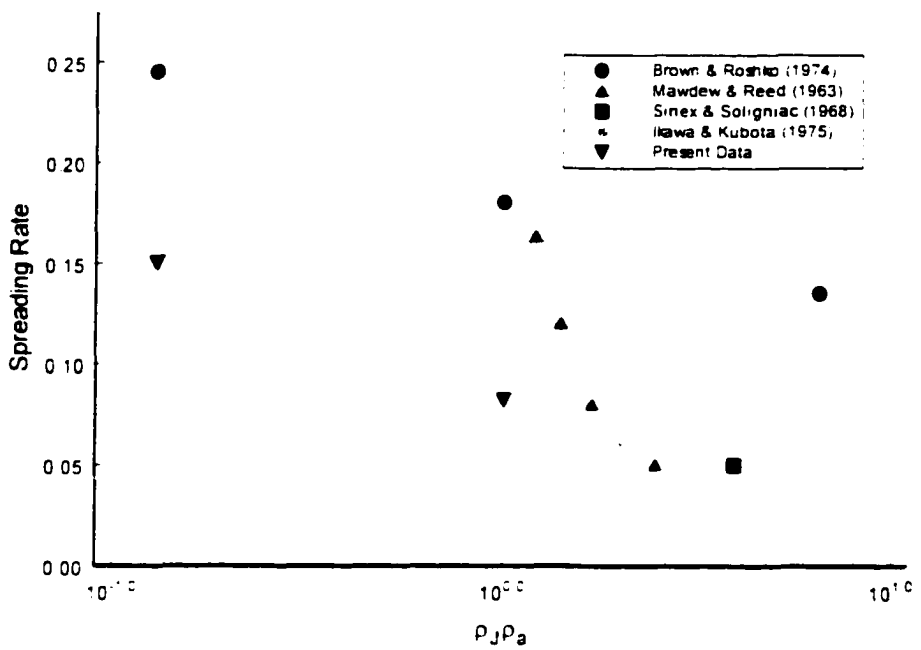

Figure 4.30: Spreading Rate Comparison Based on Density Ratio

4.6 Summary

The pressure distribution along the centerline and in the transverse direction gives us interesting information. The centerline pressure was observed to increase first before it starts its decay for helium and nitrogen only. The reason is the potential core of the jet flow, which is close to the jet exit, where the flow is accelerated without mixing with ambient air. As the location x along the centerline goes downstream, the potential core shrinks, due to more and more mixing with ambient air. Because of the viscous effect, the edge of the potential core forms a new boundary that separates the jet flow and the mixture. The boundary is "compressed" by the mixture out of it. And the compression from the ambient flow becomes larger when the location is further away from the exit, because the mixing is increasing with the location. As the entrainment of ambient air is not rapid enough to "leak" the flow inside the core, the velocity inside goes up because of continuity, with the distance increasing, which leads to the effect that the pressure inside the potential core goes up.

In the krypton cases, where this was not observed, the explanation is that this increase happens very close to the jet exit. The pressure probe could not go too close to the jet exit as it will obstruct the flow. This was one of the disadvantages discussed in the Chapter I as the introduction of experimental approach. Fortunately, the increase was captured by the PIV measurement, which will be shown in the following Chapter. So it is believed that the pressure will rise first then drop along the centerline for the present jet flows.

In such phenomenon, the pressure increases were not observed in the transverse direction, along which, the pressure keeps dropping to ambient pressure. There is a difference between these transverse pressure distributions: when the location chosen on the centerline is farther from the jet exit, then the transverse pressure distribution lasts longer before it reaches to the ambient pressure. This on the one hand means that the measurement was taken inside the jet flow, so the pressure does not drop to ambient yet, on the other hand it shows that the jet flow is still developing.

As the exit Mach number changes for the same jet flow, i.e. the nitrogen jets at M_J=0.3, 0.6, and 0.9, the decay rate of pressure indicates when the exit Mach number is higher, the decay is faster; while when the exit Mach number is lower, the decay is slower. If the decay rate is faster, the mixing with ambient is said to be better, and vice versa. This phenomenon takes place when the major difference between these cases is the exit Mach number. Therefore, it could be concluded that Mach number is one important parameter for this type of jet flows at an exit Mach number range from 0.3 to 0.9. Experiments with helium jets and krypton jets all showed the same results, which gave us a solid conclusion for the Mach number effect (or compressibility effect).

One thing that should be mentioned is that for the same gas, when the exit Mach number changes, the gas density changes as well because the local temperature changes. We may wonder if this change is enough to cause density effects of the type investigated here. Reviewing Table 1.2, which lists the exit density information, it can be seen for the same

type of gas, there is slightly difference on density when used under different exit Mach numbers. However, such small difference, (i.e. for krypton jets at M_J=0.3 and M_J=0.6, the percentage difference is 3%) itself will account for such a great difference in the pressure decay, it is not reasonable. Therefore, Mach number is still the key parameter for the jet mixing. As to the density difference, it will be discussed in the following part.

Mach number effects have been documented here in cases of constant density ratios. However, in the cases that other gases with different density are used, what could be the difference? This was resolved by using different gases under the same exit Mach number. Again, interesting results were found, which shows the difference when the gas used was changed to another one. The major difference shown was that when the density ratio changed, the pressure decay rate changed dramatically. So we concluded that the density effect, as well as the Mach number effect is a key factor of jet flows. In most cases, both effects show up, therefore a combination of both effects is expected.

More proof that the Mach number effect and density effect comes from the measurements of total pressure fluctuations. The fluctuations showed above also offered a possible comparison for the Mach number and density ratio effects. It was shown that fluctuations increase along the centerline to a certain point and then starts decaying. The reason is that inside the potential core, no mixing is happening that will lead to large disturbance or fluctuations. However, out of the core, where mixing is more intense, the fluctuations become stronger. There's a difference between the level of fluctuations at different exit Mach number and different gases used, in addition, the level of

fluctuations might decrease with increased exit Mach numbers. The position of maximum total pressure fluctuation is not the same in all cases investigated here.

To see the Reynolds number effect, some jets with the same level of Reynolds numbers were examined. No direct evidence from the pressure information that shows a relation to the Reynolds number. (refer to Figure 4.27) So further research has to be done to find out the Reynolds number effect under constant Mach number and density ratio.

Chapter V. Results from Velocity Measurement

With the PIV setup introduced in Chapter III, velocity experiments were carried out with different gases issuing into air at various Mach numbers.

As it was discussed in Chapter IV, the pressure probe could not go too close to the jet exit to take measurement of the total pressure as it obstructs the flow. This shows that PIV is a better solution to resolve the detailed jet flows.

5.1 Spreading Rate Measurement

In order to see the jet flow pattern, and the spreading of jet structure, jet images were taken with single Nd:YAG laser illuminating the flow field in Aerodynamics Laboratory, CCNY. Images shown in Figure 5.1 were from three types of jets running at M_J=0.9. Notice that tracer particles were used for visualization, therefore, the particle concentration could give the spreading rate information.

1. Helium jet

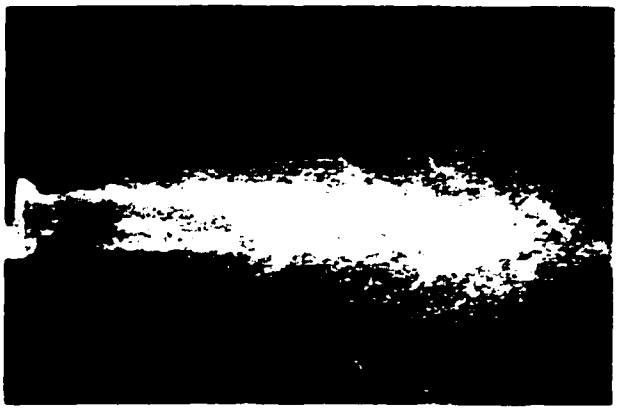

2. Air Jet

3. Krypton Jet

Figure 5.1: Images Taken for Different Jets at M_J=0.9

To find the spreading rate, the edge enhancement software package ImageJ 1.26 was used. Here's a brief introduction to the powerful software.

ImageJ is a public domain Java image processing program inspired by NIH Image for different operation systems including windows. The author, Wayne Rasband (wayne@codon.nih.gov), is at the Research Services Branch, National Institute of Mental Health, Bethesda, Maryland, USA. The software can be downloaded from http://rsb.info.nih.gov/ij/download.html

It runs, either as an online applet or as a downloadable application, on any computer with a Java 1.1 or later virtual machine. It can display, edit, analyze, process, save and print 8-bit, 16-bit and 32-bit images. It can read many image formats including TIFF, GIF, JPEG, BMP, DICOM, FITS and "raw". It supports "stacks", a series of images that share a single window. It is multithreaded, so time-consuming operations such as image file reading can be performed in parallel with other operations. It can calculate area and pixel value statistics of user-defined selections. It can measure distances and angles. It can create density histograms and line profile plots. It supports standard image processing functions such as contrast manipulation, sharpening, smoothing, edge detection and median filtering. It does geometric transformations such as scaling, rotation and flips. Image can be zoomed up to 32:1 and down to 1:32. All analysis and processing functions are available at any magnification factor. The program supports any number of windows (images) simultaneously, limited only by available memory.

Spatial calibration is available to provide real world dimensional measurements in units such as millimeters. Density or gray scale calibration is also available.

Figure 5.2 is the software interface running on Windows 2000 Operation System.

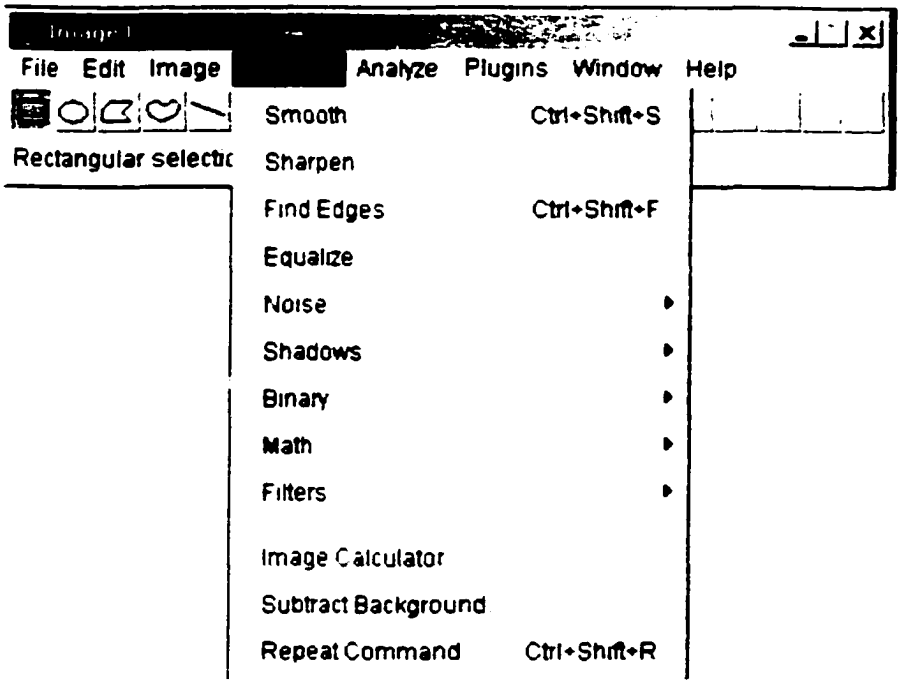

Figure 5.2: ImageJ 1.26 Software Interface

To extract spreading edge, simply open the files with any images similar to those in Figure 5.1, then sharpen them using the Process menu, until the edges wanted are shown clearly. Then, from the Process menu again, choose Find Edge function to find the jet

edges, and the angle between the edges as well. Everything is digitized and measured by the software.

To compare the results with existing data, our data was plotted with existing data together. Figure 5.3 indicates all previous work and our data, which are illustrated by inverse triangle symbols. Density ratio refers to gas density divided by air density, therefore, for nitrogen gas, the ratio is close to 1. Spreading rate refers to the angle between the edge of jet flow and its centerline. This angle was measured after the jet structure was captured by camera. The spreading rates obtained through total pressure measurements are also listed.

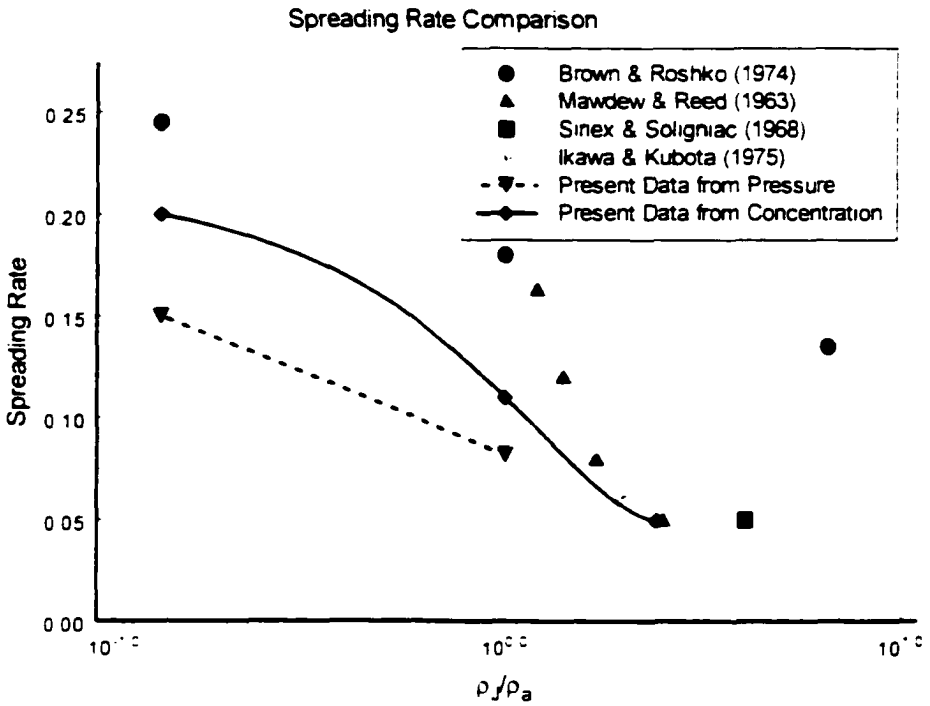

Figure 5.3: Spreading Rate Based on Density Ratio

The difference between the results obtained from total pressure measurements and the concentration measurements is due to a different reading technique. The determination scheme for mixing layer from pressure measurements was introduced in Chapter IV. The concentration scheme is based on the light intensity. When the light intensity becomes 5% of the maximum light intensity of the image, it is considered to be the spreading layer. It can be seen that different definitions of spreading rate may result in small change.

If three jets were plotted together, the difference could be displayed. The particle concentration for krypton is the highest, while for helium, the least, meaning that velocity changes it's spreading at different jet flow conditions. The captured images indicated that the spreading rate of the jets is 0.2 for the helium jet, 0.11 for the nitrogen and 0.05 for the krypton jet. Figure 5.4 shows the difference for three types of jets at Mach number 0.9. Helium, nitrogen and krypton are located off to each other, meaning that when different gases issue into air, their spreading rate is also different.

We expected that the experiments for spreading rate would give us some more evidence to support the compressibility and density effect, instead of Reynolds number effect. To achieve this, different images of jet profiles were put together for comparison. However, the basic findings showed us only the density effect. There is a distinct difference among jets with different gases. For instance, the krypton jets in any exit Mach number give us a thin line, inside which particles can be found. This implies that the krypton jets do not

spread out easily at any Mach number or Reynolds number. In contrast, helium jets, no matter at which Mach number or Reynolds number, spread in a wide range. The spreading region for nitrogen jets is between helium jets and krypton jets, independent of Mach number.

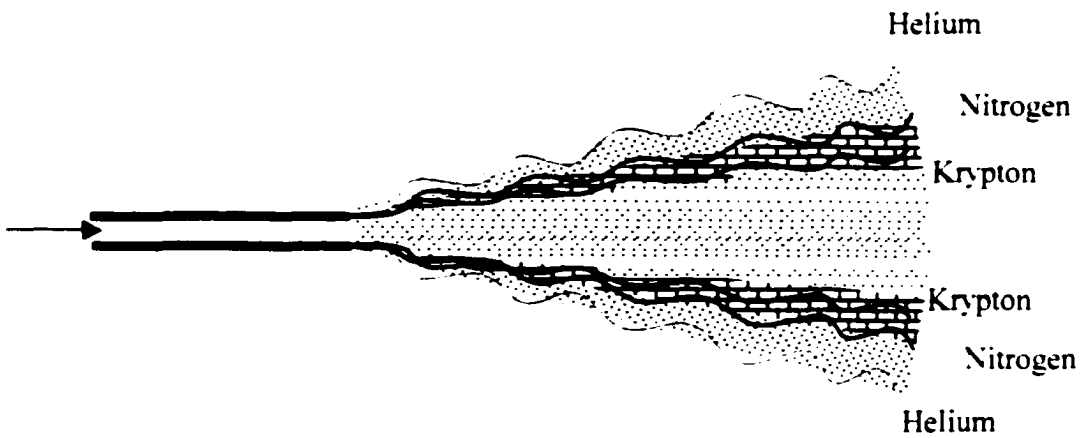

Figure 5.4: Spreading Rate of Three Different Jets

It seems to us that for the spreading rate, density effect plays an important role here. This conclusion is supported by Papamoschou, D. and Roshko [74], who gave a few speculations. Mach number effect was also reported in the same work, but further investigations on this effect are needed.

5.2 Centerline Velocity Measurement

Crosscorrelation and Autocorrelation were used for velocity measurements. The theory was introduced in Chapter III. The results will be displayed for both cases of measurements schemes.

Crosscorrelation has the best signal-to-noise ratio among all the PIV techniques, but due to hardware limitations, the minimum time difference between 2 laser shots can be set as small as 4.5 μs. But for flow faster than 250m/s, smaller time difference is necessary. Therefore, autocorrelation was chosen for these cases. The minimum time difference that can be set is 200 ns, which is not supposed to be used so far. From our experiments, the autocorrelation works perfectly at very high speed up to 300 m/s. At low speed, say for krypton, there is no problem using either autocorrelation or crosscorrelation, but crosscorrelation will be better because of the noise problem. Both results from nitrogen jets are shown later.

The Camera used in PIV measurements has very high resolution, however, because of the extremely small size of tracer particles, the picture size cannot be enlarged by much, therefore, 4cm was chosen as the picture size. Particles captured can be shown clearly on this field for vector processing. To have the view of the whole field or velocity vectors, pictures captured at different location are patched together. This is done for both

crosscorrelation and autocorrelation. Our concern is focused on autocorrelation because it works under different cases. also it is convenient for comparison between different jets.

The following graphs were all obtained from our experiments. Because of the easy availability of nitrogen. both Crosscorrelation and Autocorrelation were performed using this gas. However. when the velocity goes above 300m/s or above. Crosscorrelation does not work well due to the laser pulse setup. We then turned to the use of autocorrelation method.

To verify the PIV technique. the resultant velocity from PIV measurement was compared to another technique. the pressure probe. The following table shows the comparison between the results from both techniques. The measuring point was chosen to be close to the jet exit. where small fluctuations (compared to velocity) are expected. and the pressure probe does not disturb the flow. It can be seen that the results agree well with each other.

Table 5.1 Comparison of Exit Velocity Between Two Types of Experiments

Nitrogen at	M_J=0.3	M_J=0.6	M_J=0.9
PIV	106 m/s	200 m/s	250 m/s
Pressure Probe	104 m/s	199 m/s	270 m/s

Results from Crosscorrelation

Now that the picture size for PIV measurements is limited by 4cm X 4cm because of the resolution requirement, enough information could not be obtained by one shot only. To solve this problem, several pictures were taken along the centerline direction; each having an interval of 4cm, then these pictures were patched together to show the complete flow field. Later results show that there is no velocity discrepancy among these pictures, which supported the use of the PIV system.

Figure 5.5 illustrates the velocity distribution along centerline of a nitrogen jet at Mach number 0.3, starting from the jet exit. The velocity was shown to increase after the exit, then decay continuously. The same result for Mach number 0.6 jets is displayed in Figure 5.6, but the increasing part is missing because of resolution setup.

The decay rate of velocity was seen to be faster when the velocity is larger, while slower when the velocity is smaller. The result is not a surprise after the pressure measurements, for which the explanation is due to the compressibility effect. So the same comments are applied.

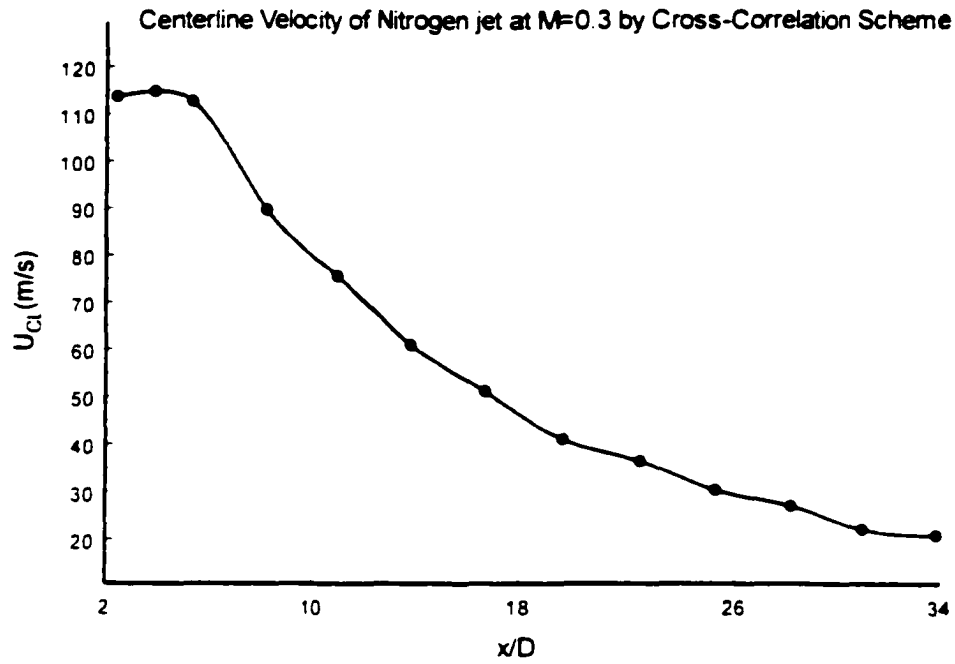

Figure 5.5: Mean Velocity at the Centerline of a Nitrogen Jet at M_J=0.3 by Crosscorrelation

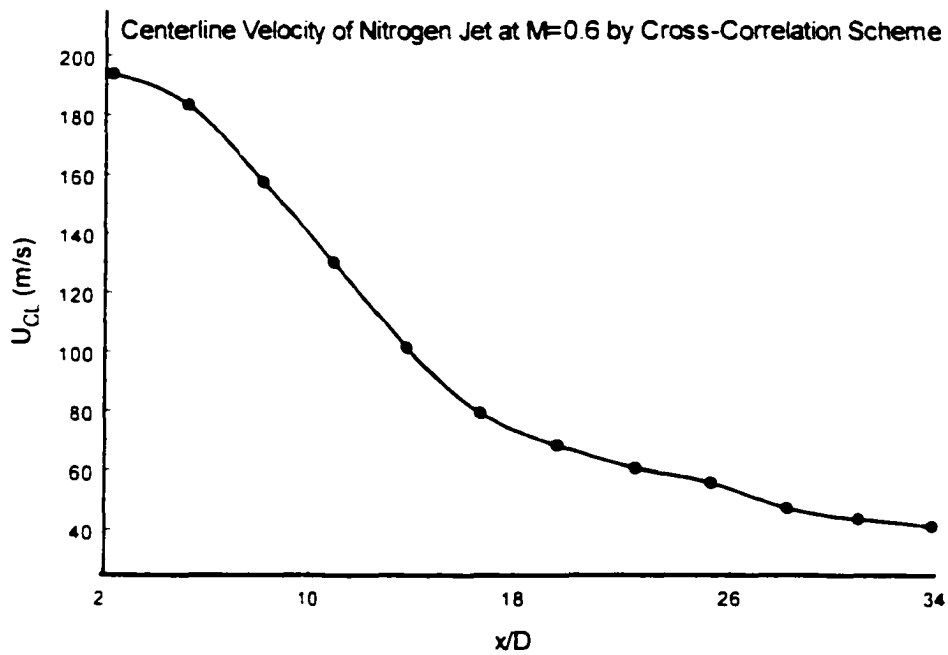

Figure 5.6: Mean Velocity at the Centerline of a Nitrogen Jet at M_J=0.6 by Crosscorrelation

For higher Mach number flows, crosscorrelation techniques cannot be used to extract velocity information due to high uncertainties and low data validation rate. Therefore, autocorrelation technique was used at M_J=0.6 and 0.9. In order to evaluate the two techniques, velocity measurement at M_J=0.3 were also obtained by autocorrelation. Figure 5.7 compares velocity data obtained by both autocorrelation and crosscorrelation techniques in the case of nitrogen jets at M_J=0.3. There is agreement between the two data sets, indicating that the signal to noise ratio is acceptable when autocorrelation techniques are used. Also, it shows the experiment repeatability is good enough to allow us to perform the rest of the measurements. The following results presented are all from autocorrelation technique.

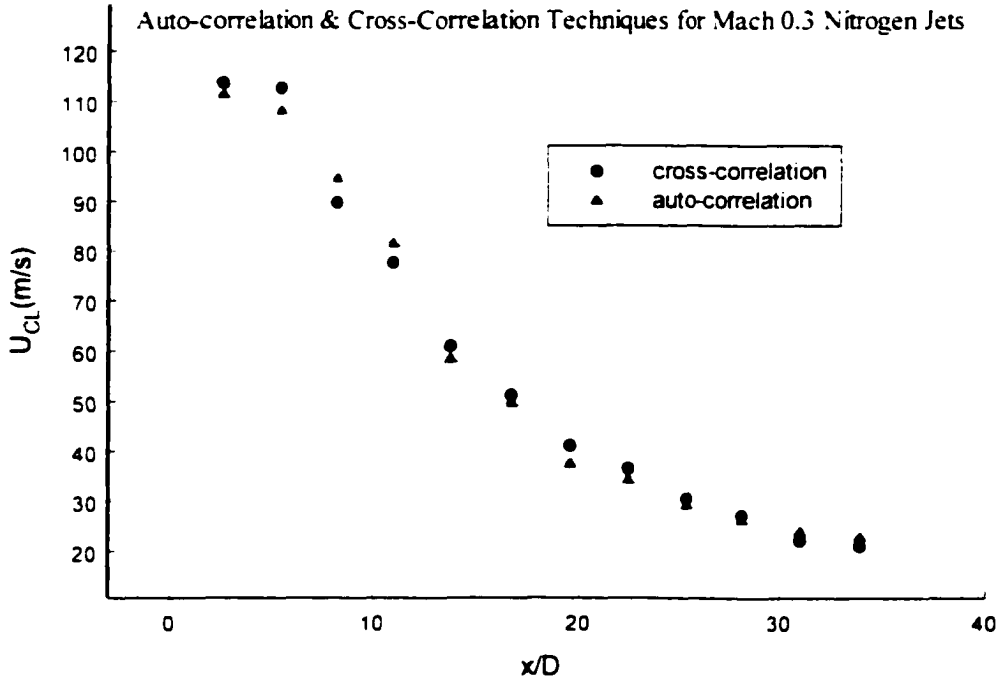

Figure 5.7: Comparison of Autocorrelation and Crosscorrelation Techniques for Mach 0.3 Nitrogen Jets

Figure 5.8 shows the velocity data along the centerline obtained by autocorrelation in the case of nitrogen jets, at three different Mach numbers. All distributions indicate flow acceleration close to the exit, which is due to viscous effects at the edges of the jet where the flow has low velocity values.

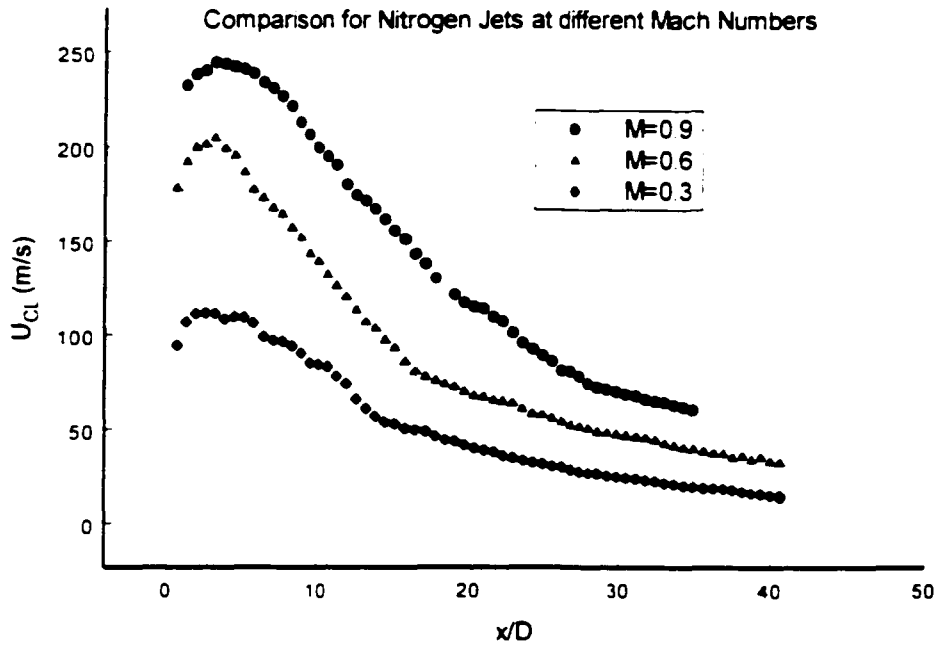

Figure 5.8: Mean Centerline Velocity Obtained by Autocorrelation for Nitrogen Jets at M_J=0.3, 0.6 & 0.9

Figure 5.9 shows the velocity distribution along the centerline of the nitrogen jet at Mach 0.3, 0.6 & 0.9, obtained by autocorrelation. The data are non-dimensionalized by the exit velocity U_J. This comparison shows that the velocity decay is faster for M_J=0.3

jets. but further analysis is needed to determine the effect of Mach number on the decay rate of subsonic jets.

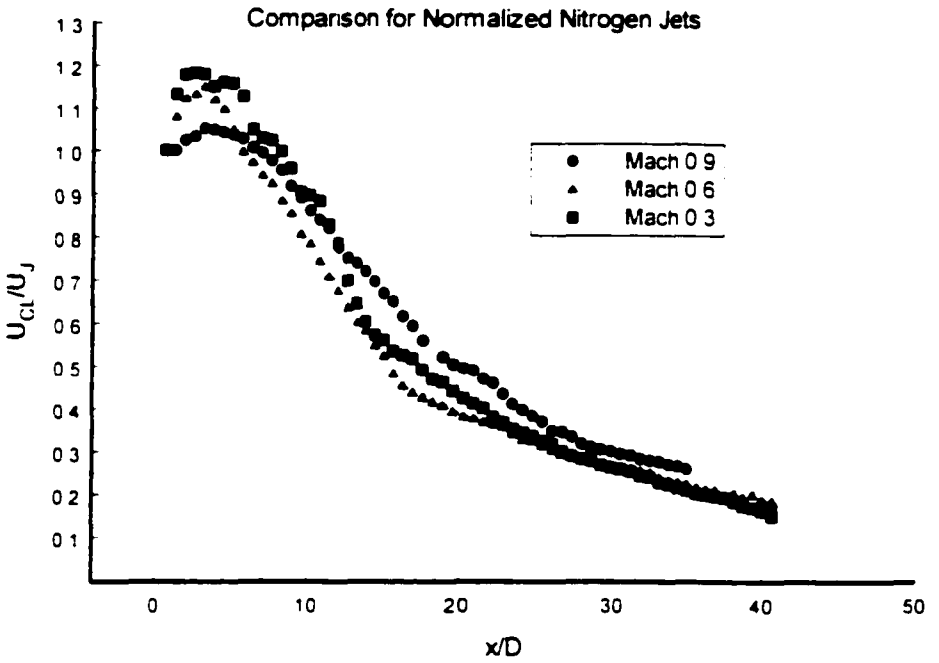

Figure 5.9: Normalized Velocity Along the Centerline of Nitrogen Jets at M_J=0.3. 0.6 & 0.9. Obtained by Autocorrelation.

To visualize the jet exit more clearly. more dense velocity vectors were extracted at this location. Figure 5.10 shows how the velocity is distributed for nitrogen jets along the centerline close to the jet exit with higher resolution. As it can be seen. the time that the velocity reaches the peak is different for these three jets. Because of the potential core

effect. usually when the jet has a higher exit velocity. the velocity peak is achieved at a further downstream location. This was verified by our experiments.

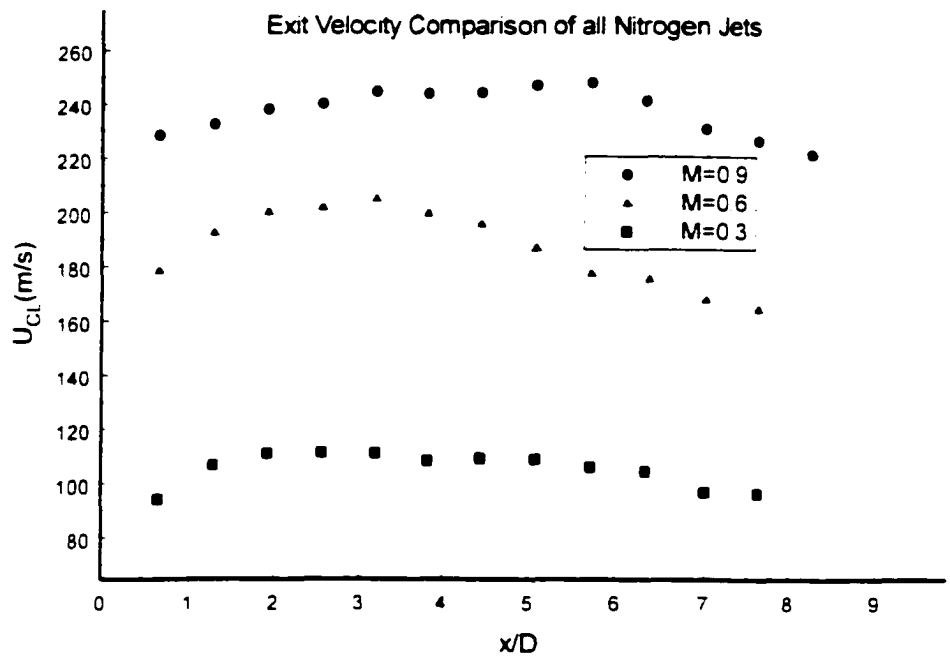

Figure 5.10: Exit Velocity Along the Centerline of Nitrogen Jets at M_J=0.3. 0.6 & 0.9

Figure 5.11 and 5.12 displayed the comparison for Mach number 0.6 and 0.9 jets respectively with previous existing data. It can be seen that the agreement was satisfactory for both exit Mach numbers. The difference at the exit is believed to be because of the exit conditions. according to Boersma & Lele [10]. The downstream difference in Figure 5.12 is mainly because of the potential core length. which in our work lasts longer.

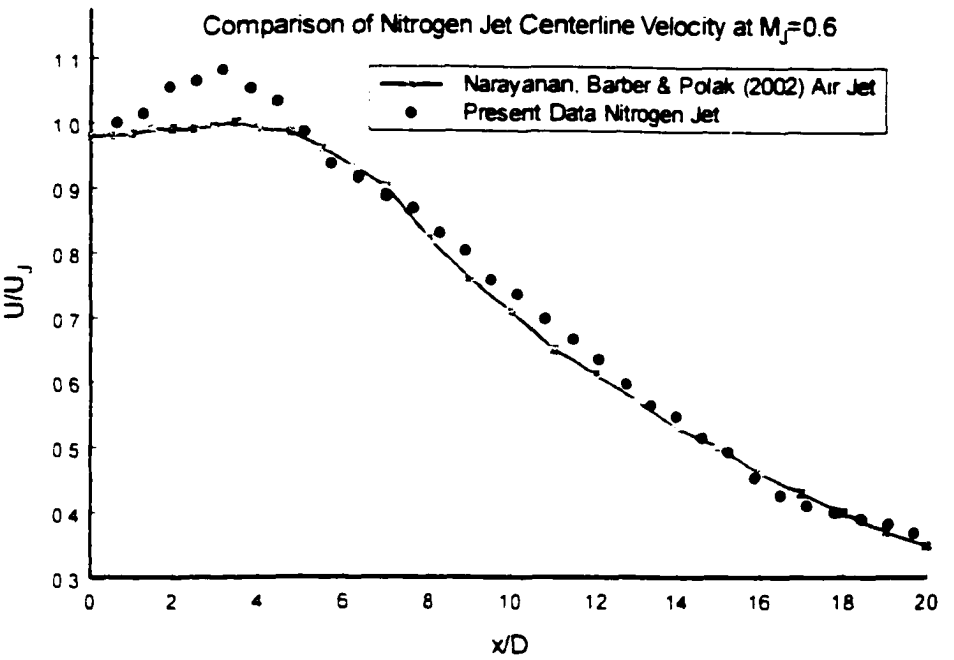

Figure 5.11: Comparison of Centerline Velocity for Nitrogen Jets at M_J=0.6

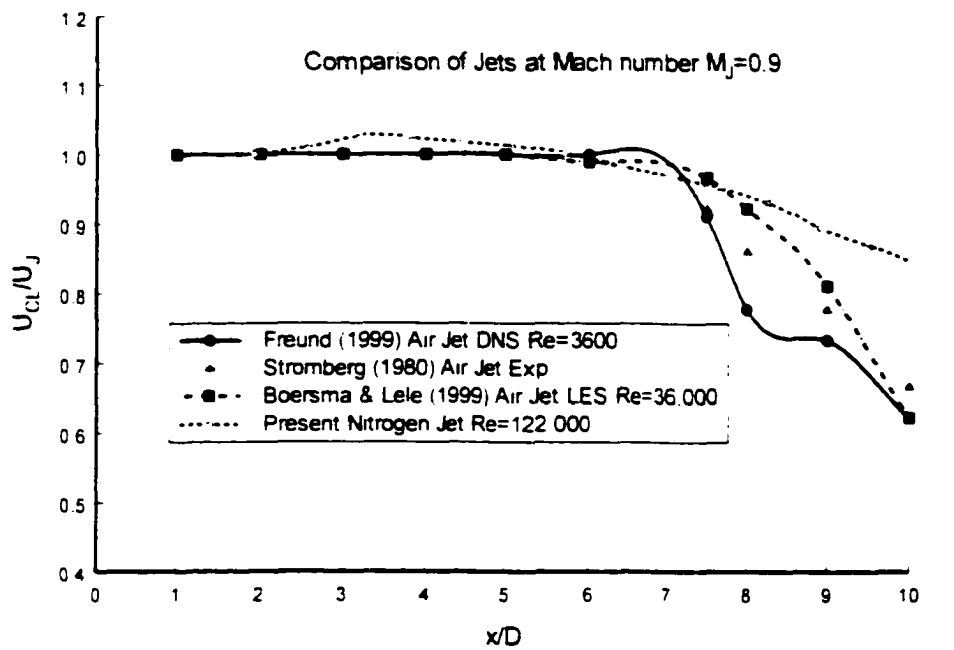

Figure 5.12: Comparison of Centerline Velocity for Nitrogen Jets at M_J=0.9

Figure 5.13 illustrates the velocity distribution along the jet centerline of a helium jet at M_J=0.3, from autocorrelation. Judging from the images taken, large amount of particles were found to be lost from one exposure to the other, which leads to a low data validation rate. This requires more image pairs for averaging.

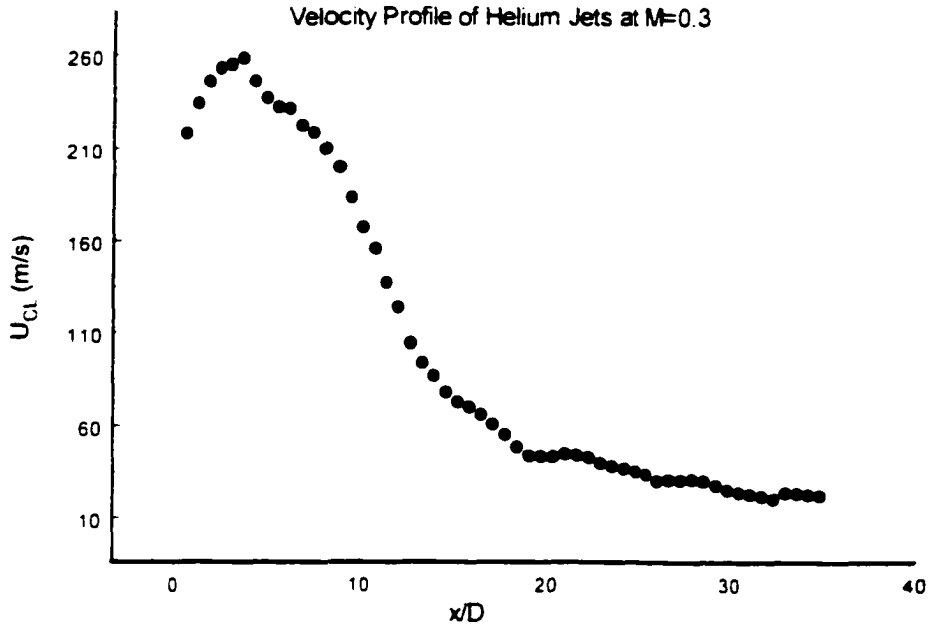

Figure 5.13: Autocorrelation of Helium Jets at M_J=0.3

For Mach 0.6 & 0.9 helium jets, the measurement was not very successful because of too much turbulence existing in this type of flow, which has very good mixing with ambient air. So the measurement technique is still under development, and the major change would be the particle size.

Figure 5.14 indicates the Autocorrelation for krypton jet at M_J=0.3. Different from nitrogen jet and helium jet, krypton jet changes in its velocity very slowly along the jet centerline, which is similar to the pressure measurement.

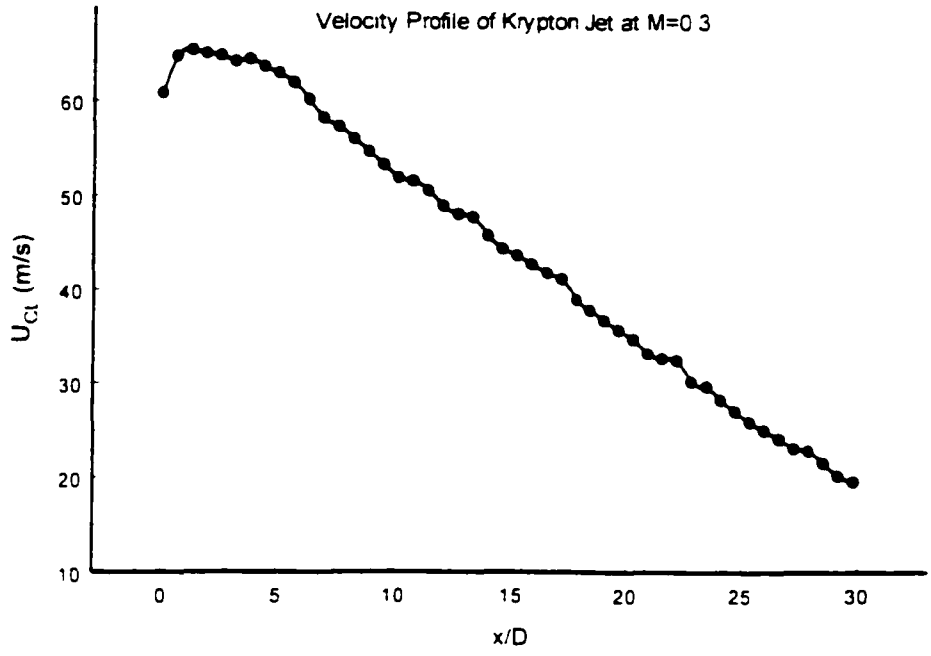

Figure 5.14: Autocorrelation of Krypton Jets at M_J=0.3

Because of the high density of this type of jets, the seeding particles follow the jet flow very well. Therefore, it is very easy to control the seeding. Also due to the very high density, there is nearly no mixing with ambient air. Thus the turbulence level is very low, which allows simple measurements.

Figure 5.15 shows a comparison of the measured centerline velocity U_{CL} in the cases of helium, nitrogen and krypton jets at Mach number 0.3. The difference of velocity values among the three data sets at locations very close to the jet exit are due to the different value of the speed of sound in each of the three gases. Further downstream, the three flows seem to have the same velocity. It can be seen that for helium jet at M_J=0.3, three different regions can be distinguished. The first region is located close to the exit where the flow accelerates. The second region is characterized by a fast decay that is indicative of intense mixing with the ambient air and the third region further downstream, which is characterized by a slow decay rate. There is also some scattering in these data, which could be a result of intense turbulence activities. The same graph also shows the decay rate of the centerline velocity data for krypton jets, indicating a linear variation with x/D, a behavior, which has also been found in the Mach number distribution along the centerline. Because of the high density of this type of jets, the seeding particles follow the jet flow very well. Therefore, it is very easy to control the seeding. Also due to the very high density difference, there is nearly no mixing with ambient air. Thus the turbulence is very low, which simplifies the effort of measuring velocity by using PIV techniques.

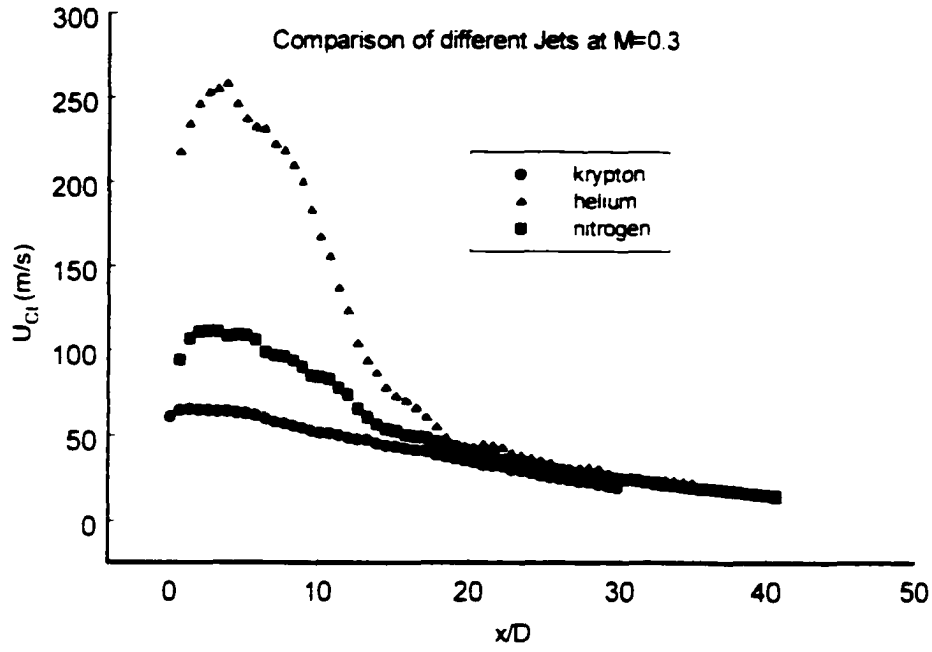

Figure 5.15: Comparison of Centerline Velocity for Different Jets at M_J=0.3.

The centerline velocity data normalized by the exit velocity U_J are shown in Figure 5.16. This graph clearly indicates the different decay rates of the three jets. Helium jets decay much faster than the other two jets. Krypton jets show the slowest decay rate.

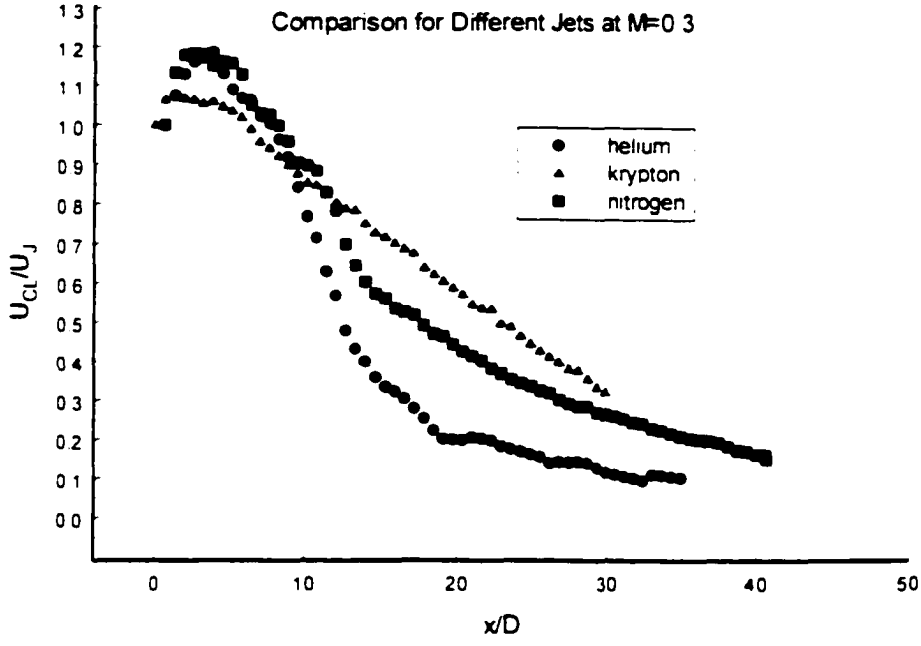

Figure 5.16: Comparison of Normalized Centerline Velocity for Different Jets at M_J=0.3.

Again, to visualize the jet exit more clearly, more dense velocity vectors were extracted. Figure 5.17 shows how the velocity is distributed along the centerline close to the jet exit with higher resolution for different jets. As can be seen, the time that the velocity reaches to the peak is different for these three jets, because of the density effect. When the jet flow has a higher density, the velocity peak is achieved closer to the jet exit.

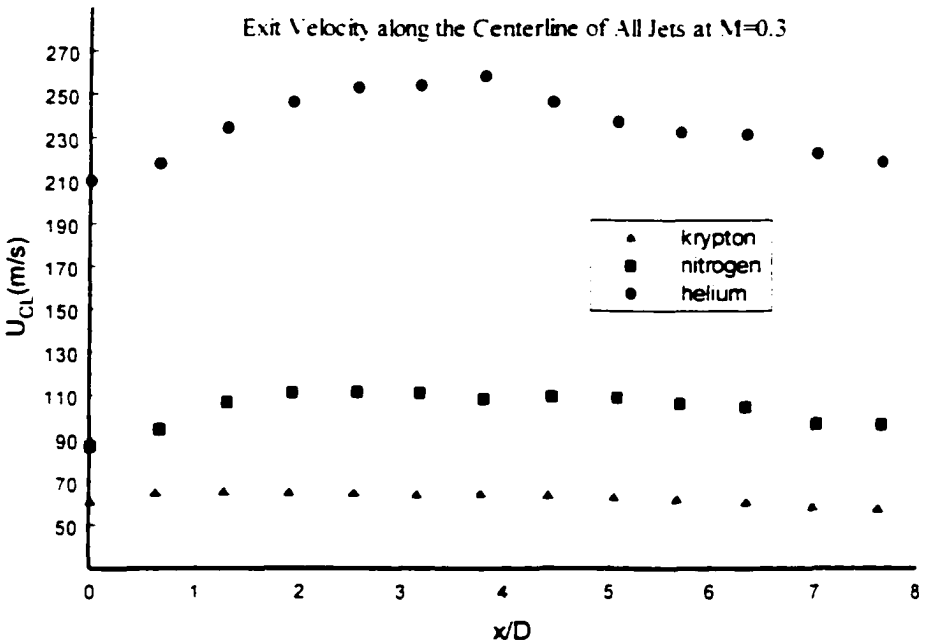

Figure 5.17: Exit Velocity Along the Centerline of All Jets at M_J=0.3

5.3 Transverse Velocity Measurement

The transverse velocity distribution was obtained by PIV measurements with other than centerline velocity information. Thanks to the PIV images, which cover a 4cm by 4cm region, we can extract transverse velocity without taking measurements again. A few transverse velocity profiles are listed here.

Figure 5.18 illustrates the velocity profile of krypton jets at M_J=0.3. It can be seen that the velocity is symmetric along the centerline of the jet (y/D=0). Gaussian distribution fitting was performed and it works well with the existing data for this type of distribution. [105]

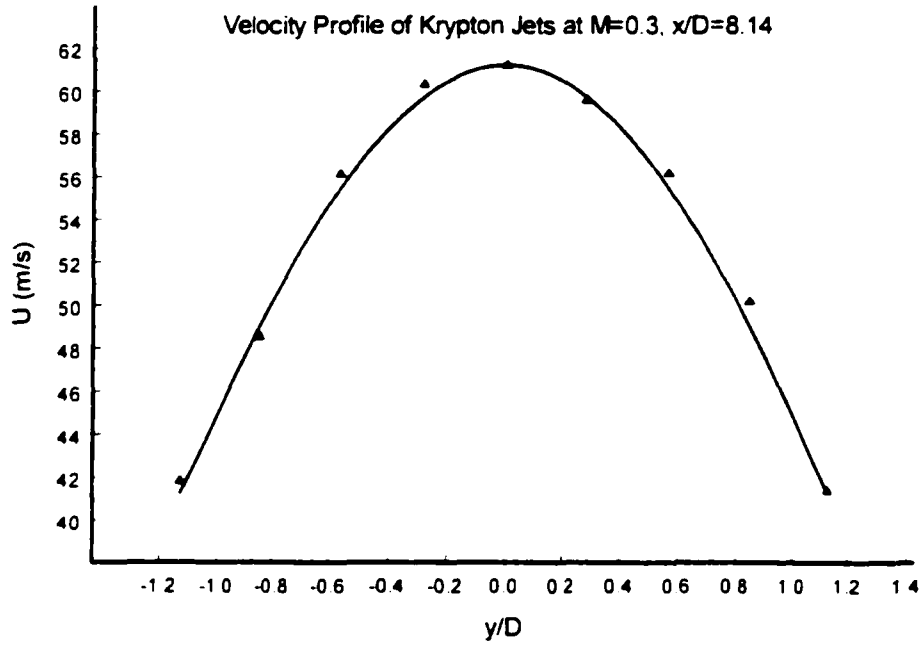

Figure 5.18: Transverse Velocity Profile of Krypton Jets at M_J=0.3

Figure 5.19 illustrates the velocity profile of helium jets at M_J=0.3. The symmetric property still exists in helium jets. But different from krypton jets, the velocity profile for helium is still developing here, therefore, the middle part has almost the same velocity. But a large velocity gradient can be seen on the edge of the profile, where the mixing happens.

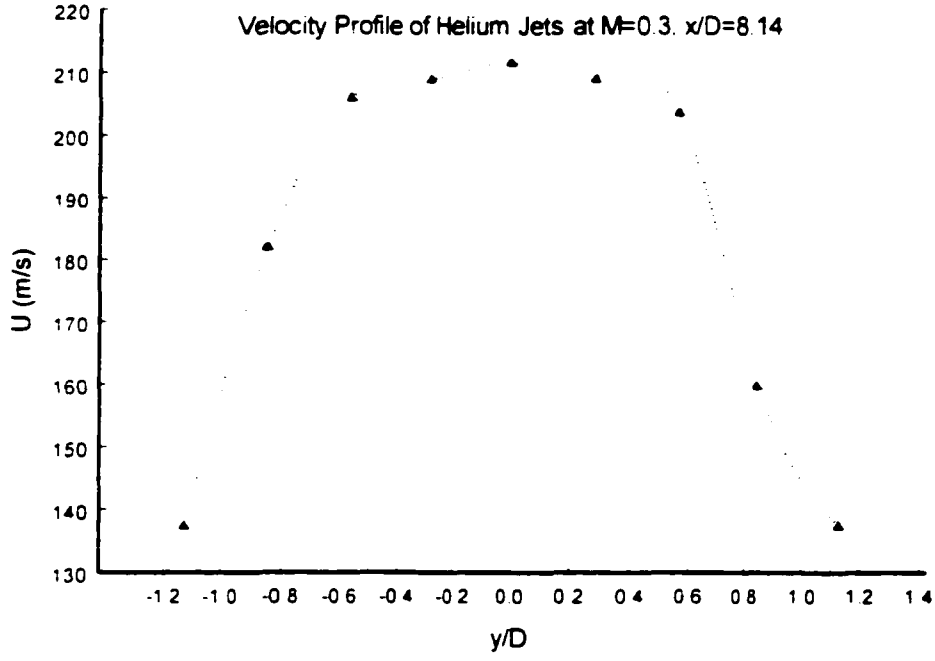

Figure 5.19: Transverse Velocity Profile of Helium Jets at M_J=0.3.

Figure 5.20 illustrates velocity profile of nitrogen jets at M_J=0.3. The shape is very similar the krypton jets. The velocity profile at this location is still developing.

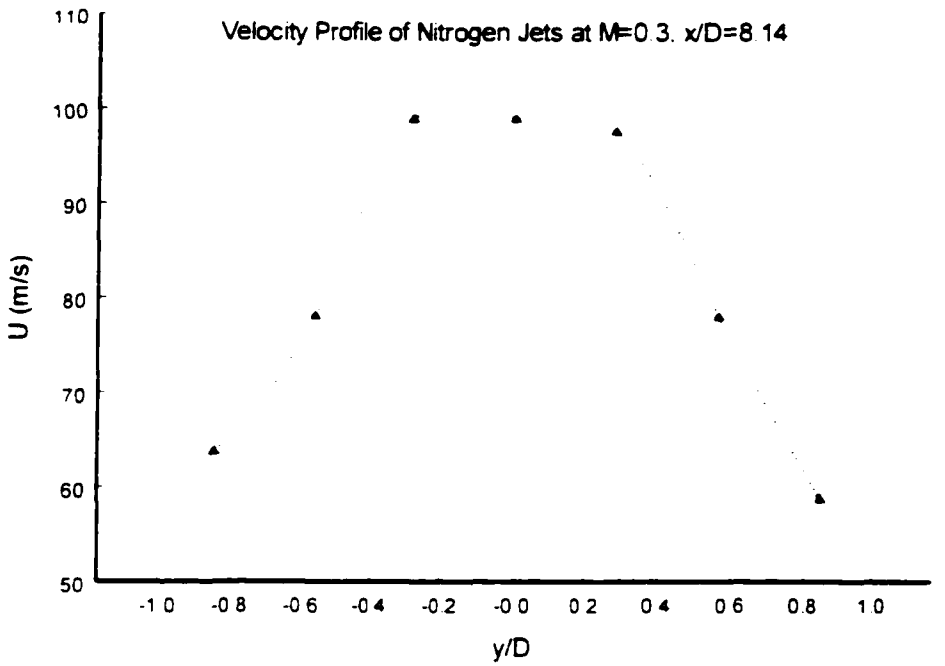

Figure 5.20: Transverse Velocity Profile of Nitrogen Jets at M_J=0.3.

5.4 Downstream Region

Axisymmetric jets have been the subjects of continuous research for several decades, and much information on the mixing characteristics of various configuration exists. The knowledge obtained from observing this basic flow has been useful in gaining insight into many engineering problems. Circular turbulent jets in particular are involved in many practical systems because of there ability to provide high mixing rates in simple and safe configurations. This far field behavior and the attainment of self-similarity has drawn much of the attention focused on jet flows recently.

As was discussed in Chapter I, for jet flows after the transition zone, the mean velocity along the axis of the jet conforms to the x^{-1}. [81] The same phenomenon was observed in our experiments, and the decay constant was calculated and compared.

Data obtained in the downstream regions of krypton jets at M_J=0.3, nitrogen jets at M_J=0.3 and M_J=0.6 are shown below. Since U_{CL} is proportional to x^{-1}, then U_{CL}/U_J must be proportional to x^{-1}. So the coefficient between these two terms are defined as decay coefficient. For instance, in Figure 5.21, the curve fitted for U_J/U_{CL} is $y=0.0711x-0.3548$, then the decay constant is $1/0.0711=14.06$. Figure 5.22, 5.23, and 5.24 listed the self-similar regions for nitrogen jets at exit Mach number M_J=0.3, 0.6, and 0.9 respectively.

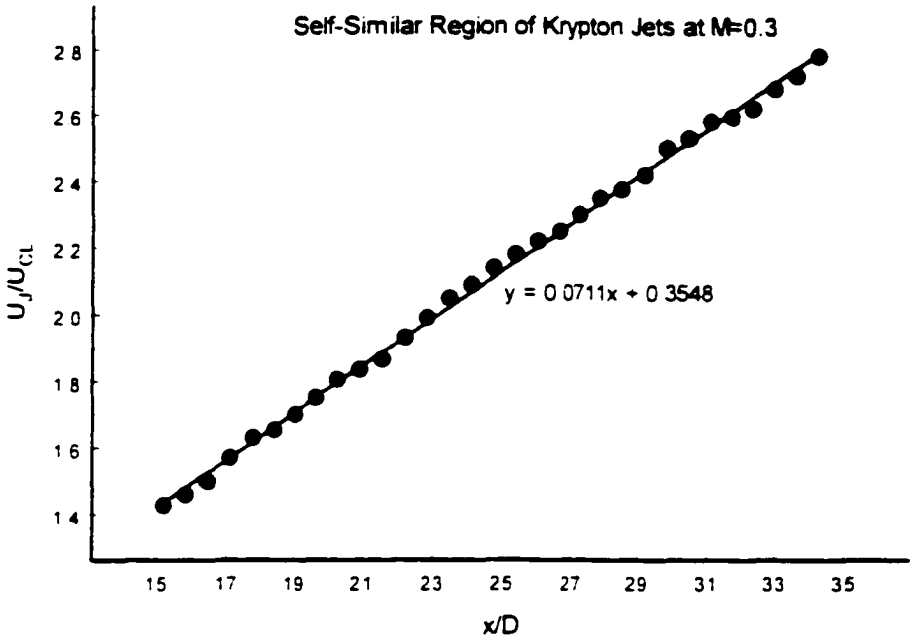

Figure 5.21: Self-Similar Region of Krypton Jets at M_J=0.3

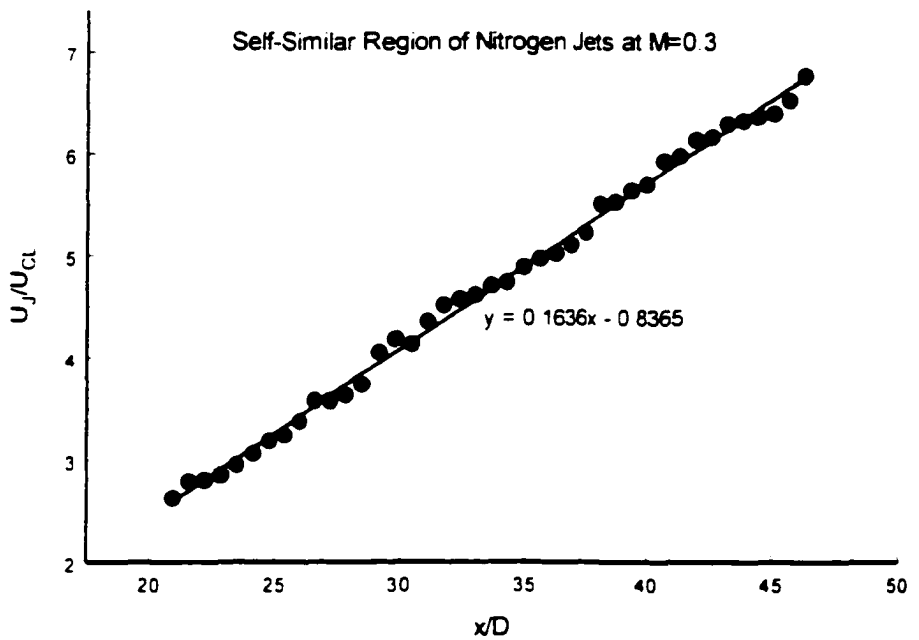

Figure 5.22: Self-Similar Region of Nitrogen Jets at M_J=0.3

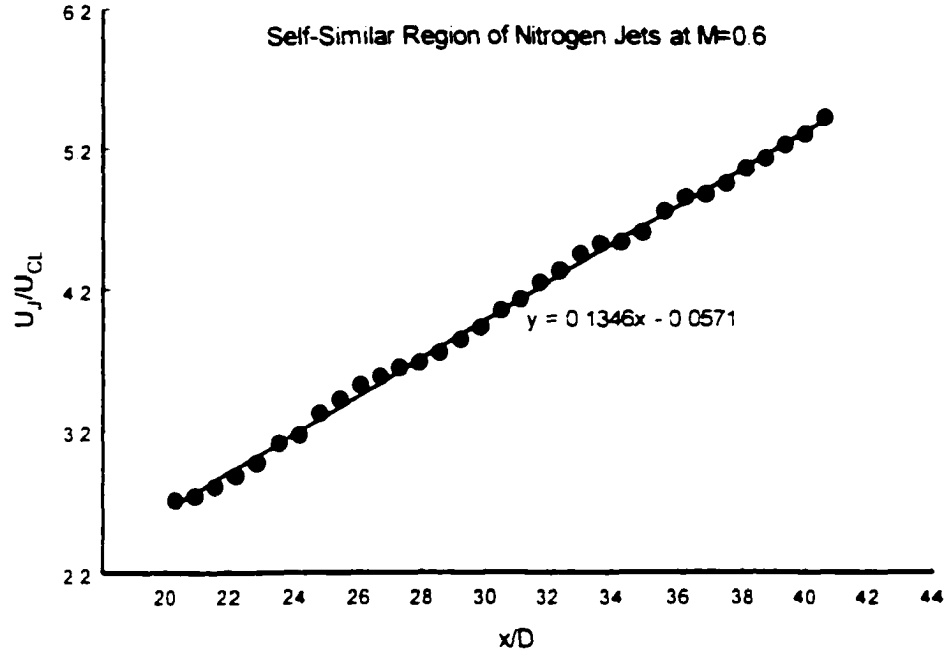

Figure 5.23: Self-Similar Region of Nitrogen Jets at M_J=0.6

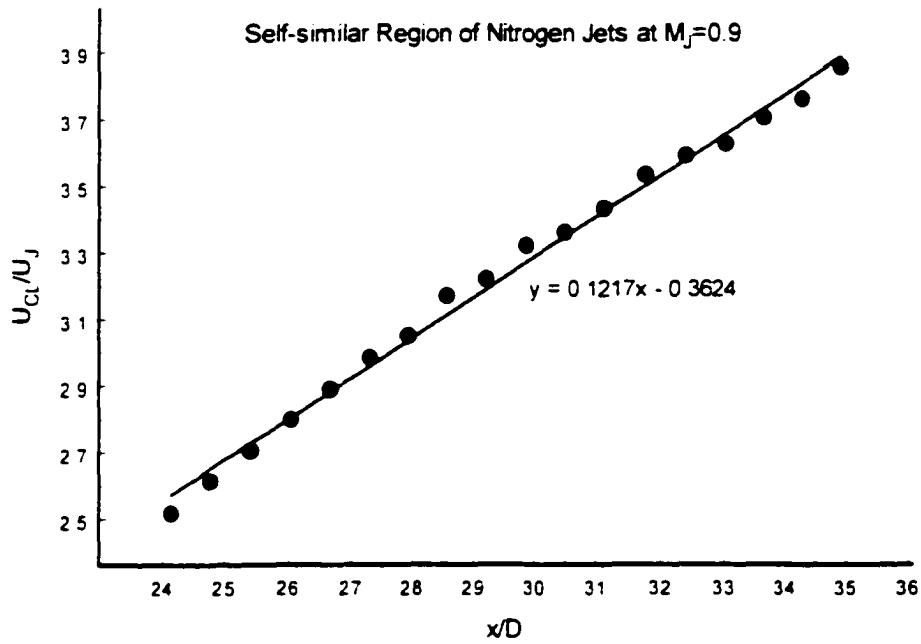

Figure 5.24: Self-Similar Region of Nitrogen Jets at M_J=0.9

The computed decay rates were calculated and compared with existing experiments. The comparison is listed in Table 5.2. Notice that, all the references that are discussed on air jets. U_J is in relation to the exit velocity and D is the diameter of the exit.

Table 5.2 Comparison of Velocity Decay Constant with References

	References					Present Results			
	W&F [102]	Rodi [81]	Capp [14]	Capp [14]	P&L [66]				
Jet Gas	Air	Air	Air	Air	Air	Krypton	Nitrogen		
Reynolds Number	~10^5	87,000	~10^5	~10^5	11,000	45,000 M_J=0.3	34,000 M_J=0.3	74,000 M_J=0.6	122,000 M_J =0.9
U_J(m s)	51	101	56	56	27	57	103	199	288
D(mm)	25.4	12.0	25.4	25.4	6.1	7.0	7.0	7.0	7.0
Method	SHW	SHW	SHW	LDA	Hotwire	PIV	PIV	PIV	PIV
Decay Constant	5.4	5.9	5.9	5.8	6.06	14.06	6.11	7.43	8.22

The decay rate for nitrogen jets at M_J=0.3 is very close to P & L [88], but as for M_J=0.6 jets, because of the compressibility effect, the constant becomes larger. The same reason applies for M_J=0.9 jets. This validates the conclusion made after the comparison of

normalized velocity for nitrogen jets at the three Mach numbers that the normalized velocity seemed to have a slower decay rate at a higher exit Mach number. For krypton jets, the constant is not in the same range, because of the extremely slow mixing with the ambient.

The comparison data mentioned above were plotted together with the existing data from references, as shown in Figure 5.25. It can be seen that the linear development regions have been reached regardless of what types of jets were used. Again, krypton jets showed a distinct velocity decay pattern. The difference seen in all the jet flows is mainly because of the jet exit condition, such as the exit diameter, gas used, and so on. The slope of each curve stands for the inverse of the decay rate, so a higher slope means a slower decay.

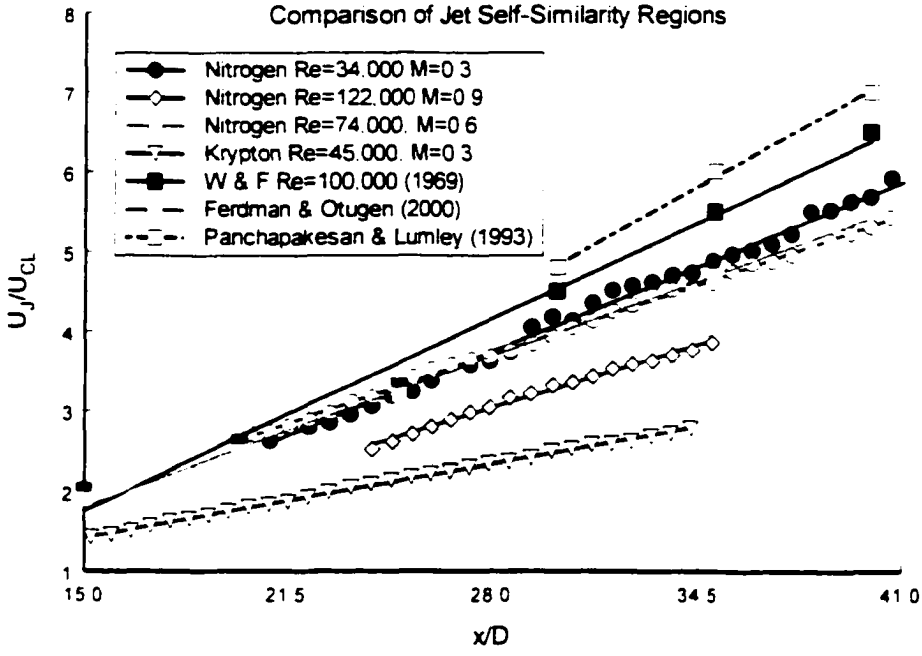

Figure 5.25: Comparison of Downstream Regions

5.5 Summary

The pressure measurement in Chapter IV, as was discussed, could not offer detailed information for velocity field. Therefore, the PIV method was used for investigating the details, without intruding in the flow field.

The results obtained with the PIV technique showed the velocity along the centerline of the jet flow and the profile in the transverse direction. The centerline velocity distribution illustrates that the velocity, similar to the results from pressure measurements, increases in the potential core, and then starts decreasing. As was discussed in previous Chapter, this increase is due to the reduction of the cross section of the potential core. The peak velocity for nitrogen gas being issued into the ambient air was shown to take place at different locations, depending on the exit Mach number. When the exit Mach number was higher, the peak was observed further downstream, which indicates that the potential core lasts longer. After the potential core, as velocity decays, it can be seen that the decay rate D_r varies with the corresponding exit Mach number. The decay rate is higher when the exit Mach number is higher, i.e. for nitrogen jet flow running at three exit Mach numbers, the decay rate was found to be the highest in the case of the Mach number M_j=0.9 jet. Again the Mach number effect then was verified to exist by velocity measurement.

Velocity was also compared for different gases being issued into still air at the same exit Mach number. The velocity decay rate was also found to be varying with the gases used. In the case of the helium jet, the decay rate was found to be much higher than the other two cases. This indicates better mixing with the ambient air. Density effect is the cause for the great difference.

The transverse PIV measurement offered three profiles of velocity for nitrogen jets, krypton jets, and helium jets. The location off the jet exit was chosen to be x/D=8.14. The profiles showed firstly that the circular jet flow is axisymmetric. Secondly the edge of each profile (the corresponding location for the jet flows is also on the edge), showed great velocity gradients compared to the center portion in the case of the helium jets, meaning that the helium jets had better mixing with the ambient. Physically, the change was due to the viscous effect from the free interface where the jet flow edge is located. Lastly, the shape of the profile illustrates the flow property at that chosen x/D location. The shape of the krypton profile was observed to be like a bell shape, or Gaussian distribution. From the incompressible jet theory [94], incompressible jets reach this shape or reach to self-similar state after a distance of 8 diameters of flow development. Thus it seemed that the krypton jets have reached such state because the velocity is self-preserving, and it might be treated as an incompressible fluid flow. For helium and nitrogen jets, it can be seen that at this chosen location, the jet flow is still developing. So it could be concluded that the density effect does exist.

Self-similar region was found for krypton jets running at M_J =0.3, nitrogen jets running at M_J =0.3, 0.6, and 0.9 respectively. Krypton jets were found to reach such state the earliest. They were followed by the M_J=0.3 jets and M_J=0.6 jets. There seemed to be a transition from incompressible flow to compressible flow for this starting point of the self-similar region. Thus the Mach number effects are responsible for the difference. The self-similar region was not found for helium jets within 40 times of the jet diameter. [67] So it can be concluded that the density ratio affects the jet decay in its self-similar region. The decay constants for velocity in the self-similar region were found and compared to some existing references. The results for krypton jets were found to have big gap from air jets due to the fact of its incompressible properties.

PIV measurements were also attempted in the helium and krypton. Due to restricted availability of krypton gas, only data for exit Mach number 0.3 are presented. The lack of high rate of validated data led to a poor quality images. In the case of helium jets at exit Mach number 0.6 and 0.9. It appears that the reason for this behavior is the high velocity fluctuations which are present in the mixing zone close to the exit, which drive the particles away from the illumination plane.

Our last discussion addresses the PIV technique, which has been used for a decade. But due to the difficulties of seeding and laser illuminating, this technology used to be limited to low speed flows. These difficulties were conquered by the TSI PIV system, which allows the Mach number to be more than 4.0 and the velocity to be more than 1500m/s [30]. The use of PIV in our experiment is a successful example. The

comparison between the two types of correlation techniques and the comparison between the PIV measurement and Pitot tube measurement have fully proved these conclusions.

Chapter VI. Results from Total Temperature Measurement

Thermocouple was used to measure total temperature distribution of three different turbulent jets running at 0.3, 0.6, and 0.9. As introduced before, J type thermocouple with diameter 0.25mm was used in the experiments, because this thermocouple has high frequency response and thus is suitable for turbulent jet temperature measurement.

6.1 Thermocouple Calibration

Before the thermocouple was put to use, calibration was performed in order to extract correct total temperature information. Table 6.1 lists the calibration temperature and the corresponding signal output from computer.

Table 6.1 Thermocouple Calibration Data

	Gain	Filename	Mean Signal	Temperature (°C)
Ice	1000	ICE	-4512.87	0.4
Room	1000	ROOM	-3144	22.0
Boiling	1000	BOILING	1644.69	99.2

Assume there is linear relation between total temperature and the signal output,

$$T_0 = aV + b \qquad (6.1)$$

where T_0 is the total temperature, while V is the signal output from computer. a and b are constants that need to be calibrated. Figure 6.1 shows the least square fitting for total temperature T_0 and signal output V.

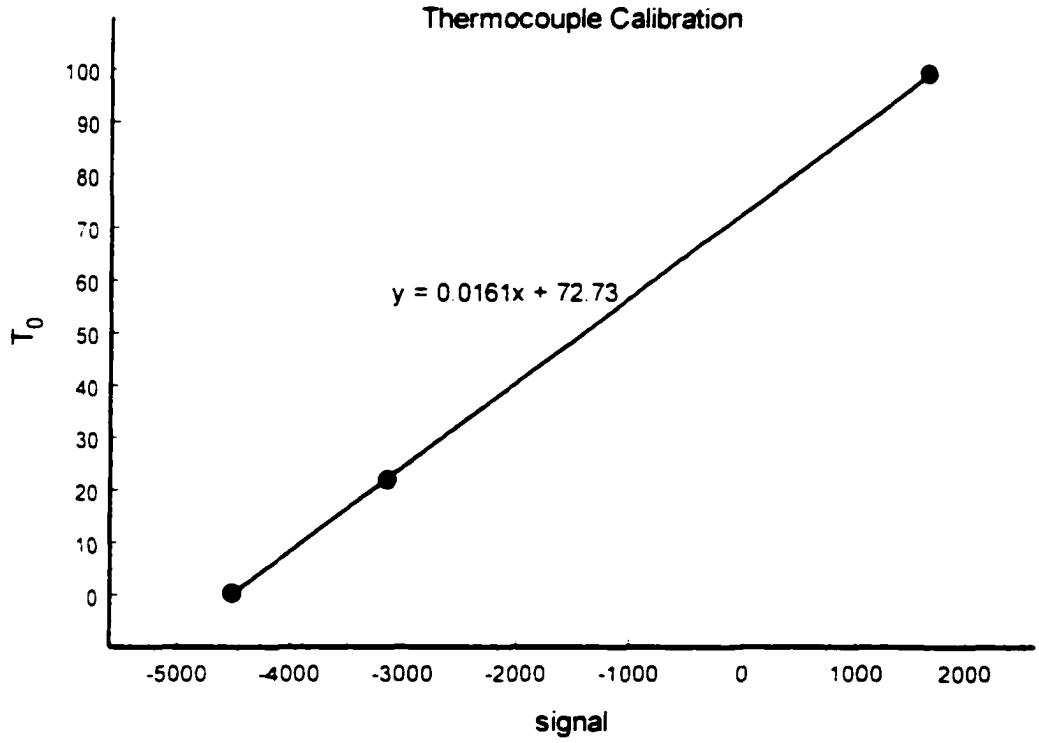

Figure 6.1: Thermocouple Calibration

It can be seen from the picture that the relation for temperature and signal is perfectly linear. The corresponding coefficients a and b were found to be.

$$a=0.161,\ b=72.73$$

So the relation between temperature and voltage output is.

$$T_0 = 0.161V + 72.73$$

From the experiments, we can obtain the voltage output information for each individual experiment, then the corresponding temperature is extracted.

The sampling frequency used was 50K Hz; the amplifier gain was 1000; and the sample size was 80K.

6.2 Centerline Temperature Measurement

Temperature measurements were taken along the centerline of nitrogen jets at M_J= 0.3, 0.6, and 0.9; krypton jets at M_J= 0.3; helium jets at 0.3, 0.6, and 0.9 respectively.

Figure 6.2 illustrates centerline temperature of nitrogen jets at Mach number 0.3. Total temperature and static temperature has large difference close to the jet exit because of the potential core, inside which the velocity is very high. It can be seen that the total temperature overall is steady, close to ambient temperature (24°C).

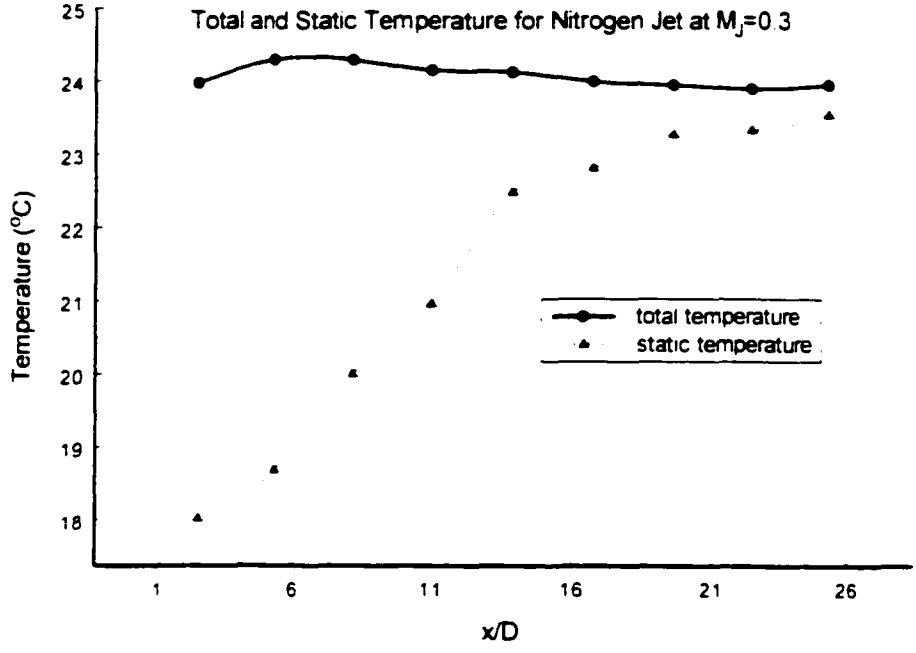

Figure 6.2: Centerline Temperature Of Nitrogen Jets At Mach 0.3

Figure 6.3 illustrates the centerline total temperature of krypton jets at M_J=0.3. It can be seen that the temperature is almost constant throughout all the locations measured. It is believed that because of the low mixing with ambient air, total temperature does not have a difference from the ambient temperature.

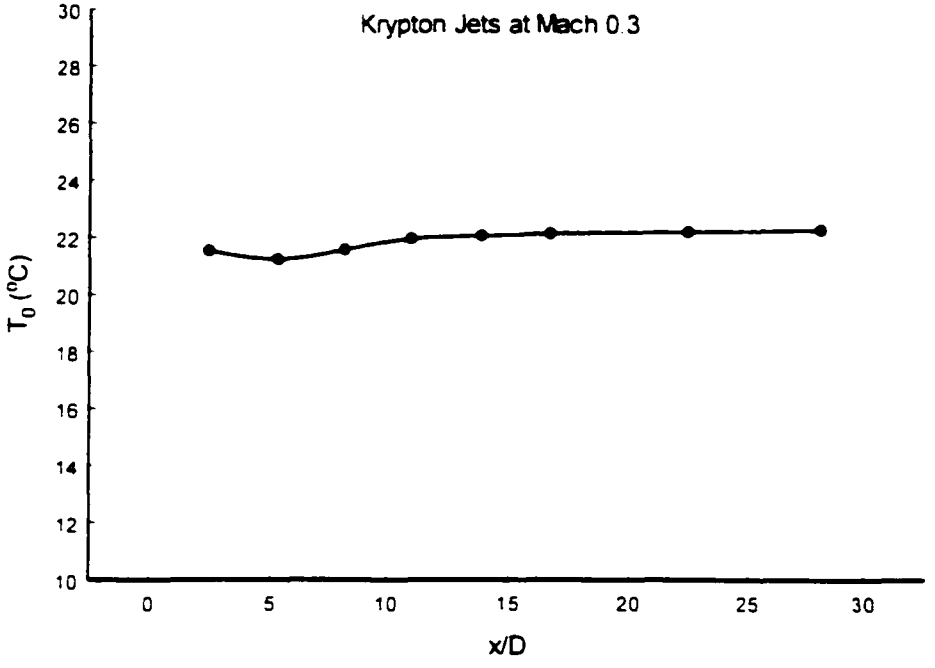

Figure 6.3: Centerline Total Temperature Distribution Of Krypton Jets At M_J=0.3

Figure 6.4 and 6.5 illustrates centerline temperature of nitrogen jets at exit Mach number 0.6 and 0.9. Because of extremely high velocity at the jet exit, the total temperature and static temperature have the larger gap near to the jet exit compared to the M_J=0.3 jets. The static temperature right out of the jet exit for M_J=0.9 jet has a temperature below the freezing point.

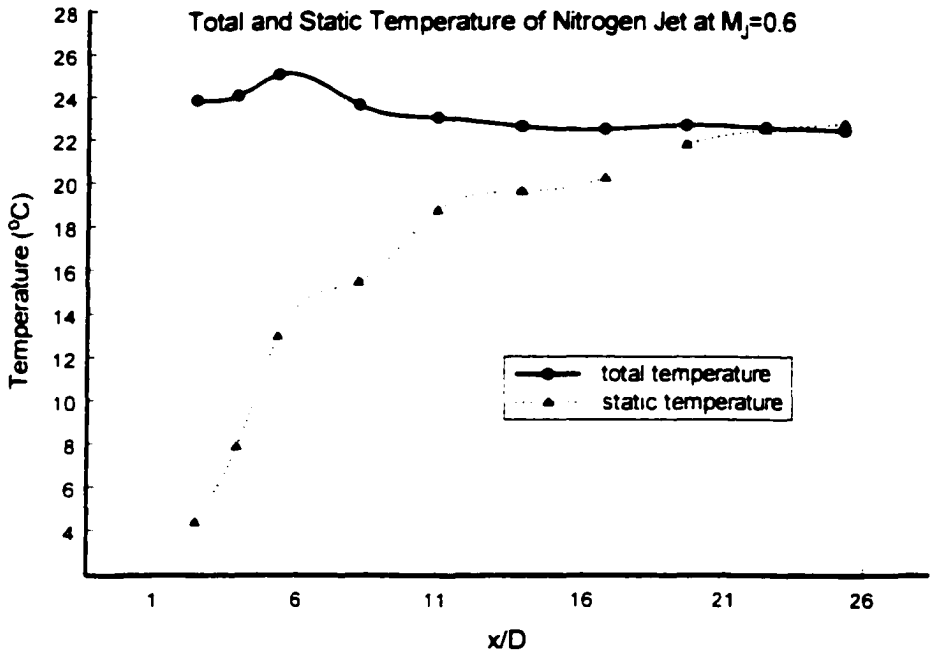

Figure 6.4: Centerline Temperature Of Nitrogen Jets At Mach 0.6

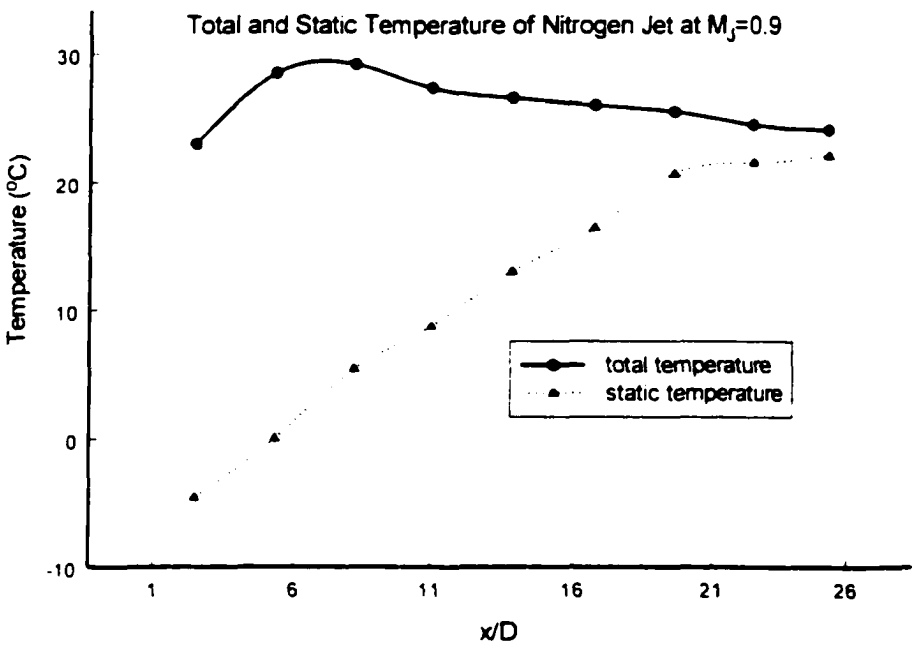

Figure 6.5: Centerline Temperature Of Nitrogen Jets At Mach 0.9

Figure 6.6 displays the static temperature for nitrogen jets at different Mach numbers. The temperature level recovers to ambient temperature after a certain distance for each jet. Mach 0.9 jet is found to have the largest slope.

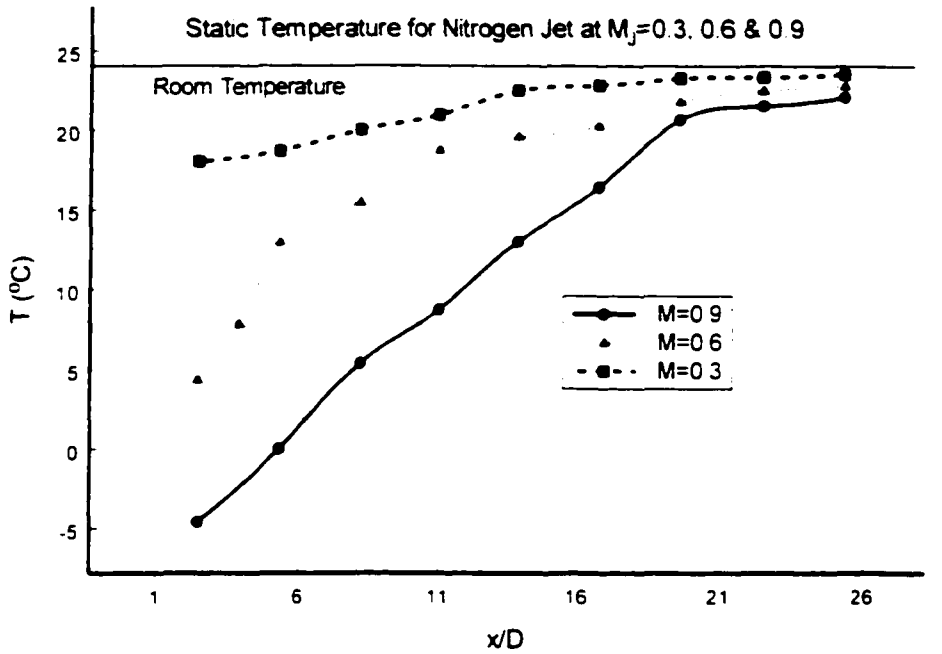

Figure 6.6: Comparison Of Static Temperature Measurement For Nitrogen Jets At Different Mach Number

Figure 6.7 illustrates the centerline total temperature of Helium jets at M_J=0.3, 0.6, and 0.9. It can be seen that the total temperature increases first then decreases. This total temperature increase is believed to happen because of the heat exchange with the ambient air and will be explained later in this section.

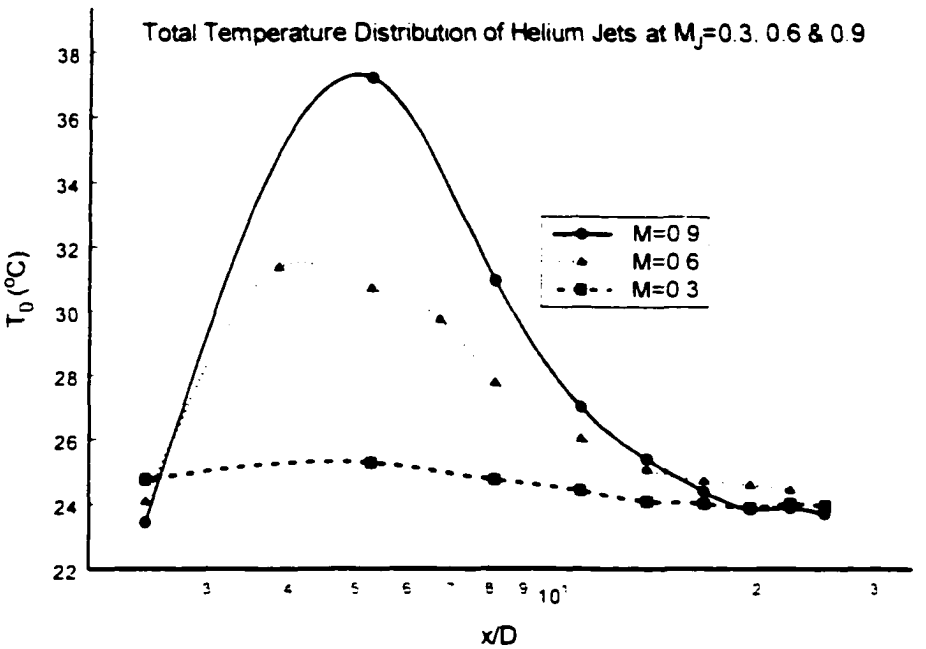

Figure 6.7: Centerline Total Temperature Distribution Of Helium Jets At M_J=0.3, 0.6, And 0.9

6.3 Transverse Temperature Measurement

Having known the pressure along the centerline, it will be helpful if the transverse temperature profile is obtained. Figure 6.8 indicates the transverse temperature distribution for helium jets. It can be seen from Figure 6.8 that the temperature is the highest in the centerline of the jet flow due to the highest velocity at the centerline. On both edges of the jet flow, the mixing lowered down the temperature. Across the jet flow edge, the temperature is recovering to ambient temperature, and so it is shown in the transverse direction that the temperature is increasing.

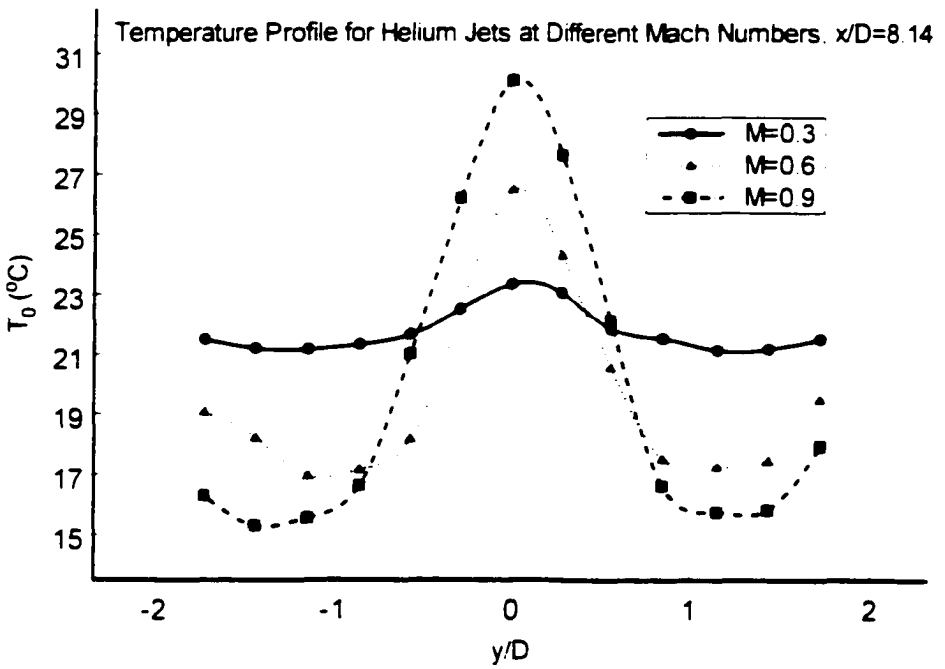

Figure 6.8: Temperature Profile For Helium Jet At Different Mach Numbers, X/D=8.14

Figure 6.9 shows the transverse temperature distribution for nitrogen jets. Similar phenomenon was found for the temperature distribution. The total temperature at the centerline has the maximum value, then it decreases to a point below ambient temperature where the distance off the centerline becomes larger. When this distance becomes large enough, the temperature rises to approach the ambient temperature.

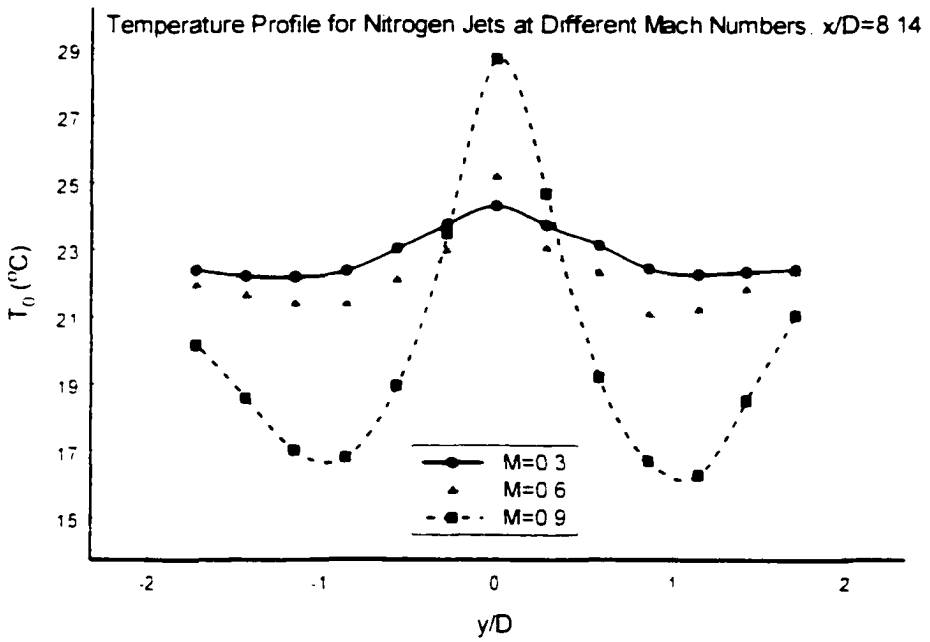

Figure 6.9: Temperature Profile For Nitrogen Jets At Different Mach Numbers.

X D=8.14

The explanation to the temperature change is as follows.

The jet flow from the gas tank is expanding inside the insulated jet pipe from the same ambient temperature T_0 which is kept as a constant during the adiabatic process until the

gas is injected into the still air. The relation between total temperature and static temperature for isentropic flows is

$$T = T_0 - \frac{V^2}{2C_p} \qquad (6.2)$$

where T is static temperature: T_0 is total temperature: V is the velocity and C_p is the heat capacity, which is treated as a constant.

It can be seen that if velocity is high, then the corresponding static temperature T is low. In the case of helium jets running at exit Mach number 0.9, the static temperature is 67°C below the ambient temperature. Thus after the jet flow is running inside the still air, there is a temperature gradient from the ambient to the inside of the jet flow. Such gradient will result in a temperature change. Recall equation (1.2.4) and rewrite,

$$\frac{DT}{Dt} = \frac{1}{\rho C_p}\frac{Dp}{Dt} - \frac{k}{\rho C_p}\frac{\partial}{\partial x}\left(\frac{\partial T}{\partial x}\right) + \frac{d_{..}}{\rho C_p}\frac{\partial u}{\partial x}$$

It can be seen clearly that a negative temperature gradient along the transverse direction will increase the jet flow energy and bring up the static temperature. Thus the total temperature will rise above the ambient temperature. This explained why the temperature level was seen to increase without being heated. The different rise in total temperature can be explained by the diffusivity $\frac{k}{\rho C_p}$ and temperature gradient $\frac{\partial T}{\partial x}$.

According to equation (1.2.4) on page 9, larger diffusivity or larger temperature gradient can cause a higher temperature change. Helium has the maximum diffusivity of the three

gases. moreover. the static temperature gradient from the ambient to the jet flow is the largest in this case. therefore. the maximum temperature change was found in the helium jets running at M_J=0.9.

The heat transfer between the ambient air and the jet flow. is shown in Figure 6.9. The static temperature is below ambient temperature. which is the reason for heat exchange to happen between the ambient air and jet flows. Such heat exchange will lead to a lower total temperature on the ambient air as it loses energy. therefore. one part between the center of the jet flow and the edge of the jet flow has seen to have a lower temperature despite the kinetic temperature generated by the velocity.

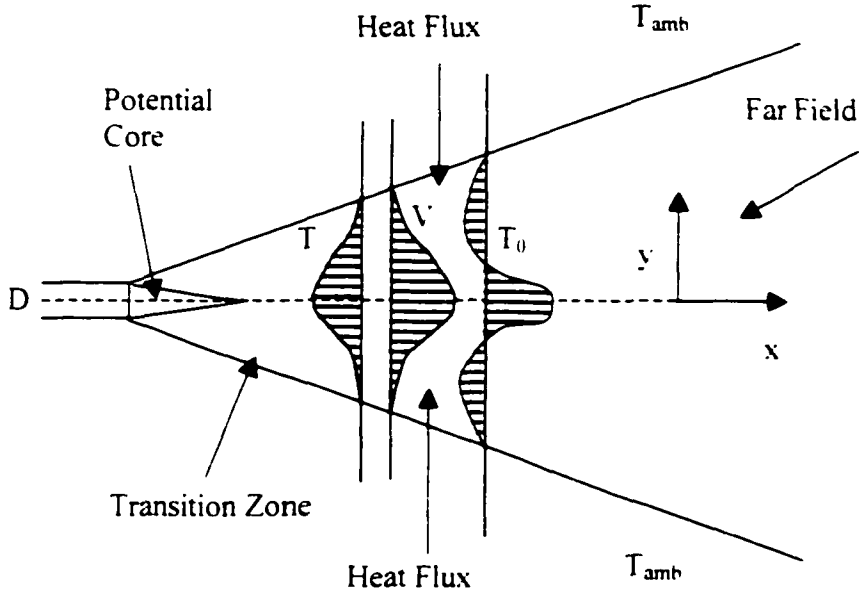

Figure 6.10: Schematic Heat Transfer Between Jet Flow And Ambient Air

6.4 Summary

Total temperature measurements were performed originally for the purpose of finding out the concentration distribution in the cases of helium and krypton gases used in the experiments. It was shown later that the temperature information itself could explain a few phenomena of the jet flows.

The total temperature consists of two components, the static temperature and kinetic temperature from the kinetic energy part. Whichever component's change will result in a corresponding change for the total temperature. For this reason, it was seen in the potential core, the temperature increases with velocity increasing, the same as the results from the pressure measurements. It is interesting to check the effect from the jet mixing with the ambient air. Starting from the centerline, the total temperature is higher because of the high velocity, no mixing is in this region; however, going out of the potential core towards the jet flow edge, the total temperature decreases due to the change in velocity as the jet flow is mixing with ambient, which results in a decrease in the total temperature. At a later stage, the total temperature out of the jet flow is rising to ambient temperature.

Static temperature was calculated from the total temperature for nitrogen jets by equation (1.2.7) by utilizing the Mach number results from total pressure measurements. The results showed that the static temperature downstream is increasing to the ambient temperature.

Chapter VII. Obtaining Other Parameters

In the last three Chapters, the total pressure, total temperature, and velocity information was obtained directly by experiments. The results explained most of the jet flows and the turbulence involved. However, some other parameters, such as concentration, Mach number, and density, which cannot be measured directly, are also important parameters of jet flows.

7.1 Formulate Concentration

As it was discussed in Chapter IV Total Pressure measurement, if the jet flow is different from the ambient, then it is impossible to extract the Mach number from the total pressure information due only to the uncertain properties of the mixture. Therefore, more measurements on total temperature (Chapter VI) and velocity (Chapter VII) were taken in order to resolve the mixture uncertainty.

Assume that we have the instantaneous total pressure P_0, total temperature T_0, and velocity V for any fixed measurement point, then concentration x, Mach number M, and

density ρ can be developed by the relations in Chapter I. To clarify this, some necessary equations are brought in from Chapter I as follows.

$$C_p T + \frac{V^2}{2} = const \qquad (1.2.7a)$$

$$h + \frac{V^2}{2} = h_0 = C_p T_0 = \frac{a_0^2}{\gamma - 1} = \frac{\gamma}{\gamma - 1}\frac{p_0}{\rho_0} = \frac{\gamma}{\gamma - 1} R T_0 \qquad (1.2.8)$$

$$\frac{T_0}{T} = 1 + \frac{\gamma - 1}{2}\frac{V^2}{\gamma RT} = 1 + \frac{\gamma - 1}{2} M^2 \qquad (1.2.11)$$

$$\frac{p_0}{p} = \left(\frac{T_0}{T}\right)^{\frac{\gamma}{\gamma - 1}} \text{ and } \frac{\rho_0}{\rho} = \left(\frac{T_0}{T}\right)^{\frac{1}{\gamma - 1}} . \qquad (1.2.12)$$

$$\frac{p_0}{p} = \left(1 + \frac{\gamma - 1}{2} M^2\right)^{\frac{\gamma}{\gamma - 1}} \qquad (1.2.13)$$

$$\frac{\rho_0}{\rho} = \left(1 + \frac{\gamma - 1}{2} M^2\right)^{\frac{1}{\gamma - 1}} \qquad (1.2.14)$$

Combining equations (1.2.7a) and (1.2.8), the relation between total temperature and static temperature is obtained.

$$C_p T + \frac{V^2}{2} = C_p T_0 \qquad (7.1)$$

So static temperature, based on total temperature and velocity is derived as follows.

$$T = T_0 - \frac{V^2}{2C_p} \qquad (7.2)$$

Thus equation (1.2.12) can be expressed by three parameters P_0, T_0, and V, which were obtained from experiments.

$$\frac{P_0}{P} = \left(\frac{T_0}{T}\right)^{\frac{\gamma}{\gamma-1}} = \left(\frac{T_0}{T_0 - \frac{V^2}{2C_p}}\right)^{\frac{\gamma}{\gamma-1}} \tag{7.3}$$

where P_0, T_0, and V can be measured, while P is the static pressure, equivalent to the ambient pressure. So from equation (7.3), if C_p was known, then γ could be derived, and vice versa. Unfortunately, none is available because both parameters depend on the mixture. However, if one relation can be found between these two parameters, then it will be easy to find out both the heat capacity C_p and the gas constant γ.

Since both C_p and γ depend on the mole fraction of gases in the mixture, for example, in case of the helium jet issuing into air, assume that the mole fraction is c, then both C_p and γ are defined as follows.

$$\gamma = c \cdot \gamma_H + (1-c) \cdot \gamma_a \tag{7.4}$$

$$C_p = c \cdot C_{pH} + (1-c) \cdot C_{pa} \tag{7.5}$$

where,

γ_H is the gas constant for helium; γ_a is the gas constant of air; C_{pH} is the heat capacity for helium, and C_{pa} is the heat capacity for air. They are all constants and available on any thermodynamics reference book.

If equation (7.4) and (7.5) are substituted into equation (7.3), then the concentration c is formulated. To find the concentration, a program is needed to let c go from 0 to 1. If any value of c satisfies the equation (7.3), then the concentration is determined. Appendix IV has the program for concentration calculation.

Once concentration is defined, the static temperature can be derived from equation (7.2).

$$T = T_0 - \frac{V^2}{2C_p} \qquad (7.2)$$

With

$$\frac{p_0}{p} = (1 + \frac{\gamma - 1}{2} M^2)^{\frac{\gamma}{\gamma - 1}} \qquad (1.2.13)$$

The Mach number can be calculated.

$$M = \sqrt{\frac{2}{\gamma - 1}[(\frac{P_0}{P})^{\frac{\gamma - 1}{\gamma}} - 1]} \qquad (7.6)$$

The density can be calculated by

$$\rho = \frac{P}{RT} \qquad (7.7)$$

where,

$$R = c \cdot R_H + (1 - c) \cdot R_a \qquad (7.8)$$

with R_H being the specific gas constant for helium, while R_a being the specific gas constant for air.

The total density is obtained by

$$\frac{\rho_0}{\rho} = \left[1 + \frac{\gamma - 1}{2} M^2\right]^{\frac{1}{\gamma - 1}} \qquad (1.2.14)$$

All the above parameters were programmed in Appendix D.

For krypton jets, if γ_H : C_{pH} , and R_H are replaced by γ_K : C_{pK} , and R_K respectively, then the concentration, Mach number, static density and total density also become available. Furthermore, this method can be used for any jet flow.

Discussion

As mentioned before, the formulas developed rely on the condition that all the parameters, P_0, T_0, and V can be measured instantaneously. However, it is impossible to take all the measurements together for everything, as they will interfere with each other. By applying the mean values obtained by experimental data in equation (7.3), (7.4), (7.5), the mean concentration can be calculated as follows.

$$\frac{\overline{P_0}}{P} = \left(\frac{\overline{T_0}}{T}\right)^{\frac{\gamma}{\gamma-1}} = \left(\frac{\overline{T_0}}{\overline{T_0} - \frac{\overline{V}^2}{2C_p}}\right)^{\frac{\gamma}{\gamma-1}} \tag{7.9}$$

$$\gamma = \overline{\overline{c}} \cdot \gamma_H + \left(1 - \overline{\overline{c}}\right) \cdot \gamma_a \tag{7.10}$$

$$C_p = \overline{\overline{c}} \cdot C_{pH} + \left(1 - \overline{\overline{c}}\right) \cdot C_{pa} \tag{7.11}$$

The Symbol $\overline{\overline{c}}$ is used here to show the difference from the real mean concentration $\overline{c}$ which should be obtained through each individual concentration. The difference between $\overline{\overline{c}}$ and $\overline{c}$ is calculation error, and will be further discussed in Chapter VIII.

7.2 Results for Concentration, Density, and Mach number

With the program developed in previous section, centerline concentration, density, and Mach number were obtained for krypton jets at M=0.3.

Figure 7.1 displays the centerline concentration distribution of krypton jets at 0.3. It can be seen that close to the jet exit, there is potential core, so the concentration does not change by much and so on. While after that, the concentration decays very quickly.

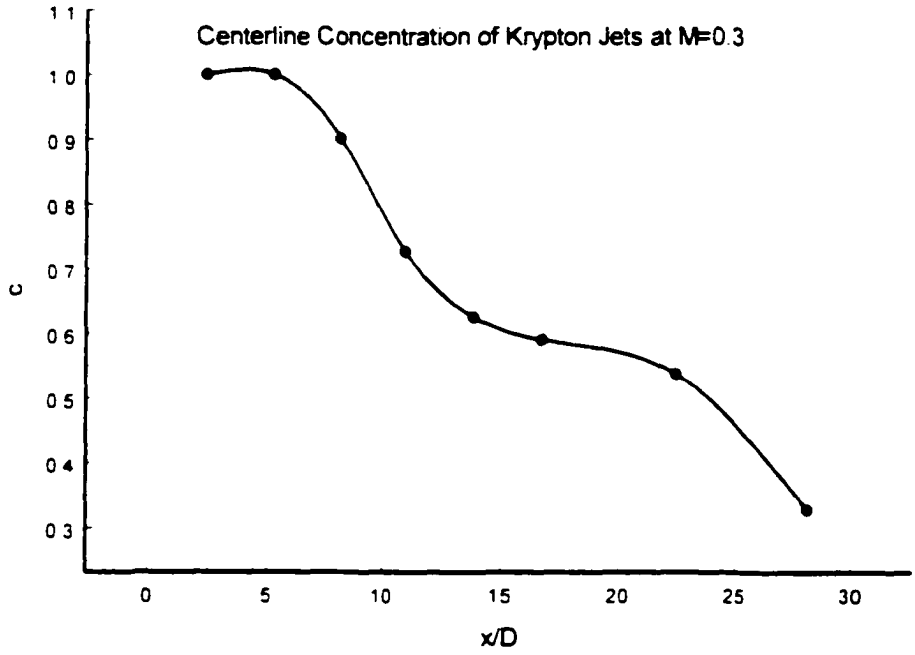

Figure 7.1: Centerline Concentration Distribution of Krypton Jets at M=0.3

Figure 7.2 shows the Centerline Mach number distribution. and it was compared with the Mach number from total pressure P_0. It can be seen that there is good agreement between the method introduced above and the estimated Mach number.

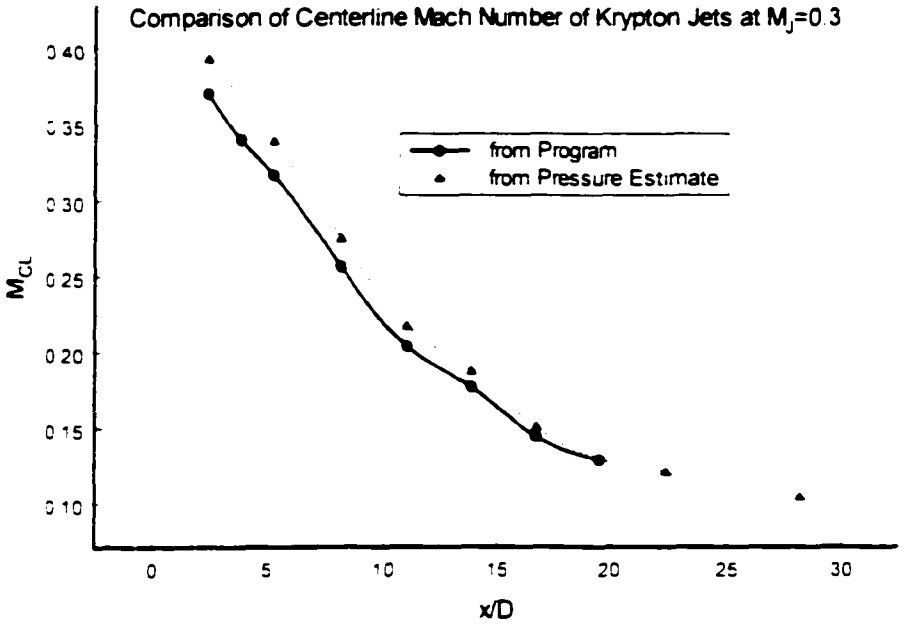

Figure 7.2: Centerline Mach Distribution of Krypton Jets at M=0.3

Figure 7.3 indicates the Centerline Density Distribution. It can be seen that within the potential core, the density does not vary by much, while beyond that, it decreases rapidly to ambient unlike in helium jets.

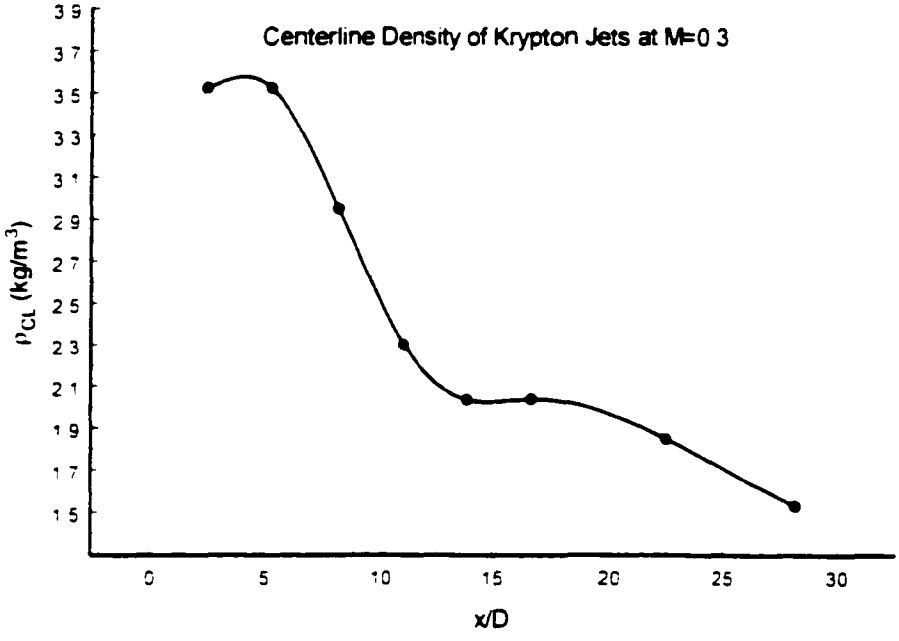

Figure 7.3: Centerline Density Distribution of Krypton Jets at M=0.3

Figure 7.4 shows the static temperature distribution.

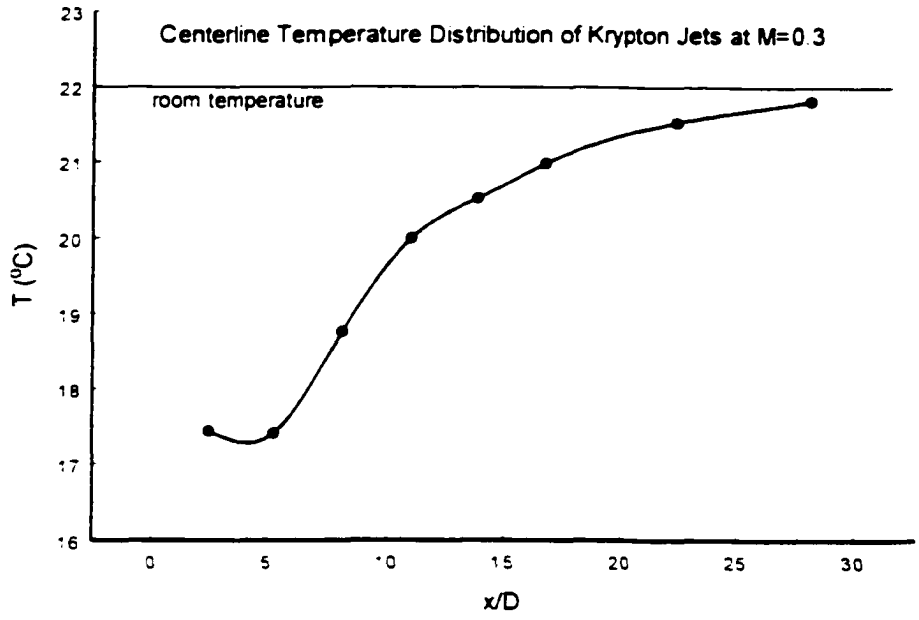

Figure 7.4: Centerline Temperature Distribution of Krypton Jets at M=0.3

The following results are from helium jet flows. The results were obtained as before by programming, based on the three measured quantities, total pressure, total temperature, and velocity.

Figure 7.5 displays the centerline concentration distribution of helium jets. It can be seen that close to the jet exit, there is potential core, so the concentration does not change too much. While after that, the concentration decays very quickly.

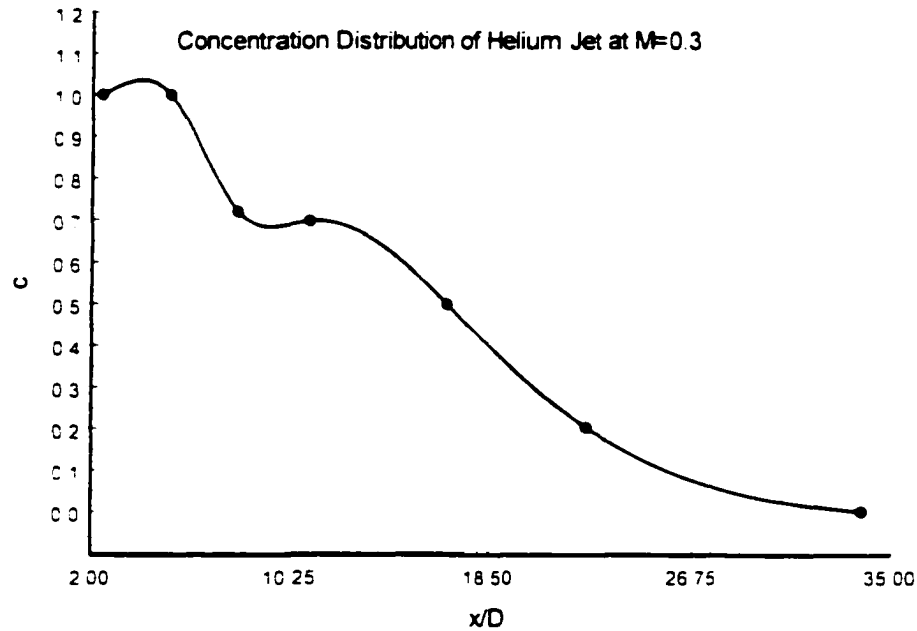

Figure 7.5: Centerline Concentration Distribution of Helium Jets at M=0.3

Figure 7.6 shows the Centerline Mach number Distribution and it was compared to the Mach number obtained by a total pressure estimate. It can be seen that the centerline Mach number has good agreement at the jet exit. But at downstream, because of the mixing, the pressure estimate does not provide correct information. Figure 7.7 indicates the Centerline Density Distribution. It can be seen that within the potential core, the density does not vary too much, while after that, it increases rapidly to ambient.

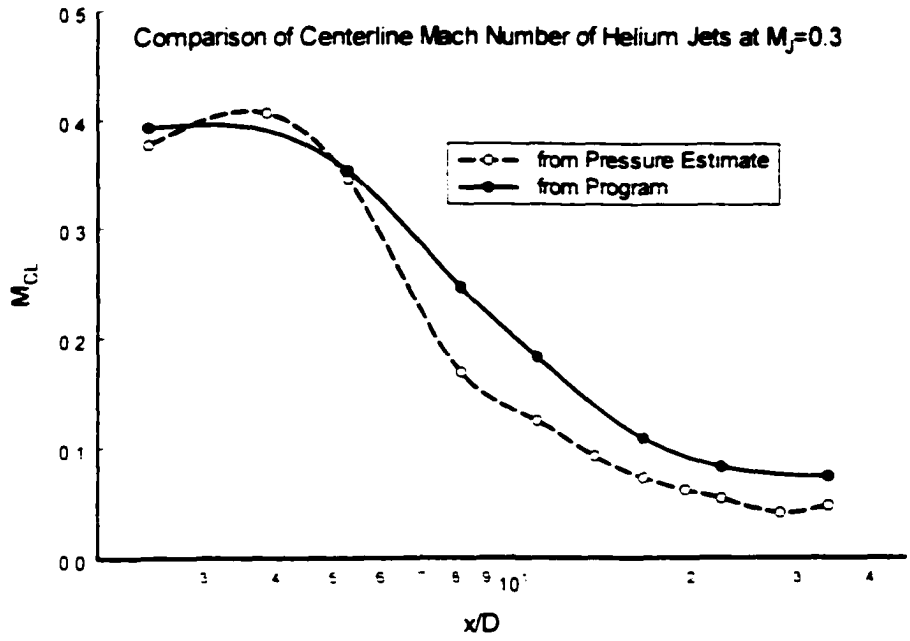

Figure 7.6: Centerline Mach Distribution of Helium Jets at M=0.3

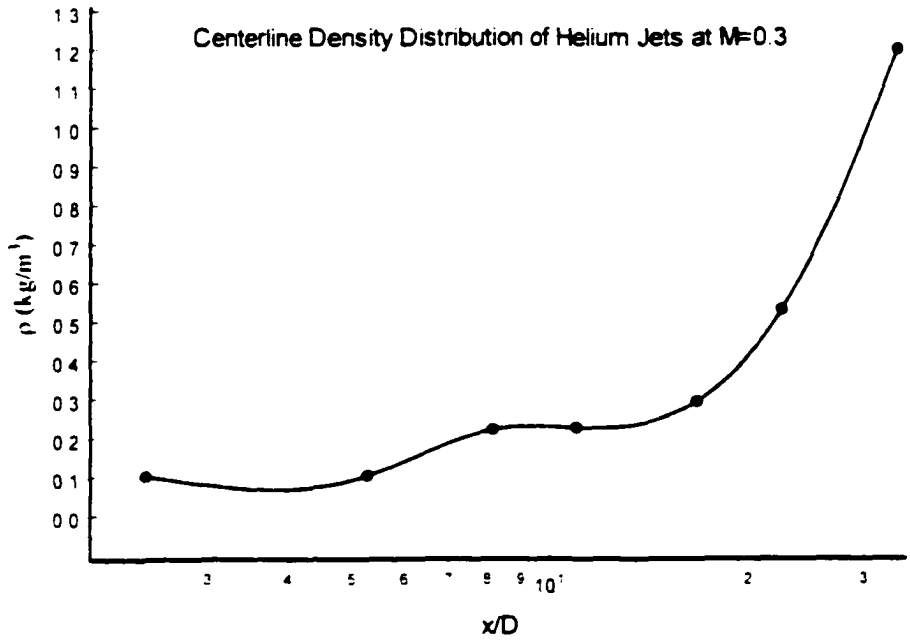

Figure 7.7: Centerline Density Distribution of Helium Jets at M=0.3

Summary

The method uses three measured quantities, the total pressure, total temperature, and velocity to find out the rest of the parameters including concentration and so on to our interest. This requires all the measurement techniques to be accurate, so that the accumulated error associated with the concentration will not have a large impact on the results. The results from concentration calculation showed that the concentration inside the potential core keeps a constant value of 1, then it starts decaying at a certain point. The concentration decay rate for helium is also faster than that of krypton. At a distance of x/D=35 for helium jets, the concentration is close to 0, which means the helium spreads out quickly. In conclusion, the method gives reasonable results for concentration.

In order to validate all the previous experiments, Energy Balance was achieved with all the quantities obtained by means of experiments and formulas. (Refer to Appendix V)

Chapter VIII. Error Analysis

In Chapter IV. the following equation was used to calculate the mean Mach number for nitrogen jets. because the gas constant $\gamma = 1.4$ stays the same throughout the entire flow field.

$$\frac{P_0}{P} = (1 + \frac{\gamma - 1}{2} M^2)^{\frac{\gamma}{\gamma - 1}} \qquad (1.2.13)$$

Where. P is static pressure. which is also ambient pressure. therefore.

$$P = 14.7 \text{ psi}$$

P_0 is total pressure. measured by the pressure transducer. Consider turbulence.

$$P_0 = \overline{P_0} + P_0'$$

Where. $\overline{P_0}$ is the mean total pressure. while P_0' is the turbulence or total pressure fluctuation. Mach number can be calculated from equation (1.2.13) based on the total pressure signal. Thus mean Mach number is available. which is $\overline{M}$. However. because of turbulence. P_0 might go less than ambient pressure. then it is impossible to find out the Mach number based with the above equation. Fortunately we can always find out $\overline{P_0}$. and through the given relation between P_0 and M to calculate the corresponding Mach number. We call it $\overline{\overline{M}}$. which is the mean Mach number that is obtained by applying mean total pressure $\overline{P_0}$ (refer to Chapter IV).

$$\overline{\overline{M}} = \sqrt{\frac{2}{\gamma - 1}\left[\left(\frac{\overline{P_0}}{P}\right)^{\frac{\gamma-1}{\gamma}} - 1\right]}$$

The difference between $\overline{\overline{M}}$ and $\overline{M}$ is the calculation error since we are using $\overline{\overline{M}}$ instead of $\overline{M}$.

Another source of Mach number error comes from the measuring system as uncertainty. such as the transducer itself. the data acquisition board. and the software resolution.

8.1 Error analysis for mean Mach Number Obtained through equation

$$\frac{P_0}{P} = \left(1 + \frac{\gamma - 1}{2} M^2\right)^{\frac{\gamma}{\gamma-1}} \qquad (1.2.13)$$

- **Uncertainty**

Rewrite the given equation (1.2.13):

$$\ln\frac{P_0}{P} = \frac{\gamma}{\gamma - 1}\ln\left(1 + \frac{\gamma - 1}{2} M^2\right) \qquad (8.1.1)$$

or

$$\ln P_0 - \ln P = \frac{\gamma}{\gamma - 1}\ln\left(1 + \frac{\gamma - 1}{2} M^2\right) \qquad (8.1.2)$$

Differentiate Eq. (8.1.2)

$$\frac{\delta P_0}{P_0} = \frac{\gamma}{\gamma - 1} \frac{\frac{\gamma - 1}{2} \cdot 2M \cdot \delta M}{1 + \frac{\gamma - 1}{2} \cdot M^2}$$

$$\frac{\delta P_0}{P_0} = \frac{\gamma \cdot M \cdot \delta M}{1 + \frac{\gamma - 1}{2} \cdot M^2}$$

Then $$\frac{\delta M}{M} = \frac{1}{\gamma} \cdot \left(\frac{1}{M^2} + \frac{\gamma - 1}{2} \right) \frac{\delta P_0}{P_0} \qquad (8.1.3)$$

Apply $\gamma = 1.4$ into Eq (8.1.3), then

$$\frac{\delta M}{M} = \left(\frac{1}{1.4M^2} + \frac{1}{7} \right) \frac{\delta P_0}{P_0} \qquad (8.1.4)$$

$\frac{\delta P_0}{P_0}$ is the uncertainty from the measuring system including the pressure transducer, data acquisition board, and amplifier. Each uncertainty was given by the manufacturer. Pressure transducer has an uncertainty u_1=0.5%, data acquisition board has an uncertainty u_2=10/2^{14}=0.06%, the amplifier has a much lower uncertainty u_3= 0.01%. So overall,

$$\frac{\delta P_0}{P_0} = \sqrt{u_1^2 + u_2^2 + u_3^2} = \sqrt{0.005^2 + 0.0006^2 + 0.0001^2} \approx 0.5\%$$

Table 8.1 lists the uncertainties at different Mach numbers based on this assumption.

Table 8.1 Uncertainties at Different Mach Numbers

M	0.3	0.4	0.5	0.6	0.7	0.8	0.9	1.0
$\frac{\delta M}{M}$ (%)	4.03	2.30	1.50	1.06	0.80	0.63	0.51	0.43

It can be seen that the larger the Mach number is, the more accuracy is expected. The uncertainties showed here are in a reasonable range.

Calculation Error

As it was explained in the beginning of this Chapter, the calculation error is shown because ofthe calculation method used. The following equation was used to calculate the mean Mach number which was supposed to be obtained from the Mach number signal.

$$\frac{p_0}{p} = (1 + \frac{\gamma - 1}{2} M^2)^{\frac{\gamma}{\gamma - 1}} \qquad (1.2.13)$$

The calculation error is analyzed by rewriting the above equation

$$M = \sqrt{\frac{\gamma - 1}{2}\left[\left(\frac{P_0}{P}\right)^{\frac{\gamma-1}{\gamma}} - 1\right]} = f(P_0) \qquad (8.1.5)$$

As we know P_0 varies slightly against $\overline{P_0}$, which is the mean value of total pressure.

Assume that

$$\frac{P_0 - \overline{P_0}}{\overline{P_0}} << 1$$

then we can expand $f(P_0)$ at $\overline{P_0}$ with Taylor expansion as follows.

$$f(P_0) = f(\overline{P_0}) + f'(P_0)_{\overline{P}} \cdot (P_0 - \overline{P_0}) + \frac{1}{2} f''(P_0)_{\overline{P}} (P_0 - \overline{P_0})^2 + ... \qquad (8.1.6)$$

This formula can be applied to each individual P_0 obtained by pressure transducer so we have.

$$f(P_{01}) = f(\overline{P_0}) + f'(P_0)|_{\overline{P_0}} \cdot (P_{01} - \overline{P_0}) + \frac{1}{2} f''(P_0)|_{\overline{P_0}} (P_{01} - \overline{P_0})^2$$

$$f(P_{02}) = f(\overline{P_0}) + f'(P_0)|_{\overline{P_0}} \cdot (P_{02} - \overline{P_0}) + \frac{1}{2} f''(P_0)|_{\overline{P_0}} (P_{02} - \overline{P_0})^2$$

.....

$$f(P_{0n}) = f(\overline{P_0}) + f'(P_0)|_{\overline{P_0}} \cdot (P_{0n} - \overline{P_0}) + \frac{1}{2} f''(P_0)|_{\overline{P_0}} (P_{0n} - \overline{P_0})^2$$

Sum up all the samples and then divide by N.

$$\frac{f(P_{01}) + f(P_{02}) + \ldots + f(P_{0n})}{N} = f(\overline{P_0}) + f'(P_0)|_{\overline{P_0}} \cdot \frac{1}{N} \sum_{i=1}^{N} (P_{0i} - \overline{P_0})$$

$$+ \frac{1}{2} f''(P_0)|_{\overline{P_0}} \cdot \frac{1}{N} \sum_{i=1}^{N} (P_{0i} - \overline{P_0})^2 + \ldots$$

Notice $M = f(P_0)$, so the above formula yields.

$$\overline{M} = \overline{\overline{M}} + f'(P_0)|_{\overline{P_0}} \cdot \frac{1}{N} \sum_{i=1}^{N} (P_{0i} - \overline{P_0}) + \frac{1}{2} f''(P_0)|_{\overline{P_0}} \cdot \frac{1}{N} \sum_{i=1}^{N} (P_{0i} - \overline{P_0})^2$$

or

$$\overline{M} = \overline{\overline{M}} + \frac{1}{2} f''(P_0)|_{\overline{P_0}} \cdot S^2 \qquad (8.1.7)$$

where,

$S^2 = \frac{1}{N}\sum_{i=1}^{N}\left(P_{0_i} - \overline{P_0}\right)^2$ is the variance. $\overline{\overline{M}}$ and $\overline{M}$ were defined at the beginning of this chapter, as the mean Mach number from the mean total pressure and from the individual total pressure respectively.

To get the calculation error, $f''(P_0)_{\overline{P_0}}$ is needed, which can be obtained through the Taylor's Expansion. First, by rewriting equation (8.1.5),

$$f(P_0) = \left\{\frac{2}{\gamma-1}\left[\left(\frac{P_0}{P}\right)^{\frac{\gamma-1}{\gamma}} - 1\right]\right\}^{\frac{1}{2}} = \sqrt{\frac{2}{\gamma-1}}\left[\left(\frac{P_0}{P}\right)^{\frac{\gamma-1}{\gamma}} - 1\right]^{\frac{1}{2}} \qquad (8.1.8)$$

Taking the derivative of Eq. (8.1.8),

$$f'(P_0) = \sqrt{\frac{2}{\gamma-1}}\cdot\frac{1}{2}\cdot\left[\left(\frac{P_0}{P}\right)^{\frac{\gamma-1}{\gamma}} - 1\right]^{-\frac{1}{2}}\cdot\frac{\gamma-1}{\gamma}\cdot\left(\frac{P_0}{P}\right)^{-\frac{1}{\gamma}}\cdot\frac{1}{P}$$

$$f'(P_0) = \sqrt{\frac{\gamma-1}{2}}\cdot\frac{1}{\gamma P}\cdot\left[\left(\frac{P_0}{P}\right)^{\frac{\gamma-1}{\gamma}} - 1\right]^{-\frac{1}{2}}\cdot\left(\frac{P_0}{P}\right)^{-\frac{1}{\gamma}} \qquad (8.1.9)$$

Taking another derivative,

$$f''(P_0)=\sqrt{\frac{\gamma-1}{2}}\cdot\frac{1}{\gamma}\cdot\left\{\left(-\frac{1}{2}\right)\left[\left(\frac{P_0}{P}\right)^{\frac{\gamma-1}{\gamma}}-1\right]^{-\frac{3}{2}}\cdot\frac{\gamma-1}{\gamma}\cdot\left(\frac{P_0}{P}\right)^{-\frac{2}{\gamma}}\cdot\frac{1}{P^2}+\right.$$

$$\left.\left[\left(\frac{P_0}{P}\right)^{\frac{\gamma-1}{\gamma}}-1\right]^{-\frac{1}{2}}\cdot\left(-\frac{1}{\gamma}\right)\left(\frac{P_0}{P}\right)^{-\frac{1}{\gamma}-1}\cdot\frac{1}{P^2}\right\}$$

or

$$f''(P_0)=\sqrt{\frac{\gamma-1}{2}}\cdot\frac{1}{\gamma^2P^2}\cdot\left[\left(\frac{P_0}{P}\right)^{\frac{\gamma-1}{\gamma}}-1\right]^{-\frac{3}{2}}\left(\frac{P_0}{P}\right)^{-\frac{1}{\gamma}-1}\left\{\frac{\gamma-1}{2}\cdot\left(\frac{P_0}{P}\right)^{1-\frac{1}{\gamma}}+\left(\frac{P_0}{P}\right)^{\frac{\gamma-1}{\gamma}}-1\right\}$$

(8.1.10)

Apply $P_0=\overline{P_0}$

$$f''(\overline{P_0})=\sqrt{\frac{\gamma-1}{2}}\cdot\frac{1}{\gamma^2P^2}\cdot\left[\left(\frac{\overline{P_0}}{P}\right)^{\frac{\gamma-1}{\gamma}}-1\right]^{-\frac{3}{2}}\left(\frac{\overline{P_0}}{P}\right)^{-\frac{1}{\gamma}-1}\left\{\frac{\gamma-1}{2}\cdot\left(\frac{\overline{P_0}}{P}\right)^{1-\frac{1}{\gamma}}+\left(\frac{\overline{P_0}}{P}\right)^{\frac{\gamma-1}{\gamma}}-1\right\}$$

(8.1.11)

$$f''(\overline{P_0})P^2 = \sqrt{\frac{\gamma-1}{2}}\cdot\frac{1}{\gamma^2}\cdot\left[\left(\frac{\overline{P_0}}{P}\right)^{\frac{\gamma-1}{\gamma}}-1\right]^{-\frac{3}{2}}\left(\frac{\overline{P_0}}{P}\right)^{\frac{1}{\gamma}-1}\left\{\frac{\gamma-1}{2}\cdot\left(\frac{\overline{P_0}}{P}\right)^{1-\frac{1}{\gamma}}+\left(\frac{\overline{P_0}}{P}\right)^{\frac{\gamma-1}{\gamma}}-1\right\}$$ is

plotted in Figure 8.1. It can be seen that $f''(\overline{P_0})P^2$ is very small (<1) and it becomes smaller when pressure increases.

The calculation error for the Mach number is.

$$\overline{M}-\overline{\overline{M}} = \frac{1}{2}f''(P_0)|_{\overline{P}}\cdot S^2 \qquad (8.1.12)$$

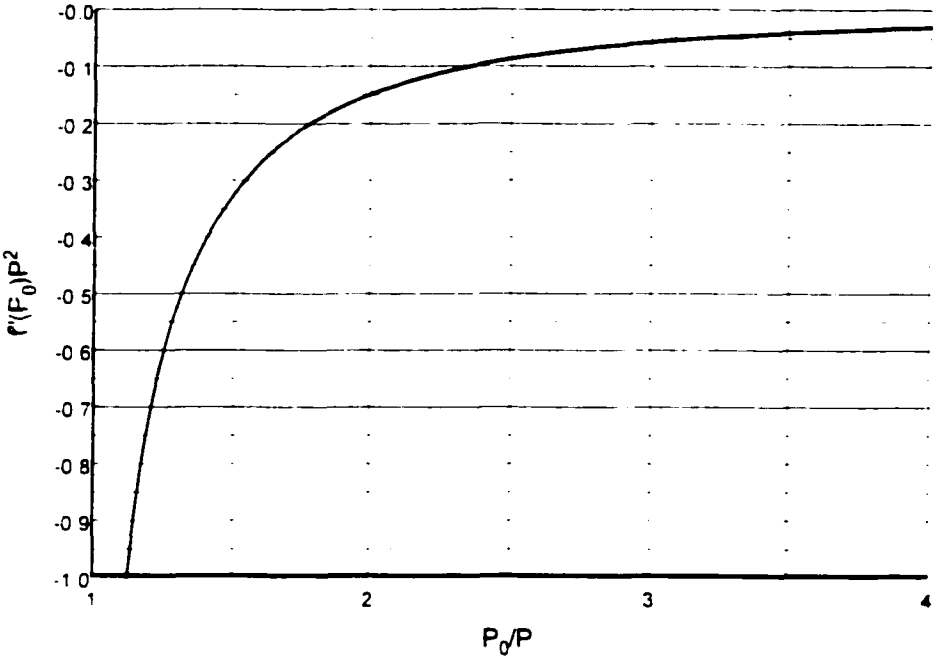

Figure 8.1: Coefficient of Taylor Expansion Changes with Pressure Ratio

Two extreme cases. M=0.3 and M=0.9 were calculated for the maximum and minimum calculation error.

When M=0.9.

$$\overline{M} - \overline{\overline{M}} = \frac{1}{2} f''(P_0)\Big|_{\overline{P_0}} \cdot S^2 = 0.5 \times (-0.25) \times \frac{2.7}{14.7^2} = -0.00156$$

or in percentage error of 0.17%

When M=0.3.

$$\overline{M} - \overline{\overline{M}} = \frac{1}{2} f''(P_0)\Big|_{\overline{P_0}} \cdot S^2 = 0.5 \times (-1.0) \times \frac{0.4}{14.7^2} = -0.000925$$

or in percentage error of 0.31%

Calculation errors between M=0.9 and 0.3 should also be between 0.17% and 0.31%. Obviously, this scheme of the Mach number calculation is very accurate. It can also avoid the turbulence calculation, which is difficult to estimate in our case.

8.2 Error Analysis For Concentration

In Chapter VII. the following equation was used to calculate the concentration.

$$\frac{P_0}{P} = \left(\frac{T_0}{T}\right)^{\frac{\gamma}{\gamma-1}} = \left(\frac{T_0}{T_0 - \frac{V^2}{2C_p}}\right)^{\frac{\gamma}{\gamma-1}} \tag{8.2.1}$$

where.

$$\gamma = c \cdot \gamma_H + (1-c) \cdot \gamma_a \tag{8.2.2}$$

$$C_p = c \cdot C_{pH} + (1-c) \cdot C_{pa} \tag{8.2.3}$$

p. γ_H . γ_a . C_{pH} . and C_{pa} are constants. while P_0 . T_0 . and V were obtained through different experiments. c is the concentration.

Eq (8.2.1) is used to find out concentration. The following part will discuss the corresponding system uncertainty and calculation error. similar to the previous part for the Mach number calculation.

Uncertainty

Rewriting Eq (8.2.1).

$$-\ln\frac{P_0}{P}=-\frac{\gamma}{\gamma-1}\cdot\ln\left(\frac{T_0}{T_0-\frac{V^2}{2C_p}}\right)$$

or

$$\ln P-\ln P_0=\frac{\gamma}{\gamma-1}\cdot\ln\left(1-\frac{V^2}{2C_pT_0}\right) \tag{8.2.4}$$

Taking the derivatives of both sides of Eq (8.2.4)

$$-\frac{\delta P_0}{P_0}=\left(\frac{\gamma}{\gamma-1}\right)'\cdot\ln\left(1-\frac{V^2}{2C_pT_0}\right)+\frac{\gamma}{\gamma-1}\cdot\frac{-\left(\frac{V^2}{2C_pT_0}\right)'}{1-\frac{V^2}{2C_pT_0}}$$

or

$$-\frac{\delta P_0}{P_0}=-\frac{\delta\gamma}{(\gamma-1)^2}\cdot\ln\left(1-\frac{V^2}{2C_pT_0}\right)-\frac{\gamma}{\gamma-1}\cdot\frac{V^2}{2C_pT_0}\cdot\frac{2\frac{\delta V}{V}-\frac{\delta C_p}{C_p}-\frac{\delta T_0}{T_0}}{1-\frac{V^2}{2C_pT_0}} \tag{8.2.5}$$

Notice, both C_p and γ are functions of x. Rearranging Eq (8.2.5),

$$\frac{\ln\left(1-\frac{V^2}{2C_pT_0}\right)}{(\gamma-1)^2}\delta\gamma-\frac{\gamma}{\gamma-1}\cdot\frac{V^2}{2C_pT_0}\cdot\frac{1}{1-\frac{V^2}{2C_pT_0}}\cdot\frac{\delta C_p}{C_p}=\frac{\delta P_0}{P_0}-\frac{\gamma}{\gamma-1}\cdot\frac{V^2}{2C_pT_0}\cdot\frac{2\frac{\delta V}{V}-\frac{\delta T_0}{T_0}}{1-\frac{V^2}{2C_pT_0}} \quad (8.2.6)$$

From Eq (8.2.2) and (8.2.3), we have,

$$\delta\gamma=(\gamma_H-\gamma_L)\delta c \quad (8.2.7)$$

$$\delta C_p=(C_{pH}-C_{pL})\delta c \quad (8.2.8)$$

Substitute Eq (8.2.7) and (8.2.8) into Eq (8.2.6),

$$\left[\frac{\ln\left(1-\frac{V^2}{2C_pT_0}\right)\cdot(\gamma_H-\gamma_L)}{(\gamma-1)^2}-\frac{\gamma\cdot V^2\cdot(C_{pH}-C_{pL})}{(\gamma-1)\cdot 2C_p^2T_0\cdot\left(1-\frac{V^2}{2C_pT_0}\right)}\right]\delta c=\frac{\delta P_0}{P_0}-\frac{\gamma\cdot V^2\cdot\left(2\frac{\delta V}{V}-\frac{\delta T_0}{T_0}\right)}{(\gamma-1)\cdot 2C_pT_0\cdot\left(1-\frac{V^2}{2C_pT_0}\right)}$$

.....(8.2.9)

Since the sign of $\frac{\delta P_0}{P_0}$, $\frac{\delta V}{V}$, and $\frac{\delta T_0}{T_0}$ are unknown, we need to find out the maximum uncertainty of concentration x. This will result in an enlargement on the error several times. But as an estimate, it helps us understand the experiments.

$$\delta c \le \frac{\left|\frac{\delta P_0}{P_0}\right| + \frac{\gamma \cdot V^2}{2(\gamma-1)\cdot C_p T_0 \cdot \left(1-\frac{V^2}{2C_p T_0}\right)}\left(2\left|\frac{\delta V}{V}\right| + \left|\frac{\delta T_0}{T_0}\right|\right)}{\left|\frac{\ln\left(1-\frac{V^2}{2C_p T_0}\right)\cdot(\gamma_H-\gamma_a)}{(\gamma-1)^2} - \frac{\gamma\cdot V^2\cdot(C_{pH}-C_{pa})}{2(\gamma-1)\cdot C_p^2 T_0\cdot\left(1-\frac{V^2}{2C_p T_0}\right)}\right|} \tag{8.2.10}$$

where γ, C_p have to be found out by concentration.

Several cases were tested for the system uncertainty, which is dependent on the measured parameters. Pressure uncertainty was given in previous part as 0.5%. Temperature uncertainty was calculated as 0.3%. The velocity uncertainty was given by TSI in Table 8.2. Based on each uncertainty available, Table 8.3 lists the uncertainty for several cases with the parameters obtained by measurements.

Table 8.2 Uncertainty for TSI PIV System

Factor	Random Error	Systematic Error
Illumination interval	0.2%	
Photographic magnification	0.3%	
Photographic distortion		0%-0.3%
Illumination plane flatness		0%-0.3%
Illumination plane thickness	0.1%	
Scanning-beam time effect		0%-0.2%
Seeding not following flow		0.1%
Combined errors	0.4%	0.1-0.8%

Table 8.3 Uncertainty for Concentration

Jet Type	P_0 (psi)	V(m/s)	T_0 (K)	c	System uncertainty
Krypton	16.16	64.78	294.69	1.00	5.8%
Krypton	15.41	62.52	294.72	0.90	7.6%
Helium	16.48	251.81	300.19	1.00	10%

Calculation Error

It is similar to the previous Mach number analysis. Since P_0, T_0, V cannot be measured simultaneously, it is very difficult to find out the concentration signal. We can only get the mean value for concentration. However, the mean value is important enough to derive the flow field. The difficulty is not only the three measured parameters, or in another words, three variables, but also the equation is an implicit equation.

To find out the uncertainty, the following assumptions were made:

$$\frac{P_0 - \overline{P_0}}{\overline{P_0}} << 1$$

$$\frac{T_0 - \overline{T_0}}{\overline{T_0}} << 1$$

$$\frac{V - \overline{V}}{\overline{V}} << 1$$

Then, Taylor's expansion can be applied again for each individual parameter. Assume that we have an explicit equation for concentration as follows.

$$c = f(P_0, T_0, V) \qquad (8.2.11)$$

Apply Taylor's expansion at $(\overline{P_0}, \overline{T_0}, \overline{V})$. Then the following relation is derived

$$c = f(\overline{P_0}, \overline{T_0}, \overline{V}) + \left.\frac{\partial f}{\partial P_0}\right|_{\overline{P}} (P_0 - \overline{P}) + \left.\frac{\partial f}{\partial T_0}\right|_{\overline{T}} (T_0 - \overline{T}) + \left.\frac{\partial f}{\partial V}\right|_{\overline{V}} (V - \overline{V}) +$$
$$\frac{1}{2}\left.\frac{\partial^2 f}{\partial P_0^2}\right|_{\overline{P}} (P_0 - \overline{P})^2 + \frac{1}{2}\left.\frac{\partial^2 f}{\partial T_0^2}\right|_{\overline{T}} (T_0 - \overline{T})^2 + \frac{1}{2}\left.\frac{\partial^2 f}{\partial V^2}\right|_{\overline{V}} (V - \overline{V})^2 + \qquad (8.2.12)$$
$$\left.\frac{\partial^2 f}{\partial P_0 \partial T_0}\right|_{(\overline{P},\overline{T})} (P_0 - \overline{P})(T_0 - \overline{T}) + \left.\frac{\partial^2 f}{\partial P_0 \partial V}\right|_{(\overline{P},\overline{V})} (P_0 - \overline{P})(V - \overline{V}) +$$
$$\left.\frac{\partial^2 f}{\partial T_0 \partial V}\right|_{(\overline{T},\overline{V})} (T_0 - \overline{T})(V - \overline{V}) + \cdots\cdots$$

Express individual concentration from (8.2.12):

$$c_i = f(\overline{P_0}, \overline{T_0}, \overline{V}) + \left.\frac{\partial f}{\partial P_0}\right|_{\overline{P}} (P_{0i} - \overline{P_0}) + \left.\frac{\partial f}{\partial T_0}\right|_{\overline{T}} (T_{0i} - \overline{T_0}) + \left.\frac{\partial f}{\partial V}\right|_{\overline{V}} (V_i - \overline{V}) +$$
$$\frac{1}{2}\left.\frac{\partial^2 f}{\partial P_0^2}\right|_{\overline{P}} (P_{0i} - \overline{P_0})^2 + \frac{1}{2}\left.\frac{\partial^2 f}{\partial T_0^2}\right|_{\overline{T}} (T_{0i} - \overline{T_0})^2 + \frac{1}{2}\left.\frac{\partial^2 f}{\partial V^2}\right|_{\overline{V}} (V_i - \overline{V})^2 +$$
$$\left.\frac{\partial^2 f}{\partial P_0 \partial T_0}\right|_{(\overline{P},\overline{T})} (P_{0i} - \overline{P_0})(T_{0i} - \overline{T_0}) + \left.\frac{\partial^2 f}{\partial P_0 \partial V}\right|_{(\overline{P},\overline{V})} (P_{0i} - \overline{P_0})(V_i - \overline{V}) +$$
$$\left.\frac{\partial^2 f}{\partial T_0 \partial V}\right|_{(\overline{T},\overline{V})} (T_{0i} - \overline{T_0})(V_i - \overline{V}) + \cdots\cdots$$

$$c_2 = f(\overline{P}, \overline{T}, \overline{V}) + \left.\frac{\partial f}{\partial P_0}\right|_{\overline{P}} (P_2 - \overline{P}) + \left.\frac{\partial f}{\partial T_0}\right|_{\overline{T}} (T_2 - \overline{T}) + \left.\frac{\partial f}{\partial V}\right|_{\overline{V}} (V_2 - \overline{V}) +$$
$$\frac{1}{2}\left.\frac{\partial^2 f}{\partial P_0^2}\right|_{\overline{P}} (P_2 - \overline{P})^2 + \frac{1}{2}\left.\frac{\partial^2 f}{\partial T_0^2}\right|_{\overline{T}} (T_2 - \overline{T})^2 + \frac{1}{2}\left.\frac{\partial^2 f}{\partial V^2}\right|_{\overline{V}} (V_2 - \overline{V})^2 +$$
$$\left.\frac{\partial^2 f}{\partial P_0 \partial T_0}\right|_{(\overline{P},\overline{T})} (P_2 - \overline{P})(T_2 - \overline{T}) + \left.\frac{\partial^2 f}{\partial P_0 \partial V}\right|_{(\overline{P},\overline{V})} (P_2 - \overline{P})(V_2 - \overline{V}) +$$
$$\left.\frac{\partial^2 f}{\partial T_0 \partial V}\right|_{(\overline{T},\overline{V})} (T_2 - \overline{T})(V_2 - \overline{V}) + \cdots\cdots$$

.....

$$c_n = f(\overline{P}, \overline{T}, \overline{V}) + \left.\frac{\partial f}{\partial P_0}\right|_{\overline{P}} (P_n - \overline{P}) + \left.\frac{\partial f}{\partial T_0}\right|_{\overline{T}} (T_n - \overline{T}) + \left.\frac{\partial f}{\partial V}\right|_{\overline{V}} (V_n - \overline{V}) +$$
$$\frac{1}{2}\left.\frac{\partial^2 f}{\partial P_0^2}\right|_{\overline{P}} (P_n - \overline{P})^2 + \frac{1}{2}\left.\frac{\partial^2 f}{\partial T_0^2}\right|_{\overline{T}} (T_n - \overline{T})^2 + \frac{1}{2}\left.\frac{\partial^2 f}{\partial V^2}\right|_{\overline{V}} (V_n - \overline{V})^2 +$$
$$\left.\frac{\partial^2 f}{\partial P_0 \partial T_0}\right|_{(\overline{P},\overline{T})} (P_n - \overline{P})(T_n - \overline{T}) + \left.\frac{\partial^2 f}{\partial P_0 \partial V}\right|_{(\overline{P},\overline{V})} (P_n - \overline{P})(V_n - \overline{V}) +$$
$$\left.\frac{\partial^2 f}{\partial T_0 \partial V}\right|_{(\overline{T},\overline{V})} (T_n - \overline{T})(V_n - \overline{V}) + \cdots\cdots$$

Sum up from c_1 to c_n If the concentration was measured N times then the average concentration could be expressed as.

$$\frac{1}{N}\sum c = f(\overline{P},\overline{T},\overline{V}) + \left.\frac{\partial f}{\partial P_0}\right|_{\overline{P}} \frac{1}{N}\sum (P - \overline{P}) + \left.\frac{\partial f}{\partial T_0}\right|_{\overline{T}} \frac{1}{N}\sum (T - \overline{T}) + \left.\frac{\partial f}{\partial V}\right|_{\overline{V}} \frac{1}{N}\sum (V - \overline{V}) +$$
$$\frac{1}{2}\left.\frac{\partial^2 f}{\partial P_0^2}\right|_{\overline{P}} \frac{1}{N}\sum (P - \overline{P})^2 + \frac{1}{2}\left.\frac{\partial^2 f}{\partial T_0^2}\right|_{\overline{T}} \frac{1}{N}\sum (T - \overline{T})^2 + \frac{1}{2}\left.\frac{\partial^2 f}{\partial V^2}\right|_{\overline{V}} \frac{1}{N}\sum (V - \overline{V})^2 +$$
$$\left.\frac{\partial^2 f}{\partial P_0 \partial T_0}\right|_{(\overline{P},\overline{T})} \frac{1}{N}\sum (P - \overline{P})(T - \overline{T}) + \left.\frac{\partial^2 f}{\partial P_0 \partial V}\right|_{(\overline{P},\overline{V})} \frac{1}{N}\sum (P - \overline{P})(V - \overline{V}) +$$
$$\left.\frac{\partial^2 f}{\partial T_0 \partial V}\right|_{(\overline{T},\overline{V})} \frac{1}{N}\sum (T - \overline{T})(V - \overline{V}) + \ldots\ldots$$

(8.2.13)

If the fluctuation (mean value removed) u' of one signal has no correlation with another fluctuation (mean value removed) u' , then the product $u'\,u'$ has a mean value of 0. If u' and u' are correlated, then the mean is no longer 0.

Figure 8.2 can be used to explain correlation. The fluctuating variable a has the same sign as the variable b for most of the time: this makes $\overline{ab} > 0$. The variable c, on the other hand, is uncorrelated with a and b, so that $\overline{ac} = 0$ and $\overline{bc} = 0$ (note that $\overline{ab} \neq 0$, $\overline{bc} \neq 0$ does not necessarily imply that $\overline{bc} \neq 0$).

The correlation coefficient is defined as

$$C_{ij} = \frac{\overline{u_i' u_j'}}{\overline{u_i'^2} \cdot \overline{u'^2}}$$

If u_i' and u' have no correlation, C = 0.

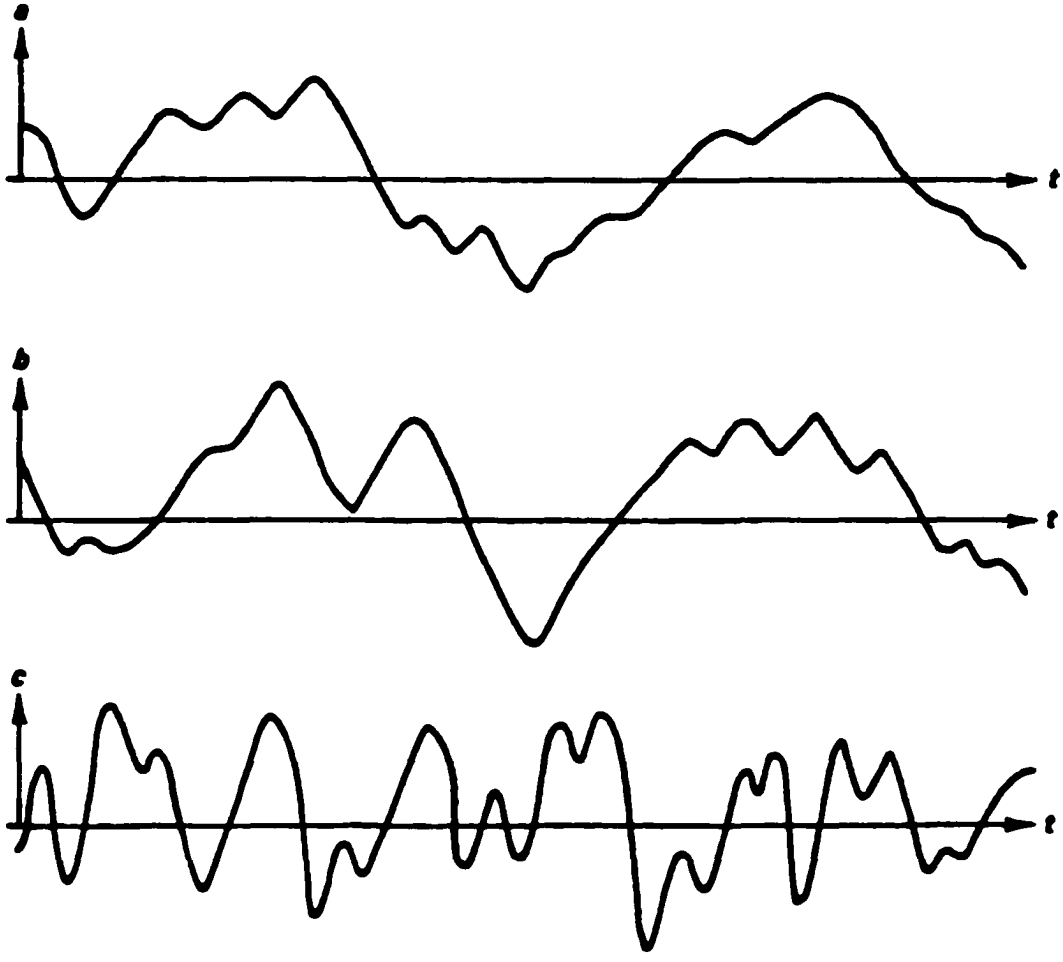

Figure 8.2: Correlated and Uncorrelated Fluctuations

(Tennekes, H. and Lumley, J.L. A First Course in Turbulence Sixteenth Printing)

Pressure, temperature, and velocity were measured separately. The data was analyzed for correlation, and no substantial correlation was found. Therefore, the following terms:

$$\left.\frac{\partial^2 f}{\partial P_0 \partial T_0}\right|_{(\bar{P},\bar{T})} \frac{1}{N}\sum_{i=1}^{N}(P_{0_i}-\bar{P})\cdot(T_{0_i}-\bar{T})\cdot$$

$$\left.\frac{\partial^2 f}{\partial P_0 \partial V}\right|_{(\bar{P},\bar{V})} \frac{1}{N}\sum_{i=1}^{N}(P_{0_i}-\bar{P})\cdot(V_i-\bar{V})\cdot$$

and

$$\left.\frac{\partial^2 f}{\partial T_0 \partial V}\right|_{(\bar{T},\bar{V})} \frac{1}{N}\sum_{i=1}^{N}(T_{0_i}-\bar{T})\cdot(V_i-\bar{V})=0$$

This simplifies that the average concentration is given by,

$$\bar{\bar{c}}=\bar{c}+\frac{1}{2}\left.\frac{\partial^2 f}{\partial P_0^2}\right|_{\bar{P}}\frac{1}{N}\sum_{i=1}^{N}(P_{0_i}-\bar{P})^2+\frac{1}{2}\left.\frac{\partial^2 f}{\partial T_0^2}\right|_{\bar{T}}\frac{1}{N}\sum_{i=1}^{N}(T_{0_i}-\bar{T})^2+\frac{1}{2}\left.\frac{\partial^2 f}{\partial V^2}\right|_{\bar{V}}\frac{1}{N}\sum_{i=1}^{N}(V_i-\bar{V})^2$$

(8.2.14)

where $\bar{c}$ is the time averaged concentration, while $\bar{\bar{c}}$ is calculated from the experimental data. To find the error of $\bar{c}-\bar{\bar{c}}$, the following terms are needed which will be developed:

$$\left.\frac{\partial^2 f}{\partial P_0^2}\right|_{\bar{P}},\ \left.\frac{\partial^2 f}{\partial T_0^2}\right|_{\bar{T}},\ \left.\frac{\partial^2 f}{\partial V^2}\right|_{\bar{V}}$$

By rewriting equation (8.2.1)

$$\frac{P_0}{P} = \left(\frac{T_0}{T}\right)^{\frac{\gamma}{\gamma-1}} = \left(\frac{T_0}{T_0 - \frac{V^2}{2C_p}}\right)^{\frac{\gamma}{\gamma-1}} \tag{8.2.1}$$

$$\left(1 - \frac{1}{\gamma}\right)(\ln P - \ln P_0) = \ln\left(1 - \frac{V^2}{2C_p T_0}\right) \tag{8.2.15}$$

Define as follows.

$$F = F(P_0, T_0, V, c) = \left(1 - \frac{1}{\gamma}\right)(\ln P - \ln P_0) - \ln\left(1 - \frac{V^2}{2C_p T_0}\right) \tag{8.2.16}$$

Then full derivative of F is

$$dF = \frac{\partial F}{\partial P_0} dP_0 + \frac{\partial F}{\partial T_0} dT_0 + \frac{\partial F}{\partial V} dV + \frac{\partial F}{\partial c} dc = 0$$

(8.2.17)

also. we have

$$c = f(P_0, T_0, V) \tag{8.2.11}$$

it follows that.

$$dc = \frac{\partial f}{\partial P_0} dP_0 + \frac{\partial f}{\partial T_0} dT_0 + \frac{\partial f}{\partial V} dV \tag{8.2.18}$$

Substituting (8.2.18) into (8.2.17).

$$\left(\frac{\partial F}{\partial P_0}+\frac{\partial F}{\partial c}\frac{\partial f}{\partial P_0}\right)dP_0+\left(\frac{\partial F}{\partial T_0}+\frac{\partial F}{\partial c}\frac{\partial f}{\partial T_0}\right)dT_0+\left(\frac{\partial F}{\partial V}+\frac{\partial F}{\partial c}\frac{\partial f}{\partial V}\right)dV=0$$

(8.2.19)

therefore.

$$\frac{\partial f}{\partial P_0}=-\frac{\partial F}{\partial F}\frac{\partial P_0}{\partial c}\cdot\frac{\partial^2 f}{\partial P_0^2}=-\frac{\partial}{\partial P_0}\left(\frac{\partial F}{\partial F}\frac{\partial P_0}{\partial c}\right) \qquad (8.2.20a)$$

$$\frac{\partial f}{\partial T_0}=-\frac{\partial F}{\partial F}\frac{\partial T_0}{\partial c}\cdot\frac{\partial^2 f}{\partial T_0^2}=-\frac{\partial}{\partial T_0}\left(\frac{\partial F}{\partial F}\frac{\partial T_0}{\partial c}\right) \qquad (8.2.20b)$$

$$\frac{\partial f}{\partial V}=-\frac{\partial F}{\partial F}\frac{\partial V}{\partial c}\cdot\frac{\partial^2 f}{\partial V^2}=-\frac{\partial}{\partial V}\left(\frac{\partial F}{\partial F}\frac{\partial V}{\partial c}\right) \qquad (8.2.20c)$$

Software Mathematica was used to solve these tedious derivatives. But notice that to show concentration is a variable instead of a constant. we replaced the symbol c by x in Mathematica as follows.

$$\frac{\partial F}{\partial x}=\frac{\partial}{\partial x}\left\{\left[1-\frac{1}{x\gamma_h+(1-x)\gamma_a}\right]\cdot[\log(P)-\log(P_0)]-\log\left[1-\frac{V^2}{2\cdot[xC_{ph}+(1-x)C_{pa}]T_0}\right]\right\}$$

$$=-\frac{V^2(-C_{pa}+C_{ph})}{2[(1-x)C_{pa}+xC_{ph}]^2\left[1-\frac{V^2}{2[(1-x)C_{pa}+xC_{ph}]T_0}\right]T_0}+\frac{[\log(P)-\log(P_0)]\cdot(-\gamma_a+\gamma_h)}{[(1-x)\gamma_a+x\gamma_h]^2}$$

(8.2.21a)

$$\frac{\partial F}{\partial P_0} = \frac{\partial}{\partial P_0}\left\{\left[1 - \frac{1}{x\gamma_n + (1-x)\gamma_a}\right]\cdot[\log(P) - \log(P_0)] - \log\left[1 - \frac{V^2}{2\cdot[xC_{pn} + (1-x)C_{pa}]T_0}\right]\right\}$$

$$= -\frac{1 - \frac{1}{(1-x)\gamma_a + x\gamma_n}}{P_0} \qquad (8.2.21b)$$

$$\frac{\partial F}{\partial T_0} = \frac{\partial}{\partial T_0}\left\{\left[1 - \frac{1}{x\gamma_n + (1-x)\gamma_a}\right]\cdot[\log(P) - \log(P_0)] - \log\left[1 - \frac{V^2}{2\cdot[xC_{pn} + (1-x)C_{pa}]T_0}\right]\right\}$$

$$= -\frac{V^2}{2[(1-x)C_{pa} + xC_{pn}]\cdot\left[1 - \frac{V^2}{2\cdot[(1-x)C_{pa} + xC_{pn}]T_0}\right]\cdot T_0^2} \qquad (8.2.21c)$$

$$\frac{\partial F}{\partial V} = \frac{\partial}{\partial V}\left\{\left[1 - \frac{1}{x\gamma_n + (1-x)\gamma_a}\right]\cdot[\log(P) - \log(P_0)] - \log\left[1 - \frac{V^2}{2\cdot[xC_{pn} + (1-x)C_{pa}]T_0}\right]\right\}$$

$$= \frac{V}{[(1-x)C_{pa} + xC_{pn}]\cdot\left[1 - \frac{V^2}{2\cdot[(1-x)C_{pa} + xC_{pn}]T_0}\right]\cdot T_0} \qquad (8.2.21d)$$

The second order of derivatives are calculated as follows.

$$\frac{\partial^2 y}{\partial P_0^2} = -\frac{\partial}{\partial P_0}\left(\frac{\partial F}{\partial F}\frac{\partial P}{\partial x}\right)$$

$$= -\frac{\partial}{\partial P_0}\left\{\frac{1-\dfrac{1}{(1-x)\gamma_a + x\gamma_w}}{P_0} - \frac{V^2(-C_{wa}+C_{ww})}{2\left[(1-x)C_{wa}+xC_{ww}\right]^2\left[1-\dfrac{V^2}{2\left[(1-x)C_{wa}+xC_{ww}\right]T}\right]T} - \frac{[\log(P)-\log(P_0)](-\gamma_a+\gamma_w)}{[(1-x)\gamma_a+x\gamma_w]^2}\right\}$$

$$= \frac{1-\dfrac{1}{(1-x)\gamma_a+x\gamma_w}}{P^2} - \frac{V^2(-C_{wa}+C_{ww})}{2\left[(1-x)C_{wa}+xC_{ww}\right]^2\left[1-\dfrac{V^2}{2\left[(1-x)C_{wa}+xC_{ww}\right]T}\right]T} - \frac{[\log(P)-\log(P_0)](-\gamma_a+\gamma_w)}{[(1-x)\gamma_a+x\gamma_w]^2}$$

(8.2.22a)

$$\frac{\partial^2 f}{\partial T_c^2} = -\frac{\partial}{\partial T_c}\left(\frac{\partial F}{\partial F}\frac{\partial T_c}{\partial x}\right) =$$

$$-\frac{\partial}{\partial T_c}\left\{\frac{-\dfrac{P^2}{2\left[(1-x)C_{pa}+xC_{pb}\right]\cdot\left[1-\dfrac{P^2}{2\cdot\left[(1-x)C_{pa}+xC_{pb}\right]\cdot T_c}\right]\cdot T_c^2}}{\dfrac{P^2(-C_{pa}+C_{pb})}{2\left[(1-x)C_{pa}+xC_{pb}\right]\cdot\left[1-\dfrac{P^2}{2\cdot\left[(1-x)C_{pa}+xC_{pb}\right]\cdot T_c}\right]\cdot T_c}-\dfrac{\left[\log(P)-\log(P_0)\right](-\gamma_a+\gamma_b)}{\left[(1-x)\gamma_a+x\gamma_b\right]}}\right\}$$

$$=\left\{\frac{P^2}{4\left[(1-x)C_{pa}+xC_{pb}\right]\cdot\left[1-\dfrac{P^2}{2\left[(1-x)C_{pa}+xC_{pb}\right]\cdot T_c}\right]\cdot T_c^2}-\frac{P^2(-C_{pa}+C_{pb})}{2\left[(1-x)C_{pa}+xC_{pb}\right]\cdot\left[1-\dfrac{P^2}{2\left[(1-x)C_{pa}+xC_{pb}\right]\cdot T_c}\right]\cdot T_c^2}\right\}$$

$$\left\{\frac{-P^2(-C_{pa}+C_{pb})}{2\left[(1-x)C_{pa}+xC_{pb}\right]\cdot\left[1-\dfrac{P^2}{2\left[(1-x)C_{pa}+xC_{pb}\right]\cdot T_c}\right]\cdot T_c}-\frac{\left[\log(P)-\log(P_0)\right](-\gamma_a+\gamma_b)}{\left[(1-x)\gamma_a+x\gamma_b\right]}\right\}^2$$

$$\frac{P^4}{4\left[(1-x)C_{pa}+xC_{pb}\right]\cdot\left[1-\dfrac{P^2}{2\left[(1-x)C_{pa}+xC_{pb}\right]\cdot T_c}\right]^2\cdot T_c^4}\left\{\frac{-P^2(-C_{pa}+C_{pb})}{2\left[(1-x)C_{pa}+xC_{pb}\right]\cdot\left[1-\dfrac{P^2}{2\left[(1-x)C_{pa}+xC_{pb}\right]\cdot T_c}\right]\cdot T_c}-\frac{\left[\log(P)-\log(P_0)\right](-\gamma_a+\gamma_b)}{\left[(1-x)\gamma_a+x\gamma_b\right]}\right\}$$

$$\frac{P^2}{\left[(1-x)C_{pa}+xC_{pb}\right]\cdot\left[1-\dfrac{P^2}{2\left[(1-x)C_{pa}+xC_{pb}\right]\cdot T_c}\right]\cdot T_c^2}\left\{\frac{-P^2(-C_{pa}+C_{pb})}{2\left[(1-x)C_{pa}+xC_{pb}\right]\cdot\left[1-\dfrac{P^2}{2\left[(1-x)C_{pa}+xC_{pb}\right]\cdot T_c}\right]\cdot T_c}-\frac{\left[\log(P)-\log(P_0)\right](-\gamma_a+\gamma_b)}{\left[(1-x)\gamma_a+x\gamma_b\right]}\right\}$$

(8.2.22b)

$$\frac{\partial^2 f}{\partial V^2}=-\frac{\partial}{\partial V}\left(\frac{\partial F}{\partial F}\frac{\partial V}{\partial x}\right)=-\frac{\partial}{\partial V}\left\{\frac{\dfrac{V}{\left[(1-x)C_{pa}+xC_{ph}\right]\cdot\left[1-\dfrac{V^2}{2\cdot\left[(1-x)C_{pa}+xC_{ph}\right]\cdot T_0}\right]\cdot T_0}}{V^2(-C_{pa}+C_{ph})}+\frac{[\log(P)-\log(P_0)](-\gamma_a+\gamma_h)}{[(1-x)\gamma_a+x\gamma_h]}\right\}$$

$$=-\left\{\frac{V^2(-C_{pa}+C_{ph})}{2\left[(1-x)C_{pa}+xC_{ph}\right]\cdot\left[1-\dfrac{V^2}{2\left[(1-x)C_{pa}+xC_{ph}\right]T_0}\right]\cdot T_0^2}-\frac{V^2(-C_{pa}+C_{ph})}{\left[(1-x)C_{pa}+xC_{ph}\right]\left[1-\dfrac{V^2}{2\left[(1-x)C_{pa}+xC_{ph}\right]T_0}\right]T_0}\right\}$$

$$\frac{V^2}{\left[(1-x)C_{pa}+xC_{ph}\right]\left[1-\dfrac{V^2}{2\left[(1-x)C_{pa}+xC_{ph}\right]T_0}\right]T_0}\left\{\frac{-V^2(-C_{pa}+C_{ph})}{2\left[(1-x)C_{pa}+xC_{ph}\right]\left[1-\dfrac{V^2}{2\left[(1-x)C_{pa}+xC_{ph}\right]T_0}\right]T_0}-\frac{[\log(P)-\log(P_0)](-\gamma_a+\gamma_h)}{[(1-x)\gamma_a+x\gamma_h]}\right\}$$

$$\frac{V^2}{\left[(1-x)C_{pa}+xC_{ph}\right]\left[1-\dfrac{V^2}{2\left[(1-x)C_{pa}+xC_{ph}\right]T_0}\right]T_0^2}\left\{\frac{-V^2(-C_{pa}+C_{ph})}{2\left[(1-x)C_{pa}+xC_{ph}\right]\left[1-\dfrac{V^2}{2\left[(1-x)C_{pa}+xC_{ph}\right]T_0}\right]T_0}-\frac{[\log(P)-\log(P_0)](-\gamma_a+\gamma_h)}{[(1-x)\gamma_a+x\gamma_h]}\right\}$$

$$\frac{1}{\left[(1-x)C_{pa}+xC_{ph}\right]\left[1-\dfrac{V^2}{2\left[(1-x)C_{pa}+xC_{ph}\right]T_0}\right]T_0}\left\{\frac{-V^2(-C_{pa}+C_{ph})}{2\left[(1-x)C_{pa}+xC_{ph}\right]\left[1-\dfrac{V^2}{2\left[(1-x)C_{pa}+xC_{ph}\right]T_0}\right]T_0}-\frac{[\log(P)-\log(P_0)](-\gamma_a+\gamma_h)}{[(1-x)\gamma_a+x\gamma_h]}\right\}$$

(8.2.22c)

Several cases were calculated to verify these results. The pressure, temperature, and velocity fluctuations are also taken into account for the calculation error.

Table 8.4 Calculation Errors for Concentration

Jet Type	P_0 (psi)	V (m/s)	T_0 (K)	c	Calculation Error
Krypton	16.16	64.78	294.69	1.00	0.17%
Krypton	15.41	62.52	294.72	0.90	0.46%
Helium	16.48	251.81	300.19	1.00	0.31%
Helium	15.09	149.62	296.14	0.70	2.20%

it can be seen that the indirect calculation algorithm is very accurate for concentration calculation.

Discussion:

Density and Mach number were also obtained through equation (8.2.1), so the errors should be analyzed the same way. If needed, readers can follow the same algorithm to find out the corresponding errors. Small differences are expected.

Chapter IX. Conclusions

Experimental studies of compressible turbulent jet flows were conducted in the Aerodynamics Laboratory, City College of New York.

The experiments have been designed with the objective of increasing the physical understanding of compressible turbulence and enhance its structure. The behavior of compressible jets issuing in still air in the absence of shock waves was investigated at three different subsonic Mach numbers 0.3, 0.6, and 0.9. Helium, nitrogen and krypton gases were used to generate the jet flows and investigate the effects of density difference on the structure of turbulence.

Measurements of total pressure, total temperature, and velocity were carried out by using a high frequency response pressure transducer used as a Pitot tube, thermocouples, and Particle Image Velocimetry (PIV) techniques respectively.

The decay of the Mach number at the centerline of the axisymmetric jets increases with increasing the initial Mach number at the exit of the flow for all jets. The decay of mean velocity at the centerline of the jets is also higher at higher exit Mach numbers. However, the velocity non-dimensionalized by the exit velocity seems to decrease faster

at low exit Mach numbers suggesting a reduced mixing with increasing the exit flow Mach numbers.

Helium jets were found to have the largest spreading rate among the three different gas jets used in the present investigation, while krypton had the lowest spreading rate.

Total pressure fluctuations appear to decrease with increasing exit flow Mach numbers. Unusually high turbulence intensities were measured in helium jets issuing in still air.

The results also showed clearly that a potential core exists in the near region to the exit, inside which the velocity increases along the jet centerline exists for all types of jets. The viscous effect present in the shear layer, which forms outside of the potential core, is most probably the cause of this increase. The shearing stress created in this region reduces the cross sectional area of the potential core, and in return, the velocity inside is increased. The total pressure increase inside the potential core is due to the velocity increase, which accounts for the dynamic pressure. The total temperature increase along the centerline is due to the heat exchange with the ambient air, that has a higher static temperature than that of the jet flow. Therefore, it is concluded that the jet mixing with the ambient fluid is not adiabatic.

Compressibility (based on Mach number) and density effect were found to be the key factors for jet flows in present work. The decay rate from the experimental results indicate that at a higher exit Mach number, the decay rate is also higher for the three

quantities measured. Helium jets have better mixing with the ambient air than the nitrogen jets and krypton jets. The length for the potential core is longer in the case of a lower jet flow density, i.e., the helium jet. It is also longer in the case of a higher exit Mach number. Density effect was also showed to affect the spreading rate. These results indicate that compressibility and density effects control substantially the development of the jet.

There is evidence to suggest that since the centerline velocity decay is inversely proportional to the distance from the jet exit, fully developed regions further downstream may exist.

For helium and krypton jets, because of their mixing with ambient fluid, Mach number, density, and concentration are not available directly from our experiments because properties of the mixture are subject to separate research. Formulas based on the measured quantities of total pressure, total temperature, and velocity were developed and programmed to obtain values of concentration, density and Mach numbers in the case of helium and krypton. The error analysis for this calculation shows that the method gives results that make good sense.

Appendix A Derivation of Equations to Calculate Frictional, Compressible Flow in Ducts

The jet used in this research can be considered as a duct with constant cross-sectional area. The compressible flow, such as air in a duct is always accompanied by friction, heat transfer, which will change the flow properties. It is difficult to separate these factors, however, depending on special cases, the problem may be simplified. If the process lasts short, then it can be treated as an adiabatic process, which involves no heat transfer effect. This requires that either the jet itself is short enough, or the jet is insulated so the thermal effect is negligible. Thus only friction needs to be considered in this case. Due to friction, the entropy of the system will always increase because friction is associated with the turbulence and viscous shear of molecules of the gas, and the movement of gas molecules near the wall as well. Refer to reference [82].

There is one important assumption that cannot be omitted: the gas from the jets behaves as a perfect gas, so that the known relations based on perfect gas can be used directly.

Consider steady-state one-dimensional flow of a perfect gas with constant specific heats across a control surface, as shown in Figure A.1.

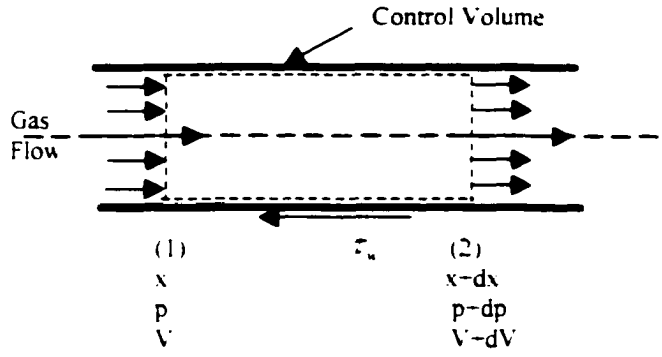

Figure A.1: Adiabatic Frictional Flow in a Constant Area Duct

Momentum relationships are expressed by the following equation.

$$Ap - A(p + dp) - \tau_w P dx = \rho A V^2 (V + dV - V) \tag{A.1}$$

where τ_w is the shear stress at the walls of the duct and P represents the wetted perimeter. The friction factor f is related to the shear stress in the flow direction τ_w in the following formula.

$$f = \frac{\tau_w}{\frac{1}{2}\rho V^2} \tag{A.2}$$

where $\frac{1}{2}\rho V^2$ is the dynamic pressure of the stream. The wetted perimeter of the duct P is defined in terms of the "hydraulic diameter" D_H of the duct.

$$P = \frac{4A}{D_H} \tag{A.3}$$

where P is the cross-sectional area of the duct. Note that for a duct of circular cross section, $D_H = D$.

These expressions for shear stress and wetted perimeter are substituted in the momentum equation, and the following is obtained.

$$dp + \frac{4f}{D_H}\frac{\rho V^2}{2}dx + \frac{\rho V^2}{2}\frac{dV^2}{V^2} = 0 \tag{A.4}$$

The friction factor f is a function of the Reynolds number of the flow and the roughness at the boundaries. The Reynolds number is calculated on the basis of the hydraulic diameter of the duct. The relationship among f, the Reynolds number Re, and the relative roughness ε/D is experimentally determined and plotted in Figure A.2, which is called the Moody diagram. The diagram applies to compressible and incompressible flows. At large values of Reynolds number for a fixed value of relative roughness, the friction factor becomes independent of Reynolds number. An expression for calculating the friction factor for turbulent flow in smooth ducts, which agrees well with Figure A.2, is the Von Karman-Nikuradse formula.

$$\frac{1}{\sqrt{4f}} = -0.8 + 2\log_{10}(\mathrm{Re}\sqrt{4f}) \tag{A.5}$$

The Renolds number is defined as $\mathrm{Re} = \frac{VD}{\nu}$, where V is the velocity of the flow, D the tube diameter and ν the kinematic viscosity of the fluid. In complete tube diameter and V the kinematic viscosity of the fluid. In complete turbulent flow with high Reynolds numbers, the f becomes independent of the Reynolds number. Because of the high velocity of the flow and the fact that the flow is seeded with a huge amount of particles, a complete turbulent flow is supposed. The average friction coefficient f is taken as the friction coefficient f from the Moody diagram Figure A.2, based on a mean Reynolds number, taken from the exit velocity and the supply velocity

Other equations necessary to the solution of the problems pertaining to frictional flow in constant-area ducts are.

Perfect gas.

$$p = \rho RT \quad \text{or} \quad \frac{dp}{p} = \frac{d\rho}{\rho} + \frac{dT}{T} \tag{A.6}$$

Continuity.

$$\frac{\dot{m}}{A} = \rho V = const \quad \text{or} \quad \frac{d\rho}{\rho} + \frac{dV}{V} = 0 \tag{A.7}$$

Energy.

$$h_0 = h + \frac{V^2}{2} = const \quad \text{or} \quad dh + VdV = 0 \tag{A.8}$$

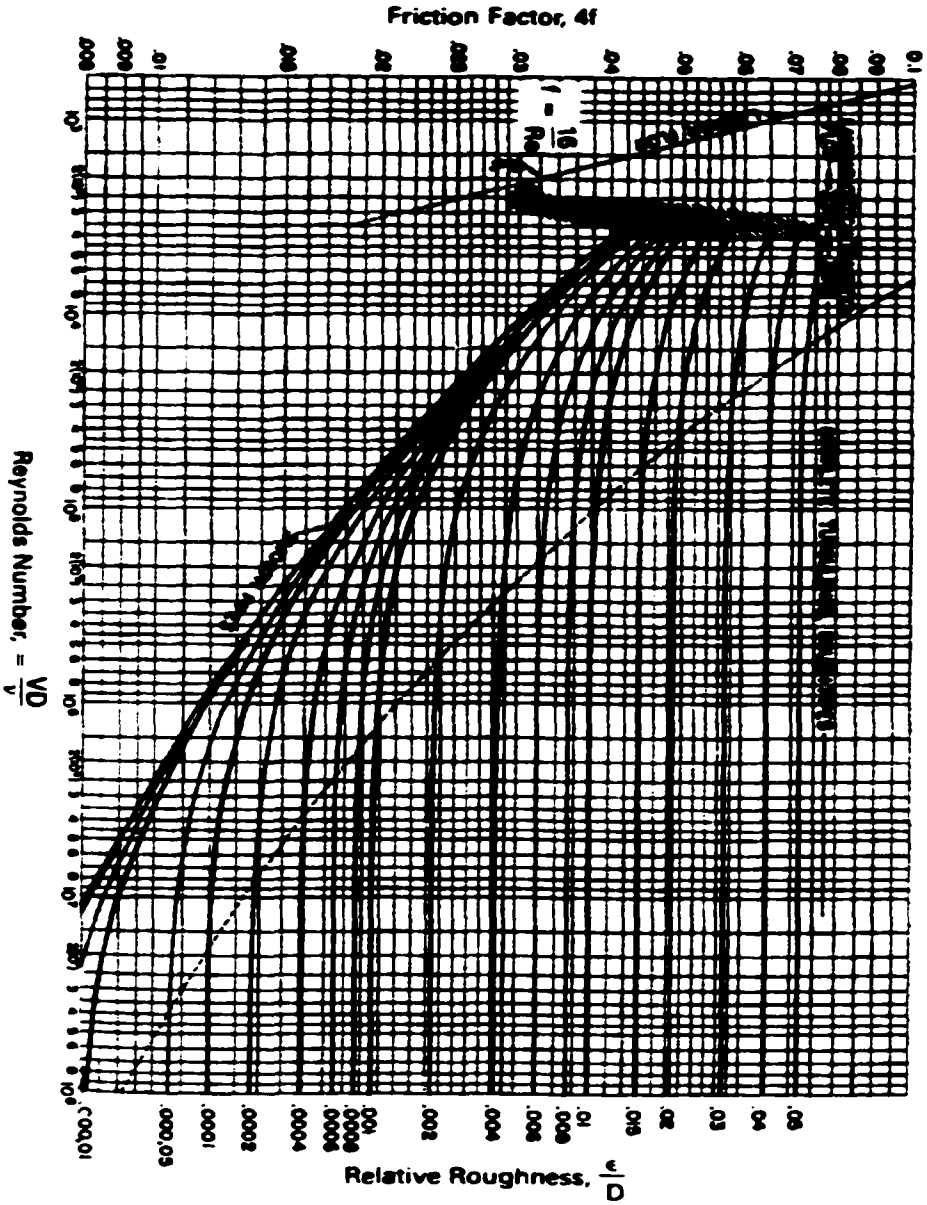

Figure A.2: Moody Diagram

Definition of Mach number.

$$M^2 = \frac{V^2}{\gamma RT} \qquad \text{or} \qquad \frac{dM^2}{M^2} = \frac{dV^2}{V^2} - \frac{dT}{T} \tag{A.9}$$

Second law in Thermodynamics.

$$ds \geq 0 \tag{A.10}$$

The seven variables M, V, p, ρ, T, s and $4fdx/D_H$ appear in the six equations. Eqs. From (A.4) and (A.6) through (A.10). Only one of these variables needs to be specified, and the other six become the dependent variables. Since the question is how friction affects flow properties, the term $4fdx/D_H$ is often chosen as the independent variable. If the Mach number is chosen instead as the independent variable, the friction factor may be expressed directly in terms of Mach number M. To develop the corresponding relations, divide terms in the momentum equation (A.4) by pressure p as follows.

$$\frac{dp}{p} + \frac{4f}{D_H}\frac{\rho V^2}{2p}dx + \frac{\rho V^2}{2p}\frac{dV^2}{V^2} = 0 \tag{A.11}$$

But since

$$\rho V^2 = \rho \frac{V^2}{\gamma RT}\gamma RT = \gamma M^2 p \tag{A.12}$$

it follows that,

$$\frac{dp}{p} + \frac{4f}{D_H}\frac{\gamma M^2}{2}dx + \frac{\gamma M^2}{2}\frac{dV^2}{V^2} = 0 \tag{A.13}$$

From energy relationships. Eq. (A.8). $c_p dT = -dV^2/2$. Dividing this equation by $c_p dT$, substituting $c_p = \gamma R/(\gamma - 1)$ and setting $M^2 = V^2/\gamma RT$ gives.

$$\frac{dT}{T} = -\frac{\gamma - 1}{2} M^2 \frac{dV^2}{V^2} \tag{A.14}$$

By combining this equation with Eq. (A.9). the following is obtained.

$$\frac{dV^2}{V^2} - \frac{dM^2}{M^2} = -\frac{\gamma - 1}{2} M^2 \frac{dV^2}{V^2} \tag{A.15}$$

or

$$\frac{dV^2}{V^2} = \frac{1}{1 + \frac{\gamma - 1}{2} M^2} \frac{dM^2}{M^2} \tag{A.16}$$

From the perfect gas law and from continuity relation. it can be shown that.

$$\frac{dp}{p} = -\frac{dV}{V} + \frac{dT}{T} \tag{A.17}$$

But as Eq. (5.11) shows. dT/T can be replaced as follows.

$$\frac{dp}{p} = -\frac{dV}{V} - \frac{\gamma - 1}{2} M^2 \frac{dV^2}{V^2} = \frac{dV^2}{V^2}\left(-\frac{1}{2} - \frac{\gamma - 1}{2} M^2\right) \tag{A.18}$$

The dp/p term and the dV^2/V^2 term in Eq. (A.13) can now be replaced to give.

$$\frac{dV^2}{V^2}\left(-\frac{1}{2} - \frac{\gamma - 1}{2} M^2 + \frac{\gamma M^2}{2}\right) + \frac{4f}{D_H} \frac{\gamma M^2}{2} dx = 0 \tag{A.19}$$

Since velocity can be expressed in terms of Mach number, according to Eq. (A.16), this equation becomes.

$$\frac{1}{1+\frac{\gamma-1}{2}M^2}\frac{dM^2}{M^2}[-1-(\gamma-1)M^2+\gamma M^2]+\frac{4f}{D_H}\gamma M^2 dx=0 \tag{A.20}$$

or

$$\frac{4fdx}{D_H}=\frac{2(1-M^2)}{\gamma M^2(1+\frac{\gamma-1}{2}M^2)}\frac{dM}{M} \tag{A.21}$$

By similar procedures, expressions for dV/V, dp/p, dT/T and $d\rho/\rho$ can be derived. These variables are then expressed as functions of the Mach number.

$$\frac{dV}{V}=-\frac{d\rho}{\rho}=\frac{\gamma M^2}{2(1-M^2)}\frac{4fdx}{D_H}=\frac{dM}{M(1+\frac{\gamma-1}{2}M^2)} \tag{A.22}$$

$$\frac{dp}{p}=-\frac{\gamma M^2[1+(\gamma-1)M^2]}{2(1-M^2)}\frac{4fdx}{D_H}=-\frac{1+(\gamma-1)M^2}{M(1+\frac{\gamma-1}{2}M^2)}dM \tag{A.23}$$

$$\frac{dT}{T}=-\frac{\gamma(\gamma-1)M^4}{2(1-M^2)}\frac{4fdx}{D_H}=-(\gamma-1)\frac{MdM}{1+\frac{\gamma-1}{2}M^2} \tag{A.24}$$

Entropy changes are determined from.

$$ds=c_v\frac{dT}{T}-R\frac{dp}{p}=\frac{\gamma RM^2}{2}\frac{4fdx}{D_H}=\frac{R(1-M^2)}{(1+\frac{\gamma-1}{2})}\frac{dM}{M} \tag{A.25}$$

The second law of thermodynamics states that ds ≥ 0. It is evident from this equation that the friction coefficient f is positive. Also for subsonic flow the Mach number increases, and for supersonic flow the Mach number decreases as a result of frictional flow.

The stagnation pressure can be calculated from.

$$p_0 = p\left(1+\frac{\gamma-1}{2}M^2\right)^{\frac{\gamma}{\gamma-1}} \tag{A.26}$$

Therefore,

$$\frac{dp_0}{p_0} = -\frac{\gamma M^2}{2}\frac{4fdx}{D_H} = -\frac{(1-M^2)}{\left(1+\frac{\gamma-1}{2}M^2\right)}\frac{dM}{M} \tag{A.27}$$

It is evident by comparing Eq. ((A.26) with Eq. (A.27) that changes in entropy and in stagnation pressure are related as follows.

$$\frac{ds}{R} = -\frac{dp_0}{p_0} \tag{A.28}$$

The relative change in stagnation pressure therefore provides an indication of the degree of irreversibility of the process. Note also that frictional flow results in a reduction of stagnation pressure regardless of whether the flow is subsonic or supersonic.

Based on the relations above, relative parameters can be determined by Mach number only, because dx and f are both positive. The following table A.1 explains how each parameter changes along the jet's x-direction.

Table A.1 Parameter Changes along the Jet's x-Direction

Parameter Change	M<1	M>1
dp/dx	<0, decreasing	>0, increasing
DV/dx	>0, increasing	<0, decreasing
$d\rho/dx$	<0, decreasing	>0, increasing
dT/dx	<0, decreasing	>0, increasing
dM/dx	>0, increasing	<0, decreasing
dp_0/dx	<0, decreasing	
dF/dx	<0, decreasing	
ds/dx	>0, increasing	

Equations relating flow variables

The properties of a fluid at any section of a duct may be related to the properties at any other section. Equation (A.21) shows how the Mach number changes with displacement along the duct. By separating the variables and by establishing the limits $M=M_1$ at the entrance of the duct and $M=M_2$ at a distance L, the following integral equation applies.

$$\int_0^L \frac{4f\,dx}{D_H} = \int_{M_1}^{M_2} \frac{1-M^2}{\gamma M^4\left(1+\frac{\gamma-1}{2}M^2\right)}\,dM^2 \tag{A.29}$$

By applying the method of partial fractions to the right-hand side, the following fraction terms are obtained.

$$\frac{1-M^2}{\gamma M^4\left(1+\frac{\gamma-1}{2}M^2\right)} = -\frac{1+\frac{\gamma-1}{2}}{M^2} + \frac{1}{M^4} + \frac{\frac{\gamma-1}{2}\left(1+\frac{\gamma-1}{2}\right)}{1+\frac{\gamma-1}{2}M^2} \tag{A.30}$$

and by treating the friction factor as a constant, the resulting equation can be integrated to give.

$$\frac{4\bar{f}L}{D_H} = \frac{1}{\gamma}\left(\frac{1}{M_1^2}-\frac{1}{M_2^2}\right) + \frac{\gamma+1}{2\gamma}\ln\frac{M_1^2}{M_2^2}\left(\frac{1+\frac{\gamma-1}{2}M_2^2}{1+\frac{\gamma-1}{2}M_1^2}\right) \tag{A.31}$$

where the average friction coefficient $\bar{f}$ is defined as $\bar{f} = \frac{1}{L}\int_0^L f dx$.

Since friction causes the properties of any flow, whether subsonic or supersonic to approach those characteristic of Mach 1, this state is chosen as the reference state and it is denoted by the asterisk (*). Properties of a gas at any section of the duct can therefore be described either on an absolute basis or in relationship to the properties at Mach 1. To express a property in dimensionless form at a particular Mach number, the corresponding expression is integrated between the limits corresponding to that Mach number and the limits and corresponding to Mach 1. These properties expressed nondimensionally in terms of Mach number, are tabulated as follows.

$$\frac{V}{V^*} = M\sqrt{\frac{\gamma+1}{2+(\gamma-1)M^2}} \tag{A.32}$$

$$\frac{p}{p^*} = \frac{1}{M}\sqrt{\frac{\gamma+1}{2+(\gamma-1)M^2}} \tag{A.33}$$

$$\frac{T}{T^*} = \frac{\gamma+1}{2+(\gamma-1)M^2} \tag{A.34}$$

$$\frac{\rho}{\rho^*} = \frac{V^*}{V} = \frac{1}{M}\sqrt{\frac{2+(\gamma-1)M^2}{\gamma+1}} \tag{A.35}$$

$$\frac{s-s^*}{c_p} = \ln M^2\left[\frac{\gamma+1}{[2+(\gamma-1)M^2]M^2}\right]^{\frac{\gamma+1}{2\gamma}} \tag{A.36}$$

Maximum duct Length

When the exit has a flow of Mach number 1, it is said that the duct has the maximum length L_{max}, because, if the length is longer than L_{max}, a shock wave is developed inside the duct. Therefore L_{max} can also be defined as follows: for any given fixed Mach number at the entrance of a duct with length L_{max}, the exit has Mach 1. Eq. (A.30) then it can be rewritten as,

$$\frac{4\bar{f}L_{max}}{D_H} = \frac{1-M^2}{\gamma M^2} + \frac{\gamma+1}{2\gamma}\ln\frac{(1+\gamma)M^2}{2(1+\frac{\gamma-1}{2}M^2)} \qquad (A.37)$$

If the Mach number at the entrance is changed, the maximum length also changes.

To better understand the maximum length L_{max}, variable λ is defined to replace M with the following relation,

$$\lambda = \frac{V}{a^*} \qquad (A.38)$$

where a^* is the reference sonic speed where velocity is equal to local sonic speed. In this case, $V = a = a^*$.

From the energy equation,

$$\frac{V^2}{2} + \frac{a^2}{\gamma-1} = const \qquad (A.39)$$

or

$$\frac{V^2}{2}+\frac{a^2}{\gamma-1}=\frac{a^{*2}}{2}+\frac{a^{*2}}{\gamma-1}=\frac{\gamma+1}{\gamma-1}\frac{a^{*2}}{2} \tag{A.40}$$

or

$$\frac{a^2}{a^{*2}}=\frac{\gamma+1}{2}-\frac{\gamma-1}{2}\lambda^2 \tag{A.41}$$

Since

$$M^2=\frac{V^2}{a^2}=\frac{V^2}{a^{*2}}\frac{a^{*2}}{a^2} \tag{A.42}$$

The relation between M and λ is given by.

$$M^2=\frac{\lambda^2}{1-\frac{\gamma-1}{2}(\lambda^2-1)} \tag{A.43}$$

or

$$\lambda^2=\frac{M^2}{1+\frac{\gamma-1}{\gamma+1}(M^2-1)} \tag{A.44}$$

Then Eq. (A.37) can be rewritten as.

$$\frac{4\bar{f}L_{max}}{D_H}=\frac{\gamma+1}{2\gamma}\left(\frac{1}{\lambda^2}-1-\ln\frac{1}{\lambda^2}\right) \tag{A.45}$$

Appendix B Details of PIV Technique

This Appendix discusses the general aspects of PIV, including the principle, techniques used, the rules, laser optics and synchronization, based on TSI PIV system.

The PIV system used in our experiment is a standard system by TSI, the first company to commercialize PIV systems worldwide. In the following introduction of PIV techniques, TSI will mentioned solely because some theories are based on this TSI system specifically.

B.1 Principle of Particle Image Velocimetry

The experimental set-up of a PIV system typically consists of several sub-systems. In most applications tracer particles have to be added to the flow. These Particles have to be illuminated in a plane of the flow at least twice within a short time interval. The light scattered by the particles has to be recorded either on a single frame or on a sequence of frames. The displacement of the particle images between the light pulses has to be determined through an evaluation of the PIV recordings. In order to be able to handle the great amount of data which can be collected employing the PIV technique, sophisticated post-processing is required.

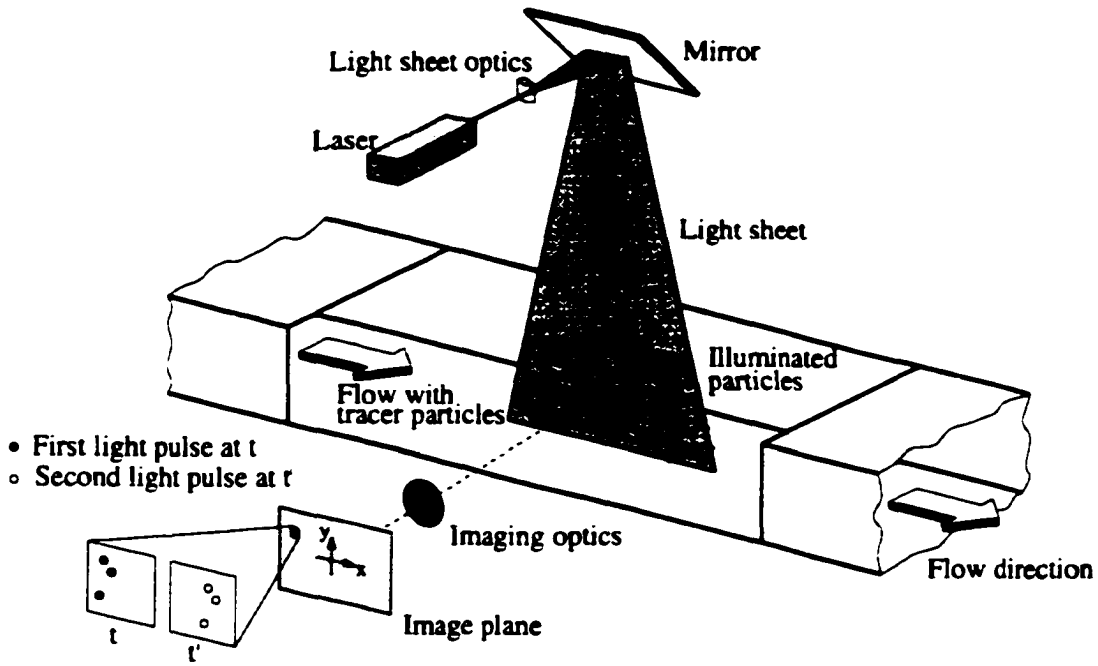

Figure B.1: Experimental Arrangement for Particle Image Velocimetry in a Wind Tunnel

(Raffel. M.. Willert. C.. Kompenhans. J. Particle Image Velocimetry *Springer*)

Figure B.1 briefly explains a typical set-up for PIV recording in a wind tunnel. Small tracer particles are added to the flow. A plane (light sheet) within the flow is illuminated twice by means of a laser (the time delay between pulses depends on the mean flow velocity and the magnification at imaging). It is assumed that the tracer particles move with local flow velocity between the two illuminations. The light scattered by the tracer particles is recorded via a high quality lens either on a single photographical negative or on two separate frames on a special cross correlation CCD sensor. After development

the photographical PIV recording is digitized by means of a scanner. The output of the CCD sensor is stored in real time directly in the memory of a computer.

For evaluation the digital PIV recording is divided in small subareas called "interrogation areas". The local displacement vector for the images of the tracer particles of the first and second illumination is determined for each interrogation area by means of statistical methods (auto- and cross- correlation). It is assumed that all particles within one interrogation area have moved homogeneously between the two illuminations. The projection of the vector of the local flow velocity into the plane of the light sheet (2-component velocity vector) is calculated taking into account the time delay between the two illuminations and the magnification at imaging.

The process of interrogation is repeated for all interrogation areas of the PIV recording. With modern video cameras (i.e. 1k x 1k sensor elements) it is possible to capture more than 100 PIV recordings per minute. The evaluation of one video PIV recording with 3600 instantaneous velocity vectors (depending on the size of the recording and of the interrogation area) is of the order of a few seconds with standard computers. if even faster availability of the data is required for on line monitoring of the flow, dedicated hardware processors are commercially available which can perform evaluations of similar quality within fractions of a second.

B.2 Lasers and Optics

In a PIV experiment, lasers are used to produce the high-energy pulsed lightsheet for taking PIV photographs of small particle images. TSI has developed the PIV system using three types of lasers: Argon Ion laser, Single/Double Pulsed Nd:YAG laser, and Dual Nd:YAG laser.

Two Nd:YAG Lasers

In the two-laser configuration one laser fires first, then the other fires after a time delay. This allows from either one short or long pulse separation with the full power of each laser. The beams from the two lasers illuminate the same flow field at a different time in order to capture the particle movement. Several Nd:YAG laser manufactures make PIV laser systems with two laser cavities and beam combination optics built into a single box. The TSI Model 610010 Beam Combination Optics can be used to combine the laser beams from two Continuum Surelite Nd:YAG lasers.

Double Pulsed Nd:YAG

An alternative to using two Nd:YAG lasers is the double pulsed Nd:YAG laser. The double pulsed Nd:YAG laser fires the Q-Switch twice during a single flashlamp discharge. The double pulsed laser has the advantage of being easier to align than a two-laser system. The Q-Switch delay time must be set with the time between pulses (ΔT) to get two equal energy pulses. A double pulsed laser can produce two pulses with about

1/3 the single pulse energy of the laser single pulsed. The pulse energy is a function of the time between pulses and the energy declining with increase time between pulses. The maximum time between pulses with a double pulsed laser is about 200 μs. This makes the double pulsed laser appropriate for flows with velocities of 1 m/s or higher.

Lightsheet Optics

The flow in a PIV experiment is illuminated with a pulsed laser lightsheet. Typically, a collimated laser beam is transmitted through a cylindrical lens to diverge the beam in the height direction and a spherical lens is used to control the thickness of the lightsheet. Figure B.2 shows the lightsheet optics. The camera usually is focused near the lightsheet waist, at the focal length of the spherical lens.

The cylindrical lens has a negative focal length and diverges the beam. Small focal lengths diverge the lightsheet faster than longer focal lengths. The focal length of the spherical lens is much longer than the cylindrical lens making the selection of the spherical and cylindrical lenses independent of each other. The spherical lens was selected to provide the proper-sized lightsheet thickness where the photograph was taken. The cylindrical lens was selected to give the proper lightsheet height at that point.

When selecting the lightsheet dimensions, keep in mind that the larger the cross sectional area is, the lower the light intensity is. To expose the particles, the light intensity must be high enough. The photograph can be taken anywhere along the

lightsheet. but usually the best place is at the focal distance of the spherical lens near the lightsheet thickness waist. where the lightsheet is the thinnest. so the light intensity is higher.

When selecting the lightsheet dimensions. we must also consider the variation in the beam intensity over the photograph area. A typical problem arises when getting the thinnest lightsheet. then a short focal length spherical lens is used. Since the thickness divergence is larger for short focal-length lenses. there may be a large difference in intensity due to the lightsheet thickness.

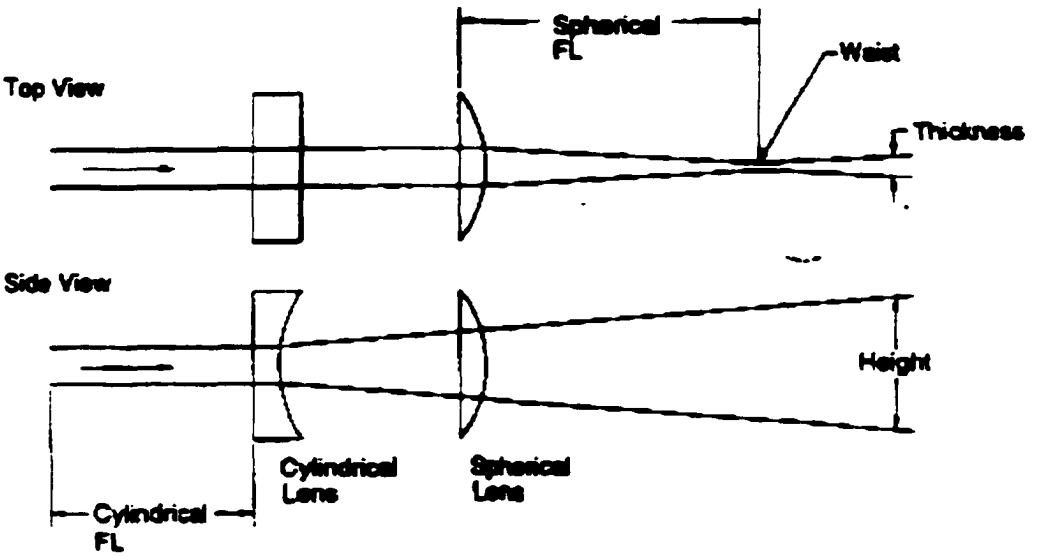

Figure B.2: Lightsheet Optics

B.3 Synchronization

In TSI system, Model 610030 Synchronizer provides the timing and the sequence of events while taking a PIV photograph. Having all of the components working together is critical a good photograph to capture and to render a good PIV image. Each of the components requires some time to operate and only by sequencing properly, good photograph can be obtained.

There are however, a couple of cases where sequencing the operation of the equipment by a Synchronizer is not really necessary. One such case is when using an Argon ion laser that is operating in the continuous pulse mode. Here, synchronization is not necessary because the laser is always pulsing, and the camera can capture the image at any time. The number of pulses depends on the camera's shutter speed. For instance, if the laser is pulsing with 1 ms between pulses and the camera shutter is set for 1/30 sec, 33 ms exposure then camera records about 33 pulses. However, since image shifting cannot be used, the determination of flow direction is not possible.

In very low-speed flows case, using a video camera without a synchronization is possible for measurement. For instance, the Model RS-170 system with 30 frames per second image capture rate is used, and the particle is not moving very much within the 1/30 second, then the laser lightsheet does not have to be pulsed and by cross correlating two frames, maybe several camera frames apart, then the velocities can be measured.

However, in cases where the laser is being double pulsed or image shifting is being used, we have to ensure that all the parts are working together. The following sections describe the tiring sequence for all the PIV components.

Timing Requirements for PIV Components

The following discusses the timing requirements for each PIV component.

- **Nd:YAG Lasers**

Nd:YAG lasers require two signals to create a laser pulse: the first one triggers the flashlamp, and the second signal opens the Q-Switch that pulses the laser. With single, double pulsed lasers, the second pulse is created by Q-Switching the other Marx bank in the laser. With dual, Nd:YAG laser systems, each laser receives a flashlamp and W-Switch signal. The delay time from flashlamp to Q-Switch is usually 150 to 200 μs.

- **Cameras**

The PIV system can operate with a variety of cameras. Cameras with external triggers and mechanical shutters such as 35mm and KODAK™ and MEGAPIMS™ cameras are triggered by the Synchronizer to start the exposure. When the mechanical shutter is fully open the camera signals the Synchronizer camera shutter feedback to flash the laser.

Other externally triggered cameras without a flash synchronization can also be used with the Synchronizer. The Synchronizer triggers the camera and then waits for the programmed Pulse Delay time before firing the laser.

- **Without Image Shifting**

The sequence of events for capturing a series of frames without image shifting is:

1. Synchronizer triggers the camera to start exposure
2. Camera starts exposure and triggers the Synchronizer then the shutter is open with the flash sync output
3. Synchronizer sends fire signals to the laser for the first pulse.
4. Synchronizer waits the selected pulse separation time
5. Synchronizer sends signals for the second pulse of light.
6. The camera shutter closes at the end of the exposure time.
7. Camera winds up the film to the next frame or outputs the video data.
8. Repeat the sequence for the number of frames to capture. The camera must be ready for the next exposure to trigger before the frame rate time or an error will occur.

B.4 Post Processing

Post Processing refers to the analysis of the velocity vector field after the vectors have been extracted from the PIV image. Post processing consists of two basic functions—vector editing and computing flow properties.

Vector editing is necessary because some wrong peaks may be chosen as the velocity peak. In vector fields with 1,000 points, ninety-nine percent correct vectors still give 10 wrong vectors. During the image processing the signal-to-noise ratio at each spot must pass the threshold values to be considered a valid peak. Usually these thresholds are set to filter out most of the bad points, but if the thresholds are too high to filter out all the bad points, many good points are also eliminated.

In post processing, the vectors are compared against the neighboring vectors. Vectors that vary by more than the validation tolerance from the neighborhood average, are removed. This neighborhood check enforces continuity on the flow. Places that are left empty can be filled in by interpolating the neighboring vectors to get the best estimate of the velocity at that point.

After the vector has been validated and the missing points filled in, the properties of the flow can be computed. Measuring the flow properties like vorticity from the accurate vector field data is one of the key reasons for performing PIV measurements. The post

processing module computes vorticity, five strain rates, and the velocity magnitude. These parameters can be displayed by color-coding the arrows or by contour displays.

The post processing is performed using another Windows application called DATASHOW for Windows. On UNIX systems, post processing can be done from within the INSIGHT program.

B.5 PIV Techniques

Knowing the principle of PIV, we may develop a few techniques to perform velocity measurement. Three of these techniques are popular. Autocorrelation, 1-frame Crosscorelation and 2-frame Crosscorrelation. 1-frame Crosscorrelation is more complicated and requires the Image Shifter to remove ambiguity, therefore, it is not used in our experiment.

B.5.1: Autocorrelation

To better understand autocorrelation, computing autocorrelation with convolutions is shown here as an example. Figure B.3 shows direct correlation between one frame and itself.

In the convolution method, two copies of the interrogation spot are used. One image is overlaid on top of the other with a pixel offset corresponding to the displacement being checked. The autocorrelation function is the sum of the products of the aligned pixel values. The summation of pixel intensity products is computed for each displacement of the correlation being checked. Graphing the summation at each offset gives the autocorrelation function.

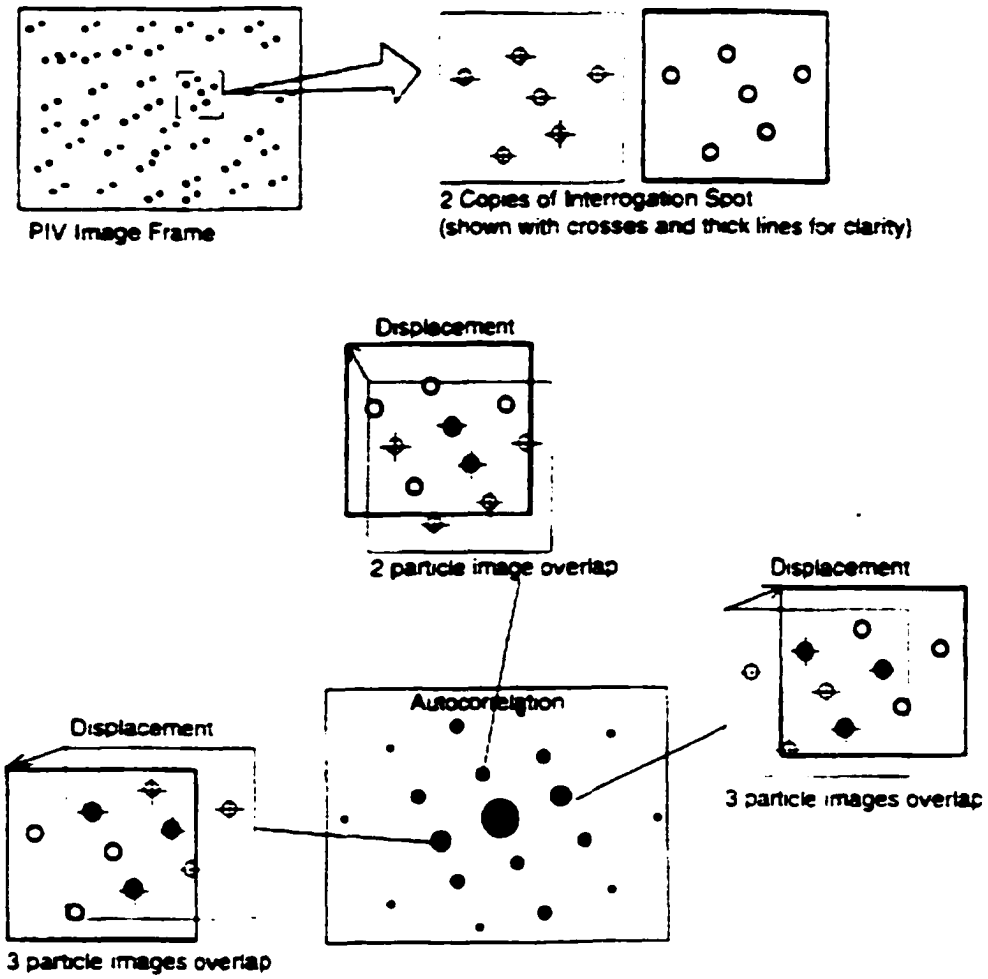

Figure B.3: Direct Correlation

Correlation by convolution can be done using two positive transparencies and an overhead projector. Each of the positive transparencies has a black background with clear particle images. The light passes through areas where two particle images are lined up while in areas where a particle image aligns with the black background of the other transparency, no light is transmitted. The total light transmitted through both

transparencies is the correlation function.

When the two transparencies are overlaid with no displacement. all of the particle images from the first transparency are aligned with a particle image in the second transparency and light is transmitted. This is the zero peak and produces the strongest correlation possible.

To measure the correlation for a given particle displacement. the second transparency is translated by the particle displacement distance relative to the first transparency. The transmitted light through the transparencies is the correlation at that displacement. To compute the autocorrelation function each possible displacement is tried and the results are plotted on a graph. The displacement with the highest correlation is the particle image displacement.

Autocorrelation Using FFTs

Having seen the particle tracking and convolution methods of performing autocorrelation. let us now examine how INSIGHT NT performs autocorrelation using FFTs. The following is a non-mathematical explanation of how 2D FFTs are performed with the INSIGHT NT software.

A two-dimension FFT is a one-dimensional FFT performed on each column of data followed by a one-dimensional FFT on each row of data. The input image data is real.

the FFT output is complex, with real and imaginary components. The complex FFT output data is converted into the real power spectrum, without the phase information. The power spectrum contains the information about the distance between particle images, while the phase contains information about the particle location.

B.5.2: 2-Frame Crosscorrelation

2-frame crosscorrelation uses two image frames with one pulse of light on each frame. The flow velocity is found by measuring the distance that the particles have traveled from frame 1 to frame 2. With 2-frame crosscorrelation, only the images from laser pulse 1 are on frame 1, and only second laser pulse images are on frame 2. This complete separation of the particle images allows the velocity to be without directional ambiguity. Image shifting is not required to resolve the directional ambiguity for 2-frame crosscorrelation. Zero-velocity does not exist of 2-frame crosscorrelation techniques. Since the particle image is recorded on two image frames, a particle with zero velocity shows up on both image frames at the same location can be measured, the velocity will be zero.

The signal-to-noise ratio of 2-frame crosscorrelation is the best among all the correlation methods. This is because only first particle images are in the image window 1 and only second particle images are in image window 2. There is NO overlapping of first and second particle images as in the case with single image frame system.

The limitation of using 2-frame crosscorrelation is in the effective image capture rate, or frame rate. The particle must move less than one-fourth of the interrogation spot in the time between the first and second laser pulses. The framing rate for 35mm film cameras, and many high resolution CCD cameras, makes the 2-frame crosscorrelation PIV not practical. With standard RS-170, the time between frames is 33 ms, or 30 Hz. With CCD, the time between frames is 40 ms, or 25 Hz. The time interval of 33 ms between images is only useful for low velocity flows. To increase the effective frame rate, "frame straddling" is used. In frame straddling the laser is pulsed at the end of the first exposure period and then at the start of the second exposure period. This allows short time intervals between pulses for high velocity flows to be measured. When frame straddling is used with a 30-Hz camera, two image frames are required for each measurement and the flow sampling rate is 15 Hz. For best results, a camera that can capture a picture, then move the image into memory and starts integrating the next image frame quickly is desired. The movement of charge between the photosensitive pixels and memory must be very fast for high-speed 2-frame cross-correlation. The time it takes from the end of one exposure period and the start of the next exposure period determines the maximum flow velocity that can be measured. The time it takes to readout the image from the CCD to the computer determines the frame rate or how frequently the flow can be sampled.

This power spectrum that result from the 2D FFT is a computed Young's Fringe pattern. The particle displacements are in the frequency domain. In many early PIV analysis systems, the Young's Fringe was optically obtained using a HeNe laser to illuminate a

PIV transparency. This processing technique was used primarily because less computing power was available at that time. With Young's Fringe patterns as the input image only, a single 2D FFT is computed to get the autocorrelation. An inverse 2D FFT and power spectrum on the Young's Fringe pattern produces the autocorrelation.

The power spectrum is computed from the sum of the squares of the real and imaginary components. The square root of the computed power spectrum should be used to get the same scaling factors for the peak intensities to compare the direction correlation techniques with FFT correlation. Calculating the square root of the computer power spectrum was skipped to save processing time. It does not affect which peak is selected as the displacement peak, but it does change the relative peak intensities and the signal-to-noise ratio numbers.

One difference between processing the data using direct correlation methods and FFT correlation processing method is aliasing. With the particle tracking histogram technique, the maximum displacement is the full interrogation spot size. With the correlation by convolution the maximum displacement is limited to the displacements checked. In both these cases if the displacement is too large the particle pair peak is unlikely to be measured. With FFT autocorrelation displacements, from two particle image diameters up to half the interrogation spot are measured correctly. Displacements between half to the full spot size are measured in the wrong location.

Displacements larger than half the spot are in an aliased position in the autocorrelation. With these large displacements, the peak moves back towards the center. The true displacement is the distance to the edge of the autocorrelation plus the distance from the edge to the peak. The peak location measured as the distance from the center to the peak is not the true distance. Because of the danger of aliasing, the autocorrelation is not searched to the edges for peaks. With the outer 1/8 of the autocorrelation not searched displacements from 3/8 to 5/8 the spot are not allowed. This leaves only displacements from 5/8 to 1 spot that can be measured in an alias position. Care must be taken to set up the processing parameters so that these very large displacements do not happen.

B.6 Rules of Correlations

This section gives some guidelines on optimizing experiment for best PIV results. To get the best results from a PIV experiment, the image capture and the interrogation zone must match the flow. Typically, the parameters that can be set to optimize the measurement are: the time between laser pulses (dT); interrogation spot size; photograph magnification; lightsheet dimensions; seed particle and seed concentration. With these parameters in mind, the following rules were developed. Since the difference between autocorrelation and crosscorrelation is only the storage for images, the rules are about the same. Therefore we list only the rules for autocorrelation.

Rule-of-Thumb for Autocorrelation PIV Analysis

Rule 1: Interrogation spot size should be small enough so that one vector describes the flow within that spot.

Rule 2: There should be more than ten particle image pairs per interrogation spot.

Rule 3: Maximum in plane displacements should be less than ¼ of the interrogation spot size.

Rule 4: Maximum out-of-plane displacement should be less than ¼ of the lightsheet thickness.

Rule 5: Minimum in-plane displacement should be two particle-image diameters.

Rule 6: Exposure must be large enough to clearly show the particles.

Rule 1: Interrogation-Spot Size Should be Small Enough For One Vector to Describe Flow for That Spot

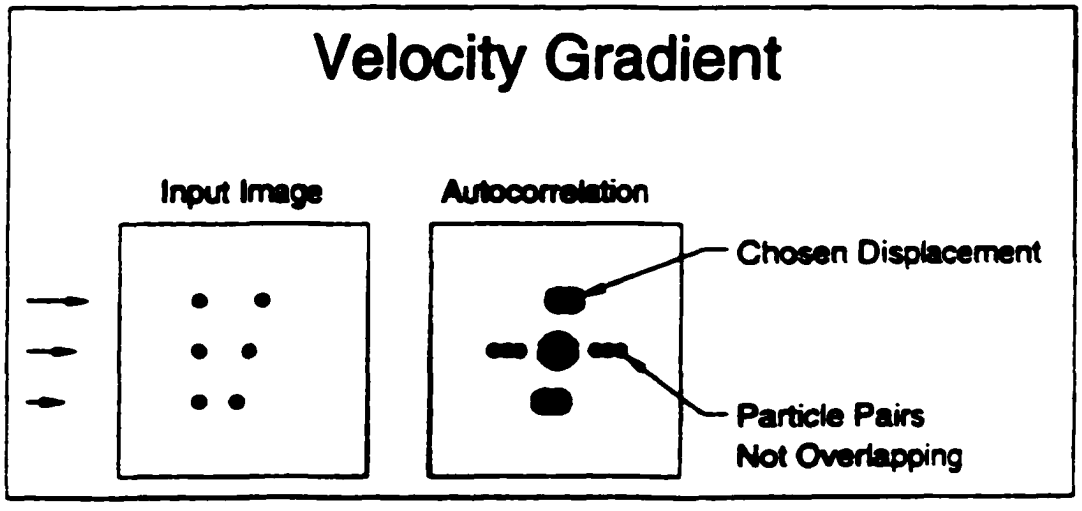

Figure B.4: Error from Velocity Gradient

Rule 2: Should Have More than Ten Particle Image Pairs Per Interrogation Spot

The percentage of correct velocity measurements as a function of the number of particle pairs has been established by Keane and Adrian. Their results are shown in Figure B.5. These results show that the percentage of correct velocity measurements correlates strongly with the number of particle image pairs in the spot. (This work also takes lost pairs, and Rules 3 and 4 into account.) As the concentration increases beyond one per spot, the percentage of valid measurements increases. This is because many pairs of

particle images contribute to the displacement peak. The noise peaks caused by the correlation of the images of different particles decrease relative to the displacement peak. The loss of some pairs is tolerable because many others pairs are still creating the displacement peak.

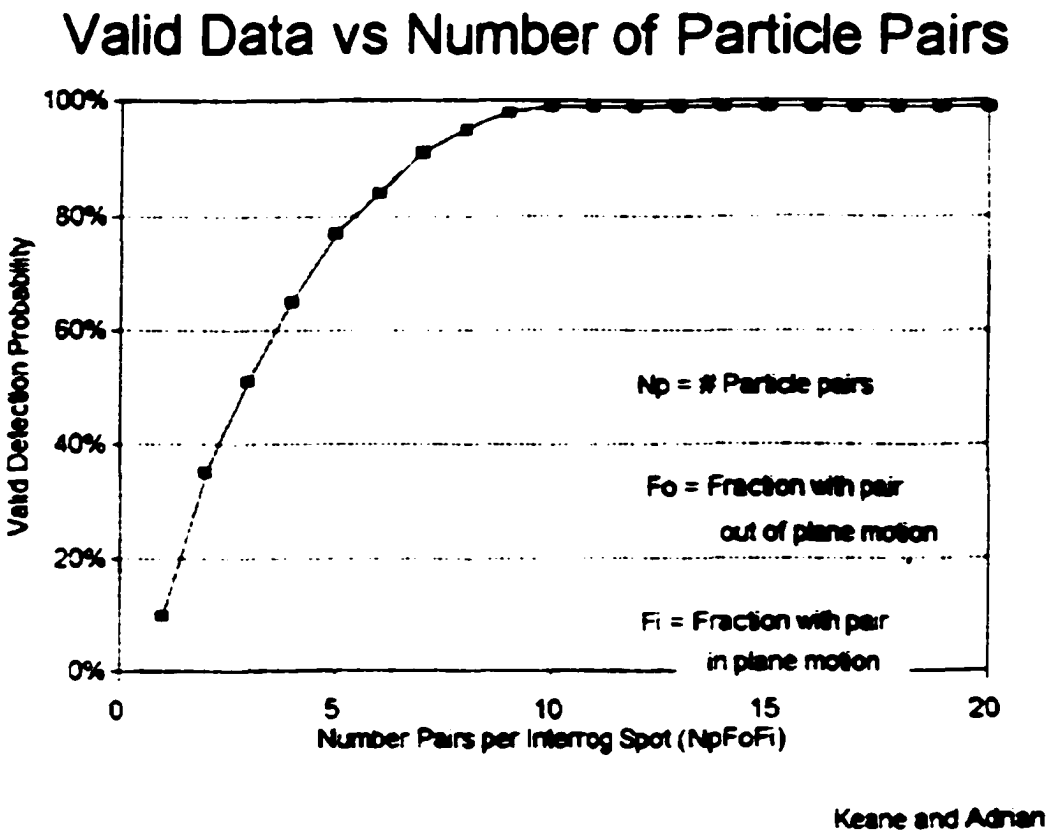

Figure B.5: Correlation of Correct Velocity Measurements with The Number of Particle Images

Particle image concentrations with an average of one per interrogation spot produce the most erroneous measurements. This is because there is a high probability of having two

pairs. or one and a half pairs or two half pairs in the interrogation spot. With two pairs of particles of equal size. the correlation for the distance between the two particles is as strong as the distance between the first and second image. With two pairs of particles of equal size. the wrong measurement is made fifty-percent of the time. With these low concentrations. a single particle that crosses the interrogation spot boundary can cause wrong measurements to be made. Figure B.6 illustrates these errors for low particle-image concentration images.

The percentage of correct velocity measurements increases with decreasing particle image concentrations from an average of one pair per spot down to very low concentrations. This is because where a pair of particles is found. it is unlikely that a second particle will also be in that same spot to cause confusion about the correct pairing. A velocity measurement is only possible where a pair of particles is found. threfore very low seeding concentration pictures produce sparse vector fields. If the goal of the experiment is to measure the flow on a high resolution grid. low seeding concentrations must be avoided. This increasing correct vectors with decreasing particle concentrations lead us to assume that the processor is set to reject areas with very low signals and that it can distinguish between the gray scale variations in background light and the particle images.

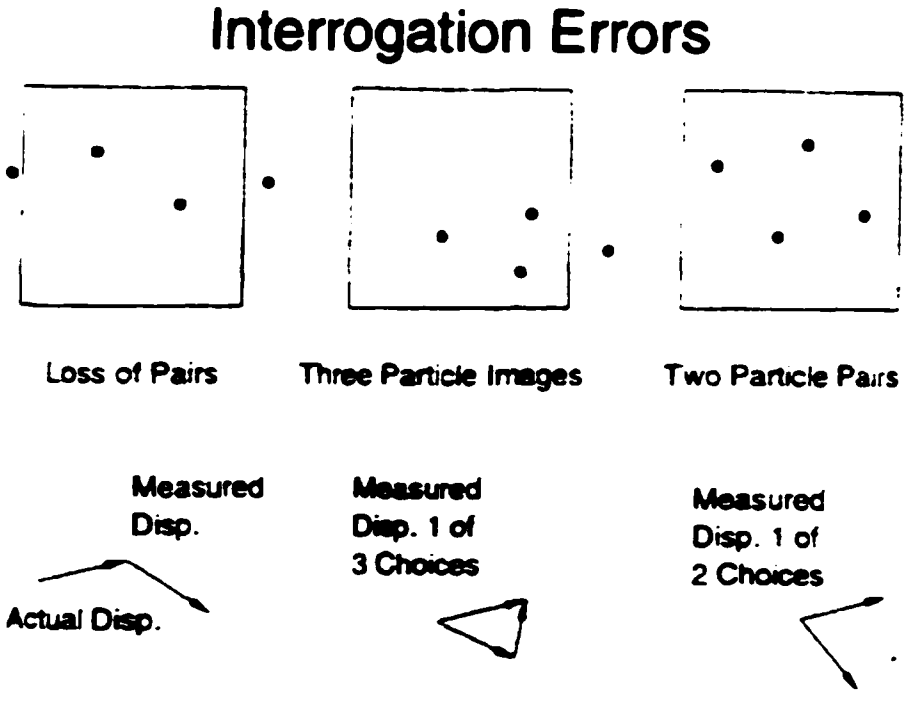

Figure B.6: Interrogation Errors

Effective seeding can be increased by increasing the interrogation spot size. With a larger interrogation spot there are more pairs per spot. When you increase the spot make sure that you are not violating the velocity gradient requirement of Rule 1. Decreasing the interrogation spot gives more velocity vectors with the same interrogation spot overlap. For high-resolution work and for investigating small flow structures, you should select small interrogation spots.

Rule 3: Maximum In-Plane Displacements Should Be Less than One-Fourth Interrogation Spot Size

This maximum displacement is a compromise between two parameters: Large displacements for the best percent of reading accuracy and small displacements to minimize lost pairs.

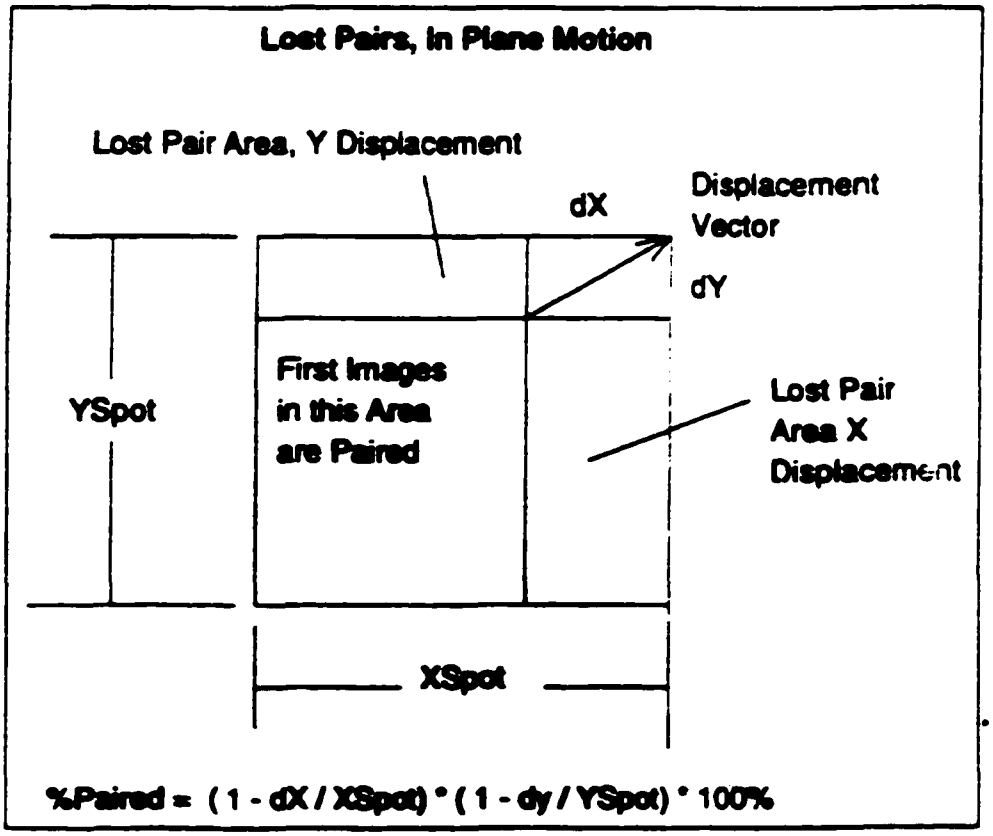

Figure B.7: Lost Pairs

As explained before, the velocity is measured by finding the location of the particle displacement peak. The location of the peak is measured with centroid or curve fit to a fraction of a pixel. The accuracy of the PIV measurement is a percent of full scale, or a number of pixels. The peak location error is the same wherever it is located, near the center zero velocity peak or near the edge. With large displacements the peak location error is a smaller percent on the reading than small displacement peaks. The absolute maximum displacement that gives the correct displacement is half of the interrogation spot. If large displacements are used, the FFT aliases, the peak location, and the measured peak give the wrong velocity.

Lost pairs refers to particles that are inside the interrogation spot for only one laser pulse. In-plane motion causes particles to move across the spot border. Fast moving particles are more likely to lose a pair than in the case of slow particles. Lost pairs create a velocity bias towards slow velocity flow. The lost pair estimation is given in Rule 4. The compromise between these two objectives is 1/4 spot displacement, to give good pairing and to give accuracy of the system.

Rule 4: Maximum Out-of-Plane Displacement Should be Less Than One-Fourth of Lightsheet Thickness

This rule is established to keep the lost pairs (due to out-of-plane motion) to an acceptable level. In many experiments the lightsheet is about 1 mm thick and the interrogation spot is 1mm *x* 1mm. With this 1mm cube measurement volume, the restrictions on out-of-plane displacement is no greater than the in-plane displacement. With both in-plane and out-of-plane displacements considered, the estimated percentage of particles with pairs in the interrogation spot is:

Percentage Paired=(1-dX/Xspot)*(1-dY/YSpot)*(1-dZ/Thick)*100%

where

Percentage Paired= Percent of particles with a pair in the interrogation spot

dX=Particle image displacement in X direction

dY=Particle image displacement in Y direction

dZ=Particle image displacement is Z direction, out of plane motion

XSpot=Interrogation spot size in X direction

YSpot=Interrogation spot size in Y direction

Thick=Lightsheet thickness

When the maximum one-fourth interrogation spot and lightsheet thickness image displacement is used, an average of 42% of the particle images are paired. The seeding concentration must be increased for the lost pairs to get the same results. For one-fourth

spot displacements in all three directions. the required seeding concentration is ten pairs per spot divided by the .42 paired. which is equal to 24 pairs per spot.

Rule 5: Minimum In Plane Displacement Should Be Two Particle Image Diameters

If the particle image displacement is less than two particle image diameters. the image would be one elliptical particle image instead of two particle images. The autocorrelation zero peak and displacement peaks must be separated to accurately measure the centroid of the displacement peak. If the peaks overlap. the centroid will include some of the zero peak and bias the measurement towards zero displacement.

Figures B.8 and B.9 show the autocorrelation at two points in a turbulent flow. The displacement at the first spot is about two particle-image diameters. In the autocorrelation. the displacement peak has separated from the central zero peak. This point gives a good velocity measurement.

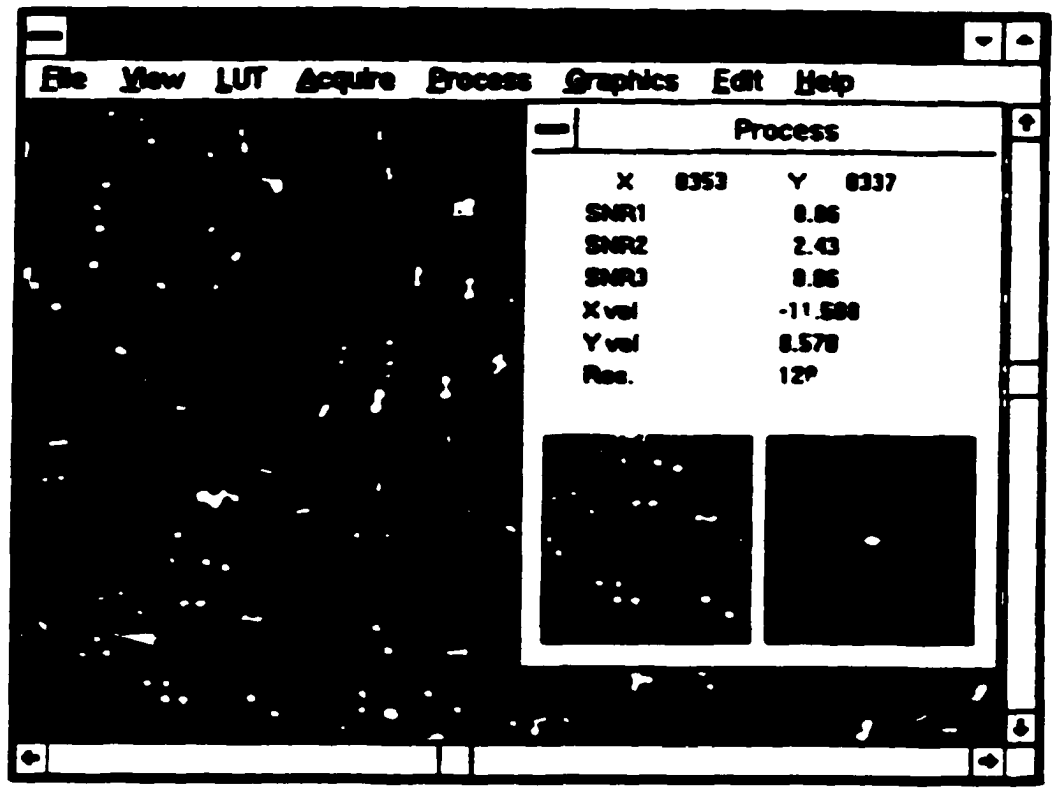

Figure B.8: Autocorrelation at Two Points in a Turbulent Flow

Figure B.9 shows an interrogation spot with about one particle-image diameter displacement. Here the displacement peak is connected to the central zero peak producing a single oval central peak. When the displacement peak blends into the zero peak, velocity measurement error occurs. In this case the measured velocity is the distance between particles and not the particle image displacement.

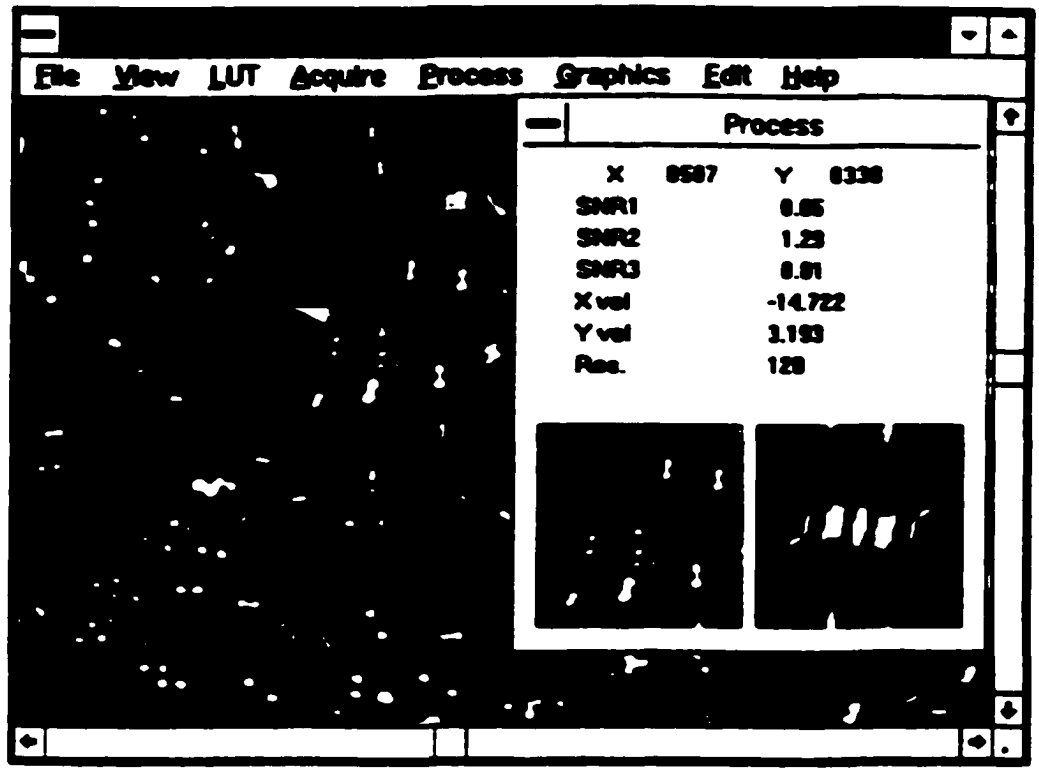

Figure B.9: An interrogation Spot with One Particle-image Diameter Displacement

Rule 6: Exposure Should be Large Enough To Show Particles

There are many factors that determine the exposure. These are:

1. Laser energy

2. Lightsheet dimensions

3. Camera Focal length number

4. Photograph magnification

5. Film Speed and resolution

6. Particle size, and

7. Particle material

The PIVCALC program uses all the above experimental parameters, except particle scattering parameters, to compute the lightsheet intensity and camera exposure.

Regarding particle scattering, the particle size and material determine the scattered light power in the image of each particle. The particle scattering is in the Mie regime for most PIV applications. Mie scattering is complex and the scattered energy varies greatly with scattering direction, particle size, and particle index of refection. The complexity of Mie scattering makes it difficult to make general statements about how much exposure is required for a given experiment. In most applications, the correct exposure can be found through trial and error.

It is difficult to quantify the parameters that affect exposure and come up with a clear recommendation. Generally, you can use a 5-Watt Argon Ion laser for water flows that have low velocities. Use a Nd:YAG laser for higher velocity flows, especially for air flows with micron-sized seed particles.

B.7 Characteristics of PIV

With the introduction above. we outlined the characteristics of PIV measurement.

- **Nonintrusive velocity measurement.** In contrast to techniques for the measurement of flow velocities employing probes as pressure tubes or hot wires. the PIV technique being an optical technique works nonintrusively. This allows the application of PIV even in high speed flows with shocks or in boundary layers close to the wall. where the flow may be disturbed by the presence of probes.

- **Indirect velocity measurement**. In the same way as with laser Doppler velocimetry the PIV technique measures the velocity of a fluid element indirectly by means of measuring the velocity of tracer particles within the flow. which in most applications have been added to the flow before the experiment started. In two phase flows the particles are already present in the flow. In such a case it will be possible to measure the velocity of the particles themselves as well as the velocity of the fluid (to be additionally seeded with small tracer particles).

- **Whole field technique**. PIV is a technique which allows one to record images of large parts of flow fields in a variety of applications in gaseous and liquid media and to extract the velocity information out of these images. This feature is unique to the PIV technique. Except Doppler global velocimetry (DGV). which is a new technique

particularly appropriate for high speed air flows. All other techniques for velocity measurements allow only the measurement of the velocity of the flow at a single point, and in most cases with a high temporal resolution. With PIV the spatial resolution is large, whereas the temporal resolution (frame rate of recording PIV images) is limited due to technical restrictions. These features must be observed if comparing results obtained by PIV with those obtained with traditional techniques. Instantaneous image capture and high spatial resolution at PIV allow the detection of spatial structures even in unsteady flow fields.

- **Velocity lag.** The need to employ tracer particles for the measurement of the flow velocity requires us to check carefully on each experiment whether the particles will faithfully follow the motion of the fluid elements. At least to the extent required by the objectives of the investigation. Small particles will follow the flow better.

- **Illumination.** For applications in gas flows a high power light source for illumination is required in order for the light scattered by the tiny tracer particles to expose the photographic film or the video sensor. However, the need to utilize larger particles because of their better light scattering efficiency is in contradiction to the demand to have as small particles as possible in order that they follow the flow faithfully. In most applications a compromise has to be found. In liquid flows larger particles can usually be accepted which scatter much more light. Thus, light sources of considerably lower peak power can be used here.

- **Duration of illumination pulse**. The duration of the illumination light pulse must be short enough so that the motion of the particles is "frozen" during the pulse exposure in order to avoid blurring of the image ("no streaks").

- **Time delay between illumination pulses**. The time delay between the illumination pulses must be long enough to be able to determine the displacement between the images of the tracer particles with sufficient resolution, and short enough to avoid particles with an out-of-plane velocity component from leaving the light sheet between subsequent illuminations.

- **Distribution of tracer particles in the flow**. At qualitative flow visualization certain areas of the flow are made visible by marking a stream tube in the flow with tracer particles (smoke, dye). According to the location of the seeding device the tracers will be entrained in specific areas of the flow (boundary layers, wakes behind models, etc.). The structure and the temporal evolution of these structures can be studied by means of qualitative flow visualization. For PIV the situation is different: a homogeneous distribution of the medium density is desired for high quality PIV recordings in order to obtain optimal evaluation. No structures of the flow field can be detected on a PIV recording of high quality.

- **Density of images of tracer particles on the PIV recording**. Qualitatively three different types of image density can be distinguished, which is illustrated in Figure B.10. In the case of low image density (Figure B.10a), the images of individual particles can be detected and images corresponding to the same particle originating from different illuminations can be identified. Low image density requires tracking methods for evaluation. Therefore, this situation is referred to as "particle tracking velocimetry", abbreviated "PTV". In the case of medium image density (Figure B.10 b) the images of individual particles can be detected as well. However, it is no longer possible to identify image pairs by visual inspection of the recording. Medium image density is required to apply the standard statistical PIV evaluation techniques. In the case of high image density (figure B.10c) it is not even possible to detect individual images as they overlap in most cases and form speckles. This situation is called "laser speckle velocimetry" (LSV), a term which has been used at the beginning of the 80's for the medium image density case as well, as the (optical) evaluation techniques were quite similar for both situations.

- **Number of components of the velocity vector**. Due to the planar illumination of the flow field only two (in plane) components of the velocity vector can be determined in standard PIV (2C-PIV). Methods are already available to extract the third component of the velocity vector as well (stereo techniques, dual-plane PIV, holographic recording). This would be labeled 3C-PIV. Both methods work in planar domains of the flow field (2D-PIV).

Number of illuminations per recording. For both photographic and video techniques, we have to distinguish whether it is possible to store images of the tracer particles on different frames for each illumination, or whether all particle images due to the different illuminations are stored on a single frame.

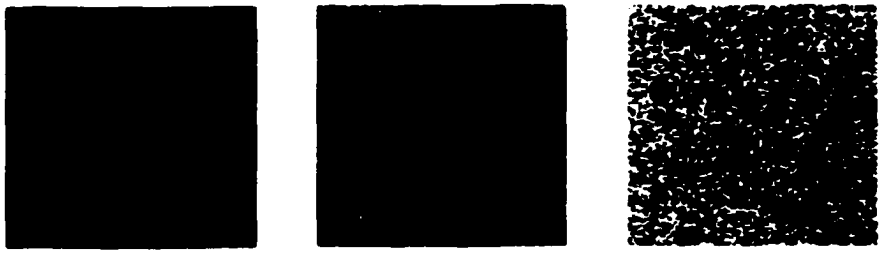

Fig. B.10: The Three Modes of Particle Image Density: (a) Low (PTV), (b) Medium (PIV), and (c) High Image Density (LSV).

Extension of observation volume. In the most general way an extension of the observation volume is possible by means of holographic techniques (3D-PIV). Other methods such as establishing several parallel light sheets in a volume or scanning a volume in a temporal sequence would be referred to as 2+1D-PIV.

Extension in time. By means of repetitively working cameras it is already possible to record temporal sequences of PIV recordings. However, as the repetition rate of pulse

lasers and cameras is limited, it is not possible to record fast enough as it would be required due to the temporal scales of most flows.

Size of interrogation area. The size of the interrogation area at evaluation must be small enough for velocity gradients to have no significant influence on the results. Furthermore, it determines the number of independent velocity vectors. Therefore the maximum spatial resolution of the velocity map can be obtained at a given spatial resolution of the sensor employed for recording.

Repeatability of evaluation. In PIV full information about the flow velocity field (except the time delay between pulses and magnification at imaging) is stored during recording time at a very early stage of data reduction. This leads to a very interesting feature that on PIV recordings, information can easily be exchanged for evaluation and post processing with others, employing different techniques. The information about the flow velocity field completely contained in the PIV recording can be exploited later on, in quite a different way from what it had originally been planned without the need of repeating the experiment.

In this section the main features of the PIV technique have been described briefly to support a general understanding of its unique features. PIV offers new insights in fluid mechanics especially in unsteady flows as it allows to capture of whole velocity field instantaneously. Together with other quantitative flow visualization techniques giving information about other important physical quantities of a fluid such as density,

temperature, concentration, etc., which are already well known and widely used, and new optical methods for the measurement of quantities on the surface of a model such as pressure or deformation, a more complete experimental description of a complex flow field will be possible and will be available for comparison with the results of numerical calculations in future.

Appendix C Program Jet Exit Pressure

The following is the Fortran program for Gauge pressure. which is used to control the exit Mach number.

```
      program main

      real ms_in. ms_exit
      real ms_in_max. ms_in_min

c     gama=1.667  for helium
c     gama=1.24 for krypton
c     gama=1.4 for nitrogen

      print*." This program is used to find the gage pressure"
      print*." at which the required exit mach number of the "
      print*." jet has been achieved"

      ms_in_max=0.99
      ms_in_min=0.01

      print*. "gama=1.667  for helium"
      print*. "gama=1.24 for krypton"
      print*. "gama=1.4 for nitrogen"
      print*. "input gas constand gama:"
      read(*.*)gama
      print*. "ms_exit=0.3"
      print*. "ms_exit=0.6"
      print*. "ms_exit=0.9"
      print*. "input required mach number at exit:"
      read(*.*)ms_exit
      fbar=0.0068
      dh=0.277
      tube_l=6.7-13.6-30*dh
      p_exit=14.7
      p_star=sqrt((gama-1)/(2-(gama-1)*ms_exit**2))
      p_star=p_exit*ms_exit p_star
      print*. "p_star=". p_star
```

```
111 continue
    ms_in=(ms_in_max-ms_in_min)/2.0

    error1=(1-(gama-1)/2*ms_exit**2)/(1-(gama-1)/2*ms_in_max**2)
    error1=(gama-1)/2/gama*log(ms_in_max**2/ms_exit**2*error1)
    error1=(1/ms_in_max**2-1/ms_exit**2)/gama-error1
    error1=4*fbar*tube_l/dh-error1

c     print*, "error1=", error1

    error2=(1-(gama-1)/2*ms_exit**2)/(1-(gama-1)/2*ms_in_min**2)
    error2=(gama-1)/2/gama*log(ms_in_min**2/ms_exit**2*error2)
    error2=(1/ms_in_min**2-1/ms_exit**2)/gama-error2
    error2=4*fbar*tube_l/dh-error2

c     print*, "error2=", error2

    error=(1-(gama-1)/2*ms_exit**2)/(1-(gama-1)/2*ms_in**2)
    error=(gama-1)/2/gama*log(ms_in**2/ms_exit**2*error)
    error=(1/ms_in**2-1/ms_exit**2)/gama-error
    error=4*fbar*tube_l/dh-error

    print*, "error=", error

    if(error1.ge.0.0.and.error.ge.0.0) then
    ms_in_max=ms_in
    ms_in_min=ms_in_min

    end if

    if(error1.ge.0.0.and.error.le.0.0) then
    ms_in_max=ms_in_max
    ms_in_min=ms_in

    end if

    if(error1.le.0.0.and.error.ge.0.0) then
    ms_in_max=ms_in_max
    ms_in_min=ms_in

    end if

    if(error1.le.0.0.and.error.le.0.0) then
    ms_in_max=ms_in
    ms_in_min=ms_in_min
```

```
      end if

      p_in=sqrt((gama-1)/(2+(gama-1)*ms_in**2))
      p_in=p_star*p_in/ms_in
      p_gage=p_in-14.7

      if(abs(error).ge.0.0001) go to 111

      print*, "p_gage=", p_gage

      pause 1

222 stop
    end
```

Appendix D Program Concentration

The following is the Fortran program used to find concentration, mach number and density from a mixture.

```
      program main

c     This program is used to find out the density & mixture quantities
c     with given total pressure, total temperature & velocity
c
          dimension error(0:1000)
          real mach

          print*, "1. Helium   gama=1.667"
      print*, "2. Nitrogen gama=1.4"
      print*, "3. Krypton  gama=1.24"
          print*, "Which gas is from the Jet(1, 2 or 3)?"
          read(*,*) num_gas
          print*, "What is the distance (cm)"
          read(*,*) dist



          if(num_gas.eq.1) then

      gama_gas=1.667
          cp_gas=5188.5
          R_gas=2077

          end if

          if(num_gas.eq.2) then

      gama_gas=1.4
```

```
      cp_gas=1003.5
      R_gas=287

      end if

      if(num_gas.eq.3) then

    gama_gas=1.24
      cp_gas=5115.5
      R_gas=99

      end if

      print*, "Input total pres(psi), total temp(C), velocity(m/s)"
      read(*,*)pres_total, Temp_total, vel
      Temp_total=Temp_total-273.15

      gama_amb=1.4
      cp_amb=1003.5
      R_amb=287
      pres_amb=14.7


      error_least=1000

      do 10 I=0, 1000
      x=float(I)/1000

      gama=x*gama_gas+(1.0-x)*gama_amb
      cp=x*cp_gas+(1.0-x)*cp_amb

      error(I)=Temp_total/(Temp_total-vel*vel/2.0/cp)
      error(I)=pres_total/pres_amb-error(I)**(gama/(gama-1.0))
      print*, error(I)

c     The following finds the least error
      if(abs(error(I)).lt.error_least)then
      error_least=abs(error(I))
      gama_final=gama
      cp_final=cp
      x_final=x

      end if

10    continue
```

```
      gama=gama_final
      cp=cp_final
      x=x_final
      R=x*R_gas+(1.0-x)*R_amb


30    print*, "x,gama,cp,R,error", x, gama, cp, R, error_least

      pause 3


      temp_static=Temp_total-vel**2/2.0/cp

      mach=(pres_total/pres_amb)**(1.0-1.0/gama)-1.0
      mach=sqrt(2.0/(gama-1.0)*mach)

      ro_static=pres_amb*101325/14.7/R/temp_static

      ro_total=ro_static*(1.0+(gama-1)/2*mach**2)**(1.0/(gama-1.0))

    open(9,file="param.txt", status="old", access="append")

      write(9,100) dist/0.7, x, mach, ro_static, ro_total
100   format(1x, 5(1x, f10.4))

      close(9)

      pause 4

      stop
      end
```

Appendix E Energy Balance

As being mentioned in Chapter VII, one method of validating the jet flow is by means of Energy Balance, which will be introduced as below.

Consider the jet flow modeled in Figure E.1. The jet flow is issuing into still air with the exit diameter 7mm. One cone with the centerline overlapping with the jet flow centerline and two planes perpendicular to the centerline, one of which is at the jet exit plane, while the other is at any downstream location, were chosen to form the control volume.

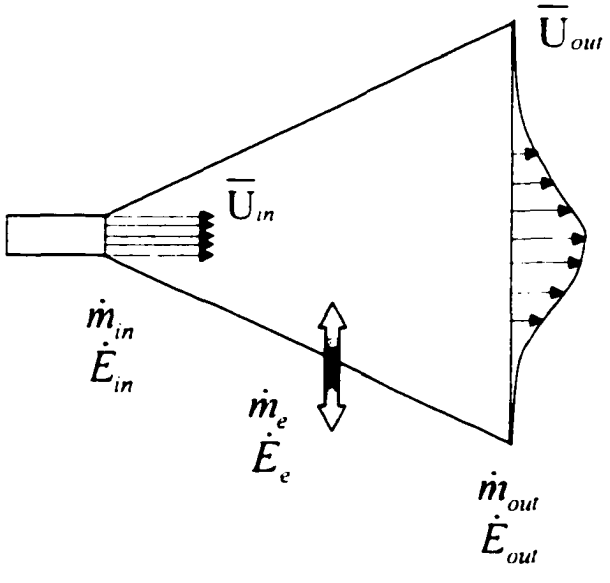

Figure E.1: Energy Balance Concept

Outside of the control volume, the condition is the same as the ambient. If both planes have known conditions, such as velocity, density, and total temperature, the corresponding mass flow rates, shown in Figure E.1 as $\dot{m}_{in}$ and $\dot{m}_{out}$ respectively, will also be available by integration of ρV over the cross sectional area, where ρ is the density and V is the velocity. Thus the entrained mass flow rate $\dot{m}_e$ can be obtained by continuity,

$$\dot{m}_e = \dot{m}_{out} - \dot{m}_{in} \qquad \text{(E.1)}$$

So the mass in the control volume is balanced, it is then possible to verify correspondingly if the energy in the control volume is also balanced, that is to show

$$\dot{E}_e = \dot{E}_{out} - \dot{E}_{in} \qquad \text{(E.2)}$$

One example based on Mach number 0.9 nitrogen jet is given below to demonstrate the whole procedure to verify energy balance in the jet flow. The right side plane of the control volume was selected at x/D=8.14.

To calculate static temperature, density and velocity, the following formulas are used,

$$\frac{p_0}{p} = \left[\frac{T_0}{T}\right]^{\frac{\gamma}{\gamma-1}} \qquad \text{(E.3)}$$

$$\rho = \frac{p}{RT} \tag{E.4}$$

$$V = \sqrt{2C_p(T_0 - T)} \tag{E.5}$$

With the known quantities, total pressure and total temperature from our experiments, static temperature, density and velocity are obtained for the mass and energy calculation.

$$\dot{m}_{in} = \rho V A = 0.01498 \text{ kg/s}$$

$$\dot{m}_{out} = \int \rho V 2\pi r dr = 0.1511 \text{ kg/s}$$

$$\dot{m}_e = \dot{m}_{out} - \dot{m}_{in} = 0.1361 \text{ kg/s}$$

$$\dot{E}_e = \dot{m}_e C_p T_0 = 42119 \text{ J/s}$$

$$\dot{E}_{in} = \dot{m}_{in} C_p T_i = 4635 \text{ J/s}$$

$$\dot{E}_{out} = \int \rho V T_0 2\pi r dr = 45203 \text{ J/s}$$

It can be seen that the energy entering the control volume from both the jet exit and the entrainment is slightly (4%) larger than that from the outgoing energy, which illustrates a good balance.

Bibliography

[1] Adrian, J.R. "Image Shifting Technique To Resolve Directional Ambiguity In Double-Pulsed Velocimetry" *Applied Optics*, Vol. 25, No. 21, November 1986, pp. 3855-3858

[2] Aihara, Y., Koyama, H. and Morishita, E. "Effects Of An Air Stream On Turbulent Diffusion Of A Helium Jet From A Small Nozzle" *The Physics of Fluids*, Vol 17, No. 4, April 1974, pp. 665-673

[3] Al-Ammar, K., Agrawal, A.K., Gollahalli, S.R., Griffin, D. "Application of Rainbow Schlieren Deflectometry for Concentration Measurements in an Axisymmetric Helium Jet "*Experiments in Fluids* 25(1998)89-95, pp. 89-95

[4] Andreopoulos, Y., Agui, J.H., Wang, Z. and Hermening, K. "Interactions of Turbulent Jets with Traveling Shock Waves" *AIAA-2000-0929 38th Aerospace Sciences 10-13 January 2000, Reno, NV*

[5] Antonia, R.A., Zhao, Q. "Effect of Initial Conditions on a Circular Jet" *Experiments in Fluids* 31 (2001) 319-323

[6] Armstrong, R.R., Michalke, A. and Fuchs, H.V. 1977 "Coherent Structures In Jet Turbulence And Noise", *AIAA J.* 15, 1011-1017.

[7] Arnette, S.A., Samimy, M., and Elliott G.S. "On Streamwise Vortices In High Reynolds Number Supersonic Axisymmetric Jets" *Phys. Fluids A* 5 (1), January 1993, pp. 187-202

[8] Barre, S., Bonnet, J.P., Gatski, T.B., and Sandham, N.D. Compressible, High Speed Flows, Closure Strategies for Turbulent and Transitional Flows *Cambridge University Press*, 2002, 768 pp

[9] Bastin, F., Lafon, P. and Candel, S. "Computation of jet mixing noise due to coherent structures: the plane jet case" *J. Fluid Mech.* (1997), vol. 335, pp. 261-304

[10] Boersma, B.J. & Lele, S.K. "Large Eddy Simulation of Compressible Turbulent Jets" *Annual Research Briefs 1999*

[11] Bogdanoff, D.W. "Compressibility Effects in Turbulent Shear Layers" *AIAA Journal*, Vol. 21, No. 6, pp. 926-927

[12] Bremhorst, K. and Hollis, P.G. "Velocity Field of an Axisymmetric Pulsed, Subsonic Air Jet" *AIAA Journal*, vol. 28, NO. 12, December 1990, pp. 2043-2049

[13] Brown, G.L., and Roshko, A. "On Density Effects And Large Structure In Turbulent Mixing Layers" *J. Fluid Mech.* (1974), vol. 64, pp. 775-816

[14] Capp, S.P., Hussein, H.J. & George, W.K. 1990 "Velocity Measurements in a High Reynolds Number Momentum-Conserving Axisymmetric Turbulent Jet" Tech. Rep. 123

[15] Clements, N.T., Petullo, S.P. and Dolling D. S. "Large Scale Structure Evolution In Supersonic Interacting Shear Layers" *AIAA Journal*, vol. 34, NO. 10, October 1996, pp. 2062-2070

[16] Colonius, T., Lele, S.K. and Moin, P. 1997 "Sound Generation In A Mixing Layer". *J. Fluid Mech.* 330, 375-409.

[17] Corriveau, A.F., Baines, W.D. "Measurements of the Velocity of High-Concentration Zones in a Turbulent Jet" *Experiments in Fluids* 23(1997)193-201

[18] Crow, S.C. and Champagne, F.H. 1971 "Orderly Structure In Jet Turbulence". *J. Fluid Mech.* 48, 547-591.

[19] Damkevala, R.J., Grosche, F.R. and Guest, S.H. 1973 "Direct Measurement Of Sound Sources In Air Jets Using The Crossed Beam Correlation Technique". *Noise Mechanisms AGARD CP* 131, pp. 3-1 to 3-16.

[20] Davey, R.F. and Roshko, A. "The Effect Of A Density Difference On Shear Layer Instability" *J. Fluid Mech.* (1972), vol. 53, pp. 523-543

[21] Favre-Marinet, M., Camano, E.B., Sarboch, J. "Near-Field Of Coaxial Jets With Large Density Differences" *Experiments in Fluids* 26 (1999), pp. 97-106

[22] Fenno Jr., C.C., Bayliss, A. and Maestrello, L. "Interaction of Sound from Supersonic Jets with Nearby Structures" *AIAA Journal* vol. 36, NO. 12, December 1998, pp. 2153-2162

[23] Ferdman, E., Ötügen, M.V., and Kim, S. "Effect Of Initial Velocity Profile On The Development Of Round Jets" *Journal of Propulsion and Power* Vol. 16, No. 4, July-August 2000, pp. 676-686

[24] Ffowcs Williams, J.E. 1963 "The Noise From Turbulence Convected At High Speed". *Phil. Trans.* A 255, 469-503

[25] Ffowcs Williams, J.E. 1973 "Technical evaluation report. Noise Mechanisms". *AGARD CP* 131, VII-XIX.

[26] Freund, J.B. 2001 "Noise Sources In A Low-Reynolds-Number Turbulent Jet At Mach 0.9" *J. Fluid Mech.* 438, 277-305.

[27] Fukushima, C., Aanen, L., Westerweel, J. "Investigation Of The Mixing Process In An Axisymmetric Turbulent Jet Using PIV And LIF" *10th Int. Symp. on Applications of Laser Techniques to Fluid Mechanics (Lisbon, Portugal)* July 10-13, 2000.

[28] Gibson, M.M. and Younis, B.A. "Modeling the Curved Turbulent Wall Jet" *AIAA Journal* vol. 20, NO. 12 December 1982, pp. 1707-1712

[29] Gutmark, E., J., Schadow, K., C., & Yu, K., H., 1995, "Mixing Enhancement in Supersonic Free Shear Flows." *Ann. Rev. Fluid Mech.*, vol. 27, 375.

[30] Haertig, J., Havermann, M., Rey, C., George, F. "PIV Measurements In Mach 3.5 And 4.5 Shock Tunnel Flow" *AIAA-2001-0699 39th Aerospace Sciences Meeting and Exhibit, 8-11 January 2001, Reno, NV*

[31] Hammad, K.J. and Shekarriz, A. "Turbulence in Confined Axisymmetric Jts of Newtonian and Non-Newtonian Fluids" *1998 ASME Fluids Engineering Division Summer Meeting* June 1998 pp 1-8

[32] Hileman, J. and Samimy, M. "Turbulence Structures and the Acoustic Far Field of a Mach 1.3" Jet *AIAA Journal* vol. 39, NO. 9, September 2001, pp. 1716-1727

[33] Hileman, J. and Samimy, M. "An Attempt To Identify Noise Generating Turbulent Strictures In A High Speed Axisymmetric Jet" *AIAA-2000-2020 38th Aerospace Sciences 10-13 January 2000, Reno, NV*

[34] Hu, H., Saga, T., Kobayashi, T. and Taniguchi, N. "Simultaneous Velocity And Concentration Measurements Of A Turbulent Jet" *Mixing Flow Proceddings of International Symposium on Visualization and Image in Transport Phenomena, Turkey*, 14-19 Oc. 2001

[35] Hurdle, P.M., Meecham, W.C. and Hodder, K. 1974 "Investigation Of The Aerodynamic Noise Generating Region Of A Jet Engine By Means Of The Simple Source Fluid Dilatation Model". *J. Acoust. Soc. Am.* 56, 1708-1721.

[36] Hussain, A.K.M.F. and Clark, A.R. 1977 "Upstream Influence On The Near Field Of A Plane Turbulent Jet". Phys. Fluids 20, 1416-1426.

[37] Ikawa, H. (1973) "Turbulent Mixing layer in supersonic flow" *Ph.D. Thesis*, California Institute of Technology

[38] Jiang, L.Y. and Sislian, J.P. 1998 "Velocity And Density Measurements In Supersonic High-Temperature Exhaust Plume". *AIAA J.* 36, 1216-1222.

[40] Kinzie, K.W. "Measurements of Supersonic Helium Air Mixture Jets" *AIAA Journal* vol. 37, NO. 11, November 1999, pp. 1363-1369

[41] Kouros, H., Medina, R., and Johari, H. "Spreading Rate of an Unsteady Turbulent Jet" *AIAA Journal*, Vol. 31, No. 8, pp. 1524-1526

[42] Kulik, R.A., Leithem J.J., and Weinstein, H. "Turbulence Measurements In A Ducted Coaxial Flow" AIAA Journal vol. 8, NO. 9, Septemer 1970, pp. 1694-1696

[43] Lachowicz, J.t., Yao, C., Wlezien, R.W. "Flow Field Characterization of a Jet and Vortex Actuator" *Experiments in Fluids* 27 (1999) 12-20

[44] Lam, K.M. and Ko, N.W.M. "Investigation of Flow Structures of a Basic Annular Jet" *AIAA Journal*, Vol. 24, No. 9, pp. 1488-1493

[45] Lau, J.C. 1981 "Effects Of Exit Mach Number And Temperature On Mean Flow And Turbulence Characteristics In Round Jets". *J. Fluid Mech.* 105, 193-218.

[46] Lau, J.C. "Mach Number and Temperature on Jets". *AIAA Journal*, Vol. 18, No. 6, June 1980, pp. 609-610

[47] Lele, S. K., 1994, "A Compressibility Effects on Turbulence." *Ann. Rev. Fluid Mech.*, vol. 26, pp. 211-254.

[48] List, E.J. "Turbulent Jets And Plumes" Ann. *Rev. Fluid Mech.* 1982. 14:189-212

[49] Liepmann, H.W. and Roshko, A. 1958 Elements of Gasdynamics *John Wiley & Sons*, 1957, 456 pp

[50] Lighthill, M.J. 1954 "On Sound Generated Aerodynamically I. General Theory". *Proc. R. Soc. Lond. A* 221, 564-587.

[51] Lilley, G.M. 1972 "The Generation And Radiation Of Supersonic Jet Noise IV". *Theory of turbulence generated noise*. USAPL TR-72-53.

[52] Lowson, M.V. and Ollerhead, J.B. 1968 "Visualization Of Noise From Cold Supersonic Jets". *J. Acoust. Soc. Am.* 64, 624-630.

[53] Maydew, R.C., and Reed, J.F. (1963) "Turbulent Mixing of Compressible Free Jets" *AIAA J.* 1, 1443-1444.

[54] McLaughlin, D.K., Morrison, G.L. and Troutt, T. R. 1975 "Experiments On The Instability Waves In Supersonic Jets And Their Acoustic Radiation". *J Fluid Mech.* 69, 73-95.

[54] McMackin, L., Hugo, R.J., Bishop, K.P., Chen, E.Y., Pierson, R.E., Truman, C.R. "High Speed Optical tomography System for Quantitative Measurements and Visualization of Dynamic Features in a Round Jet" *Experiments in Fluids* 26(1999) 249-256

[55] Meinhart, C.D., Steve, T.W., Juan, G.S. "A PIV Algorithm for Estimating Time-averaged Velocity Fields" *Journal of Fluid Engineering* JUNE 2000, Vol. 122 pp. 285-289

[56] Meinhart, C.D. and Zhang, H The flow Structure "Inside a Microfabricated Inkjet Printhead" *Journal of Microelectronmechanical Systems*, Vol. 9, No. 1, March 2000, pp. 67-75

[57] Meinhart, C.D., Wereley S.T., Santiago J.G. "PIV Measurement Of A Microchannel Flow" *Experiments in Fluids* 27 (1999), pp. 414-419

[58] Michalke, A. 1970 "A Wave Model For Sound Generation In Circular Jets". *DLR Rep. FB* 70-57.

[59] Michalke, A. 1972 "An Expansion Scheme For The Noise From Circular Jets". *Z. Flugwissensch.* 20, 229-237.

[60] Mollo-Christensen, E. 1967 "Jet Noise And Shear Flow Instability Seen From An Experimenter's Viewpoint". Trans. *ASME J.* Appl. Mech. 89, 1-7.

[61] Montealegre, P. and Weinstein, H. "The Mixing Of Homogeneous Coaxial Streams" *Israel Journal of Technology*, Vol. 9, Nos. 1-2, 1971, pp. 141-150

[62] Moore, C.J. 1977 "The Role Of Shear-Layer Instability Waves In Jet Exhaust Noise" *J. Fluid Mech.* 80, 321-367.

[63] Morris, P.J. and Tam, C.K.W. 1979 "On The Radiation Of Sound By The Instability Waves Of A Compressible Axisymmetric Jet". *In Mechanisms of Sound Generation in Flows (ed. E. A. Muller) Springer.*

[64] Morrison, G.L. and McLaughlin, D.K. 1979 "Noise Generated By Instabilities In Low Reynolds Number Supersonic Jets" *J. Sound Vib.* 65, 177-191.

[65] Narayanan, S., Barber, T.J. and Polak, D.R. "High Subsonic Jet Experiments": *Turbulence and Noise Generation Studies AIAA Journal*, Vol. 40, No. 3., March 2002, pp. 430-437

[66] Panchapakesan, N.R. and Lumley, J.L. "Turbulence Measurements In Axisymmetric Jets Of Air And Helium Part 1" *J. Fluid Mech.* (1993), vol. 246, pp. 197-223

?? Panchapakesan, N.R. and Lumley J.L "Turbulence Measurements In Axisymmetric Jets Of Air And Helium Part 2" *J. Fluid Mech.* (1993), vol. 246, pp. 225-247

?? Panda, J. and Seasholtz R.G. "Experimental Investigation Of Density Fluctuations In High-Speed Jets And Correlation With Generated Noise" *J. Fluid Mech.* (2002), vol. 450, pp. 97-130

?? Panda, J. and Seasholtz, R.G. 1999a "Velocity And Temperature Measurement In Supersonic Free Jets Using Spectrally Resolved Rayleigh Scattering", *AIAA Paper* 99-0296.

?? Panda, J. and Seasholtz, R.J. 1999b "Measurement Of Shock Structure And Shock-Vortex Interaction In Underexpanded Jets Using Rayleigh Scattering", *Phys. Fluids* 11, 3761-3777.

?? Papadopoulos, G. and Pitts, W.M. "A Generic Centerline Velocity Decay Curve For Initially Turbulent Axisymmetric Jets" *ASME* Vol. 121, March 1999, pp. 80-85

?? Papadopoulos, G. and Pitts, W.M. "Scaling the Near-Field Centerline Mixing Behavior of Axisymmetric Turbulent Jets" *ASME* Vol. 121, March 1999, pp. 80-85

?? Papamoschou, D. 1997 "Mach Wave Elimination In Supersonic Jets", *AIAA J.* 35, 1604-1611.

?? Papamoschou, D. and Roshko, A. "The Compressible Turbulent Shear Layer: An Experimental Study" *J. Fluid Mech.* (1988), vol. 197, pp. 453-477

?? Philips, O.M. 1960 "On The Generation Of Sound By Supersonic Turbulent Shear Layers" *J. Fluid Mech.* 9, 1-28.

?? Pitts, W.M. and Kashiwagi, T. 1984 "The Application Of Laser-Induced Rayleigh Scattering To The Study Of Turbulence Mixing" *J. Fluid Mech.* 141, 391-429.

?? Proudman, I. 1952 "The Generation Of Noise By Isotropic Turbulence" *Proc. R. Soc. Lond. A* 214, 119-132.

?? Raffel, M., Willert, C., Kompenhans, J. Particle Image Velocimetry *Springer*

?? Richarz, W.G. 1979 "Direct Correlation Of Noise And Flow Of A Jet Using Laser Doppler" *AIAA Paper* 79-0571.

?? Ricou, F.P. and Spalding, D.B. "Measurements Of Entrainment By Axisymmetrical Turbulent Jets" *Journal of Fluid Mechanics*, 11, pp. 21-32

[81] Rodi, W. "A New Method Of Analyzing Hotwire Signals In Highly Turbulent Flow And Its Evaluation In A Round Jet" 1975a. *DISA information* 17, Feb. 1975

[82] Saad, M.A. Compressible Fluid Flow Second Edition *Prentice-Hall, Inc.*, 1993, 560 pp.

[83] Saleh, B.E.A. and Teich, M.C. 1991 Fundamentals of Photonics. *John Wiley & Sons*, 1991, 992 pp.

[84] Samimy, M. and Wernet, M.P. "Review of Planar Multiple-Component Velocimetry in High-Speed Flows" *AIAA Journal*, Vol. 38, No. 4, pp. 553-574

[85] Schaffer, M. 1979 "Direct Measurements Of The Correlation Between Axial In-Jet Velocity Fluctuations And Far Field Noise Near The Axis Of A Cold Jet" *J. Sound Vib.* 64, 73-83.

[86] Schneider, G.M., Froud, D., Syred, N., Nathan, G.J., Luxton, R.E. "Velocity Measurements in a Precessing Jet Flow Using a Three Dimensional LDA System" *Experiments in Fluids* 23(1997)89-98

[87] Seasholtz, R.G. and Panda, J. 1999 "Multiple Point Dynamic Gas Density Measurements Using Molecular Rayleigh Scattering" *NASA TM* 1999-209295.

[88] Seasholtz, R.G., Zupanc, F.J. and Schneider, S.J. 1992 "Spectrally Resolved Rayleigh Scattering Diagnostic For Hydrogen-Oxygen Rocket Plume Studies" *J. Propulsion Power* 8, 935-942.

[89] Seiner, J.M. and Reethof, G. 1974 "On The Distribution Of Source Coherency In Subsonic Jets" *AIAA Paper* 74-4.

[90] Siriex, M., and Solignac, J.L. (1966) "Contribution a l'etude experiments de la couche de melange turbulent isobare d'un ecoulament supersonique" ONERA AGARD Symposium Rhode – Saint Genese

[91] Smits, J.A. and Dussauge, J.P. 1996 "Turbulent Shear Layers in Supersonic Flow" *AIP Press*

[92] Spina, E., F., Smits, A., J., & Robinson, S., K., 1994, "The Physics of Supersonic Turbulent Boundary Layers." *Ann. Rev. Fluid Mech.*, vol. 26, 287.

[93] Tao, B., Katz, J. and Meneveau, C. "Statistical Geometry of Subgrid-Scale Stresses Determined from Holographic Particle Image Velocimetry Measurements" *J. Fluid Mech.* (2002), vol. 457, pp. 35-78

[94] Tennekes, H. and Lumley, J.L., A First Course in Turbulence Sixteenth Printing, *The MIT Press*, 1997

[95] Tsurikov, M.S. and Clements, N.T. "The Structure of Dissipative Scales in Axisymmetric Turbulent Gas-Phase Jets" *AIAA* 2002-0164

[96] Way, J. and Libby, P.A. "Hot-Wire Probes for Measuring Velocity and Concentration in Helium-Air Mixtures" *AIAA Journal* (1970), vol. 8, NO. 5, pp. 976-978

[97] Way, J. and Libby, P.A. "Application Of Hotline Anemometry And Digital Techniques To Measurements In A Turbulent Helium Jet" *AIAA Journal* vol. 9, NO. 8, August 1971, pp. 1567-1573

[98] Weisgraber, T.H., Liepmann, D. "Turbulent Structure During Transition to Self-similarity in a Round Jet" *Experiments in Fluids* 24 (1998) 210-224

[99] Welch, P.D. 1967 "The Use Of Fast Fourier Transform For The Estimation Of Power Spectra: A Method Based On Time Averaging Over Short, Modified Periodograms", *IEEE Trans. Audio Electroacoust.* AU-15, 70-73.

[100] Westerweel, J. "Fundamentals of Digital Particle Image Velocimetry" *Meas. Sci. Technol.* 8 (1997) 1379-1392

[101] Wilson, L.N. and Damkevala, R.J. 1970 "Statistical Properties Of Turbulent Density Fluctuations" *J. Fluid Mech.* 43, 291-303.

[102] Wygnanski, I. & Fiedler, H. "Some Measurements In The Self-Preserving Jet" *J. Fluid Mech.*, 1969, Vol. 38, pp. 577-612

[103] Yu, J.C. and Dosanjh, D.S. 1972 "Noise field Of A Supersonic Mach 1.5 Cold Model Jet" *J. Acoust. Soc.* Am. 51, 1400-1410.

[104] Yüceil, K.B., Ötügen, M.V. and Arik, E. "Underexpanded Sonic Jets: A PIV Study" *10th International Symposium on the Applications of Laser*

[105] Yüceil, K.B., Ötügen, M.V. "Scaling Parameters for Underexpanded Supersonic Jets" *Physics of Fluids*, Dec. 2002, Vol. 14, No. 12, pp. 1-10

[106] Zaman, K. B. M. Q. 1986 "Flow Field And Near And Far Sound Field Of A Subsonic Jet" *J. Sound Vib.* 106, 1-16.

[107] Zhao, W., Frankel, S.H. and Mongeau, L. "Large Eddy Simulations Of Sound Radiation From Subsonic Turbulent Jets" *AIAA Journal*, vol. 39, NO. 8, August 2001, pp. 1469-1477